NCAR/CT 167

Katholieke Universiteit Leuven

Faculteit Wetenschappen
Centrum voor Plasma Astrofysica

Numerical simulation and analysis of magnetically dominated MHD bow shock flows with applications in space physics

Hans De Sterck

Proefschrift voorgelegd tot
het bekomen van de graad van
Doctor in de Wetenschappen

Promotoren:
Prof. Dr. S. Poedts
Dr. B. C. Low

MONICA: Magnetohydrodynamics Over Notoriously Incomputable Cylindrical Apparatus (T. J. Barth)

Thank you

I have really enjoyed a lot doing the work for this dissertation at the Centre for Plasma Astrophysics (CPA) in Leuven and at the High Altitude Observatory (HAO) in Boulder, and I want to thank all the people I met and interacted with at CPA and HAO.

In particular, I am much indebted to my thesis advisors Stefaan Poedts and B. C. Low, who always left me the freedom to work on what really interested me, while at the same time providing me with their expert guidance and support.

At CPA I enjoyed a nice and cosy working atmosphere for which I thank Marcel Goossens, Arnold Debosscher, Petra, Michael, Vladimir, Wouter, Hilde, Arnout, David, Peter, Robert, Balasz, Arpi, Vladimir, Ronald and the 'newer generation' that I only met occasionally after having moved to HAO.

I have also spent a few months at the FOM Institute in Nieuwegein, and I thank Hans Goedbloed, Rony Keppens and Sander Beliën for the hospitality and for the interesting and nice time spent there.

David Vanden Abeele and Herman Deconinck provided me with the von Karman multi-block code which was an invaluable starting point for the numerical work I did for my thesis. I have also had a very fruitful exchange with Gabor Tóth on numerical techniques.

During my three years in Boulder I enjoyed a working place at HAO which was at the same time very professional and very sympathetic. I thank Keith MacGregor, Art Hundhausen, Tom Holzer and Gang Lu for interesting discussions on the thesis work. Many fellow-students and postdocs became good friends, and the countless lunchtime basketball games, after-work volleyball games, the weekend hikes and dinners were welcome changes of mind and could even be counted among the sources of inspiration for this work. I thank my office-mate and brother-in-arms Chano, and my friends Rob, Cheryl, Hanli, Elain, Scott, Mausumi, Wouter, Thierry, José, Chip, Debrah, Cindy, Wayne, Graham, Colin, Colin, and many others for all of this.

When I occasionally went back to Belgium, I always got a warm welcome from Bernard, Hilke, and the whole sporex-gang, who made me feel back at home in Leuven right away.

My sisters and parents have always warmly supported me in all I wanted to do. Finally I want to thank Marina for all the support while living much of this with me.

Contents

Chapter 1

Introduction

The general subject of this dissertation is the numerical study of shock phenomena in magnetohydrodynamic (MHD) plasmas.

Shock phenomena in gases are common and can be experienced in everyday life — a well-known example is the sonic boom caused by supersonic airplanes. Shocks are discontinuous jumps in macroscopic quantities like velocity, pressure and density.

A plasma is an *ionized* gas, and exhibits more complex behavior than a neutral gas, because of electromagnetic effects. Electric and magnetic fields exert anisotropic forces on the *charged* particles which constitute a plasma, and the charge and the current carried by the particles influence the electric and magnetic fields. Like in neutral gases, shocks can form in plasmas, but plasma shock phenomena exhibit a richer complexity and variety than their neutral gas counterparts. Shock phenomena in plasmas continue to be investigated today because the basic physical processes are not fully understood.

Most of the matter in the solar system is in the plasma state, and plasma shocks are ubiquitous in the solar system. Bow shocks are formed in front of planets and comets by the supersonic solar wind. Fast ejections of mass from the solar corona induce leading shock fronts. These ejecta with associated shock fronts may travel in the direction of the earth as magnetic clouds which can cause severe disruptions of the earth's magnetic environment. Plasma shock phenomena also play an important role in other astrophysical plasmas and in laboratory plasmas.

Many scientific spacecraft have been launched in the last decades to collect observational data on solar system plasmas. Important examples include the Ulysses mission which studies planets and the interplanetary medium, the Solar and Heliospheric Observatory (SOHO) which is dedicated to the study of the sun, and the CLUSTER mission which will be launched by mid-2000 to observe the earth's bow shock and magnetosphere. These spacecraft provide a wealth of observational data on shock phenomena in solar system plasmas. Those observations reveal many unexplained features, and an increased theoretical understanding of plasma shock phenomena is necessary for the interpretation of the observations.

There exists a hierarchy of theoretical models that describe plasma motions at different levels of complexity. The MHD approximation describes a plasma as a continuous electrically conducting fluid. This approach does not take into account microscopic plasma processes which may be important for the explanation of some physical phenomena, but it provides a consistent and tractable description of plasma flows with shocks on macroscopic scales. The MHD description of a plasma is adopted in this dissertation.

The results to be presented in this dissertation aim at contributing to the general theory of shock phenomena in MHD plasmas. In particular, the influence of intrinsically magnetic effects on bow shock flow topology is studied via numerical simulations of MHD bow shock flows in two and three spatial dimensions. The problem is studied in the classical setting of stationary bow shock flows around perfectly conducting rigid obstacles — cylinders, spheres and paraboloids. This abstract context allows to concentrate on the basic physical effects and to state the results in all their generality. At the same time, real space physics applications — for example the flow of the supersonic solar wind over an unmagnetized planet — remain conceptually close to this abstract setting, so it is not difficult to keep the practical importance of these abstract basic flow problems in mind.

The following specific subjects are addressed in this dissertation.

First, it is shown that when the flow upstream from the obstacle is magnetically dominated, stationary MHD bow shock flows exhibit a surprisingly complex topology involving multiple interacting shocks with segments of various MHD shock types. We call the upstream flow magnetically dominated — as opposed to pressure-dominated — when magnetic forces dominate over thermal and dynamic pressure effects such that the intrinsically magnetic phenomenon of the *switch-on shock* is encountered on the bow shock front. The resulting bow shock flow and bow shock topology are also called magnetically dominated. The complex magnetically dominated bow shock topology was not previously known, but can be understood in terms of the geometrical properties of MHD waves and shocks. This result adds to our general understanding of the phenomenology of MHD bow shock flows. It shows that there exist two basic topologies for MHD bow shock flows. For pressure-dominated upstream flows the traditional single-front topology arises which is well-known from hydrodynamic bow shock flows. Magnetically dominated MHD bow shock flows exhibit the new complex multiple-front topology.

Second, an in-depth analysis of the simulation results is given using analytical properties of the MHD equations, which confirms the presence of peculiar nonlinear MHD wave phenomena — in particular *intermediate shocks* and *compound shocks* — in the two-dimensional (2D) and three-dimensional (3D) simulation results. In recent years there has been much debate about the existence of these types of waves. Until recently they have mainly been studied in one-dimensional (1D) systems. Our simulation results seem to be the first clear confirmation of their existence in 2D and 3D.

Third, it is described how a robust and accurate numerical code has been developed for simulation of MHD flows with shocks. The PAR-MA (PARallel MAgnetohydrodynamics) code solves the mathematically well-behaved MHD equations on massively parallel computers using advanced numerical techniques. The numerical scheme used derives from state-of-the-art methods used in the field of Computational Fluid Dynamics. It is shown through careful validation studies that the extended numerical scheme produces valid results. It seems that the use of advanced numerical techniques and fast parallel computers was essential for obtaining the new results on magnetic effects in 2D and 3D MHD bow shock flows.

Fourth, it is shown how the simulation results are relevant for bow shocks in the solar system with magnetically dominated upstream flows. Two examples are discussed, namely shocks induced by fast coronal mass ejections (CMEs) propagating out of the solar corona, and the bow shock formed by the interaction of the sometimes magnetically dominated solar wind with the earth's magnetosphere.

Outline of the dissertation

Chapter 2 serves to introduce the general subject of this dissertation in an intuitive way. We give an overview of the results on MHD bow shock flows which are presented throughout the dissertation, and we sketch the broader context of the thesis research.

In Chapter 3 we describe analytical properties of the ideal MHD system. We present a derivation of the characteristic theory of steady MHD flow in 2D. We discuss the MHD Rankine-Hugoniot jump conditions, the non-convexity of the MHD flux function, and the properties of compound shocks.

In Chapter 4 we describe the PAR-MA finite volume numerical code that was developed to perform MHD flow calculations with shocks. We describe the spatial and temporal discretization, the control of the $\nabla \cdot \vec{B}$ constraint through a source term, and the implementation on parallel computers.

Chapter 5 contains a careful validation study of the numerical technique based on the simulation and characteristic analysis of 2D model flows with shocks.

In Chapter 6 we treat 2D symmetrical MHD bow shock flows around a cylinder with the magnetic field aligned to the plasma flow. A parameter study shows that intrinsically magnetic effects substantially change the topology of bow shocks for magnetically dominated upstream flows. A complex topology with a 'dimple' and secondary shock fronts results. We perform a detailed analysis of all the discontinuities present in these flows, and prove the presence of intermediate and compound shocks using characteristic theory.

In Chapter 7 we study 3D MHD bow shock flows over a sphere. A previously unknown topology is obtained for 3D magnetically dominated bow shock flows, containing two consecutive interacting shock fronts with shock segments of fast, intermediate and slow type.

Chapter 8 discusses how the new results on bow shock topology for magnetically dominated upstream flows are relevant for two examples of bow shock flows in the solar system. We describe how observations of fast solar CMEs and observations of the earth's bow shock flow may show evidence of the complex bow shock topology which was discovered in our simulation results.

The topic of the existence of intermediate shocks is addressed in Chapter 9. We illustrate the main issues of the ongoing debate on the existence of intermediate shocks, and we show how our simulation results are relevant for this debate.

In Chapter 10 we formulate our conclusions and describe directions for future work.

Chapter 2

Fluid description of shock phenomena in gases and plasmas: a bird's eye view

In the present Chapter we introduce the general subject of this dissertation in an intuitive way. We discuss the concepts, ideas, techniques and terminology that are used to describe shock phenomena in fluids. We give an overview of the results on MHD bow shock flows which are presented throughout this dissertation. We introduce MHD shock phenomena in nature for which the simulation results are relevant.

We believe that it is important to attempt to give such a global overview of the results and their relevance in a single Chapter, which should be easily accessible. In doing so, we touch upon a great variety of often quite complicated subjects, such that our discussion cannot always be rigorous and complete, but necessarily has to remain intuitive at places. Such an intuitive introduction makes the results more easily accessible for the reader who is not so familiar with the topics addressed, while at the same time the more knowledgeable reader may appreciate being reminded of some basic aspects of the physics of shocks and space plasmas. Most of the material covered in this introductory Chapter is discussed more rigorously and completely in the following Chapters. Other topics are not revisited after their brief introduction in the present Chapter, in which case the reader is referred to the literature for more extensive information.

2.1 Hydrodynamic description of shock phenomena in gases

This dissertation deals with shock phenomena in MHD plasmas, which describe *ionized* gases. The dynamical behavior of a *neutral* gas already exhibits many phenomena which are of interest to us. Therefore we introduce some aspects of the fluid dynamics of neutral gases before turning our attention to MHD plasma phenomena.

Although gases consist of free particles which interact through collisions, it is for many purposes sufficient to give a mathematical description of a gas as a continuous fluid. Such a description is given by the hydrodynamic (HD) equations [20, 160, 90, 54]

$$\frac{\partial}{\partial t}\begin{bmatrix}\rho\\ \rho\,\vec{v}\\ e\end{bmatrix} + \nabla\cdot\begin{bmatrix}\rho\,\vec{v}\\ \rho\,\vec{v}\vec{v}+\mathsf{I}p\\ (e+p)\,\vec{v}\end{bmatrix} = \nabla\cdot(\mathsf{D}). \tag{2.1}$$

These equations are formulated in terms of the macroscopic thermodynamic quantities pressure p, mass density ρ and specific total energy e, and in terms of the bulk velocity $\vec{v}$. I is the unity matrix. These equations describe the conservation of mass, momentum and energy. The specific total energy e is given by

$$e = e_{int} + \rho\,\frac{\vec{v}\cdot\vec{v}}{2}, \tag{2.2}$$

with e_{int} the specific internal energy of the gas. The internal energy, the pressure, and the density are related by an equation of state. In this dissertation we assume ideal gas behavior for simplicity, such that (in suitable units)

$$e_{int} = \frac{p}{\gamma-1} \quad \text{and} \quad T = \frac{p}{\rho}, \tag{2.3}$$

where T is the temperature and γ is the adiabatic index. The ideal gas law is a good approximation for most space and solar plasmas. The tensorial quantity D in Eq. 2.1 represents the contribution from irreversible dissipative processes like viscosity and thermal conduction. The matrix of dissipative fluxes D depends on dissipative parameters like the viscosity, and on the state variables and gradients of the state variables. An ideal or dissipationless fluid is described by Eq. 2.1 with $\mathsf{D}\equiv 0$, in which case Eqs. 2.1 are called the Euler equations. When dissipative effects are included the equations are called the Navier-Stokes equations. Most real gasses have a finite dissipation, but this dissipation is often small. It can be neglected for many phenomena, in which case the ideal equations give a good approximate description of the behavior of the real gas.

The Euler equations (Eq. 2.1 with $\mathsf{D} \equiv 0$) allow for sound waves [20, 160, 90, 54], which for small amplitudes are linear perturbations propagating isotropically with the sound velocity

$$c = \sqrt{\frac{\gamma p}{\rho}}. \tag{2.4}$$

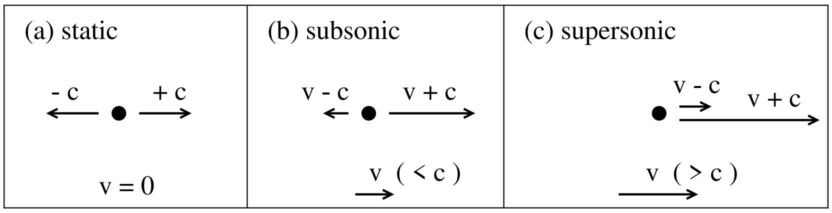

Figure 2.1: *A fixed point source sends out small-amplitude perturbations while a uniform fluid flows along the source with constant velocity v relative to the fixed source. In the frame of the moving fluid, the perturbations propagate to the left and to the right with the wave velocity c. In the frame of the source, the waves are carried by the fluid and propagate with velocities $v - c$ and $v + c$.*

Fig. 2.1 shows schematically how a small-amplitude perturbation generated by a fixed source would propagate in a hypothetical 1D system with uniform background flow. In the static case ($v = 0$), the perturbation propagates to the left and to the right with speeds $-c$ and $+c$ (a negative sign thus means propagation to the left). If there is a uniform background flow to the right with velocity $v < c$, then we say that the flow is *subsonic*. The perturbation can still propagate to the left and to the right with speeds $v - c$ and $v + c$, but $v - c$ now has a smaller magnitude than $v + c$. When the flow is *supersonic* ($v > c$), the perturbation can only propagate to the right, with speeds $v - c$ and $v + c$ both pointing rightwards. This means that in supersonic flow, information cannot propagate in the upstream direction. The sonic Mach number, which is defined as the ratio of the magnitude of the velocity vector and the sound speed

$$M = \frac{||\vec{v}||}{c}, \tag{2.5}$$

is greater than 1 for supersonic flow.

The HD equations 2.1 are *nonlinear*, which can cause large-amplitude waves (Fig. 2.2a) to steepen into shocks (Figs. 2.2b and c). The state variables jump discontinuously at shocks. For the Navier-Stokes equations, the steep shock profile actually remains smooth and the width of

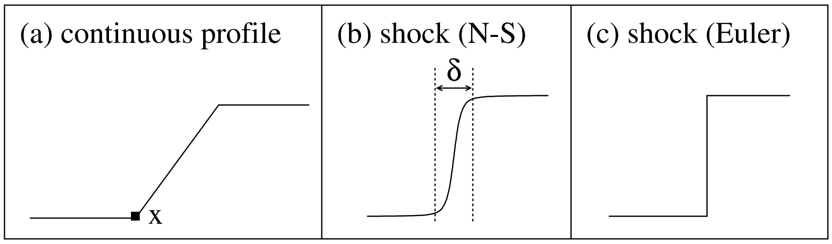

Figure 2.2: *Nonlinear steepening of a large-amplitude profile — for instance the density — into a shock.*

the shock layer δ is related to the values of the dissipative coefficients. The Euler equations, however, allow for strictly discontinuous shock solutions. Strictly speaking, a discontinuous profile cannot be a solution of the partial differential equation (PDE) 2.1, because derivatives are not defined at discontinuities. Discontinuous profiles, however, can be solutions of the *integral* form of the Euler equations, and in this case it is said that they are *weak* solutions of the PDE [90].

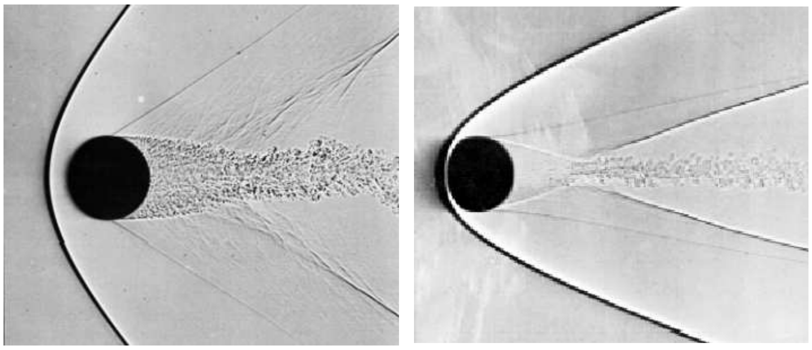

Figure 2.3: *Experimental shadowgraph pictures of a sphere in free flight through air at M=1.53 (left) and M=4.01 (right). (from* An Album of Fluid Motion*, M. Van Dyke [30])*

Fig. 2.3 shows shadowgraph pictures of an experiment where a small sphere flies freely through air (towards the left) with supersonic speeds ($M = 1.53$ and $M = 4.01$) [30]. The flow pattern around the sphere in the left panel of Fig. 2.3 shows several interesting phenomena. The sphere is preceded, on the left, by a paraboloid-like-shaped nearly stationary dark surface, which indicates a sudden jump in density. This surface is a shock surface, and is called a *bow shock*.

We can understand intuitively why this bow shock has to be present. First, let us set our mind on the coordinate system which moves to the left together with the sphere. In this frame, the sphere and the bow shock are nearly *stationary* or *steady*, which facilitates the analysis. In this frame, the gas to the left of the bow shock is no longer at rest, but moves to the right in the direction of the sphere with supersonic speed v. In this supersonic region to the left of the bow shock, information can only propagate to the right, as illustrated in Fig. 2.1c. However, the sphere has to be able to 'communicate' its presence to the flow in front of it, such that the flow field can adapt to the presence of the sphere. This requires that a *subsonic* region forms in the immediate front of the sphere, in which the sphere can make its presence felt through waves capable of propagating to the left (Fig. 2.1b). The flow far upstream (left) remains supersonic, and the subsonic region close to the sphere is connected to the supersonic region upstream by a shock surface. Conceptually, it is not immediately evident why the subsonic region close to the sphere and the supersonic region upstream necessarily have to be connected by a shock. One could imagine that the uniform supersonic upstream region could be connected to the subsonic region by a continuous profile, like in Fig. 2.2a, but stationary in the frame of the sphere. Intuitively one could say that such a continuous profile separating the two regions would steepen into a shock because of nonlinear effects, like in Fig. 2.2. A more sophisticated argument is the following. The small-amplitude perturbation at point x in Fig. 2.2a, where the uniform region would be connected to the slope, would have to move with the local small-amplitude wave speed $v - c$, which is determined by the sound speed c and the velocity v of the incoming supersonic flow. This observation shows that such a configuration can never be stationary in the frame of the sphere, because for supersonic flow $v > c$, and thus $v - c \neq 0$. The uniform supersonic region upstream thus necessarily has to be connected to the subsonic region close to the sphere by a *discontinuous profile* or shock, and analysis shows indeed that a shock can have a *shock speed* which exactly makes the shock stationary in the frame of the sphere.

At the backside of the sphere in the left panel of Fig. 2.3 we see several other structures. A *boundary layer* [160] separates from the sphere, and the flow is highly turbulent (and thus non-stationary) in the resulting wake. An additional shock can be seen where the boundary layer separates, both on the top and the bottom of the sphere in the figure. The $M = 4.01$ flow (right panel of Fig. 2.3) shows similar features as the $M = 1.53$ flow.

It is thus clear that shock phenomena in gases are quite complex. The HD equations offer an adequate description of many of these phenomena, but, mainly due to the inherent nonlinearity of the equations, it is hard to find explicit analytical solutions for 2D and 3D flow problems.

Therefore, the alternative to solve the HD equations using numerical methods on computers has proven to be a useful approach. When geometries are modeled accurately and parameter values are chosen with care, numerical simulations of Euler or Navier-Stokes flows around geometrically complex objects agree well with experiments [167]. Numerical simulations are especially useful to study physical phenomena in regimes of parameters and physical sizes for which experiments cannot reasonably be performed, and for which detailed observations are not available. It would seem that this applies to many phenomena in space physics and astrophysics.

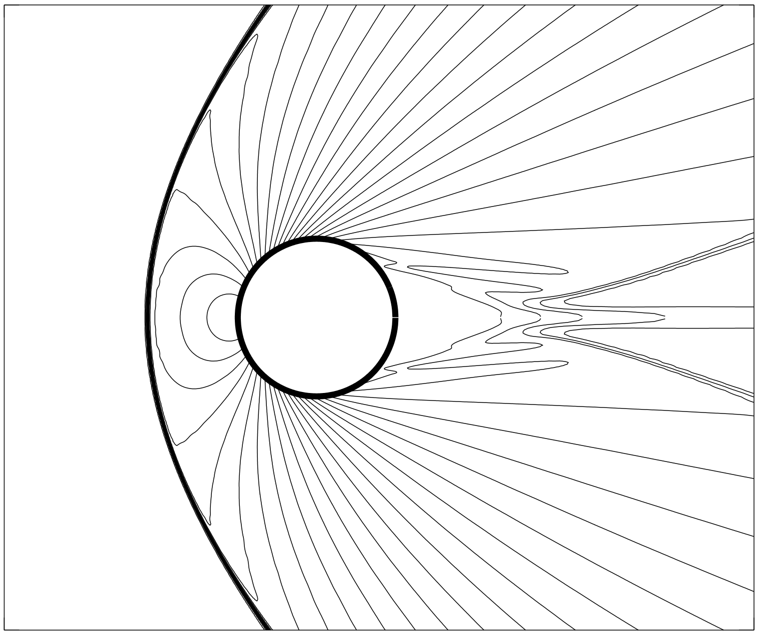

Figure 2.4: *Numerical simulation of supersonic hydrodynamic flow around a cylinder (thick solid). The flow comes in from the left ($M = 2.6$). Density contours (thin solid) pile up in shocks.*

In Fig. 2.4 we show numerical simulation results for the $M = 2.6$ flow of a gas around a cylinder. These simulations were performed with our numerical simulation code, which discretizes the ideal HD equations but introduces a small amount of numerical dissipation. Contours of equal density are shown. In this simulation we did not attempt to faithfully model the geometry and parameter regime of the experimental flows of Fig. 2.3, but we want to demonstrate in a qualitative way that the simulation results reproduce many of the flow features present in the experiments. The density contours pile up in a stationary bow shock on the left of the cylinder. Boundary layers separate from the back of the cylinder. The spatial resolution of the simulation is not high enough, however, to reproduce turbulence in the wake [167].

In this dissertation, we study stationary bow shock configurations around cylinders and spheres, much like the configurations in Figs. 2.3 and 2.4, using numerical simulation techniques. Most of the time we focus on the bow shock itself. This allows us to limit the simulation to the half-plane on the upstream side of the center of the cylinder or the sphere. We then expect a resulting flow which is in a perfect non-turbulent steady state. We are, however, not concerned with flows in non-conducting fluids which describe neutral gases, but on the contrary we are interested in bow shock flows in MHD plasmas which model *ionized* gases. Much of the discussion on neutral gas dynamics that was given above, remains relevant for plasma flows. The fact that plasma particles are charged and MHD plasmas thus conduct currents, however, introduces interesting additional dynamical effects, which are discussed next.

2.2 Magnetohydrodynamic description of shock phenomena in plasmas

At sufficiently high temperatures, the atoms or molecules in a gas lose negatively charged electrons and thus become positively charged ions themselves. Such a gas of charged particles is called a plasma.

A continuous fluid description of a plasma is given by the magnetohydrodynamic (MHD) equations [87, 118, 7, 54]. We now briefly introduce the MHD equations and the properties of MHD waves and shocks. A more complete discussion is given in Chap. 3. The MHD equations read in conservation form

$$\frac{\partial}{\partial t}\begin{bmatrix}\rho\\ \rho\,\vec{v}\\ \vec{B}\\ e\end{bmatrix} + \nabla\cdot\begin{bmatrix}\rho\,\vec{v}\\ \rho\,\vec{v}\vec{v}+\mathsf{I}\left(p+\vec{B}\cdot\vec{B}\,/2\right)-\vec{B}\vec{B}\\ \vec{v}\vec{B}-\vec{B}\vec{v}\\ \left(e+p+\vec{B}\cdot\vec{B}\,/2\right)\vec{v}-\left(\vec{v}\cdot\vec{B}\right)\vec{B}\end{bmatrix}$$
$$= \nabla\cdot(\mathsf{D}) - \begin{bmatrix}0\\ \vec{B}\\ \vec{v}\\ \vec{v}\cdot\vec{B}\end{bmatrix}\nabla\cdot\vec{B}. \tag{2.6}$$

$\vec{B}$ is the magnetic field, with units chosen such that the magnetic permeability $\mu = 1$. This equation has to be supplemented with the divergence free condition $\nabla \cdot \vec{B} = 0$ as an initial condition. The second right hand side term of Eq. 2.6 is proportional to $\nabla \cdot \vec{B} = 0$ and is thus equal to zero. For several reasons to be explained further on, it is advantageous to keep this term in the equations. The total specific energy is given by

$$e = \frac{p}{\gamma - 1} + \rho\,\frac{\vec{v} \cdot \vec{v}}{2} + \frac{\vec{B} \cdot \vec{B}}{2}. \tag{2.7}$$

For the dissipative MHD equations, the matrix of dissipative fluxes D depends on dissipative parameters like the viscosity and the electric resistivity, and on the state variables and gradients of the state variables. The ideal MHD equations describe a dissipationless conducting fluid, and are given by Eq. 2.6 with $\mathsf{D} \equiv 0$. The MHD equations describe the conservation of mass, momentum, magnetic field, and energy.

Inspection of Eq. 2.6 shows that the magnetic field influences the velocity of the plasma — through the $\vec{J} \times \vec{B}$ force, with $\vec{J} = \nabla \times \vec{B}$ — and that the magnetic field in its turn is influenced by the moving fluid. These effects result in a dynamical behavior which is quite more complicated than in the case of a non-conducting fluid. MHD allows for *three* different linear wave modes, the fast magnetosonic, the Alfvén, and the slow magnetosonic wave [87, 54]. Due to the extra $\vec{J} \times \vec{B}$ force in the momentum equation, which depends on the magnetic field and its direction, the three linear wave speeds become strongly dependent on the direction relative to the local magnetic field. It is said that MHD waves are *anisotropic*. The fact to be illustrated below that MHD bow shock flows can exhibit much more complex behavior than their HD counterparts can be related to this anisotropy. The fast, Alfvén (or intermediate) and slow wave speeds in the direction x are represented by c_{fx}, c_{Ax} and c_{sx}, respectively. The Alfvén speed is given by $c_{Ax} = |B_x|/\sqrt{\rho}$. For any direction x, it holds that $c_{fx} \geq c_{Ax} \geq c_{sx}$. In the direction of the magnetic field, the fast wave speed coincides with the largest of the sound and the Alfvén speed, while the slow wave speed coincides with the smallest of the two. Slow waves and Alfvén waves have a vanishing propagation speed in the direction perpendicular to the magnetic field.

Due to nonlinear effects large-amplitude MHD waves can steepen into shocks [4, 87, 80]. There exist three different types of MHD shocks, as shown in Fig. 2.5, and we can distinguish between them by considering the way in which they refract the magnetic field. Fast MHD shocks refract the magnetic field away from the shock normal (Fig. 2.5a), such that the upstream angle between the shock normal and the magnetic field θ_1 is smaller than the downstream angle θ_2 (in Fig. 2.5 the plasma flow in the shock frame goes from left to right). In an intermediate MHD

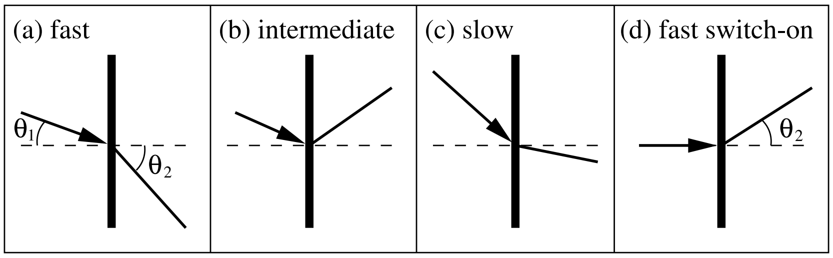

Figure 2.5: *MHD shock types. The magnetic field (arrowed) is refracted at the shock (thick). The shock normal is dashed. Region 1 is upstream, 2 is downstream.*

shock the magnetic field line is flipped over the shock normal (Fig. 2.5b). Slow MHD shocks refract the magnetic field toward the shock normal (Fig. 2.5c).

In Fig. 2.5d we show the peculiar MHD shock phenomenon which is called a fast switch-on shock. The upstream magnetic field is perpendicular to the shock front, but downstream there exists a finite angle θ_2 between the shock normal and the magnetic field.

Switch-on shocks have no analog in the hydrodynamic flow of a neutral fluid, and can thus be called an intrinsically magnetic effect. Switch-on shocks can occur when the inflow plasma β, which is defined as the ratio of the thermal pressure to the magnetic pressure ($\beta \equiv p/(B^2/2)$), is smaller than $2/\gamma = 1.2$, and when, along the magnetic field lines, the incoming plasma velocity lies between the fast MHD wave speed and roughly twice this speed [80]. This parameter regime is called the *switch-on regime*. Switch-on shocks thus arise when magnetic forces dominate over thermal pressure and dynamic pressure effects. Switch-on shocks occur when the upstream magnetic field is strong and are an intrinsically magnetic effect. Therefore we call upstream flows for which switch-on shocks occur *magnetically dominated* flows. Upstream flows for which switch-on shocks do not occur are called *pressure-dominated* flows.

It is clear that, analogous to the HD case, the formation of a bow shock can be expected when MHD flows fall in on blunt bodies with a velocity which is faster than the fast MHD wave speed — in which case we say that the flow is *superfast*. We may, however, expect additional phenomena due to the influence of the magnetic field and the more complex nature of the MHD equations. It turns out that for magnetically dominated upstream flows MHD bow shocks exhibit a new complex topology which is very different from the traditional topology obtained for bow shocks with pressure-dominated upstream flows. This motivates the introduction of the terminology of pressure-dominated versus magnetically dominated upstream flows as defined above, and warrants its extension to pressure-dominated versus magnetically dominated bow shock flows and bow shock flow topologies.

In this dissertation we discuss numerical simulation results of MHD bow shock flows around perfectly conducting cylinders and spheres. Our numerical code discretizes the ideal MHD equations, but introduces a small numerical dissipation. The numerical solutions thus describe MHD plasma flows with small dissipation. In the following Sections we give a preview of the results and the phenomena encountered.

A note on notation for wave speeds and Mach numbers

MHD wave speeds and Mach numbers — defined as the ratios of plasma velocities and wave speeds for the various waves — are anisotropic, so we have to define clearly how we refer to them. In general, we specify the direction in which we take wave speeds and Mach numbers in the subscript of the referring symbols, except for scalar quantities which do not depend on the direction. Thus c_{fx}, c_{Ax} and c_{sx} represent the (positive) MHD wave speeds in the direction x. The (positive) sound speed c is isotropic. Sometimes the Alfvén speed in the direction of the magnetic field is referred to as *the* Alfvén speed (or the total Alfvén speed), which we then represent as $c_A = ||\vec{B}||/\sqrt{\rho}$, without subscript x, and with $||\vec{B}||$ the magnitude of the magnetic field vector. $M_{fx} = |v_x|/c_{fx}$, $M_{Ax} = |v_x|/c_{Ax}$ and $M_{sx} = |v_x|/c_{sx}$ are the fast, intermediate and slow Mach numbers, respectively, with $|v_x|$ the absolute value of the plasma velocity in direction x. The sonic or acoustic Mach number in the direction x is given by $M_x = |v_x|/c$. Sometimes the sonic Mach number in the direction of the velocity is referred to as *the* Mach number (or the total Mach number), which we then represent as M, without subscript x. This quantity is thus defined as $M = ||\vec{v}||/c$, with $||\vec{v}||$ the magnitude of the velocity vector. When the magnetic field is everywhere aligned to the plasma velocity — we call this *field-aligned flow* —, the Alfvénic Mach number becomes independent of the direction, in which case we drop the subscript x. The Alfvénic Mach number is then defined as $M_A = ||\vec{v}||/c_A$.

2.2.1 Symmetrical two-dimensional flow around a cylinder

First we treat the 2D problem of uniform flow falling in on a cylinder. We basically take the configuration of Fig. 2.4, but initially we prefer to reduce the complexity of the problem as much as possible. We concentrate on the bow shock, such that the simulation domain can be restricted to the left half plane (the flow comes in horizontally from the left). We also

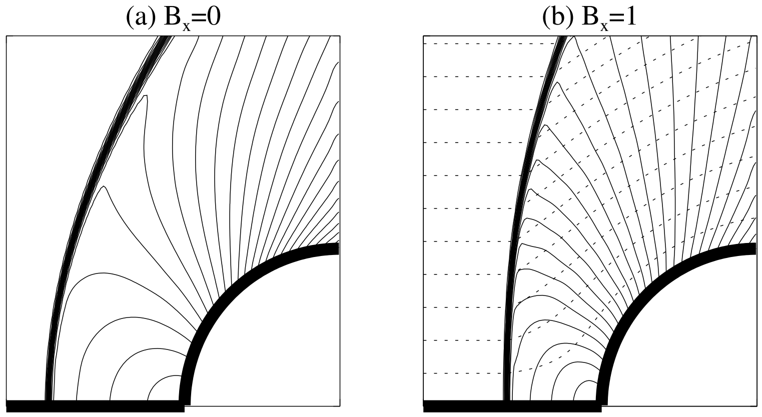

Figure 2.6: *Symmetrical bow shock flows around a cylinder (thick solid). The flow comes in horizontally from the left. Density contours (thin solid) pile up in the bow shock. Magnetic field lines are dotted. The thick solid horizontal line is a line of symmetry. (a) Hydrodynamic flow: $B_x = 0$, $M = 3.46$. (b) Pressure-dominated MHD flow: $B_x = 1$, $M = 3.46$, $M_A = 2$, $\beta = 0.4$.*

exploit the symmetry of the problem, by realizing that the horizontal line coming in from the left and going through the center of the cylinder is a line of top-bottom symmetry. This line is called the *stagnation line* because a *stagnation point* — a point with vanishing flow velocity — exists at the intersection of this line with the cylinder. This symmetry allows us to carry out the simulation in the upper left quadrant only. The simulation result for a $M = 3.46$ HD bow shock flow ($\vec{B} = 0$) is shown in Fig. 2.6a. On the stagnation line we explicitly impose symmetry boundary conditions. This flow can thus also be considered as the flow over a plate with a semi-circular bump or corner. It will turn out later that this may be an important detail for stability reasons, so we repeat that we explicitly impose the top-bottom symmetry in these bow shock flows around cylinders, and we call the bow shock flows *symmetrical*. The resulting stationary HD bow shock flow of Fig. 2.6a shows the expected bow shock geometry, with a bow shock which is curved *concave-inward* (towards the cylinder), like the bow shocks in the experimental results of Fig. 2.3.

In Fig. 2.6b we have added a horizontal magnetic field in the inflowing plasma, parallel to the incoming velocity. It can be proved theoretically that the upstream magnetic field has to be taken parallel to the flow velocity in order to obtain a steady flow solution, and that the magnetic field is then parallel to the plasma velocity in the whole bow shock solution — the flow is thus field-aligned. The sonic Mach number of the inflow is still $M = 3.46$, and the Alfvénic Mach number $M_A = 2$. The plasma β equals 0.4. Switch-on shocks cannot arise for these parameter values, so we call the upstream flow pressure-dominated. The flow is superfast, and we expect a bow shock in front of the cylinder in the stationary simulation result. This bow shock can indeed be seen in Fig. 2.6b. The magnetic field has changed the shape of the bow shock a little compared to the case with $\vec{B} = 0$, but the concave-inward bow shock orientation is preserved. The bow shock is of the fast type along the entire shock surface, because the magnetic field lines (dotted) are refracted away from the shock normal. For this pressure-dominated flow we find the same bow shock flow topology as for the hydrodynamic bow shock flow of Fig. 2.6a. We can say that the hydrodynamic bow shock flow is also pressure-dominated because $\vec{B} \equiv 0$.

Fig. 2.7 shows the simulation result of a MHD bow shock flow with upstream conditions $M = 2.6$, $M_A = 1.5$ and $\beta = 0.4$. Switch-on shocks can arise for these parameter values, so we call the upstream flow magnetically dominated. The topology of the flow is surprisingly different from the topology of the flow in Fig. 2.6b. A switch-on shock occurs at the point well above the stagnation line where the magnetic field is perpendicular to the leading shock front. We see that the central part of the bow shock is now oriented *concave-outward* (away from the cylinder). This feature has been observed first by Steinolfson and Hundhausen [147] in numerical simulations of time-dependent MHD flows related to solar coronal mass ejections, and they called it a 'dimple' in the shock front. They related this phenomenon to the occurrence of switch-on shocks, and it is indeed remarkable that the flow of Fig. 2.6b, with the 'traditional' bow shock topology, has parameters *outside* the regime in which switch-on shocks are possible, whereas the complicated bow shock of Fig. 2.7 has parameters *inside* the switch-on regime!

A second unusual feature of the flow in Fig. 2.7 is that the leading shock front is followed by several secondary shock fronts, which turn out to be of various MHD shock types, as can already be observed from the intricate way in which the magnetic field lines are refracted by these shocks. These interesting features were not anticipated in Steinolfson and Hundhausen's important earlier work [147].

These results suggest that, depending on the upstream conditions, two entirely different topologies exist for MHD bow shock flows. For magnetically dominated upstream flows — for which switch-on shocks occur —, a complex topology arises involving several interacting shock fronts with segments of various MHD shock types. For pressure-dominated upstream flows the traditional single-front topology known from hy-

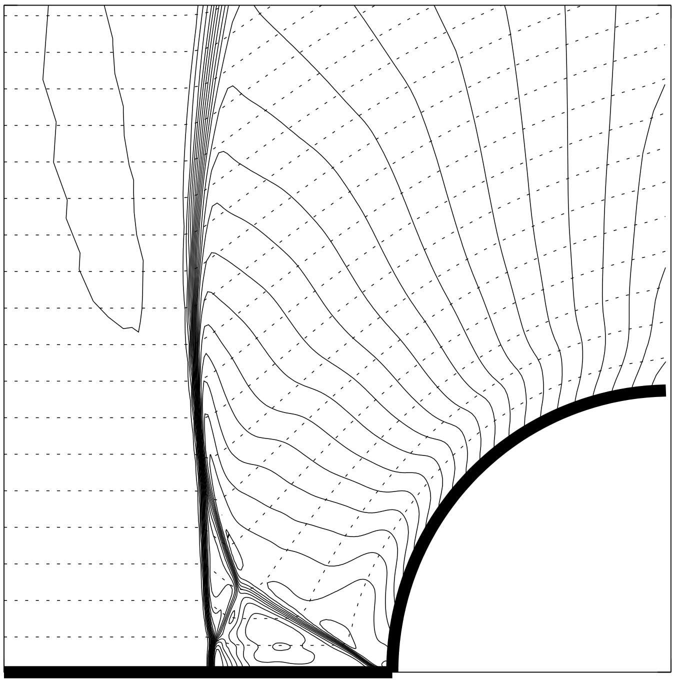

Figure 2.7: *Magnetically dominated MHD bow shock flow:* $B_x = 1$, $M = 2.6$, $M_A = 1.5$, $\beta = 0.4$. *The flow comes in from the left. Density contours (solid) pile up in shocks. Magnetic field lines are dotted. The leading shock front has a concave-outward central part ('dimple'), and is followed by secondary shock fronts.*

drodynamic bow shock flows is recovered. The magnetically dominated bow shock topology of Fig. 2.7 was previously unknown. Its complexity is due to intrinsically magnetic effects.

2D MHD bow shock flows around cylinders are discussed in detail in Chap. 6. We identify and study in detail the nonlinear wave features present in the complex magnetically dominated bow shock flows.

2.2.2 Three-dimensional flow over a sphere

3D MHD bow shock flows are important for space physics applications. The 2D results introduced above suggest that intrinsically magnetic effects may also affect the topology of 3D MHD bow shocks with magnetically dominated upstream flows. We consider stationary 3D bow shock flows over a sphere. In these 3D flows the magnetic field and the plasma velocity do not have to be aligned.

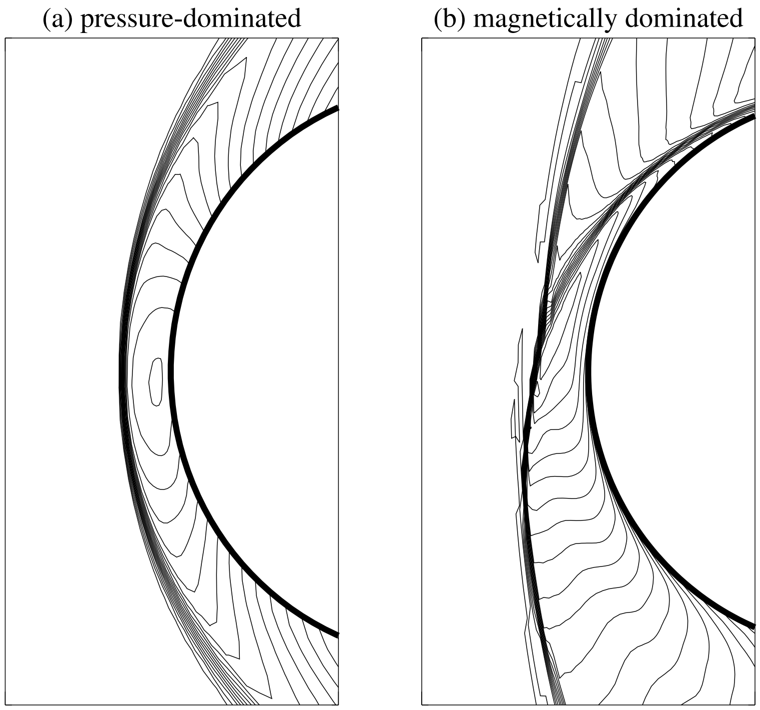

Figure 2.8: *Bow shock flows over a sphere (thick solid) with a small angle between the upstream magnetic field and velocity. The flow comes in from the left. Density contours (thin solid) in a plane through the sphere center are shown. (a) Pressure-dominated flow:* $B_x = 1$, $M_x = 6.90$, $M_{Ax} = 3.985$, $\beta = 0.4$, $v_x = 3.985$, $v_y = 0.022$. *(b) Magnetically dominated flow:* $B_x = 1$, $M_x = 2.6$, $M_{Ax} = 1.5$, $\beta = 0.4$, $v_x = 1.5$, $v_y = 0.01$.

In Fig. 2.8a we show the simulation result of a superfast pressure-dominated MHD flow over a perfectly conducting sphere, with parameters $B_x = 1$, $M_x = 6.90$, $M_{Ax} = 3.985$ and $\beta = 0.4$, and with a small angle between the horizontal magnetic field and the plasma flow ($v_x = 3.985$ and $v_y = 0.022$). Density contours are shown in the plane through the center of the sphere which contains the inflow magnetic and velocity field vectors. We are not surprised to find a stationary solution with a traditional concave-inward (towards the sphere) single shock surface, because the inflow is pressure-dominated.

Let us now investigate the case of a magnetically dominated inflow with parameters $B_x = 1$, $M_x = 2.6$, $M_{Ax} = 1.5$, $\beta = 0.4$, and a small angle between the inflow magnetic field and the velocity ($v_x = 1.5$ and $v_y = 0.01$). Fig. 2.8b shows the steady state solution for this bow shock flow. The existence of a slight dimple and a secondary shock front is confirmed (compare to the 2D flow of Fig. 2.7), and the global bow shock topology of Fig. 2.8b, for magnetically dominated parameters, is very different from the traditional concave-inward single-front bow shock topology of Fig. 2.8a for pressure-dominated parameters. This indicates that intrinsically magnetic effects change the topology of bow shock flows drastically for magnetically dominated upstream parameter values.

Analogous to the 2D case, these results suggest that depending on the upstream conditions, two entirely different topologies exist for 3D MHD bow shock flows. For pressure-dominated upstream flows the traditional single-front topology known from hydrodynamic bow shock flows is recovered. For magnetically dominated upstream flows a previously unknown complex topology arises. This is the main result presented in this dissertation.

Magnetically dominated 3D MHD bow shock flows over spheres are discussed in detail in Chap. 7.

In the next Section we give a brief overview of where MHD bow shocks can be found in nature, and where our findings on magnetically dominated MHD bow shock topology may be relevant.

2.3 MHD shock phenomena in nature

In this section we give an overview of where plasma bow shocks can be encountered in nature, and how these bow shocks have been described in the literature using the MHD model. But first we say something about the validity of the MHD model to describe a plasma, and about the stability of intermediate MHD shocks.

2.3.1 The validity of the MHD approximation

A plasma is a gas composed of charged particles. There exists a hierarchy of theories to describe plasma motion at different levels of complexity (see e.g. [84, 54] for an introduction).

Particle dynamics considers directly the forces exerted on individual particles and the influence of the particles on the electric and magnetic fields (via the *Maxwell equations*). It is obvious that such a description entails a complexity which is often prohibitive, because macroscopic volumes of gas contain an enormous amount of particles. An important consideration is the nature of the physical application at hand, i.e. whether it is necessary to follow the motion of every single particle in order to analyze the behavior of the plasma in the application. Analytical theory is not much developed, but attempts are made to describe particle plasma dynamics using supercomputer simulations.

The *kinetic theory of plasmas* is a statistical theory of plasma motion, which describes the evolution of a *distribution function*. This function represents the number density of particles in function of spatial coordinates, velocity, and time, and is a solution of a *Boltzmann equation*, which needs to be solved together with the Maxwell equations. Some analytical results can be obtained, but the complexity is often prohibitively high, even when numerical approaches are used.

The MHD equations are a continuum fluid description of a plasma, in terms of evolution equations for the macroscopic state variables, and with the Maxwell equations built-in into the formulation. This description, which can be derived by taking moments of the Boltzmann equation, is much more tractable than the particle or kinetic theories, and the mathematical properties of ideal MHD as a symmetrical hyperbolic system [21] are clearly defined. However, one pays a price for this tractability. Many complex dynamical phenomena are retained in the MHD description, but many other microscopic and some macroscopic plasma phenomena are not properly described by the MHD equations.

It is thus important to identify and bear in mind the range of parameters for which the MHD description of a plasma is a good approximation. The ideal MHD equations introduced in Sec. 2.2 describe a fully ionized plasma for which the following properties hold. The particles are considered as *one fluid*, which means that the ions and electrons have to be in thermal equilibrium. A MHD plasma is quasi-neutral, meaning that in a small volume (of the size of a Debeye sphere [54]) positive and negative charges neutralize. The pressure is isotropic. The plasma velocities are non-relativistic. All charged particles gyrate around magnetic field lines with the Larmor frequency ω_L, which is given by

$$\omega_L = \frac{qB}{m}, \tag{2.8}$$

with q the charge of the particle, and m its mass. Ions have a greater mass than electrons, so the gyro-frequency is lower and the gyro-radius is larger for ions than for electrons. This gyration is not retained in the MHD description. MHD is thus valid when the frequencies in the solution are smaller than the ion gyro-frequencies. Also, local length scales in the MHD solution have to be larger than the ion gyro radius. Similarly, MHD frequencies have to be lower than electron plasma frequencies. Electrons are much lighter than ions, such that the inertia and macroscopic velocity of a plasma are mainly due to ions, while the electric current is due to the electron motion relative to the ions. The electric resistivity η can be neglected when the magnetic Reynolds number

$$R_m = \frac{Lv}{\eta}, \tag{2.9}$$

is large, where L is a characteristic length of the problem, and v is a characteristic velocity. If in addition other dissipative mechanisms can be neglected as well, the equations of ideal MHD can be used to describe the plasma behavior. Another important point is that the particle distribution function has to be nearly Maxwellian for the MHD approximation to be valid. In ordinary gases, collisions between particles provide the necessary dissipation to relax the distribution function towards a Maxwellian. In many plasmas in the real world, however, the *mean free path* of plasma particles is much larger than the length scale of the total plasma volume, which means that they hardly undergo any collision. Those plasmas are said to be *collisionless*. But this raises the question which process provides the dissipation in plasmas necessary to relax to Maxwellian states? Or which mechanism provides the dissipation in plasma shocks? Actually, it turns out that most plasmas are not very close to be Maxwellian, and in this sense the MHD description is only an approximation. The shocks formed in collisionless space plasmas dissipate by microscopic particle-wave interactions and instabilities [27, 120].

We have thus to be aware that MHD is only an approximate description of plasma behavior. It is, however, interesting and worthwhile to investigate plasma shock phenomena in the MHD approximation (see e.g. [74] for interesting thoughts on this issue). The MHD equations are statements of the fundamental conservation of mass, momentum, magnetic field and energy, and they often give a good description of plasma phenomena on a macroscopic scale, even if not all microscopic processes are faithfully reproduced in detail. Furthermore, the equations of ideal MHD have a well-defined mathematical structure, and the complexity is tractable. The phenomena that are to be described in this dissertation, are fundamentally 2D and 3D. Plasma particle simulations or kinetic simulations are feasible in 1D, but would require non-trivial computing resources in 2D and certainly in 3D.

In this dissertation we thus study plasma shocks in the MHD approximation. It is important to understand the behavior of these nonlinear wave phenomena in the MHD system, and the well-defined mathematical nature of the system allows for rigorous analysis of the results and is useful for the development of rigorous numerical methods. We may then expect that our results on MHD bow shocks apply to shocks in real plasmas on a global macroscopic scale, although we are aware that not all plasma phenomena are retained in the MHD description. In the following paragraphs we illustrate how some plasma shock phenomena in space physics have been successfully described in the MHD model. But first we say something about the stability of intermediate shocks.

2.3.2 On the physical existence of intermediate and compound shocks

Intermediate shocks

It has been believed for a long time that intermediate shocks are unphysical [87]. Intermediate shocks were found to be unstable (in a certain peculiar sense, see [87]) in the *ideal* MHD system. Intermediate shocks were said to be 'non-evolutionary', and it was concluded that non-evolutionary shocks cannot exist in nature.

However, recently it has been shown that intermediate shocks can be stable in the *dissipative* MHD system for wide ranges of the dissipation coefficients [173, 43, 49, 110]. They can be destabilized by magnetic perturbations out of the plane formed by the shock normal and the magnetic field (Alfvén waves), but only when the amplitude of the perturbation is sufficiently large [171]. The amplitude of the perturbation required for destabilization decreases with decreasing dissipation [47, 102]. It would seem that dissipative MHD with small dissipation coefficients applies more directly to nature than perfectly ideal MHD. Consequently most authors now seem to agree that intermediate shocks can exist in nature and can persist when perturbations are not too large, although others keep on arguing against the existence of intermediate shocks [35]. In our simulation code we discretize the ideal MHD equations, but numerical dissipation plays a role analogous to a small physical dissipation. We will show that stationary intermediate shock fronts are present in our 2D and 3D MHD simulation results (Figs. 2.7 and 2.8b). This seems to be relevant for the ongoing debate on the physical existence of intermediate shocks. Intermediate shocks have been found before in one-dimensional simulations of the dissipative MHD equations [170], but it seems that our simulations are the first confirmation in 3D that intermediate shocks can indeed exist and persist for small dissipation MHD in a realistic flow configuration.

It is an interesting question what the 3D bow shock solutions with magnetically dominated upstream parameter values would be in some limit of vanishing dissipation [47], or in perfectly ideal MHD. Some authors seem to indicate that for some problems vanishing dissipation limit solutions and the perfectly ideal solution could be different, because small dissipation MHD and ideal MHD do not approach each other uniformly [48, 47] if one considers shock solutions. The precise type and magnitude of the dissipation may influence results to some problems in a non-uniform way. This non-uniform behavior of the vanishing dissipation limit is attributed to the fact that the MHD system is *non-strictly hyperbolic* — wave speeds may coincide — and *non-convex* (see below). The Euler equations are strictly hyperbolic and convex, and the Navier-Stokes equations approach the Euler equations uniformly for vanishing viscosity. This means that Euler simulation codes with numerical diffusion approach the ideal Euler solution to problems uniformly when grids are refined. The above discussion indicates that this may not be true for the MHD case. Some authors reject the use of ideal MHD to describe physical systems precisely because ideal MHD is not a uniquely defined limit of dissipative MHD [173]. However, all these considerations remain speculative because the limit of vanishing dissipation MHD, and the relation between vanishing dissipation MHD and perfectly ideal MHD, have not been understood yet in full [40, 173, 44, 46, 47].

If these considerations on non-uniformity were to be true, however, then the consequence would be that for some problems ideal MHD solutions cannot be calculated with numerical codes which introduce numerical dissipation [48], and that for small dissipation MHD calculations — which presumably would correspond to most physical applications — the dissipative effects should be modeled explicitly, because solutions may depend on the specific form of the dissipation [173]. Most researchers do not seem to be aware of these concerns. Recently many new algorithms have been presented which are intended to solve the ideal MHD equations [12, 157, 158, 183, 23, 128, 1, 118, 162, 6, 7, 99, 36, 26, 111, 5], and when those techniques are applied to space physics and astrophysics flows, it is generally believed that the solutions approach the ideal MHD solution. The above discussion indicates that it would be best to include an explicit description of dissipation mechanisms in numerical MHD simulations. However, this makes numerical MHD codes more complex and demands substantially larger computing resources. Therefore we adopt the pragmatic approach — which is customary in the field of space physics and astrophysics research — of utilizing a numerical code which discretizes the ideal MHD equations, but in which numerical dissipation plays a role analogous to a small physical dissipation. We will then argue that our simulation results are solutions of the MHD equations with small dissipation. This small dissipation remains unspecified, however, and this is not very satisfactory. It remains thus an interesting topic of future research to verify the bow shock flow solutions which are presented in this dissertation with a numerical code which explicitly models the dissipation mechanisms, and to study vanishing dissipation limits or ideal MHD solutions. As mentioned above, the small dissipation case would seem the most appropriate to describe physical systems. In this sense the discussion on vanishing dissipation limits and ideal MHD solutions is probably not so relevant for space physics applications, although these topics remain interesting mathematical problems. Our simulation results are probably relevant for bow shock flows in space physics and astrophysics flows, because they confirm in 3D that intermediate shocks can indeed exist and persist for small dissipation MHD in a realistic flow configuration.

The problem of the existence of intermediate shocks is very subtle and has probably not been resolved yet in full. Therefore we dedicate a full Chapter (Chap. 9) to the discussion of this topic. We illustrate the main issues of the ongoing debate on the existence of intermediate shocks and we discuss the relevance of our results for this debate.

Compound shocks

MHD compound shocks are intermediate shocks for which the plasma velocity exactly equals the fast or the slow wave speed in the upstream or downstream state of the shock. MHD allows for compound shocks because the MHD system is non-convex [11, 90, 109]. MHD compound shocks were initially believed to be unphysical because they are a special kind of intermediate shock, which was believed to be non-evolutionary. But compound shocks were found in 1D numerical simulations of the MHD equations [12], and they were shown to be necessary elements in the analytical solution of planar MHD Riemann problems [110].

We show in Chapters 6 and 7 of this dissertation that our simulation results of flows around cylinders and spheres (Figs. 2.7 and 2.8b) clearly contain compound shocks. These peculiar nonlinear wave structures were earlier found in 1D simulations, but our results seem to be the first clear confirmation that compound shocks can arise in 2D and 3D flows.

2.3.3 Bow shocks in the solar system: planets, comets and the heliosphere

Nearly stationary plasma bow shock configurations can be found in the solar system where the superfast solar wind [67] encounters planets or comets [84].

Fig. 2.9 shows a sketch of the earth's magnetic environment [168]. The earth has an intrinsic magnetic field, which is confined to a region

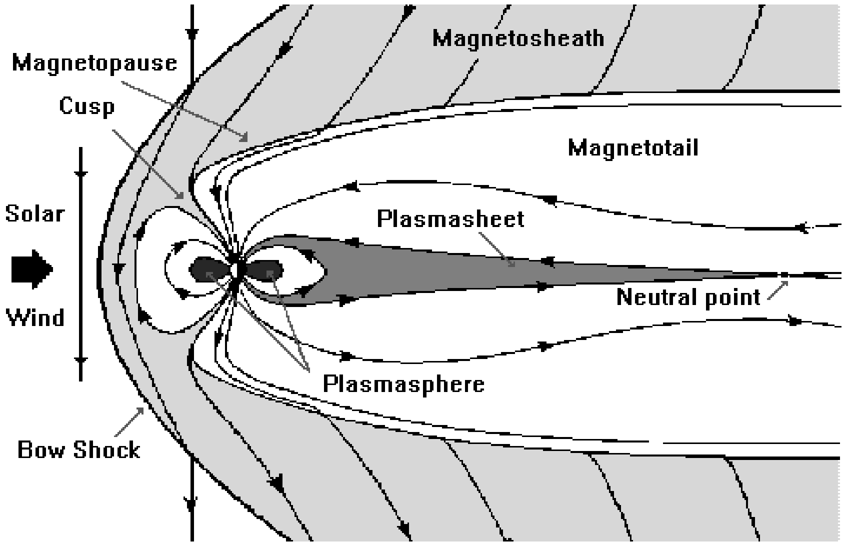

Figure 2.9: *The earth's magnetic environment. (courtesy ISPEC)*

which is called the *magnetosphere*. This region is separated from the solar wind magnetic field by the *magnetopause*. The solar wind flow is deflected to flow around the magnetopause, and this deflection involves a transition through a bow shock from a superfast to a subfast state, as was explained in Sec. 2.1 and as is seen in the MHD simulations of Sec. 2.2. The region between the bow shock and the magnetopause is called the *magnetosheath*.

Fig. 2.10 shows a time series of local magnetic field and electron temperature measurements of the Ulysses spacecraft crossing Jupiter's bow shock [115]. A clear jump in magnetic field and electron temperature can be seen at approximately 17:30 UT, which can be demonstrated to quantitatively agree with a fast MHD shock transition.

All planets are expected to have bow shocks, and this has been proven by direct measurements of passing spacecraft, except for Pluto [143]. Some spacecraft have crossed cometary bow shocks [73]. Such satellite observations are important, because they establish the presence of the bow shocks, but they are limited in the sense that they provide only datasets along a 1D curve. Direct observations of the spatial geometry and extent of planetary bow shocks are not available. The 1D observations do, however, provide us with detailed observations of local shock transitions. These observations show that those planetary and cometary bow shocks are not just 'clean' MHD shock transitions, because wave perturbations are present upstream and downstream of the shocks (Fig.

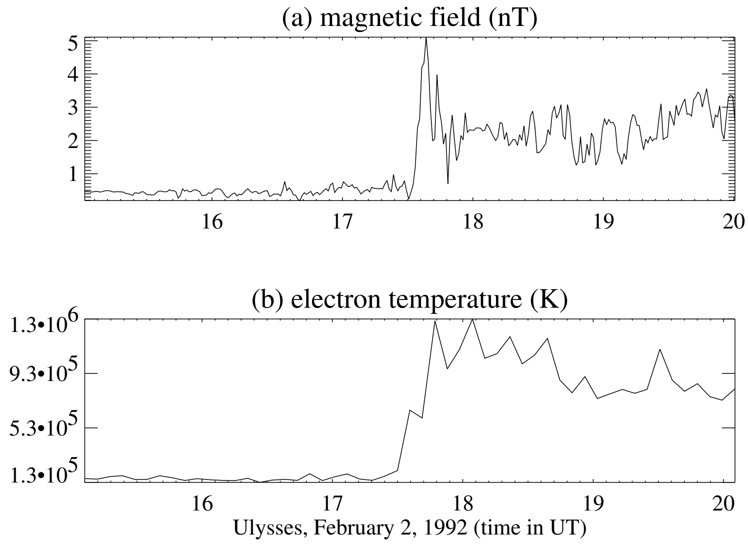

Figure 2.10: *Ulysses crosses Jupiter's bow shock. (courtesy D. Balogh and J. Phillips, NSSDC)*

2.10) and because the shock profiles have structures which indicate that particle and kinetic processes, neglected in the MHD description, are present. Explanations have been proposed for many types of observed wave perturbations and for observed shock structures, based on detailed particle and kinetic plasma models [27].

The global bow shock flows can often be modeled quite satisfactorily using the MHD model, and MHD models have reproduced successfully many aspects of the observations, for flows around planets and moons (e.g. [174, 159, 144, 17, 114, 74]) and for flows around comets ([55, 56]).

The solar wind is most often high-β and the solar wind Mach number is high ($M \sim 10$), such that pressure effects dominate over magnetic effects. The magnetically dominated parameter regime for which we do find the complex bow shock topology of Fig. 2.8b, is thus not typical for the solar wind. This explains probably why this parameter regime — to our best knowledge — has not been considered before in 3D MHD simulations of terrestrial bow shock flows [174, 16]. However, we explain further on that the solar wind can be magnetically dominated at the earth for up to 8% of the time. This means that the earth's bow shock flow may exhibit the complex topology with the secondary slow shock of Fig. 2.8b under those magnetically dominated solar wind conditions. Some satellite observations do indeed suggest that a slow shock may be

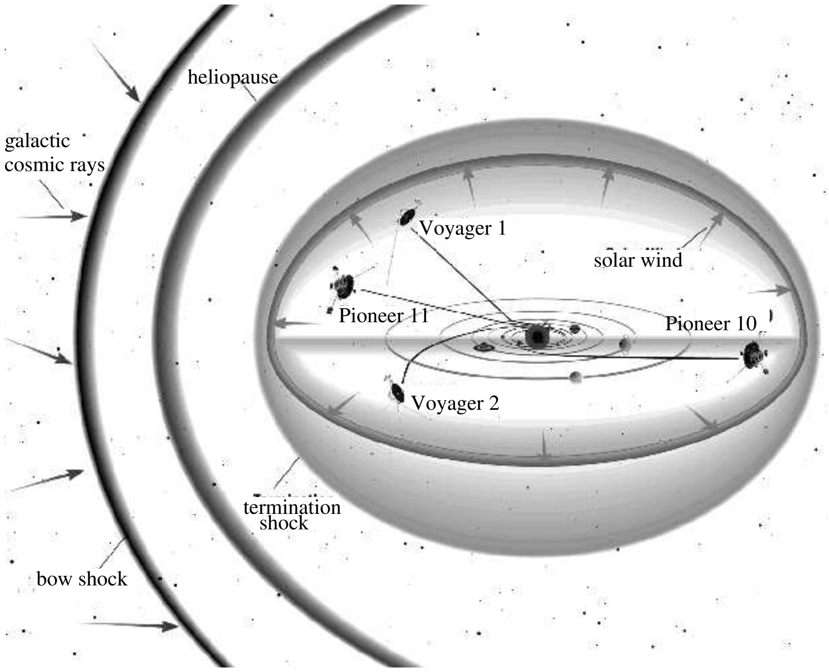

Figure 2.11: *The solar system's magnetic environment or* heliosphere. *The sun is located in the center of the picture. (courtesy NASA)*

found in the earth's magnetosheath downstream of the bow shock [141]. Our simulation results exhibit such secondary shock fronts of slow type following the leading bow shock, and the observed slow secondary shock in the earth's magnetosheath may be due to a process similar to what is described in our simulations. In particular, our 3D simulation results of Fig. 2.8b suggest that such a secondary shock front should be present only on one side of the sun-earth line. It would be interesting to verify this in the earth's magnetosheath using observations by several satellites covering different locations in the global system. The application of our simulation results to the earth's bow shock flow is discussed in detail in Chap. 8.

It is believed that a superfast interstellar wind interacts with the whole solar system to produce a *heliospheric* magnetic configuration [64] like the one sketched in Fig. 2.11. A heliospheric bow shock is expected to exist. Fig. 2.11 also shows the approximate trajectories of several spacecraft that were launched to study the solar system. The heliospheric magnetic configuration has been modeled using MHD (e.g.

[117, 124, 100]), and it is expected that observational tests for these models will become available when several outward traveling spacecraft will cross the heliospheric termination shock (Fig. 2.11) early in the 21st century. Not much is known about the conditions in the interstellar wind, so it is an open question whether the flow upstream of the heliospheric bow shock can be magnetically dominated.

2.3.4 Solar coronal mass ejections and traveling interplanetary shocks

Up to several times per day, large-scale structures in the solar corona disrupt and are ejected out of the corona at speeds ranging from 10 to 2×10^3 km s^{-1}, carrying a mass of 10^{12-13} kg and liberating an energy of 10^{24-25} J [66, 104, 68]. Many aspects of the propagation of coronal mass ejections (CMEs) in the solar coronal plasma can be described by the equations of ideal MHD. White light coronagraph observations of fast CMEs show bright leading fronts which can be interpreted as signatures of fast MHD shock fronts [68].

Fig. 2.12 shows two consecutive images taken by the SMM coronagraph, on 30 January 1989, at 2:11 and 2:28 UT. A bright spiraling prominence structure is seen to expand rapidly, and is preceded by a bright loop-like structure. This leading front contains a small 'dimple' in the image on the left. In the right image, about 17 minutes later, the leading front is less bright, but the dimple is more pronounced, and the leading front seems to be followed by secondary fronts. The plasma β in the inner solar corona is believed to be substantially smaller than unity, and the fast MHD wave speed is believed to be of the order of 600 km/s. The projected velocity of the leading front in Fig. 2.12 is 1055 km/s. These numbers indicate that the flow upstream of the leading shock front may well be magnetically dominated. Steinolfson and Hundhausen [147, 146] studied these dimpled leading fronts, they related the dimple to the properties of switch-on shocks, and they performed time-dependent numerical MHD simulations in 2D. Their simulations of moving shock fronts confirmed the existence of the dimple effect, and seemed to contain intermediate shocks.

Steinolfson and Hundhausen's work was the motivation and starting point for the work described in this dissertation. We study the formation of MHD shocks with magnetically dominated upstream flow, not in a time-dependent outflow driven by a pressure pulse as in Steinolfson and Hundhausen's case, but in the much simpler setting of a uniform flow falling in on a perfectly conducting cylinder or sphere. This simple setting allows us to analyze the stationary flow results in a rigorous way. It allows us to describe the intricate secondary shock patterns discovered in our simulation results and not anticipated by Steinolfson and Hund-

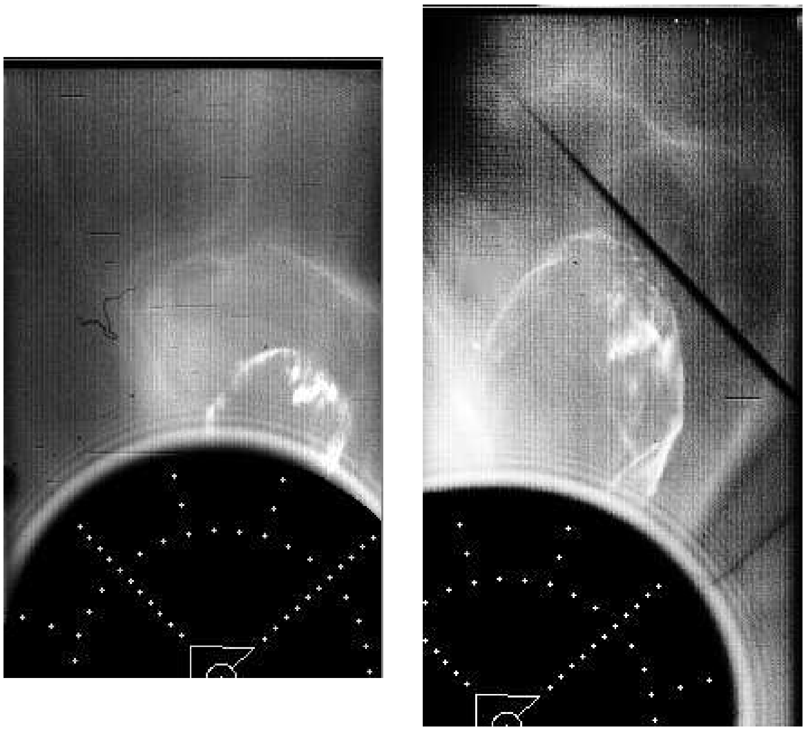

Figure 2.12: *SMM coronagraph images of a CME. The sun is blacked out by a disc with radius* 1.6 R_{sun}.

hausen's important earlier work, and to identify clearly intermediate and compound shocks. In Chap. 8 we discuss how our simulation results are relevant for shocks induced by fast CMEs.

It is believed that the shocks induced by fast CMEs propagate through the interplanetary space as interplanetary shocks [136]. They may travel in the direction of the earth as the leading edges of magnetic clouds [15, 58]. Magnetic clouds often cause magnetic storms, which are severe disruptions of the earth's magnetic environment, disturbing communications and sometimes even leading to power failures. Fig. 2.13 shows measurements by the WIND satellite, which is located in front of the earth's bow shock. Discontinuous jumps in magnetic field, ion density, and ion temperature, indicate the arrival of interplanetary shocks [58]. The magnetic effects on bow shock topology discovered in our simulation results may also become important when magnetic clouds reach the earth's bow shock, because the magnetic field is strong in magnetic clouds. We speculate in Chap. 8 that intrinsically magnetic effects may

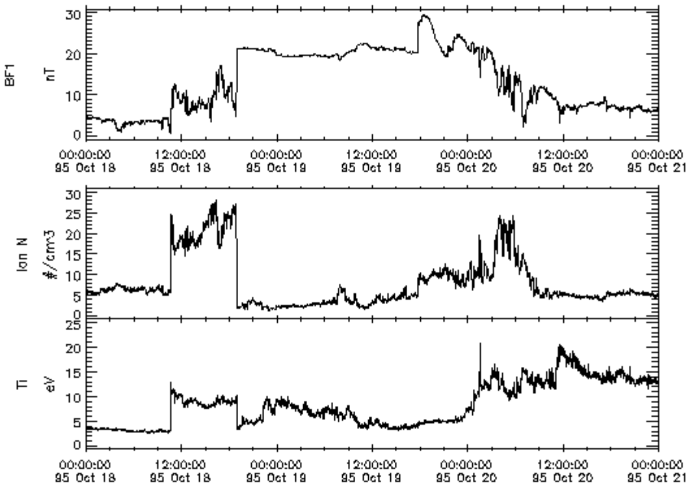

Figure 2.13: *Interplanetary shock just before it reaches the Earth's magnetic system. (WIND satellite data, courtesy R. Lin and R. Lepping, CDAWEB)*

cause a global reconfiguration of the magnetosheath flow which may determine the timing of magnetic storm onset.

An important application of space physics and solar physics is the study of 'space weather', which is concerned with disturbances of the earth's magnetic system by perturbations in the solar wind. Those perturbations are believed to originate directly on the sun. The ultimate goal is to provide operational predicting capabilities, much like weather prediction on earth, which could help in reducing the harmful effects of magnetic storms. One of the possible approaches to this problem is the global simulation of the sun-earth system, and for this the MHD model seems to offer a physical starting point that promises both accuracy and tractability. Much can be learned from problems with reduced complexity, like the stationary bow shock flows discussed in this dissertation. This knowledge then serves as a part of the intuitive basis to understand the simulation of more complex systems comprising the time-dependent evolution of magnetic disturbances originating at the sun, propagating through the solar wind, and interacting with the quasi-stationary bow shock and magnetosphere of the earth. This is an ambitious program, but first attempts are made using adaptive grids to cover the different spatial scales, and the resulting MHD models are capable of delivering faster-than-real-time turn-around on the world's largest supercomputers.

The problems faced in trying to understand these complicated interactions are obviously enormous, and as is not unusual for ambitious undertakings, the space weather project meets with a lot of criticism from many established scientists, especially about the operational aspect. Of the many points of criticism, we can mention the following two. It is argued that many essential physical processes — including the heating mechanism of the solar corona — are not understood, and that numerical methods cannot make deterministic predictions about nonlinear physical systems which may involve chaotic behavior. We believe that space weather prediction is indeed an extremely difficult task, but we are not convinced that there are solid theoretical arguments which would indicate that the prediction of space weather is fundamentally impossible. Indeed, physical processes of which the microscopic mechanisms are not well known, can be incorporated into large-scale models in a parametrized way. A good example is the relatively successful parametrization of turbulence in gasdynamic or atmospheric physics applications [167, 101]. The detection at the earth of magnetic clouds as well-structured entities with components which can directly be related to pre-CME structures in the lower solar corona [15, 58], shows that space weather events may be caused by deterministic large-scale flow patterns, and may not be influenced too much by perturbations of a chaotic nature.

We believe that the problems which can be addressed in large-scale MHD simulations of the sun-earth system are interesting and important, and next to the operational and predictional aspects, a lot has to be learned regarding the complex interaction of nonlinear phenomena in three space dimensions. We think that global MHD simulations are a good way to approach these complex interactions. It is our belief that global time-dependent MHD simulations will indeed become more and more feasible and that much can be learned from them, and we do see the results of this dissertation and the methods employed as an initial step towards such a goal.

2.3.5 Astrophysical shock phenomena

Magnetic fields are believed to play an important role in many astrophysical phenomena. Since the launch of the Hubble Space Telescope (HST), observations become available with sufficient resolution for the direct observation of shock phenomena in distant astrophysical objects. Fig. 2.14 shows HST images of jets emanating from young stellar objects. Magnetic fields are believed to be important for the collimation of these jets, and shocks are observed at the leading edges of the jets [29, 126]. Many MHD simulations have been performed on the subject of astrophysical jets [165], and it is argued that some complex morphological characteristics of those objects can be explained using MHD models.

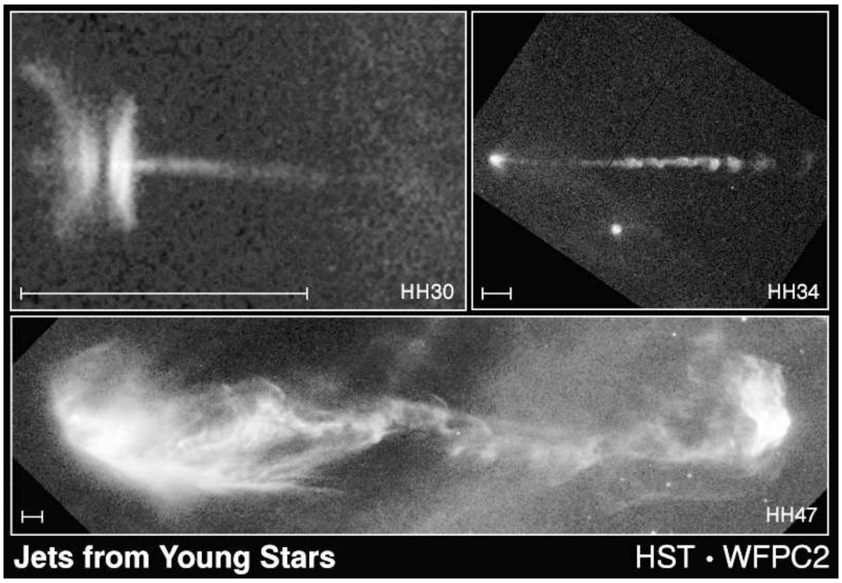

Figure 2.14: *Jets from young stellar objects. It is believed that during star formation stellar outflow is collimated into bipolar jets perpendicular to an accretion disk. In the bottom image, for instance (HH47), a large horizontally extended jet is seen. The jet induces a bow shock on the leading edge (far right), and several additional bow shocks and internal shocks have been identified [126]. (courtesy C. Burrows, J. Hester, and J. Morse, NASA)*

MHD models are employed for the study of shock phenomena in various other astrophysical objects, like jets ejected from active galactic nuclei [166] and the interaction of supernova remnants with the interstellar medium [25]. General relativistic MHD equations are used to study the formation of shock waves in magnetohydrodynamical accretion onto a black hole [181].

The use of magnetic fields in the study of astrophysical objects is, however, still relatively new and unexplored, and the magnetically dominated bow shock flows which are described in this dissertation may have applications in astrophysical flows when upstream plasmas are magnetically dominated.

2.3.6 Laboratory plasmas and magnetic reconnection

Plasmas have been studied intensively in the laboratory. MHD shocks have been studied in plasma shock tubes [4, 92]. Models of the earth's magnetic system are being studied in the laboratory, where an intense plasma flow simulating the solar wind interacts with a magnetized 'terrella' [123], resulting in a flow with a bow shock and a magnetosphere. Spacecraft re-entry is simulated in plasma wind tunnels or plasmatrons [9], where a sample is exposed to a supersonic partially-ionized plasma, resulting in a flow with a bow shock.

In the last decades much effort has been devoted to the study of controlled nuclear fusion, mainly in tokamak devices. Tokamak plasmas can be described approximatively by the MHD equations. Linear MHD stability calculations impose important bounds on tokamak stability limits [116]. The numerical MHD code described in this dissertation has been used to describe the dynamics of hot filaments in a tokamak plasma. Because it does not deal directly with MHD shock phenomena, this work is not described in this dissertation, but is reported elsewhere [155]. MHD shock phenomena are not studied so much in the context of tokamak physics, probably because shocks are generally believed to be related to disruption of the plasma, which one tries to avoid. It remains difficult to measure densities and magnetic fields inside tokamak plasmas, such that it is hard to know if, when and where shocks would be formed.

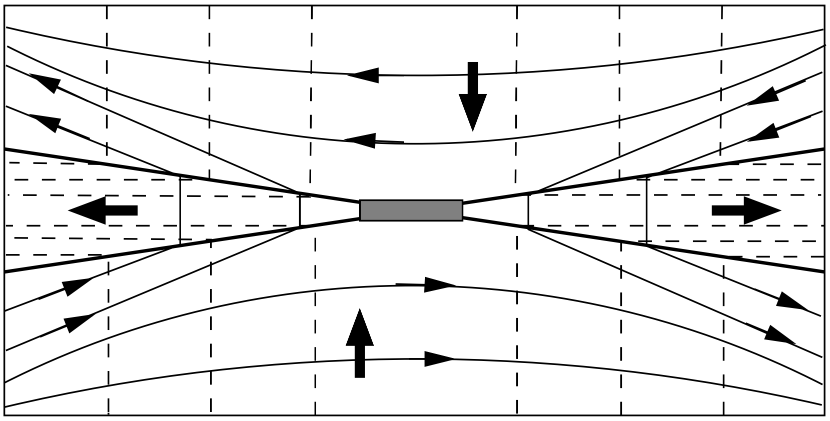

Figure 2.15: *Topology of the Petschek reconnection model. Magnetic field lines (thin solid) and streamlines (dashed) are refracted at slow shocks (thick solid). Reconnection takes place in the central shaded diffusive region.*

The process of *magnetic reconnection* is another subject of active theoretical study [86, 39, 119, 8]. Magnetic reconnection can naively be depicted as the process in which a region of plasma changes its magnetic topology by breaking magnetic field lines and connecting the broken ends to other broken field lines as the result of electrical resistivity. Magnetic reconnection is an inherently resistive process, and in highly conductive plasmas it is in general restricted to small regions where gradients of the magnetic field (and thus currents) become very large. Fig. 2.15 shows a sketch of a popular reconnection mechanism proposed by Petschek in 1963 in which shocks play an intrinsic role. Plasma is brought in from above and below, and is deflected towards the left and the right by slow MHD shocks. In a small central region the gradients of the magnetic field become very large and reconnection takes place. This is only one theoretical model of MHD reconnection, and it has not been proven that it actually works in practice [86]. Other reconnection models, however, also contain MHD shocks, and it has even been argued that the existence of intermediate MHD shocks is essential for reconnection [96]. Magnetic reconnection for plasmas in the MHD regime has recently been studied in laboratory experiments [179, 72]. Some numerical MHD simulations seem to confirm the importance of MHD shocks for reconnection phenomena [39, 132], but there is still much discussion about the true nature of MHD reconnection, and much of the numerical results seem to be critically dependent on the formulation of the boundary conditions [39, 8].

Magnetic reconnection is also believed to be an important process in many solar and space plasmas, and many numerical simulations are performed which attempt to describe this. Solar corona X-ray jets were modeled using the resistive MHD equations, and fast MHD shocks occur at the reconnection site [182]. Reconnection is believed to be important at the earth's magnetopause and magnetotail, and many numerical simulations have been performed using MHD models [133, 94, 96, 175]. The simulation results have been compared with the abundant observational data available from satellite magnetopause crossings. Recently hybrid simulations have been performed, where the electrons are treated as a massless fluid and the ions are treated as particles, and the results from these simulations seem able to explain some of the wave features present in the observations but not described by MHD [89, 176, 78, 76, 77, 95, 98, 134, 112]. These simulations are certainly a step beyond MHD simulations and may explain additional physical phenomena, but it seems that much care has to be exercised in evaluating the numerical results, because a unique closure is not available for the hybrid system, because its mathematical properties are not well-known, and because only numerical results are available. For instance, the influence of the formulation of the boundary conditions may even be more important than in the MHD case [39].

2.4 Analytical and numerical techniques to study MHD shock phenomena

An important part of this dissertation deals with analytical and numerical techniques to study MHD shock phenomena. Much of the knowledge necessary in this study did only partially exist and had to be collected and developed as a large part of the thesis work.

The main analytical technique used in this dissertation to analyze steady state MHD flows in 2D is the theory of stationary characteristics. This theory also turns out to be useful for the validation of numerical results. An extensive general theory exists for the characteristic properties of symmetric hyperbolic systems [21, 20]. This theory has been applied early on to unsteady MHD flows [21] and to steady MHD flows, including the case where the magnetic field is aligned with the flow (field-aligned or parallel flow) [79, 59]. More complete accounts of the characteristic theory of steady and unsteady MHD flows appeared later [71, 85, 70, 3]. In Chap. 3 we present a new derivation of this characteristic theory, based on the Galilean invariant symmetrizable form of the conservative MHD equations [52, 118, 7] with a source term (the right hand side term proportional to $\nabla \cdot \vec{B}$ in Eq. 2.6) and using a matrix approach [70, 19]. This derivation gives insight into the structure of the MHD equations as a system of Galilean invariant conservation laws with a constraint, and in a simple, compact, and systematic way we recover all the various results that are scattered throughout the literature.

Numerical simulations of MHD flows with shocks have been performed for many decades, but most of the time relatively primitive numerical techniques of Lax-Wendroff or Flux Corrected Transport type were used. Numerical codes typically either were excessively diffusive or produced spurious oscillations near discontinuities. In the mean time robust and accurate shock-capturing numerical techniques of the so-called high-resolution type were developed in the domain of Computational Fluid Dynamics (CFD) [90]. Only since a decade or so, some of these new numerical methods have started to be used in MHD codes. The MHD system has a few peculiar properties which impeded the straight translation of the CFD techniques, but it seems that the main obstacles have been cleared in recent work by Roe and Balsara (1996) [127], who provided a well-behaved eigensystem decomposition of the MHD Jacobian, and by Powell (1995) [118], who provided a consistent and efficient way to deal numerically with the $\nabla \cdot \vec{B} = 0$ constraint via a source term (the right hand side term proportional to $\nabla \cdot \vec{B}$ in Eq. 2.6). In Chap. 4 of this dissertation we report on the development of the massively parallel shock capturing MHD code PAR-MA (PARallel MAgnetohydrodynamics). Starting from the proven CFD concepts present in the von Karman institute multi-block solver [106], and incorporating the essential contributions of Roe and Powell [1], a robust and accurate high-resolution MHD flow solver was developed. Numerical techniques similar to the one used in this dissertation are currently being used in several application codes [118, 162, 124, 117], but not much can be found in the literature about rigorous validation of this approach. In Chap. 5 it is shown through careful validation studies based on characteristic theory that the from CFD derived numerical MHD scheme produces valid results.

Chapter 3

Analytical properties of the ideal MHD equations

In this chapter we discuss analytical properties of the ideal MHD equations which are useful for the interpretation and analysis of numerical simulation results throughout this dissertation. In Sec. 3.1 we introduce the ideal MHD equations. In Sec. 3.2 we discuss the theory of characteristics applied to the ideal MHD system. In the final section we introduce the theory of MHD discontinuities, and we discuss non-convexity and compound shocks.

3.1 The ideal MHD equations

The ideal MHD equations can be written under several different forms, each of which enlightens certain properties of the MHD system. First we discuss a formulation which gives insight in the physical forces and processes involved. Next the conservative form is discussed, which emphasizes the conservation law nature of the equations.

3.1.1 'Physical' form of the MHD equations

In the non-relativistic limit the dynamics of a perfectly conducting one-component fluid can be described by the ideal MHD equations. At a given point in space and time the fluid can be described by eight *state variables* (or *primitive variables*): the density ρ, pressure p, velocity vector $\vec{v}$ and magnetic field vector $\vec{B}$. These state variables are functions of the continuous space coordinate vector $\vec{x}$ and the time t. A full description of the dynamical evolution of the conducting fluid is given by eight equations which express the time evolution of the state variables.

The first equation is the mass continuity equation

$$\frac{\partial \rho}{\partial t} + \nabla \cdot (\rho \vec{v}) = 0, \tag{3.1}$$

which describes the conservation of mass. This equation is the same as for the case of a neutral fluid.

Three more equations are provided by the vector momentum equation

$$\rho \frac{d\vec{v}}{dt} = -\nabla p + (\nabla \times \vec{B}) \times \vec{B}, \tag{3.2}$$

which is an expression of Newton's law of motion. This equation is the same as for the case of a neutral fluid, except for the additional $\vec{J} \times \vec{B}$ force exerted by the magnetic field on the charged fluid elements. The current density $\vec{J}$ is given by Ampère's law

$$\vec{J} = \nabla \times \vec{B}, \tag{3.3}$$

with units chosen such that the magnetic permeability μ equals 1 and does thus not show up in the equations. The relation between the total or convective derivative d/dt (which can be thought of as to describe the time evolution of a quantity associated with a moving fluid element) and the partial or local derivative $\partial/\partial t$ is given by

$$\frac{d}{dt} = \frac{\partial}{\partial t} + (\vec{v} \cdot \nabla). \tag{3.4}$$

The next three equations are given by the vector induction equation

$$\frac{\partial \vec{B}}{\partial t} = \nabla \times (\vec{v} \times \vec{B}), \tag{3.5}$$

which derives directly from one of Maxwell's equations, namely, Faraday's law of induction, and from Ohm's law for an ideal plasma

$$\vec{E} = -\vec{v} \times \vec{B}, \tag{3.6}$$

with $\vec{E}$ the electric field.

The final equation describes the evolution of the pressure

$$\frac{\partial p}{\partial t} + (\vec{v} \cdot \nabla)p + \gamma p \nabla \cdot \vec{v} = 0, \tag{3.7}$$

where ideal gas behavior is assumed. This equation is the same as for the case of a neutral fluid, and describes the conservation of the specific entropy s. Indeed, we can rewrite Eq. 3.7 as

$$\frac{ds}{dt} = 0, \tag{3.8}$$

with the (specific) entropy s given by

$$s = \frac{p}{\rho^{\gamma}}, \tag{3.9}$$

for an ideal gas. We call s the entropy throughout this dissertation, although strictly speaking the thermodynamic entropy density is given by the quantity $c_v \log(s)$, with c_v the specific heat at constant volume. The adiabatic index γ is the ratio of specific heats, and is taken equal to the mono-atomic gas value of 5/3 throughout this dissertation, because the ion component of most space physics plasmas mainly consists of ionized hydrogen.

This constitutes a complete system of evolution equations describing the dynamics of a conducting fluid. However, it is an observational fact that magnetic monopoles do not exist in nature, so the above equations have to be supplemented with the divergence free condition

$$\nabla \cdot \vec{B} = 0. \tag{3.10}$$

This condition implies that the magnetic flux is conserved in space, in the sense that the net flux through the surface of a closed volume vanishes, which allows for the concept of *flux tubes*. By taking the divergence of the induction equation 3.5 one can see that once the divergence free condition is imposed as an initial condition, it automatically remains fulfilled at later times. The divergence free condition is thus in a way *compatible* with the MHD equations, and can be seen as an additional *constraint* to the MHD system.

3.1.2 Conservative form of the MHD equations

The MHD equations introduced above can be re-stated in explicit conservation law form. We introduce the specific total energy e, given by

$$e = \frac{p}{\gamma - 1} + \rho\,\frac{\vec{v}\cdot\vec{v}}{2} + \frac{\vec{B}\cdot\vec{B}}{2}. \tag{3.11}$$

Then the ideal MHD equations can be written as

$$\frac{\partial}{\partial t}\begin{bmatrix} \rho \\ \rho\,\vec{v} \\ \vec{B} \\ e \end{bmatrix} + \nabla\cdot\begin{bmatrix} \rho\,\vec{v} \\ \rho\,\vec{v}\vec{v} + \mathsf{I}\left(p + \vec{B}\cdot\vec{B}\,/2\right) - \vec{B}\vec{B} \\ \vec{v}\vec{B} - \vec{B}\vec{v} \\ \left(e + p + \vec{B}\cdot\vec{B}\,/2\right)\vec{v} - \left(\vec{v}\cdot\vec{B}\right)\vec{B} \end{bmatrix} = -\begin{bmatrix} 0 \\ \vec{B} \\ \vec{v} \\ \vec{v}\cdot\vec{B} \end{bmatrix}\nabla\cdot\vec{B}. \tag{3.12}$$

This form of the equations expresses the basic conservation of the *conservative variables* mass ρ, momentum $\rho\vec{v}$, magnetic field $\vec{B}$ and specific total energy e, and shows explicitly that the total mass, momentum, magnetic field and energy present in any given volume can only change when there is a net *flux* through the boundaries of the volume. This equation again has to be supplemented with the divergence free condition $\nabla \cdot \vec{B} = 0$ as an initial condition.

The right hand side (RHS) term of Eq. 3.12 is proportional to $\nabla \cdot \vec{B} = 0$ and is thus identically zero, but for several reasons to be explained below it is advantageous to keep this term in the equations.

The main function of the RHS term (sometimes also called the *Powell source term*) is that it makes the MHD equations *Galilean invariant* also when $\nabla \cdot \vec{B} \neq 0$. A necessary property of any well-posed theory in non-relativistic physics is that it has to be Galilean invariant. The MHD system, for instance as described by the equations given in Sec. 3.1.1 supplemented with the $\nabla \cdot \vec{B} = 0$ condition, of course is Galilean invariant. However, without this constraint, the induction equation 3.5 of Sec. 3.1.1 is *not* Galilean invariant, as can be shown as follows [34]. Making the following Galilean transformation to a new rest frame indicated by primed quantities

$$\begin{aligned} \vec{x}\,' &= \vec{x} - \vec{a}t \\ t\,' &= t \\ \vec{v}\,' &= \vec{v} - \vec{a} \\ \vec{B}\,' &= \vec{B} \\ \frac{\partial}{\partial t} &= \frac{\partial}{\partial t\,'} - \vec{a} \cdot \nabla\,' \\ \nabla &= \nabla\,', \end{aligned} \tag{3.13}$$

the induction equation Eq. 3.5 transforms to

$$\frac{\partial \vec{B}\,'}{\partial t\,'} = \nabla\,' \times (\vec{v}\,' \times \vec{B}\,') - \vec{a}\; \nabla\,' \cdot \vec{B}\,', \tag{3.14}$$

which is clearly of a different form than Eq. 3.5 (if $\nabla \cdot \vec{B} \neq 0$). We can restore Galilean invariance by changing the induction equation 3.5 to

$$\frac{\partial \vec{B}}{\partial t} = \nabla \times (\vec{v} \times \vec{B}) - \vec{v}\; \nabla \cdot \vec{B}, \tag{3.15}$$

and this is precisely the form of the induction equation in Eq. 3.12. If one does not use the $\nabla \cdot \vec{B} = 0$ condition in rewriting the equation of motion Eq. 3.2 into conservative form, then one finds the form of Eq. 3.12 with the extra RHS source term. Similarly, construction of the total energy equation without making use of the $\nabla \cdot \vec{B} = 0$ condition leads to the form with the RHS source term. We can thus summarize by saying that the conservative form of the equations *without* the RHS source term is *not* Galilean invariant when $\nabla \cdot \vec{B} \neq 0$, but that the form *with* the source term restores Galilean invariance.

Although $\nabla \cdot \vec{B} = 0$ rigorously in analytical approaches to MHD problems, it is useful to consider the form of the equations with the source term in the following three cases.

First, Godunov [51, 52, 7] proved in 1972 that this is the unique form of the MHD equations which is symmetrizable. The symmetrized form of the equations is useful for the design of numerical schemes in natural 'entropy variables' [7] and for the analysis of stability of shock waves [35].

Second, we show in Sec. 3.2 that the inclusion of this RHS term is essential for our derivation of the characteristic theory of the MHD equations in a simple, compact, and systematic procedure using a matrix approach. Characteristic analysis based on the symmetrizable form of the conservative MHD equations gives insight into the basic structure of the MHD equations as a system of Galilean invariant conservation laws with a constraint.

Third, in some numerical schemes, the $\nabla \cdot \vec{B} = 0$ constraint is only satisfied up to a discretization error. As first shown in [118], inclusion of the RHS term assures that these small $\nabla \cdot \vec{B}$ errors are consistently accounted for in a numerically stable way and do not lead to accumulation of inaccuracies. The numerical code used in this dissertation makes use of this technique to control the $\nabla \cdot \vec{B}$ errors, as is described in Chapter 4.

Next to the conservation of mass, momentum, magnetic field and energy mentioned above, there are other quantities in the ideal MHD system which are conserved in the sense that they are *frozen* into the moving plasma. As follows from Eq. 3.9, the entropy s of a moving fluid element is a conserved scalar quantity. Also, the *magnetic flux* through a surface moving with the flow is a conserved quantity associated with the magnetic field lines which are frozen into the plasma. Indeed, we can make use of a general expression for the convective time derivative of the flux Φ of a vector field $\vec{A}$ through a surface S which moves with velocity $\vec{u}$. The flux Φ is defined by

$$\Phi = \int_S \vec{A} \cdot \vec{n} dS, \tag{3.16}$$

with $\vec{n}$ the vector normal to the surface, and the total time derivative of the flux is given by

$$\frac{d\Phi}{dt} = \int_S (\frac{\partial \vec{A}}{\partial t} + \vec{u}(\nabla \cdot \vec{A}) + \nabla \times (\vec{A} \times \vec{u})) \cdot \vec{n} dS. \tag{3.17}$$

The total time derivative of the flux Φ_B of the magnetic field $\vec{B}$ through a surface moving with the plasma speed $\vec{v}$ is then given by

$$\frac{d\Phi_B}{dt} = \int_S (\frac{\partial \vec{B}}{\partial t} + \vec{v}(\nabla \cdot \vec{B}) + \nabla \times (\vec{B} \times \vec{v})) \cdot \vec{n} dS. \tag{3.18}$$

Using the Galilean invariant form of the induction equation Eq. 3.15 it follows that the magnetic flux Φ_B through a surface moving with the plasma is conserved *in time*

$$\frac{d\Phi_B}{dt} = 0, \tag{3.19}$$

also if $\nabla \cdot \vec{B} \neq 0$. It is interesting to remark that the conserved variables ρ, $\rho\,\vec{v}$, $\vec{B}$ and e remain conserved quantities in dissipative MHD (Eq. 2.6), whereas the entropy s and the magnetic flux are not conserved (frozen–in) in dissipative MHD. Another manifestation of the fact that the magnetic field is frozen into the plasma for ideal MHD, is that fluid elements which reside on a common field line at one time, remain on this magnetic field line at all times. These frozen-in quantities can be characterized and classified with more insight when one considers them in the framework of differential forms, vector fields and Lie-derivatives, as is done for instance in [65]. The magnetic field vector, for instance, is a 2-form or an *axial* vector, which in general has the property of conservation of flux. These considerations, however, are beyond the scope of this introduction to the MHD equations.

The ideal MHD system belongs to the class of symmetric hyperbolic systems [21], which have many interesting and well-defined properties. Hyperbolic systems describe wave phenomena. Characteristic analysis naturally reveals the properties of the hyperbolicity of the system and its associated waves, and is taken up in Sec. 3.2.

3.1.3 Scaling invariance of the stationary ideal MHD equations

Physical variables are expressed in certain units, and we have some freedom in choosing these units. The solution to a given physical stationary MHD problem should of course not depend on the units we choose. We can scale the primitive variables and space coordinates as

$$\begin{aligned} \rho'(\vec{x}\,') &= \bar{\rho}\,\rho(\vec{x}) \\ p'(\vec{x}\,') &= \bar{p}\,p(\vec{x}) \\ \vec{v}\,'(\vec{x}\,') &= \bar{v}\,\vec{v}(\vec{x}) \\ \vec{B}\,'(\vec{x}\,') &= \bar{B}\,\vec{B}(\vec{x}) \\ \vec{x}\,' &= \bar{x}\,\vec{x} \end{aligned} \tag{3.20}$$

with for instance ρ' the density in the new units, ρ the original density, and $\bar{\rho}$ a scaling factor. Scaling the variables in the momentum equation 3.2 with $\partial/\partial t \equiv 0$ results in

$$\frac{\bar{p}}{\bar{\rho}\,\bar{v}^2}\,\rho'\,(\vec{v}\,'\cdot\nabla\,')\,\vec{v}\,' = -\nabla\,'p' + \frac{\bar{p}}{\bar{B}^2}\,(\nabla\,'\times\vec{B}\,')\times\vec{B}\,'. \tag{3.21}$$

This equation describes the same physical problem as the momentum equation 3.2 in the original variables only if $\bar{p} = \bar{\rho}\,\bar{v}^2$ and $\bar{p} = \bar{B}^2$. This expresses the fact that we cannot completely freely choose units because the dimensions of physical quantities are not independent. For stationary ideal MHD, these are the only two independent dimensional constraints. We call scaling under these constraints *consistent scaling*.

This reasoning also implies that every class of solutions to the stationary ideal MHD system which are equivalent up to scaling, is labeled by two independent dimensionless quantities taken in an arbitrary point of the solution, for which we can choose the following:

$$\beta = \frac{p}{B^2/2} \quad \text{and} \quad M = \frac{v}{\sqrt{\gamma p/\rho}}, \tag{3.22}$$

with v and B vector magnitudes. The reader can verify that these two quantities are indeed invariant under consistent scaling. Sometimes the Alfvénic Mach number $M_A = v/(B/\sqrt{\rho})$ is taken in stead of the sonic Mach number M. These quantities do not depend on the spatial scale, so stationary ideal MHD flows are length scale invariant. For instance, in stationary bow shock flows the size of the obstacle is irrelevant, because scaling the obstacle just means that the solution has to be scaled in the same way.

Consider a stationary ideal MHD flow problem with the boundary geometry and boundary conditions specified. We can obtain physically different flow problems by scaling the values imposed at inflow boundaries without taking into account the dimensional constraints. This non-consistent scaling changes the values of β and/or M. There are only two parameters that can be changed independently, so we can say that ideal MHD problems have *two free parameters* under scaling. If one studies stationary ideal MHD problems in a general way and one wants to perform complete parameter studies, it is important to know how many free scaling parameters there are and it is helpful to label solutions with these free parameters. Therefore most of the time we express inflow conditions in terms of the dimensionless quantities β and M for the numerical simulations described in this dissertation.

3.2 Characteristic analysis of the ideal MHD equations

An extensive general theory exists for the characteristic properties of symmetric hyperbolic systems [21, 20]. This theory has been applied early on to unsteady MHD flows [21] and to steady planar ($B_z \equiv v_z \equiv 0$) MHD flows, including the case where the magnetic field is aligned with the flow (field-aligned or parallel flow) [79, 59]. More complete accounts of the characteristic theory of steady and unsteady MHD flows appeared later [71, 85, 70, 3].

In this Section we present a concise derivation of some aspects of the characteristic theory of the MHD equations with two independent variables (time-dependent MHD in the xt plane and steady MHD in the xy plane), in preparation for the characteristic analysis of MHD flows with shocks later in this dissertation. This Section serves to introduce the reader who is unfamiliar with the theory of characteristics to the concepts, nomenclature and notation that is used further on. Moreover, our derivation of this characteristic theory, based on the Galilean invariant symmetrizable form of the conservative MHD equations with a source term [51, 118, 7] and using a matrix approach [70, 19], is new and attractive in its own right, because it gives insight into the structure of the MHD equations as a system of Galilean invariant conservation laws with a constraint, and because in a simple, compact, and systematic way we recover all the various results that are scattered throughout the literature [21, 79, 59, 71, 85, 70, 3, 19]. This derivation of characteristic theory has appeared in [151]. Before deriving the characteristic properties of the MHD system with two independent variables, we briefly introduce the concept of characteristic curves, starting from the simple case of a scalar equation.

3.2.1 The theory of characteristics

The basic concepts and definitions of characteristic theory can be most clearly presented for the simple scalar case. Consider a conservation law for the *scalar* quantity $u(x,t)$ which depends on two independent variables x and t,

$$\frac{\partial u}{\partial t} + \frac{\partial f(u)}{\partial x} = 0, \tag{3.23}$$

or

$$\frac{\partial u}{\partial t} + f'(u)\frac{\partial u}{\partial x} = 0, \tag{3.24}$$

where $f(u)$ is called the flux function and the prime denotes a derivative with respect to u. If $f'(u)$ is real, then there exist curves $x(t)$ in the xt

plane defined by

$$\frac{dx(t)}{dt} = f'(u), \tag{3.25}$$

such that

$$\frac{du(x(t),t)}{dt} = 0. \tag{3.26}$$

Along these curves, which are called characteristics, the partial differential equation Eq. 3.23 reduces to the ordinary differential equation Eq. 3.26. The equation is said to be hyperbolic when $f'(u)$ is real and real characteristic curves exist. The scalar u is then invariant on the characteristic curve and is called a Riemann Invariant (RI). The slope of the characteristic $\lambda = f'(u)$ is called the characteristic speed. For the scalar case, the characteristics are straight lines (when f only depends on u and not directly on the independent variables).

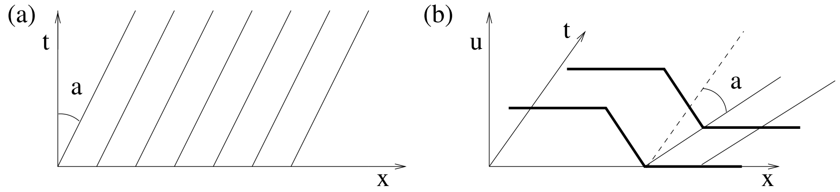

Figure 3.1: *The scalar advection equation. (a) Characteristic curves (thin solid) are parallel straight lines with slope a. (b) A wave profile u (thick solid) is advected with speed a.*

The most simple illustration of these concepts is probably the case of the *linear* scalar conservation law, with flux function $f(u) = a\ u$. The characteristics are parallel straight lines in the xt plane with slope $f'(u) = a$, as shown in Fig. 3.1a. The scalar u is constant on every characteristic, which means that a wave profile is just advected with speed a, as shown in Fig. 3.1b. A scalar conservation law with a linear flux function is therefore also called a *scalar advection equation.*

An example of a *nonlinear* scalar conservation law is Burgers' equation, with flux function $f(u) = u^2/2$. The effect of the nonlinearity of the flux function is that a smooth profile can steepen into a shock. In Fig. 3.2 we show how an initial state containing a linear profile for $x \in [0, 1]$, varying from $u = 1.5$ on the left to $u = -0.5$ on the right, steepens into a shock. Fig. 3.2a shows the characteristics with slope $f'(u) = u$ in the xt plane. The shock is formed when the characteristics first intersect at $(x = 3/4, t = 1/2)$. The discontinuity is necessary to avoid a multivalued solution where the characteristics intersect. Fig. 3.2b shows a surface plot of u.

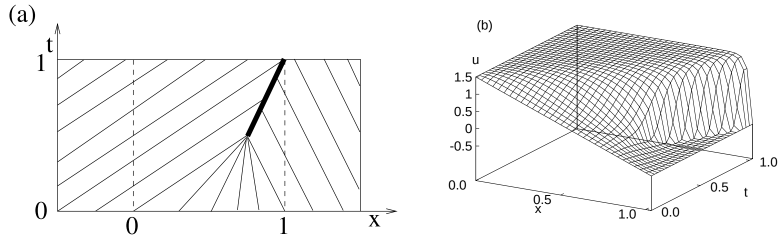

Figure 3.2: *Steepening of a linear profile into a shock for Burgers' equation. (a) Characteristic curves (thin solid) converge into the shock (thick solid). (b) Surface plot of u.*

The concept of characteristic curves carries over to a *system* of conservation laws with two independent variables in the following way.

Consider a *linear* system of n coupled equations

$$\frac{\partial \mathbf{U}}{\partial t} + \mathsf{A} \cdot \frac{\partial \mathbf{U}}{\partial x} = 0, \tag{3.27}$$

with $\mathbf{U}$ a state vector of n conserved quantities, and A a $n \times n$ constant matrix. Suppose an eigenvector decomposition of matrix $\mathsf{A} = \mathsf{R} \cdot \Lambda \cdot \mathsf{L}$ exists, with the columns of R being the right eigenvectors of A, the rows of L being the left eigenvectors of A, $\mathsf{R} = \mathsf{L}^{-1}$, and Λ being a diagonal matrix with the eigenvalues of A on the diagonal. The system is said to be hyperbolic if all the eigenvalues are real. The system can be described in terms of the *characteristic variables* $\mathbf{W} = \mathsf{L} \cdot \mathbf{U}$ as

$$\frac{\partial \mathbf{W}}{\partial t} + \Lambda \cdot \frac{\partial \mathbf{W}}{\partial x} = 0. \tag{3.28}$$

This decouples the equations, and for every component of $\mathbf{W}$ we have the conservation law

$$\frac{\partial w_i}{\partial t} + \lambda_i \frac{\partial w_i}{\partial x} = 0. \tag{3.29}$$

If the system is hyperbolic, then n families of characteristic curves exist in real space, defined by $dx/dt = \lambda_i$. These characteristics are straight lines, and each w_i is a RI on its associated family of characteristics. If some λ_i is complex, then its associated characteristic does not exist in real space, and it is said that the ith characteristic field is elliptic.

A *nonlinear* system of n coupled equations in quasi-linear form with two independent variables is described by

$$\frac{\partial \mathbf{U}}{\partial t} + \mathsf{A}(\mathbf{U}) \cdot \frac{\partial \mathbf{U}}{\partial x} = 0, \tag{3.30}$$

— where $\mathsf{A}(\mathbf{U})$ can be the Jacobian matrix of a flux function $\mathbf{F}$ associated with a set of conservation laws — and is hyperbolic in state $\mathbf{U}$ if the eigenvector decomposition of $\mathsf{A}(\mathbf{U})$ exists and all the eigenvalues of $\mathsf{A}(\mathbf{U})$ are real. The definition of the characteristic variables $\partial\mathbf{W} = \mathsf{L}(\mathbf{U})\cdot\partial\mathbf{U}$ is now only locally valid. Characteristics exist if the system is hyperbolic, and the real eigenvalues of $\mathsf{A}(\mathbf{U})$ determine the slopes of the characteristics locally. The characteristics are in general not straight lines any more, except in *simple wave* regions, where one family of characteristics consists of straight lines [20, 85, 92]. Riemann Invariants do not generally exist, but sometimes it is possible to find one or more functions χ_i of the dependent variables $\mathbf{U}$ such that $d\chi_i \sim \mathsf{L}_i \cdot d\mathbf{U}$, which defines χ_i as a Riemann Invariant. The mathematical interpretation of characteristic curves is that derivatives normal to the characteristic curve cannot be determined from the governing equations, because the equations only specify derivatives along the characteristic curves. The solution on a characteristic curve does not determine the solution in neighboring points not on this curve. This geometric property puts strict constraints on the posing of boundary conditions, namely, that characteristic curves cannot serve as boundaries on which boundary conditions are imposed. The physical interpretation is that weak discontinuities propagate as waves along characteristics, such that a characteristic variable is locally conserved on its corresponding characteristic (whereas Riemann Invariants are globally conserved on their characteristics). Equivalently, the wave information carried by a local characteristic variable follows a strict characteristic path and cannot escape in a direction perpendicular to the characteristic. It does not influence the solution away from this characteristic.

The above analysis was placed in an xt context, and the theory of characteristics was related to concepts of propagation of physical waves in a time-dependent system. The same analysis can also be applied to steady state systems of equations, in which the time variable is not present anymore. Steady equations can also be hyperbolic, and by direct analogy we can relate the characteristic structure of steady equations to the stationary analogs of time-dependent waves, which we call stationary waves. For instance, the concept of simple waves in MHD can be carried over from the time-dependent context (xt) to the stationary context (xy) [85]. The formal analogy between the analysis of xt and xy systems of equations, both special cases of the full equations in xyt – or even $xyzt$ –, can be clarified by the following considerations. In the following Sections we use this formal analogy to derive the characteristic properties of the xt and xy MHD equations in a unified and systematic way.

A general quasi-linear time-dependent system of n first order partial differential equations in two space dimensions is described by

$$\frac{\partial \mathbf{U}}{\partial t} + \mathsf{A}(\mathbf{U}) \cdot \frac{\partial \mathbf{U}}{\partial x} + \mathsf{B}(\mathbf{U}) \cdot \frac{\partial \mathbf{U}}{\partial y} = 0, \tag{3.31}$$

with $\mathbf{U}$ a vector of dependent variables and A and B $n \times n$ matrices. This system reduces to a system with two independent variables for the case of a 1D time-dependent flow ($\partial/\partial y = 0$) and for the case of a 2D steady flow ($\partial/\partial t = 0$). In the first case, the last term of Eq. 3.31 vanishes, and the procedure which was outlined above can be used to study the characteristic structure of the equations. In the second case, the first term of Eq. 3.31 vanishes, and one can examine the characteristic properties of the equation

$$\frac{\partial \mathbf{U}}{\partial x} + \mathsf{A}^{-1} \cdot \mathsf{B} \cdot \frac{\partial \mathbf{U}}{\partial y} = 0, \tag{3.32}$$

leading to characteristic analysis in the xy plane. The eigenvalues and left eigenvectors of the matrix $\mathsf{C} \equiv \mathsf{A}^{-1} \cdot \mathsf{B}$ again determine the type of the system, the characteristic directions in the xy plane, and the Riemann Invariants.

3.2.2 Characteristic analysis of time-dependent MHD in one space dimension

In this section, the above sketched general framework is applied to the MHD equations and a derivation is presented of some aspects of the characteristic theory of the MHD equations [21, 79, 59, 71, 85, 70, 3, 19]. We analyze the symmetrizable form of the equations (3.12), and do not use the condition $\nabla \cdot \vec{B} = 0$, unless where necessary and stated. In this way we are able to see how the characteristic structure of the MHD equations is independent of the $\nabla \cdot \vec{B}$ constraint, and when this constraint becomes important.

Equation 3.12 can be written in the quasi-linear form of Eq. 3.31 with $\mathbf{U} = (\rho, v_x, v_y, v_z, B_x, B_y, B_z, p)$ the vector of primitive variables, and matrices

$$\mathsf{A} = \begin{bmatrix} v_x & \rho & 0 & 0 & 0 & 0 & 0 & 0 \\ 0 & v_x & 0 & 0 & 0 & B_y/\rho & B_z/\rho & 1/\rho \\ 0 & 0 & v_x & 0 & 0 & -B_x/\rho & 0 & 0 \\ 0 & 0 & 0 & v_x & 0 & 0 & -B_x/\rho & 0 \\ 0 & 0 & 0 & 0 & v_x & 0 & 0 & 0 \\ 0 & B_y & -B_x & 0 & 0 & v_x & 0 & 0 \\ 0 & B_z & 0 & -B_x & 0 & 0 & v_x & 0 \\ 0 & c^2\rho & 0 & 0 & 0 & 0 & 0 & v_x \end{bmatrix}, \tag{3.33}$$

and

$$
\mathsf{B} = \begin{bmatrix}
v_y & 0 & \rho & 0 & 0 & 0 & 0 & 0 \\
0 & v_y & 0 & 0 & -B_y/\rho & 0 & 0 & 0 \\
0 & 0 & v_y & 0 & B_x/\rho & 0 & B_z/\rho & 1/\rho \\
0 & 0 & 0 & v_y & 0 & 0 & -B_y/\rho & 0 \\
0 & -B_y & B_x & 0 & v_y & 0 & 0 & 0 \\
0 & 0 & 0 & 0 & 0 & v_y & 0 & 0 \\
0 & 0 & B_z & -B_y & 0 & 0 & v_y & 0 \\
0 & 0 & c^2\rho & 0 & 0 & 0 & 0 & v_y
\end{bmatrix}. \tag{3.34}
$$

The xt characteristic analysis yields the following results. The eigenvalues of matrix A are

$$
\lambda_{1,2} = v_x \pm c_{fx}, \quad \lambda_{3,4} = v_x \pm c_{Ax}, \quad \lambda_{5,6} = v_x \pm c_{sx}, \quad \lambda_{7,8} = v_x. \tag{3.35}
$$

Here c_{fx}, c_{Ax} and c_{sx} are the fast magneto-sonic wave speed, the Alfvén speed, and the slow magneto-sonic wave speed, which all depend on the direction x — they are *anisotropic*—, and which are given by

$$
c_{fx}^2 = \frac{1}{2}\left(\frac{\gamma p + B^2}{\rho} + \sqrt{\left(\frac{\gamma p + B^2}{\rho}\right)^2 - 4\frac{\gamma p B_x^2}{\rho^2}}\right), \tag{3.36}
$$

$$
c_{Ax}^2 = \frac{B_x^2}{\rho}, \tag{3.37}
$$

$$
c_{sx}^2 = \frac{1}{2}\left(\frac{\gamma p + B^2}{\rho} - \sqrt{\left(\frac{\gamma p + B^2}{\rho}\right)^2 - 4\frac{\gamma p B_x^2}{\rho^2}}\right). \tag{3.38}
$$

These wave speeds satisfy the property

$$
c_{fx} \geq c_{Ax} \geq c_{sx}, \tag{3.39}
$$

for any direction x. The hydrodynamic (HD) system has only one isotropic wave speed c, but the MHD system thus has three different wave modes which are highly anisotropic. In the direction of the magnetic field, the fast wave speed coincides with the largest of the sound and the Alfvén speed, while the slow wave speed coincides with the smallest of the two. Slow waves and Alfvén waves have a vanishing propagation speed in the direction perpendicular to the magnetic field. Slow and fast waves are called magneto-sonic waves, because they are compressible (ρ and p change) like sound waves in hydrodynamics. Compressibility is a nonlinear effect which can make fast and slow waves steepen into shocks. Alfvén waves are not compressible. They are linear waves.

We can define three Mach numbers associated with the three different wave modes. These Mach numbers also depend on the direction, and are given by

$$M_{fx} = \frac{|v_x|}{c_{fx}}, \quad M_{Ax} = \frac{|v_x|}{c_{Ax}}, \quad \text{and} \quad M_{sx} = \frac{|v_x|}{c_{sx}}. \tag{3.40}$$

The eigenvalues in Eq. 3.35 are always real, meaning that the system is always hyperbolic, and the eigenvalues thus determine the characteristic directions in the xt plane. The left eigenvectors

$$\mathsf{L}_7 = (-c^2, 0, 0, 0, 0, 0, 0, 1) \text{ and } \mathsf{L}_8 = (0, 0, 0, 0, 1, 0, 0, 0), \tag{3.41}$$

can be used to derive the Riemann Invariants

$$\chi_7 = s \text{ and } \chi_8 = B_x. \tag{3.42}$$

For instance, the condition that $\mathsf{L}_7 \cdot d\mathbf{U} = 0$ in the direction of the characteristic with slope v_x, can be written as $\mathsf{L}_7 \cdot (d\rho, dv_x, dv_y, dv_z, dB_x, dB_y, dB_z, dp) = -c^2 d\rho + dp = 0$. This leads to $ds = 0$, because it follows from Eq. 3.9 that $ds = dp/\rho^\gamma - \gamma p/\rho^{\gamma+1}\, d\rho = (-c^2 d\rho + dp)/\rho^\gamma$. This means that the entropy s is a RI. Making use of $\nabla \cdot \vec{B} = 0$, it follows from Eq. 3.12 that B_x has to be constant in x and t, such that B_x is a global RI (with a constant value in the whole xt domain), and can thus be eliminated from the xt equations, resulting in the more common description of 1D time-dependent MHD with seven dependent variables. Here we can also clarify why we have started our analysis from Eq. 3.12 with the RHS term included: omission of this term results in an eigenvalue $\lambda_8 = 0$ [118], which is not a Galilean invariant property, because a change in reference frame would change v_x and thus all the wave speeds accordingly, except λ_8, which would remain zero also in the new reference frame. This zero eigenvalue makes matrix A singular, such that the general procedure outlined above to derive the xy characteristics, which uses A^{-1}, would fail.

3.2.3 Characteristic analysis of stationary MHD in two space dimensions

For steady state solutions the xy characteristic analysis yields the following results. In the stationary case, the governing equations are not always fully hyperbolic. If some eigenvalue of matrix $\mathsf{C} = \mathsf{A}^{-1} \cdot \mathsf{B}$ is not real, then its associated characteristic does not exist. It is hard to find closed expressions for the eigenvalues of matrix $\mathsf{C} = \mathsf{A}^{-1} \cdot \mathsf{B}$, but using software for symbolical calculation, we can easily factorize the condition $\det(\mathsf{C} - \lambda \mathsf{I}) = 0$ in terms of the variable

$$v_\perp^2 = \frac{(-v_y + v_x \lambda)^2}{1 + \lambda^2}, \tag{3.43}$$

which represents the square of the velocity component perpendicular to the characteristic, as the direction of the characteristic is given by $dy/dx = \lambda$. This factorization leads to the following roots:

$$v_{\perp 1}^2 = c_{f\perp}^2, \qquad v_{\perp 2}^2 = c_{A\perp}^2, \qquad v_{\perp 3}^2 = c_{s\perp}^2, \qquad v_{\perp 4}^2 = 0, \tag{3.44}$$

where $c_{f\perp}$, $c_{A\perp}$, and $c_{s\perp}$ are the fast magnetosonic, Alfvén, and slow magnetosonic velocities in the direction perpendicular to the characteristic [85, 19]. For every condition (3.44), if real λs can be found which satisfy the condition, then the associated characteristics exist and we say that the associated characteristic fields are hyperbolic.

The physical interpretation of these conditions is clear: if they exist, then the xy characteristics are curves from which no wave information carried by the associated characteristic variable can escape in a direction perpendicular to the characteristic. For instance, the wave with wave speed $v_\perp - c_{f\perp}$ perpendicular to the characteristic cannot transport information in this perpendicular direction when $v_\perp = c_{f\perp}$. This defines the steady xy characteristics as curves on which the perpendicular plasma speed equals a perpendicular wave speed. We say that the flow is sonic in the direction perpendicular to the characteristic.

The equation for $v_{\perp 4}$ always has two real solutions, $\lambda_{7,8} = v_y/v_x$, meaning that the streamlines are two-fold degenerate characteristics. The associated left eigenvectors are

$$\begin{aligned} \mathsf{L}_7 &= (-c^2, 0, 0, 0, 0, 0, 0, 1), \\ \mathsf{L}_8 &= (0, B_y/v_x, -B_x/v_x, 0, -v_y/v_x, 1, 0, 0), \end{aligned} \tag{3.45}$$

and can be used to derive the Riemann Invariants

$$\chi_7 = s \quad \text{and} \quad \chi_8 = -v_x B_y + v_y B_x = E_z, \tag{3.46}$$

with E_z the z-component of the electric field. Making use of $\nabla \cdot \vec{B} = 0$, it follows from (3.12) that Riemann Invariant $\chi_8 = E_z$ is a global invariant, as with $\nabla \cdot \vec{B} = 0$ the evolution equation of the magnetic field reduces to the classical form of the induction equation $\partial \vec{B}/\partial t = -\nabla \times \vec{E}$. Then $\partial \vec{B}/\partial t = -\nabla \times \vec{E} = 0$ leads to $\partial E_z/\partial x = \partial E_z/\partial y = 0$. E_z can thus be eliminated from the equations. The entropy is conserved on a streamline in continuous flow. However, it follows from the MHD Rankine-Hugoniot (RH) jump conditions [87, 92, 4], which are discussed in the next Section, that the entropy is discontinuous when a streamline crosses a shock.

The equation for $v_{\perp 2}$ always has two real solutions as well, $\lambda_{3,4} = (B_y \pm \sqrt{\rho} v_y)/(B_x \pm \sqrt{\rho} v_x)$.

The equations for $v_{\perp 1}$ and $v_{\perp 3}$ are much more complicated. Depending on the parameters, the equation for $v_{\perp 1}$ can have no solution or two solutions for λ. The equation for $v_{\perp 3}$ can have zero, two, or four real solutions for λ, with the total number of real solutions for the two equations not exceeding four. The slow and fast magnetosonic characteristic fields can thus be hyperbolic or elliptic depending on the parameters, and no simple formulas can be found as criteria for hyperbolicity. Graphical methods can be used to determine the hyperbolic and elliptic regions of the equations [3, 79, 59, 71, 85, 70, 19].

In the case of planar MHD ($v_z \equiv B_z \equiv 0$), the Alfvén waves disappear, meaning that the families of characteristics corresponding to characteristic speeds λ_3 and λ_4 drop out, both in the xt and in the xy case. The other characteristic families remain unchanged.

For steady MHD in two space dimensions with no variation in the z direction, the xy plane is called the *poloidal plane*, and the velocity and magnetic fields in this plane are called the *poloidal* fields $\vec{v}^{(p)}$ and $\vec{B}^{(p)}$. If $\vec{v}^{(p)}$ and $\vec{B}^{(p)}$ are aligned somewhere in the xy domain, then $E_z = 0$ at that location. It then follows from the analysis given above, that $\vec{v}^{(p)}$ and $\vec{B}^{(p)}$ have to be aligned everywhere, as E_z is a global invariant and thus vanishes everywhere. It can be proved using the MHD RH relations, that this property is also conserved at shocks (as the tangential electric field is conserved at a shock). These properties establish the concept of steady *field-aligned* MHD flow, which is sometimes also called *parallel* flow. The above derived characteristic properties of stationary MHD in two space dimensions simplify considerably for the case of field-aligned flow, as is shown in the next Section. It is interesting to note that the characteristic structure of the MHD equations is independent of the constraint $\nabla \cdot \vec{B} = 0$. The characteristic structure derived from the symmetrizable form of the equations 3.12 is consistent and complete, without the need to impose the $\nabla \cdot \vec{B} = 0$ constraint. The concept of field-aligned flow, however, requires that $\nabla \cdot \vec{B} = 0$, because only then E_z is a global invariant.

3.2.4 Characteristic analysis of stationary field-aligned MHD in two space dimensions

The 2D MHD flows which we analyze in Chapters 5 and 6 of this dissertation belong to the class of steady planar field-aligned MHD. Therefore we now show how the above derived general results on characteristic analysis of the MHD equations simplify for the special cases of field-aligned flow and planar ($v_z \equiv B_z \equiv 0$) field-aligned flow [79, 59, 70, 62, 19].

We introduce the variable α in Eq. 3.12 with $\partial/\partial t = 0$ by taking $\vec{B}^{(p)} = \alpha \vec{v}^{(p)}$. The steady MHD equations for field-aligned flow reduce then to a 7×7 system with $\mathbf{U} = (\rho, v_x, v_y, v_z, \alpha, B_z, p)$, and matrices

$$\mathsf{A} = \begin{bmatrix} v_x & \rho & 0 & 0 & 0 & 0 & 0 \\ 0 & v_x & \alpha^2 v_y/\rho & 0 & \alpha v_y^2/\rho & B_z/\rho & 1/\rho \\ 0 & 0 & (1-\alpha^2/\rho)v_x & 0 & -\alpha v_x v_y/\rho & 0 & 0 \\ 0 & 0 & 0 & v_x & 0 & -\alpha v_x/\rho & 0 \\ 0 & \alpha & 0 & 0 & v_x & 0 & 0 \\ 0 & B_z & 0 & -\alpha v_x & 0 & v_x & 0 \\ 0 & c^2\rho & 0 & 0 & 0 & 0 & v_x \end{bmatrix}, \tag{3.47}$$

and

$$\mathsf{B} = \begin{bmatrix} v_y & 0 & \rho & 0 & 0 & 0 & 0 \\ 0 & (1-\alpha^2/\rho)v_y & 0 & 0 & -\alpha v_x v_y/\rho & 0 & 0 \\ 0 & \alpha^2 v_x/\rho & v_y & 0 & \alpha v_x^2/\rho & B_z/\rho & 1/\rho \\ 0 & 0 & 0 & v_y & 0 & -\alpha v_y/\rho & 0 \\ 0 & 0 & \alpha & 0 & v_y & 0 & 0 \\ 0 & 0 & B_z & -\alpha v_y & 0 & v_y & 0 \\ 0 & 0 & c^2\rho & 0 & 0 & 0 & v_y \end{bmatrix}. \tag{3.48}$$

Note that, consistent with our earlier observations, the fifth row of the equations now automatically leads to $\nabla \cdot (\alpha\vec{v}) = \nabla \cdot \vec{B} = 0$, although we have only explicitly imposed that $\alpha\vec{v}^{(p)} = \vec{B}^{(p)}$, and not that $\nabla \cdot \vec{B} = 0$.

Analysis of the characteristic properties of this 7×7 system yields the following results. The characteristic condition $\det(\mathsf{C} - \lambda\mathsf{I}) = 0$ can be factorized in terms of λ. This factorization leads to the following roots

$$\lambda_{1,2} = \frac{1}{B^2 + \rho\left(c^2 - v_x^2\right) - c^2 B^{(p)2}/v^{(p)2}}(-\rho v_x v_y \pm \sqrt{\left(B^2 + \left(\rho - B^{(p)2}/v^{(p)2}\right)c^2\right)\left(\rho v^{(p)2} - B^2 - \left(\rho - B^{(p)2}/v^{(p)\,2}\right)c^2\right)}), \tag{3.49}$$

$$\lambda_{3-7} = \frac{v_y}{v_x}. \tag{3.50}$$

Here B^2 is the squared magnitude of the total magnetic field, and $B^{(p)2}$ and $v^{(p)2}$ are the squared magnitudes of the poloidal fields.

The $\lambda_{3-7} = v_y/v_x$ are always real and thus correspond to hyperbolic fields with associated characteristics, which means that the poloidal streamlines are five-fold degenerate characteristics. A basis for the corresponding left eigenvector space is

$$\mathsf{L}_3 = (-c^2, 0, 0, 0, 0, 0, 1) \tag{3.51}$$

$$\mathsf{L}_4 = (-\alpha/\rho, 0, 0, 0, 1, 0, 0) \tag{3.52}$$

$$\mathsf{L}_5 = (B_z/(\alpha^2 - \rho), 0, 0, 0, 0, 1, 0) \tag{3.53}$$

$$\mathsf{L}_6 = (\alpha B_z/(\alpha^2\rho - \rho^2), 0, 0, 1, 0, 0, 0) \tag{3.54}$$

$$\mathsf{L}_7 = (\frac{B_z^2 + c^2(-\alpha^2+\rho)}{\rho v_y(-\alpha^2+\rho)}, \frac{v_x}{v_y}, 1, 0, 0, 0, 0), \tag{3.55}$$

and can be used to derive the Riemann Invariants

$$\chi_3 = s = \frac{p}{\rho^\gamma} \tag{3.56}$$

$$\chi_4 = \rho/\alpha \tag{3.57}$$

$$\chi_5 = L = \frac{B^{(p)}B_z}{\rho v^{(p)}} - v_z \tag{3.58}$$

$$\chi_6 = \Omega = \frac{v^{(p)}B_z}{B^{(p)}} - v_z = \frac{E}{B^{(p)}} \tag{3.59}$$

$$\chi_7 = h = \frac{v^2}{2} + \frac{\gamma}{\gamma-1}\frac{p}{\rho} - v_z B_z \frac{B^{(p)}}{\rho v^{(p)}} + \frac{B_z^2}{\rho}, \tag{3.60}$$

with s the entropy, L related to the angular momentum, Ω related to the electric field, h the Bernoulli function and E the magnitude of the electric field.

The invariance of these quantities along streamlines can also be derived by direct manipulation of the conservation laws of Eq. 3.12. For instance, using $\nabla\cdot\vec{B} = 0$ and $\vec{B}^{(p)} = \alpha\vec{v}^{(p)}$, one can see that $\nabla\cdot(\rho\vec{v}) = \nabla\cdot(\rho/\alpha\ \alpha\vec{v}) = \alpha\vec{v}\cdot\nabla(\rho/\alpha) + \rho/\alpha\ \nabla\cdot(\alpha\vec{v}) = \alpha\vec{v}\cdot\nabla(\rho/\alpha)$. Because $\nabla\cdot(\rho\vec{v}) = 0$ in a steady state, this leads to $\vec{v}\cdot\nabla(\rho/\alpha) = 0$, which means that ρ/α is conserved on a streamline.

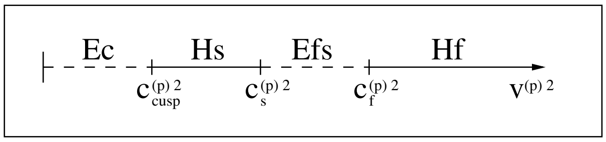

Figure 3.3: *Elliptic and hyperbolic regions in parameter space for steady field-aligned MHD. For decreasing $v^{(p)2}$, the axis is divided in a fast hyperbolic region (Hf), an elliptic region between the fast and the slow hyperbolic regions (Efs), a slow hyperbolic region (Hs), and an elliptic region below the cusp speed (Ec).*

The eigenvalues $\lambda_{1,2}$ are real and the equations are thus hyperbolic if the factor under the square root sign is positive [79, 59, 71, 85, 70, 3, 62, 19]. This factor changes sign three times, viz. when the square of the poloidal velocity equals

$$v^{(p)2} = c_{f,s}^{(p)2} = \frac{B^2 + \gamma p \pm \sqrt{(B^2+\gamma p)^2 - 4B^{(p)2}\gamma p}}{2\rho} \tag{3.61}$$

$$v^{(p)2} = c_{cusp}^{(p)2} = \frac{c_A^{(p)2} c^2}{c_A^2 + c^2}. \qquad (3.62)$$

Here $c_A = B/\sqrt{\rho}$ is the total Alfvén velocity, and $c_A^{(p)} = B^{(p)}/\sqrt{\rho}$ is the poloidal Alfvén velocity. The poloidal cusp velocity $c_{cusp}^{(p)}$ is the velocity of the slow wave cusp in the MHD Friedrichs diagram [59, 71]. This leads to a division of the parameter space into elliptic and hyperbolic regions, as depicted in Fig. 3.3. Note that the poloidal Alfvénic Mach number $M_A^{(p)}$ becomes independent of the direction for the case of field-aligned flow:

$$M_{Ax} = \frac{|v_x|}{c_{Ax}} = M_{Ay} = \frac{|v_y|}{c_{Ay}} = M_A^{(p)} = \frac{v^{(p)}}{c_A^{(p)}}. \qquad (3.63)$$

3.2.5 Characteristic analysis of stationary planar field-aligned MHD in two space dimensions

In the *planar* case ($v_z \equiv B_z \equiv 0$) the results simplify further. We can simplify the notation by dropping the superscripts (p), e. g. $c_A^{(p)} = c_A$ and $v^{(p)} = v$. The matrices A and B given in Eqs. 3.47 and 3.48 lose their fourth and sixth rows and columns. Analysis of the characteristic properties of the resulting 5×5 system yields the following results. The characteristic condition $\det(\mathsf{C} - \lambda \mathsf{I}) = 0$ can be factorized in terms of the variable $v_\perp^2$. This factorization leads to the following roots

$$v_{\perp\,1}^2 = c^2(1 - \alpha^2/\rho) + v^2\ \alpha^2/\rho \qquad \text{and} \qquad v_{\perp\,2}^3 = 0. \qquad (3.64)$$

The equation for $v_{\perp\,2}$ always has three real solutions, $\lambda_{3,4,5} = v_y/v_x$, meaning that the streamlines are three-fold degenerate characteristics. The corresponding left eigenvectors are

$$\mathsf{L}_3 = (-c^2, 0, 0, 0, 1)\ \ ,\ \ \mathsf{L}_4 = (-\alpha/\rho, 0, 0, 1, 0)\ \ ,$$
$$\text{and}\ \ \mathsf{L}_5 = (c^2/(\rho v_y), v_x/v_y, 1, 0, 0), \qquad (3.65)$$

and can be used to derive the Riemann Invariants

$$\chi_3 = s\ \ ,\ \ \chi_4 = \rho/\alpha\ \ ,\ \text{and}\ \ \chi_5 = h_s. \qquad (3.66)$$

The hydrodynamic stagnation enthalpy is defined as

$$h_s \equiv \frac{\gamma}{\gamma - 1}\frac{p}{\rho} + \frac{1}{2}v^2. \qquad (3.67)$$

The entropy, ρ/α, and the stagnation enthalpy are thus conserved on a streamline in continuous flow. It follows from the MHD Rankine-Hugoniot (RH) jump conditions [87, 92, 4], that the entropy is discontinuous when a streamline crosses a shock. However, the stagnation

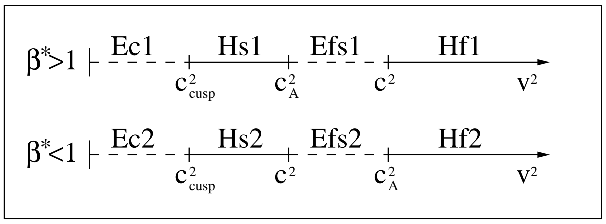

Figure 3.4: *Elliptic and hyperbolic regions in parameter space for steady planar field-aligned MHD. The top line corresponds to $\beta^* > 1$, and shows, as v^2 decreases, a division in a fast hyperbolic region (Hf1), an elliptic region between the fast and the slow hyperbolic regions (Efs1), a slow hyperbolic region (Hs1), and an elliptic region below the cusp speed (Ec1). The bottom line shows a similar division for $\beta^* < 1$. For $\beta^* = 1$, $c^2 = c_A^2$.*

enthalpy and ρ/α are conserved over a shock for the case of field-aligned flow.

The solutions of the equation for $v_{\perp 1}$ are

$$\lambda_{1,2} = \frac{\rho v_x v_y \pm \sqrt{(v^2-c^2)(\alpha^2-\rho)(c^2(\alpha^2-\rho)-v^2\alpha^2)}}{\rho(c^2-v_x^2)-\alpha^2(c^2-v^2)}. \tag{3.68}$$

If the factor under the square root sign is positive, then these eigenvalues are real, and the equations are hyperbolic [79, 59, 71, 85, 70, 3, 62, 19]. This factor changes sign three times, viz. when the square of the velocity equals

$$v^2 = c_A^2, \qquad v^2 = c^2, \qquad \text{and} \qquad v^2 = c_{cusp}^2. \tag{3.69}$$

The cusp velocity is defined as $c_{cusp}^2 = (c^2 c_A^2)/(c^2+c_A^2)$ and is the velocity of the slow wave cusp in the MHD Friedrichs diagram [59, 71]. This leads to a division of the parameter space into elliptic and hyperbolic regions, as depicted in Fig. 3.4, for high and low β^*, where the parameter β^* is defined as $\beta^* = \gamma p/B^2 = c^2/c_A^2$. When $\beta^* > 1$ — or equivalently $\beta > 2/\gamma = 1.2$ — the sound speed is larger than the Alfvén speed, or, equivalently, thermal pressure effects dominate over magnetic pressure effects.

In Fig. 3.5a the local geometry of streamlines and xy characteristics is sketched for the case of planar steady field-aligned MHD in hyperbolic regions. The streamline is a three-fold degenerate characteristic, and there are two additional families of characteristics (generalized Mach lines [21, 20]) which make equal angles ψ with the streamline. These characteristics can be of the slow or fast type, depending on which hyperbolic regime the parameters are in (Hf or Hs of Fig. 3.4). Division of

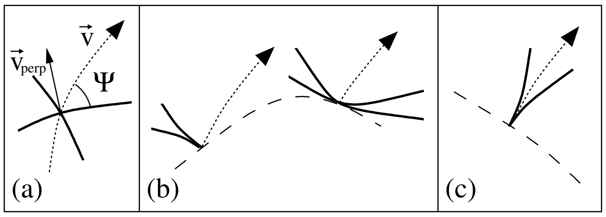

Figure 3.5: *Streamlines (dotted), slow or fast characteristics (thick), and transition lines between hyperbolic and elliptic regions (dashed), for steady planar field-aligned MHD. (a) The two families of characteristics (thick) both make an angle ψ with the streamline. (b) At transition lines where the plasma velocity equals the sound speed or the Alfvén speed, the characteristics become perpendicular to the streamline. When the streamline is perpendicular to the transition line, the characteristics are tangent to the transition line. (c) At transition lines where the plasma velocity equals the cusp speed, the characteristics cusp and are tangent to the streamline.*

the expression for $v_{\perp 1}^2$ in Eq. 3.64 by v^2 leads to the following interesting formula for the angle ψ between the streamline and the characteristic (Fig. 3.5a):

$$\sin^2\psi = \frac{v_\perp^2}{v^2} = \frac{M^2 + M_A^2 - 1}{M^2 M_A^2}. \tag{3.70}$$

The total sonic Mach number $M = v/c$ has to be distinguished from the directional Mach number $M_x = |v_x|/c$. The Alfvénic Mach number M_A is independent from the direction. The flow is hyperbolic when $0 \leq (M^2 + M_A^2 - 1)/(M^2 M_A^2) \leq 1$. For $v^2 = c_A^2$ ($M_A^2 = 1$) or $v^2 = c^2$ ($M^2 = 1$), $v_\perp^2$ equals v^2 and $\psi = 90°$, meaning that at such transition lines between elliptic and hyperbolic regions, the characteristics are perpendicular to the streamlines, as is shown in Fig. 3.5b. At transition lines of these types, characteristics can thus only be parallel to these lines when the streamline is perpendicular to the transition line. For $v^2 = c_{cusp}^2$, $v_\perp^2$ equals zero and $\psi = 0°$, meaning that at this type of transition line between elliptic and hyperbolic regions, the characteristics cusp parallel to the streamlines [62, 131], as is shown in Fig. 3.5c.

In some cases further simplifications can be made. If the stagnation enthalpy is the same on every streamline (this is called homenthalpic flow), then p can be eliminated from the equations, resulting in a 4×4 system with state vector $\mathbf{U} = (\rho, v_x, v_y, \alpha)$. In this case λ_5 and χ_5 drop out, but the rest of the analysis remains the same. Similarly, steady planar hydrodynamics in 2D results in a 4×4 system with $\mathbf{U} = (\rho, v_x, v_y, p)$. The results for this special case of vanishing magnetic field are recovered

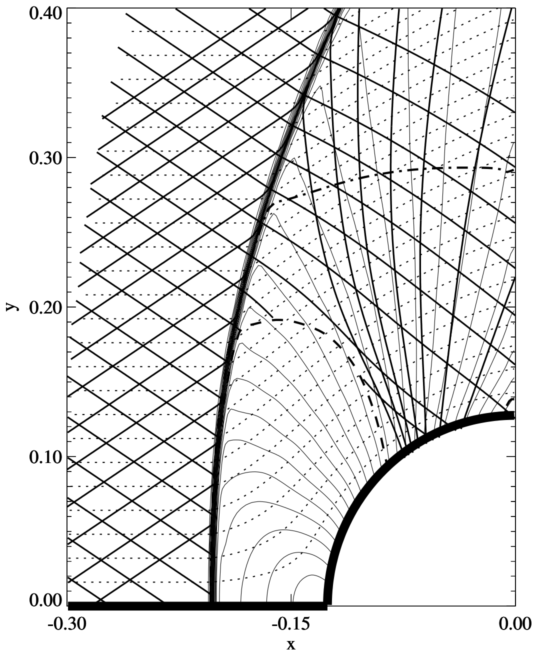

Figure 3.6: *Planar field-aligned 2D MHD bow shock flow over a perfectly conducting plate with a semi–circular bump (thick). The flow comes in from the left. Density contours (thin solid lines) pile up in the shock. The streamlines (which are also magnetic field lines) are dotted. The thick solid lines are two families of fast characteristics making equal angles with the streamlines. The thick dashed transition line is the $M = 1$ contour, separating the elliptic region close to the cylinder (Efs1) from the rest of the flow, which is fully hyperbolic (Hf2 and Hf1). The fast characteristics are perpendicular to the streamlines at the transition line. The thick dash-dotted line is the $\beta^* = 1$ contour.*

by putting $\alpha = 0$ in the formulas for planar field-aligned MHD, in which case λ_4 and χ_4 drop out.

To illustrate the above derived results, we show the characteristics of a planar 2D MHD bow shock flow in Fig. 3.6. The flow comes in from the left ($\rho = 1,\ p = 0.2,\ v_x = 2,\ v_y = 0,\ B_x = 1,\ B_y = 0$), and is obstructed by the perfectly conducting cylinder on the right. Due to top-down symmetry, this setting can also be thought of as to describe the flow over a perfectly conducting plate with a semi–circular bump (thick). Density contours (thin solid lines) pile up in the shock. The streamlines (which

Table 3.1: Overview of some characteristic properties of the MHD equations, for full (8×8) MHD in the xt and the xy planes, and for steady field-aligned MHD (7×7 and planar 5×5) in the xy plane. The first column labels the characteristic fields as in the text. The second column gives the characteristic directions λ or the condition on $v_\perp$ for every characteristic field. The third column gives the Riemann Invariants. The fourth column gives the multiplicity of the real eigenvalues, and thus indicates if the corresponding characteristic fields are hyperbolic or elliptic.

characteristic field	**λ or $v_\perp$**	**RI**	**multiplicity**
xt (8×8)			
1,2	$\lambda = v_x \pm c_f$		2
3,4	$\lambda = v_x \pm c_A$		2
5,6	$\lambda = v_x \pm c_s$		2
7,8	$\lambda = v_x$	$s,\ B_x$	2
xy (8×8)			
1,2	$v_\perp^2 = c_{f\perp}^2$		0—2
3,4	$v_\perp^2 = c_{A\perp}^2$		2
5,6,1,2	$v_\perp^2 = c_{s\perp}^2$		0—2—4
7,8	$v_\perp^2 = 0$	$s,\ v_x B_y - v_y B_x$	2
$xy,\ \vec{B}^{(p)} \parallel \vec{v}^{(p)}$ (7×7)			
1,2	$\lambda_{1,2}$		0—2
3,4,5,6,7	$v_\perp^5 = 0$	$s,\ \rho/\alpha,\ L,\ \Omega,\ h$	5
$xy,\ \vec{B} \parallel \vec{v}$ (5×5)			
1,2	$\lambda_{1,2}$		0—2
3,4,5	$v_\perp^3 = 0$	$s,\ \rho/\alpha,\ h_s$	3

are also magnetic field lines) are dotted. The thick solid lines are two families of fast characteristics making equal angles with the streamlines in the hyperbolic regions. In front of the cylinder we see an elliptic region, where the thick characteristics do not exist. We can determine the types of the hyperbolic and elliptic regions in the flow according to the classification given in Fig. 3.4. The parameter β^* is smaller than one upstream, and greater than one downstream from the shock, except far away from the cylinder (the thick dash-dotted line is the $\beta^* = 1$ contour). The thick dashed transition line is the $M = 1$ contour, separating the subsonic elliptic region close to the cylinder (Efs1) from the rest of the flow, which is supersonic and thus hyperbolic (Hf2 upstream from the shock and downstream far from the cylinder, and Hf1 downstream and closer to the cylinder). The fast characteristics are perpendicular to the streamlines at the transition line, corresponding to case (b) of Fig. 3.5.

A summary of the results on characteristic analysis of the MHD equations with two independent variables is given in Table 3.1. This characteristic theory is applied to the analysis of numerically obtained model flow solutions in Chapter 5, and to complex 2D bow shock flow solutions in Chapter 6.

As a final remark, we can note that the concepts of characteristic analysis can be extended to systems with three and four independent variables [21, 169]. The matter becomes quite more complicated, and necessitates the introduction of concepts like characteristic rays, surfaces, and cones. For the analysis of numerical results presented further on in this dissertation, however, it is not necessary to consider systems with more than two independent variables.

3.3 MHD discontinuities

3.3.1 MHD Rankine-Hugoniot relations

Consider the ideal MHD equations in one space dimension. These equations allow for solutions composed of a uniform left state and a uniform right state which are connected by a discontinuity, and this discontinuity moves with a constant speed s and has a magnitude which is constant in time. In the frame moving with speed s, the solution is thus stationary, and we call such a solution a co-stationary discontinuous traveling wave. We can easily derive the general conditions which must be fulfilled by such a co-stationary discontinuous traveling wave solution, and verify if those conditions can indeed be satisfied in the case of the MHD system. In general, a conservation law system

$$\frac{\partial \mathbf{U}(x,t)}{\partial t} + \frac{\partial \mathbf{F}(\mathbf{U})}{\partial x} = 0 \tag{3.71}$$

allows for a co-stationary traveling wave solution $\mathbf{U}(x,t) = \mathbf{U}(y = x - st)$ under the condition that

$$-s\frac{\partial \mathbf{U}(y)}{\partial y} + \frac{\partial \mathbf{F}(\mathbf{U})}{\partial y} = 0, \tag{3.72}$$

or

$$-s\mathbf{U} + \mathbf{F}(\mathbf{U}) = \mathbf{F}_{const} \tag{3.73}$$

with $\mathbf{F}_{const}$ a constant vector [173, 46]. In particular, for the *discontinuous* co-stationary traveling wave solution described above, the left and right states $\mathbf{U}_l$ and $\mathbf{U}_r$ thus have to satisfy the condition

$$\mathbf{F}(\mathbf{U}_r) - \mathbf{F}(\mathbf{U}_l) = s\ (\mathbf{U}_r - \mathbf{U}_l), \tag{3.74}$$

which expresses that the physical fluxes have to be continuous through the discontinuity in the moving frame. This can be seen more clearly when we transform to that moving frame and rewrite Eq. 3.74 as

$$\mathbf{F}(\mathbf{U}_r) = \mathbf{F}(\mathbf{U}_l). \tag{3.75}$$

Conditions 3.74 or 3.75 are called the *Rankine-Hugoniot* (RH) relations. We have to remark here that for a discontinuous solution, the derivatives in the differential form of the conservation law Eq. 3.71 are not defined. The discontinuous solution is, however, a valid solution of the integral form of the conservation law Eq. 3.73, and we say that it is a *weak solution* of the differential form of the conservation law Eq. 3.71. The RH relations actually have to be satisfied by any traveling discontinuity in the ideal system (not only by co-stationary solutions), because they describe the conservation of the physical fluxes through the discontinuity interface. The RH relations can alternatively be derived from Eq. 3.71 by applying Gauss' law on a volume which is cut by a plane shock and by taking the limit of vanishing thickness of the volume, such that the time derivative integrated over the volume vanishes as well. This can be done because the shock has vanishing thickness in the ideal system.

The MHD flux function in the x direction is given by

$$F(\begin{bmatrix} \rho \\ \rho\, v_x \\ \rho\, v_y \\ \rho\, v_z \\ B_x \\ B_y \\ B_z \\ e \end{bmatrix}) = \begin{bmatrix} \rho\, v_x \\ \rho\, v_x^2 + p + B^2/2 - B_x^2 \\ \rho\, v_x v_y - B_x B_y \\ \rho\, v_x v_z - B_x B_z \\ 0 \\ B_y v_x - B_x v_y \\ B_z v_x - B_x v_z \\ (e + p + B^2/2) v_x - B_x\, (\vec{v} \cdot \vec{B}) \end{bmatrix}. \tag{3.76}$$

This flux function allows for several different types of co-stationary discontinuous traveling wave solutions each with their particular properties. The derivation of these properties from the MHD RH relations would lead us too far here, and is well described elsewhere [4, 87, 80]. We just give a short overview of some results that are used later. We assume the x direction to be perpendicular to the shock, and the magnetic field to lie in the xy plane.

MHD discontinuities can be divided in three classes. For shocks there is both a mass flow through the surface of discontinuity, and an increase in the entropy. For contact and tangential discontinuities, there is an entropy jump, but no mass flow. For rotational discontinuities, there is a mass flow, but no entropy change. A general property of MHD discontinuities is that the normal component of the magnetic field B_x is continuous, as follows directly from the $\nabla \cdot \vec{B} = 0$ constraint.

3.3.2 Shocks

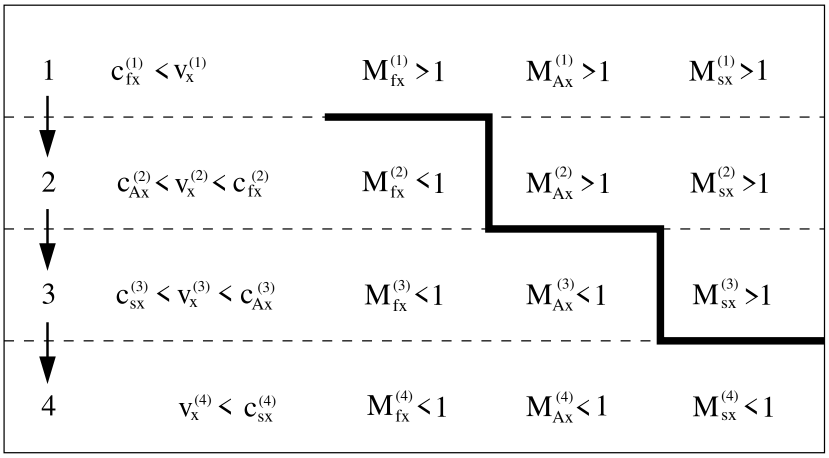

Figure 3.7: *Possible states that can be connected through a MHD shock. They are ordered by increasing entropy, with the lowest entropy for state 1. The normal fast, Alfvén, and slow wave speeds are c_{fx}, c_{Ax}, and c_{sx}, respectively. The normal plasma speed is v_x. The fast, Alfvén, and slow normal Mach numbers are M_{fx}, M_{Ax}, and M_{sx}, respectively. State 1 is superfast, because its normal velocity in the shock frame is larger than the normal fast MHD wave speed. Therefore the fast, Alfvénic and slow Mach numbers are all greater than one. State 2 is subfast but super-Alfvénic. State 3 is sub-Alfvénic but superslow. State 4 is subslow. Possible shock transitions are 1–2 (fast), 3–4 (slow), and 1–3, 1–4, 2–3, 2–4 (intermediate).*

A general property of MHD shocks is that the left and the right state are *co-planar*. This means that the plane defined by the shock normal and the magnetic field is the same plane on both sides of the shock. This property can easily be derived from the MHD RH relations. Another property is that if the magnetic field and velocity field are parallel on one side of a shock, then the fields are also parallel on the other side of the shock.

Generally up to four plasma states can be found that satisfy given values for the fluxes of mass, momentum, magnetic field and energy through the discontinuity surface. This follows from analysis of the RH conditions [87, 80]. Each pair of those states satisfies the RH conditions and can thus be connected by a shock. These states are conventionally labeled states 1, 2, 3, and 4, ordered by increasing entropy (Fig. 3.7). State 1 has the lowest entropy, and in a frame moving with the shock

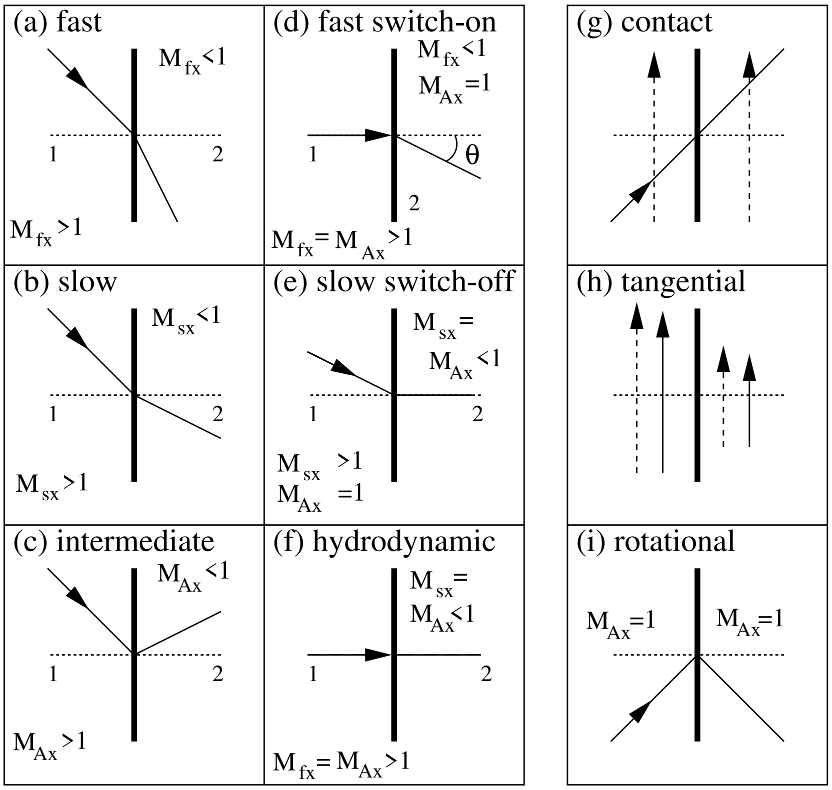

Figure 3.8: *Some properties of MHD shocks and discontinuities. The thick vertical line is the shock surface. The shock normal is dotted. The full arrowed lines are magnetic field lines that are refracted through the shock surface. The dashed arrowed lines are velocity vectors. Region 1 is upstream, 2 is downstream.*

the normal plasma velocity $v_x^{(1)}$ is larger than the normal fast MHD wave speed, so that the flow is superfast (and, therefore, also super-Alfvénic and superslow). This means that the normal fast Mach number $M_{fx}^{(1)}$ (normal plasma velocity divided by normal fast MHD wave speed) is greater than one (the same for the Alfvén and slow Mach number). State 2 is subfast, but super-Alfvénic and superslow. State 3 is subfast and sub-Alfvénic, but superslow. State 4 is subfast, sub-Alfvénic, and subslow. In a frame of reference that moves with the shock, a fluid element that moves from the upstream region (traditionally indicated as region 1) to the downstream region (region 2), necessarily has to undergo an increase in entropy. So 1–2, 1–3, 1–4, 2–3, 2–4, and 3–4 are the possible entropy-satisfying shock transitions. In Fig. 3.8 we summarize some of their properties.

Transition 1–2 is called a fast shock (Fig. 3.8a). The plasma is superfast upstream, and subfast (but super-Alfvénic) downstream. A fast shock increases B_y (because p is in phase with B for a fast wave), such that magnetic field lines are refracted away from the shock normal. Transition 3–4 is called a slow shock (Fig. 3.8b). The plasma is superslow (but sub-Alfvénic) upstream, and subslow downstream. A slow shock decreases B_y (because p is in anti-phase with B for a slow wave), such that magnetic field lines are refracted towards the shock normal. Transitions 1–3, 1–4, 2–3, and 2–4 are called intermediate shocks (Fig. 3.8c). The plasma is super-Alfvénic upstream, and sub-Alfvénic downstream. An intermediate shock changes the sign of B_y, such that magnetic field lines are flipped over the shock normal.

There exist limiting cases of these types of shocks for which the upstream and/or downstream magnetic field is parallel to the shock normal. A fast 1–2=3 switch-on shock (Fig. 3.8d) has $B_{y,1} = 0$ upstream. The downstream $B_{y,2}$, however, does not vanish. The tangential component of the magnetic field is thus switched on, hence the name of this shock. For a fast switch-on shock, the downstream normal Alfvénic Mach number is exactly equal to one. A slow 2=3–4 switch-off shock (Fig. 3.8e) has $B_{y,2} = 0$ downstream. The upstream $B_{y,1}$ however does not vanish. The tangential component of the magnetic field is thus switched off, hence the name of this shock. For a slow switch-off shock, the upstream normal Alfvénic Mach number is exactly equal to one. A limiting case of intermediate shocks are shocks that do not change the magnetic field, and those shocks are called 1–4 hydrodynamic (or parallel) shocks (Fig. 3.8f). Both $B_{y,1}$ and $B_{y,2}$ are equal to zero.

Intermediate shocks and switch-on shocks can only occur for some well-specified regime of the upstream parameters [80, 147]. For switch-on shocks, the downstream angle θ (Fig. 3.8d) is non-vanishing only if the upstream plasma $\beta_1 < 2/\gamma$ and if the upstream normal velocity component $v_{x,1}$ lies in the switch-on region between the upstream Alfvén speed and a critical velocity defined by

$$c_{A,1} < v_{x,1} < c_{A,1}\sqrt{\frac{\gamma(1-\beta_1)+1}{\gamma-1}} = v_{crit}. \tag{3.77}$$

The upstream tangential component of the velocity, $v_{y,1}$, does not play a role in condition 3.77. In fact, one can always make a transformation to a new frame in the direction tangential to the shock front, and choose the new frame such that $v_{y,1} = 0$. The magnetic field does not change in this transformation of frames. The shock properties can then be analyzed in this new frame. The parameter regime for which switch-on shocks occur is called the *switch-on regime*. Intermediate shocks arise for the same parameter regime, and can only exist when the angle between the upstream magnetic field and the shock normal is small, as will be illustrated shortly.

Switch-on shocks have no analog in the hydrodynamic flow of a neutral fluid, and can thus be called an intrinsically magnetic effect. A plasma state upstream from a shock with the magnetic field normal to the shock is a superfast state — type 1 — if $v_{x,1} > c_1$ and $v_{x,1} > c_{A,1}$, or equivalently

$$\rho_1 \, v_{x,1}^2 > \gamma \, p_1 \tag{3.78}$$

and

$$\rho_1 \, v_{x,1}^2 > B_1^2. \tag{3.79}$$

Here $v_{x,1}$ is the velocity component along the shock normal and along the upstream magnetic field. The 1–2 shock with this state of type 1 as upstream state is a switch-on shock when

$$B_1^2 > \gamma \, p_1 \tag{3.80}$$

and

$$B_1^2 > \rho_1 \, v_{x,1}^2 \, \frac{\gamma - 1}{\gamma(1 - \beta_1) + 1}. \tag{3.81}$$

The latter inequality can be deduced from Eq. 3.77. The expression $(\gamma - 1)/(\gamma(1 - \beta_1) + 1)$ assumes values between 0.25 and 1 for $\gamma = 5/3$ and $\beta_1 < 2/\gamma$. Eqs. 3.80 and 3.81 show that switch-on shocks occur when magnetic forces dominate over the effects from both the thermal pressure p and the dynamic pressure $\rho \, v_x^2/2$ in the direction normal to the shock. Switch-on shocks can only occur when the magnetic field B is strong and are an intrinsically magnetic effect. Therefore we call upstream flows for which switch-on shocks can occur *magnetically dominated* flows. Magnetically dominated flows thus satisfy inequalities 3.78-3.81. Upstream flows for which switch-on shocks do not occur are called *pressure-dominated* flows.

Fast switch-on shocks and the parameter regime in which they occur, which we call the magnetically dominated regime, play an important role in Chapters 6, 7 and 8 of this dissertation. It is shown that for upstream parameters in this magnetically dominated regime bow shock flows exhibit a new complex topology which is very different from the traditional topology obtained for bow shocks with pressure-dominated upstream flows. This motivates the introduction of the terminology of pressure-dominated versus magnetically dominated upstream flows as defined above, and warrants its extension to pressure-dominated versus magnetically dominated bow shock flows and bow shock flow topologies. Full justification for this terminology is given in Secs. 6.3 and 7.1.

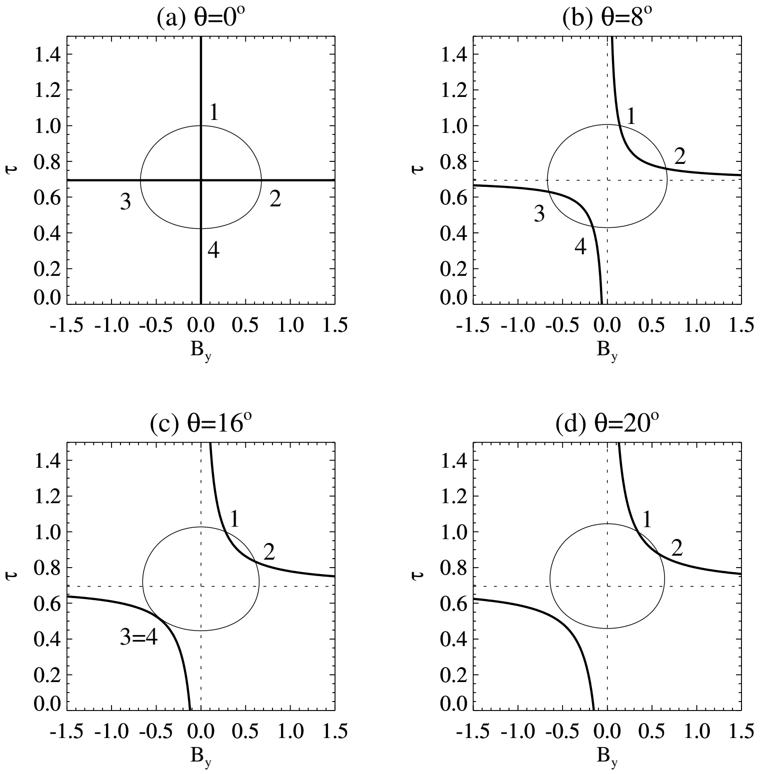

Figure 3.9: *Solutions of the RH relations for parameter values $M_A = 1.2$ and $\beta = 0.4$ for state 1 with the field aligned to the flow. These are magnetically dominated parameters for which switch-on shocks occur. θ is the angle between the fields and the shock normal. (a) For $\theta = 0°$, switch-on shocks, switch-off shocks and hydrodynamic shocks arise. (b–d) For $\theta < 16°$, intermediate shocks occur, but they cease to exist for larger θ.*

We can illustrate the above discussion on MHD shocks by explicitly plotting solutions of the RH conditions for given values of the fluxes through the discontinuity. We follow closely the procedure described in [4]. For given fluxes through the discontinuity, up to four states satisfying the RH relations can be found as the intersection of two curves in the $\tau - B_y$ plane, with $\tau = 1/\rho$ and B_y the component of the magnetic field tangential to the shock surface. The shock normal is again taken in the x direction.

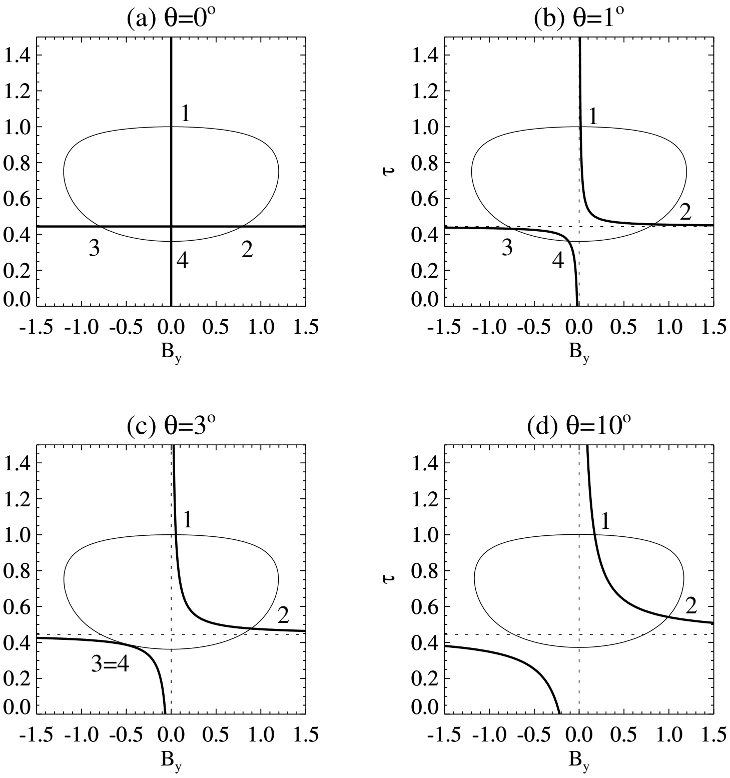

Figure 3.10: *Solutions of the RH relations for parameter values* $M_A = 1.5$ *and* $\beta = 0.4$ *for state 1 with the field aligned to the flow. These parameters still are magnetically dominated, but not strongly. The maximum angle for which intermediate shocks can occur is smaller than for the parameter values of Fig. 3.9.*

Fig. 3.9 shows RH solutions for parameter values $p = 0.2$, $\rho = 1$, $B = 1$ and $v = 1.2$ for state 1. The velocity is taken parallel to the magnetic field. We vary the angle θ between the aligned velocity and magnetic field vectors, and the shock normal. In state 1 $c_A = 1$, $M_A = 1.2$ and $\beta = 0.4$. β is smaller than $2/\gamma = 1.2$ and, for $\theta = 0°$, $v_x < v_{crit} = 1.732$ (Eq. 3.77). Intermediate and switch-on shocks occur, and we call the upstream state magnetically dominated.

Fig. 3.9b, for $\theta = 8°$, shows the generic case with four solutions of the RH relations. The horizontal dotted line indicates the inverse density

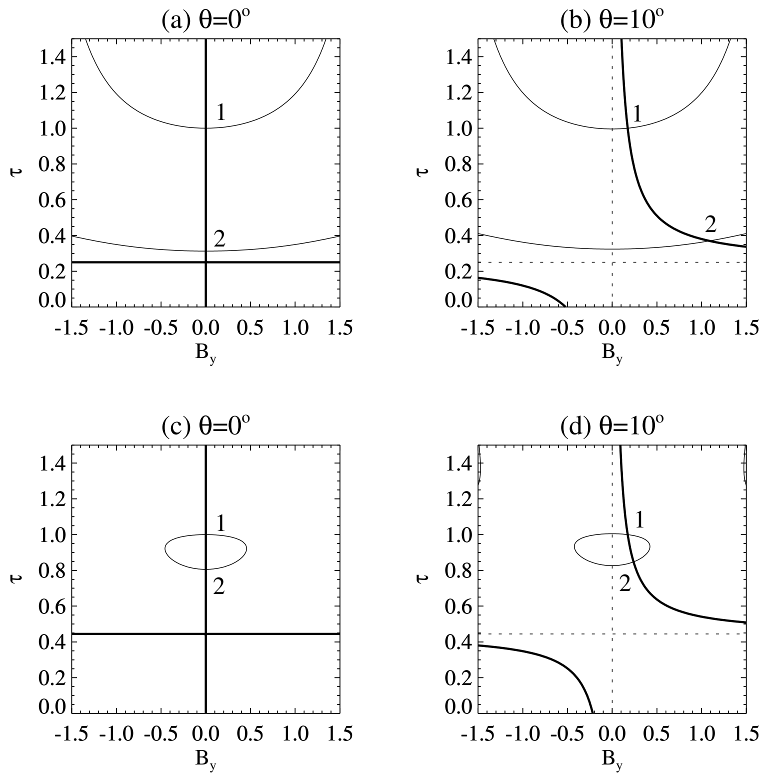

Figure 3.11: *Solutions of the RH relations for pressure-dominated parameter values for state 1. Switch-on shocks do not occur. Only 1–2 fast shocks exist. (a–b) $M_A = 2$ and $\beta = 0.4$. (c–d) $M_A = 1.5$ and $\beta = 2$.*

τ for which $v_x = c_{Ax}$. 1–2 is a fast shock (B_y increases), and 3–4 is a slow shock (B_y decreases). Transitions 1–3, 1–4, 2–3 and 2–4 all cross the $v_x = c_{Ax}$ line, and are thus intermediate shocks, which is confirmed by the fact that they change the sign of the B_y component.

Fig. 3.9a shows the limiting case for $\theta = 0°$. 1–2 and 1–3 are both fast switch-on shocks (B_y is switched on), and because states 2 and 3 are both Alfvénic ($v_x = c_{Ax}$), this type of shock is referred to as a 1–2=3 shock. The 2=3–4 shocks are slow switch-off shocks. The 1–4 shock is a hydrodynamic shock ($\vec{B}$ does not change through the shock). Figs. 3.9c and d show that for angles θ larger than approximately 16° intermediate shocks cease to exist.

Fig. 3.10 shows RH solutions for the same parameter values for state

1 as in Fig. 3.9, except that $v = 1.5$ and thus closer to $v_{crit} = 1.732$. The upstream state is still magnetically dominated as switch-on shocks can still occur — remark that the switch-on angle ($\approx B_y$) even has increased! —, but the maximum angle for which intermediate shocks occur decreases to $\theta \approx 3°$. This is a generic property: when v_x is taken closer to v_{crit}, the maximum angle for which intermediate shocks can occur decreases. This behavior can also be observed in Fig. 3 of [80] and Fig. 4 of [147].

Fig. 3.11 shows RH solutions for parameter values for state 1 not in the switch-on regime — we call the upstream state thus pressure-dominated. Fig. 3.11a–b shows RH solutions for the same parameter values for state 1 as in Fig. 3.9, except that $v = 2$ and thus exceeds $v_{crit} = 1.732$. This means that dynamic pressure effects dominate over magnetic effects — inequality 3.81 is not satisfied. Only 1–2 fast shocks exist. In Fig. 3.11c–d, $p = 1$, $\rho = 1$, $B = 1$ and $v = 1.5$. $\beta = 2$, such that thermal pressure effects dominate over magnetic effects — inequality 3.80 is not satisfied. Again only fast shocks exist.

3.3.3 Other discontinuities

Contact discontinuities (Fig. 3.8g), with vanishing v_x but nonzero B_x, have only a jump in density (and entropy). All other quantities are continuous. Tangential discontinuities (Fig. 3.8h), with vanishing v_x and B_x, have a jump in density, pressure, and tangential velocity and magnetic field. However, the total pressure $p + B^2/2$ is continuous. Planar rotational discontinuities (Fig. 3.8i) rotate the magnetic field around the normal of the discontinuity surface over an angle of 180 degrees, without a jump in entropy. Rotational discontinuities can actually rotate the magnetic field over an arbitrary angle, and the planar rotational discontinuity is just a special case. The normal plasma velocity v_x equals $B_x/\rho^{1/2}$ on both sides of a rotational discontinuity, such that the normal Alfvénic Mach number equals one on both sides. Transitions 2–3 in Figs. 3.9a and 3.10a are planar rotational discontinuities which are the limit of intermediate 2–3 shocks for zero shock strength.

3.3.4 Stability of shocks

All the types of discontinuities discussed above formally satisfy the MHD RH relations, but there exists a vigorous debate about the physical relevance of some of these types of discontinuities, notably the intermediate shocks and the rotational discontinuities. This is discussed in detail in Chap. 9. In the mean time, we refer the reader to the discussion in Sec. 2.3.2, where it was indicated that intermediate shocks can be stable in small dissipation MHD. We will thus not be surprised when intermediate shocks appear in our simulation results presented in Chapters 6, 7 and 8, but thorough discussion of the relevance of these results for the debate on the existence of intermediate shocks is postponed to Chap. 9.

3.3.5 Non-convexity and MHD compound shocks

In this Section we show how the non-convexity of characteristic fields leads to the occurrence of compound shocks. Large parts of our exposition derive from material presented in [90] and [173].

Let us first consider the *scalar* conservation law Eq. 3.23. A *Riemann problem* is an initial value problem with an initial condition in the form of a step discontinuity with uniform states to the left and the right of the discontinuity. Fig. 3.12a and b shows the solution of a Riemann problem for the scalar conservation law with flux function $f(u) = u^2/2$, which is called the inviscid Burgers equation, and with left and right states $u_l = 1$ and $u_r = -1$. We can investigate if these two states can be connected by a co-stationary discontinuous traveling wave solution (a traveling shock). From Eq. 3.74 we can derive that the shock speed would equal $s = (f(u_r) - f(u_l))/(u_r - u_l) = 0$.

For now we adopt the — naive, see Chap. 9 — criterion that shocks are admissible when the characteristics enter the shock on both sides. We assume that if the characteristics do not enter the discontinuity on both sides — such discontinuities are called *undercompressive* —, then the discontinuity is not stable and cannot be formed. Physically this criterion corresponds to the fact that the entropy has to increase at a shock, as is explained in Chap. 9 [90].

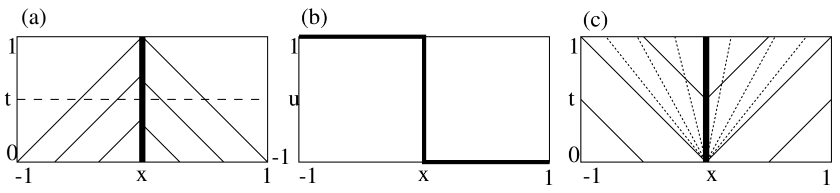

Figure 3.12: *Solution of a Riemann problem for the inviscid Burgers equation. (a) Left and right states $u_l = 1$ and $u_r = -1$ lead to an admissible shock (thick solid) with speed $s = 0$ and characteristics (thin solid) converging into the shock. (b) Shock profile of the solution presented in (a) for $t = 1/2$. (c) Left and right states $u_l = -1$ and $u_r = 1$ do not allow for a shock, because the characteristics leave the shock. In stead, a centered rarefaction (dotted) results.*

In Fig. 3.12 we see that a shock with left and right states $u_l = 1$ and $u_r = -1$ is an admissible shock, because the characteristics converge into the shock. The solution of the Riemann problem is thus given by a shock solution which happens to be stationary in the frame considered. If we switch the left and the right states, we find the same shock speed $s = 0$, but a shock clearly would be undercompressive and thus inadmissible, as shown in Fig. 3.12c. In stead of a shock, we find a *centered rarefaction wave* which broadens in time as the solution of the Riemann problem (indicated by the dotted lines in the figure). The admissibility of rarefactions is, of course, not questionable, because they are regular continuous solutions.

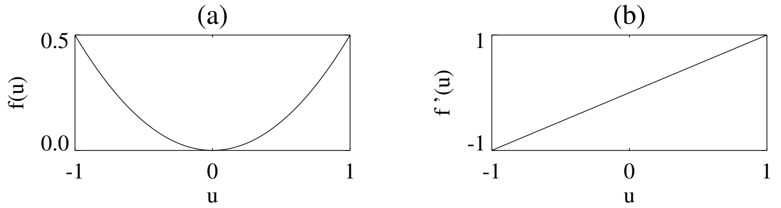

Figure 3.13: *Flux function $f(u)$ and characteristic speed function $f'(u)$ for Burgers' equation. $f(u)$ is convex because $f'(u)$ is monotone.*

Figs. 3.13a and b show plots of the flux function $f(u)$ and the characteristic speed function $f'(u)$ for Burgers' flux function $f(u) = u^2/2$. This flux function is called *convex* because $f'(u)$ is monotone, or, equivalently, $f''(u)$ does not change sign. This property is important, because it guarantees that every Riemann problem can be solved either with an admissible traveling shock or with a rarefaction. Indeed, given two states u_1 and u_2, with the indices chosen such that $f'(u_1) > f'(u_2)$, the property of convexity guarantees that $f'(u_1) \geq s = (f(u_2) - f(u_1))/(u_2 - u_1) \geq f'(u_2)$, which means that states $u_l = u_1$ and $u_r = u_2$ can be connected by an admissible shock. If the left and the right states are switched, the solution to the Riemann problem would consist of a rarefaction between two constant states. If f were non-convex, then the shock speed s would *not* be guaranteed to lie between the characteristic speeds of the two states, so pairs of states would exist which could never be connected by an admissible shock.

So what happens with the Riemann problem in the case of a *non-convex* flux function? Fig. 3.14 shows the solution of a Riemann problem for the non-convex scalar conservation law with flux function $f(u) = u^3/3$, and with left and right states $u_l = 1$ and $u_r = -3/4$. Fig. 3.15a and b show plots of the flux function $f(u)$ and the characteristic speed function $f'(u)$ for the flux function $f(u) = u^3/3$. Clearly $f'(u)$ is not monotone, and the flux function is thus non-convex. For these left and

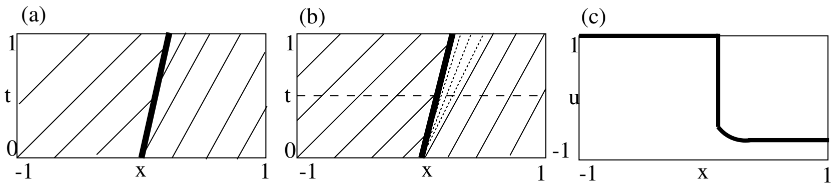

Figure 3.14: *Solution of a Riemann problem for the scalar conservation law with flux function $f(u) = u^3/3$. (a) Left and right states $u_l = 1$ and $u_r = -3/4$ do not allow for an admissible shock, because the characteristics leave the shock on the right. (b) The solution of the Riemann problem consists of a compound shock, composed of a sonic shock followed by an attached centered rarefaction. (c) Shock profile of the solution presented in (b) for $t = 1/2$.*

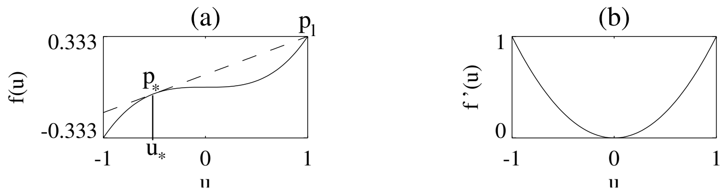

Figure 3.15: *Flux function $f(u) = u^3/3$ and characteristic speed function $f'(u)$. $f(u)$ is non-convex because $f'(u)$ is not monotone. In a compound shock, the right state u_* of the shock is chosen such that it can be connected to $u_l = 1$ by a sonic shock, with the characteristic parallel to the shock. To this end the straight line connecting p_l and p_* has to be tangent to the curve $f(u)$ in point p_*.*

right states, the shock speed $s = 37/168 = 0.22$, and the characteristic speeds are $f'(u_l) = 1$ and $f'(u_r) = 9/16$, such that $f'(u_l) \geq f'(u_r) \geq s$. The shock is thus undercompressive, as shown in Fig. 3.14a. A rarefaction solution is not possible either, because the characteristics intersect. So we have to look for a different type of solution for this case of a non-convex flux function.

It turns out that the solution of Fig. 3.14b and c is admissible. It consists of a shock with a rarefaction attached, and with the peculiar property that the characteristic is parallel to the shock where the rarefaction is attached to the shock. This combined shock-rarefaction structure is called a *compound shock*. The compound shock solution can be constructed as follows. In Fig. 3.15a we fix the point p_l on the curve corresponding to the left state $u_l = 1$. We can connect this point to any other point on the curve with a straight line, and the slope of this line gives the speed of the shock which could connect the states corresponding to the two points on the curve. This is precisely the geometrical interpretation of relation Eq. 3.74. We now connect p_l to the point p_* on the curve (at $u = -1/2$) such that the straight line connecting the two points is *tangent* to the curve. We choose $u_* = -1/2$, and connect u_l with u_* via a shock, with shock speed $s = 1/4$. This shock speed s is also equal to the characteristic speed $f'(u_*)$ in state u_*, because the straight line connecting u_l and u_* is tangent to the curve in u_*, and because the characteristic speed is given by the slope of the curve $f(u)$, and the shock speed by the slope of the straight line. The shock connecting u_l and u_* is thus admissible, because the characteristic enters the shock on the left, and is parallel to the shock on the right.

We call the shock *sonic* because the shock speed equals the characteristic speed on one side of the shock. State u_* can then be connected to state u_r by a continuous rarefaction. What happens if we switch u_l and u_r? In this case a solution with a single shock or rarefaction is not possible either, because the characteristics cross and would enter the shock on one side, but leave the shock on the other side. So again we find that a compound shock is necessary. This compound shock can be constructed by drawing a line now starting from the point corresponding to $u = -3/4$ (because the characteristics originating from this state enter the shock) and tangent to the curve $f(u)$.

We can thus conclude that non-convexity leads to the occurrence of compound shocks in solutions of Riemann problems. Compound shocks are composed of a sonic shock with an attached rarefaction which broadens in time, as shown in Fig. 3.14c for $t = 1/2$. The characteristic is parallel to the shock on the sonic side.

We can also have another look at the property of non-convexity which allows us to make the link with the MHD case. We follow the reasoning presented in [173]. Eq. 3.73 describes the propagation of co-stationary traveling waves, and the scalar version reads

$$-su + f(u) = f_{const} \tag{3.82}$$

We ask ourselves how many solutions Eq. 3.82 has for u, for given shock speed s and flux constant f_{const}, and whether admissible shocks with shock speed s exist which connect the solutions. For the convex Burgers flux function $f(u) = u^2/2$ this equation has zero or two real solutions, and the shock speed s always lies between the characteristic speeds of the two solutions, such that an admissible shock can always be constructed connecting the two solutions. For the non-convex flux function $f(u) = u^3/3$, however, Eq. 3.82 has 1 or 3 real solutions. The sum of these roots vanishes, such that if there are three roots, two roots have the same sign,

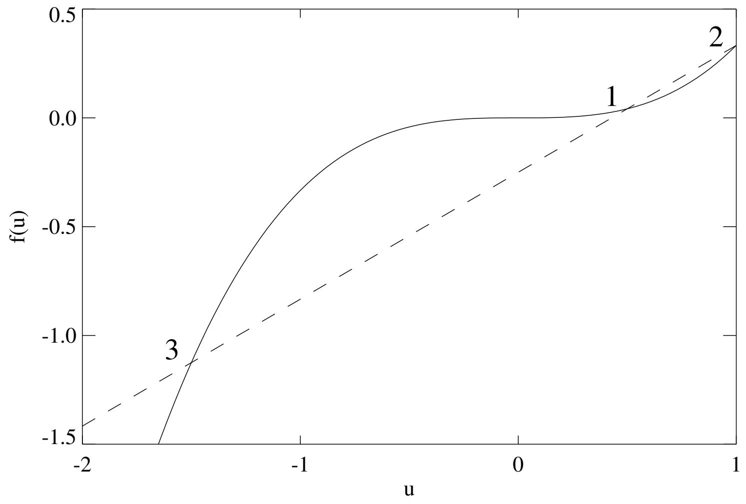

Figure 3.16: *Three solutions exist for the scalar conservation law with non-convex flux function $f(u) = u^3/3$ and for $s = 7/12$ and $f_{const} = -3/12$. State 1 and 2 have the same sign, and state 3 has the opposite sign.*

and the third one has the opposite sign. Let us label those first two roots 1 and 2, with root 1 of the smaller magnitude, and let us give the label 3 to the root with the opposite sign. For instance, and as shown in Fig. 3.16, for $s = 7/12$ and $f_{const} = -3/12$, we find $u = 1/2$ for state 1, $u = 1$ for state 2 and $u = -1.5$ for state 3. We now investigate if the pairs of solutions (1,2), (1,3) and (2,3) can be connected by admissible shocks with speed s.

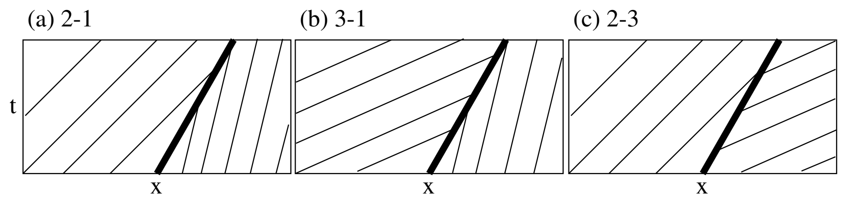

Figure 3.17: *Possible shock connections between the fixed points of Fig. 3.16. (a-b) Connections 2–1 and 3–1 are admissible shocks. (c) Pair (2,3) cannot be connected by an admissible shock.*

Fig. 3.17 shows that pair (1,2) can indeed be connected by an admissible shock 2–1, with state 2 on the left and state 1 on the right. Pair (1,3) can also be connected by a 3–1 shock. Pair (2,3), however, cannot be connected by an admissible shock. The shock with shock speed s is undercompressive in this case. We see thus that the non-convex case is very different from the convex case. In the convex case, there is just one type of admissible shock. In the non-convex case, we see that there are *two different types of admissible shocks* associated with just *one characteristic field*. The 1–2 (or 2–1) shock does *not* change the sign of the scalar u, and we could call it a *regular* shock. The 1–3 (or 3–1) shock *does* change the sign of the scalar u, and we could call it an *intermediate* shock. According to this definition, shock 2–3 (or 3–2) is also of the intermediate type, but this shock is undercompressive and thus inadmissible.

For the compound shock of Figs. 3.14 and 3.15, states 1 and 2 coincide, so the compound shock is composed of a 3–1=2 sonic intermediate shock followed by an attached rarefaction. The fact that 1=2 in the right state (u_*) precisely makes the shock sonic.

We can thus learn from this analysis that non-convexity allows for several different types of shocks associated with a single characteristic field. Alternatively, we could also say that different types of shocks are encountered when Eq. 3.82 has more than two real solutions [173].

The concept of a compound shock carries over to the separate non-convex characteristic fields of *systems* of hyperbolic equations. At least one family of characteristics has to converge into a shock on both sides in order to have an admissible shock. In the case of a 1D Riemann problem, the attached rarefaction is a simple wave, with the consequence that one family of characteristics in the rarefaction consists of straight lines [20, 85, 92]. This family of characteristics is parallel to the shock on the sonic side. Brio and Wu [12] show that the MHD flux function is not convex for the fast and the slow characteristic fields, and they encounter compound shocks in numerical solutions of 1D MHD Riemann problems. Myong and Roe [109, 110] show that compound shocks are essential elements for the solution of some planar ($v_z \equiv B_z \equiv 0$) MHD Riemann problems.

The properties of the MHD shock system 1–2–3–4 can be related to the shock properties of the scalar non-convex equation described above. This has been done rigorously by several authors who derive 'model systems' by simplifying the MHD equations [81, 109, 110, 46]. Here we have to restrict ourselves to suggesting some of the analogies and stating some important results. The non-convex fast characteristic field of MHD can be thought of as to allow for shock states labeled 1–2–3, and the non-convex slow field gives rise to states 2–3–4. These three states are in both instances analogous to the three states associated with the scalar non-convex flux function $f(u) = u^3/3$. The change of sign of u can be associated with the change of sign of the tangential component of the magnetic field B_y, and the MHD intermediate shocks 1–3 and 2–4 are analogous to the scalar intermediate shock 1–3. In MHD, however, the fast and the slow characteristic fields are 'merged together' in a 1–2–3–4 system, and this merged system contains other degenerate phenomena in addition to the compound shock phenomenon. A fast MHD compound shock contains a 1=2–3 shock, with $v_x = c_{fx}$ upstream, analogous to the 1=2–3 sonic intermediate shock in the scalar compound shock described above. Analogously, a slow MHD compound shock contains a 2–3=4 shock, with $v_x = c_{sx}$ on the downstream side of the shock.

This analysis thus shows that compound shocks can arise in MHD flows. They were indeed encountered in numerical simulations of 1D MHD Riemann problems, but they have never been found in 2D or 3D simulations of realistic flow problems. In Chapters 6 and 7 we investigate bow shock flows with magnetically dominated upstream parameters for the presence of compound shocks.

Another interesting conclusion follows from the above analysis. It seems that the intermediate shocks are associated to the non-convex fast and slow modes, and *not* to the Alfvén mode, as could be expected intuitively. This explains for instance why intermediate shocks can arise in planar MHD flows while there are no Alfvén waves in planar MHD. This also explains the following contradiction. We have suggested that nonlinearity is necessary for the steepening of shocks, for instance in our description of the steepening of profiles for the Burgers equation in Fig. 3.2. However, the Alfvén characteristic field is a *linearly degenerate* field [90], or, equivalently, the Alfvén waves are not compressible. (It is exactly the compressibility which makes the fast and slow waves nonlinear and steepening.) But then how can intermediate shocks steepen if they are associated with a linearly degenerate field?

Part of the answer is that 1–3 and 2–4 intermediate shocks are not associated with the Alfvén characteristic field, but rather with the fast and the slow fields. We have to mention here that linearly degenerate fields can also 'carry' discontinuous waves, but those discontinuities are not 'self-steepening' and thus more prone to (turbulent) instability. They are not shocks (in the MHD context), because there is no entropy change or no mass flow across them. For instance, the entropy field is linearly degenerate, and the associated discontinuities are contact discontinuities, which do not steepen, but can form for instance downstream of λ-points where three shock branches meet in 2D flows. Chap. 6 shows some examples of this. The linearly degenerate Alfvén field has *rotational discontinuities* as associated discontinuous waves. These rotational discontinuities do not steepen. This picture is interesting but too simple, because 2–3 intermediate shocks can also directly be associated with the Alfvén mode [41].

We can thus conclude that 1–3 and 2–4 intermediate shocks are not the discontinuous solutions directly associated with the Alfvén mode. However, there is certainly a relationship between these intermediate shocks and Alfvén waves and Alfvén speeds, because intermediate shocks satisfy the proper Alfvén Mach number inequalities (Figs. 3.8 and 3.7). This complex behavior is related to the fact that the MHD system is non-strictly hyperbolic (wave speeds can coincide). We come back to issues like this in Chap. 9.

Chapter 4

A finite volume ideal MHD code

Numerical simulations of MHD flows with shocks have been performed for many decades, but most of the time rather primitive numerical techniques like Lax-Wendroff [90] or Flux Corrected Transport [28] were used. Numerical codes typically either were excessively diffusive or produced spurious oscillations near discontinuities. In the mean time robust and accurate shock-capturing numerical techniques of the so-called high-resolution type have been developed for Computational Fluid Dynamics (CFD) simulations. Only since a decade or so, these new numerical methods have been introduced in MHD codes [12, 157, 158, 183, 23, 24, 128, 129, 1, 118, 127, 162, 6, 7, 99, 36, 26, 111]. The MHD system has certain peculiar properties which impeded the straight translation of the CFD techniques, but it seems that the main obstacles have been removed in recent work by Roe and Balsara (1996) [127], who provided a well-behaved eigensystem decomposition of the MHD Jacobian, and by Powell (1995) [118], who provided a consistent and efficient way to deal numerically with the $\nabla \cdot \vec{B} = 0$ constraint via a source term (the right hand side term proportional to $\nabla \cdot \vec{B}$ in Eq. 2.6).

In this Chapter we report on our development of the PAR-MA (PARallel MAgnetohydrodynamics) code, which is a massively parallel shock capturing MHD code. Using the proven CFD concepts present in the von Karman institute multi-block solver [106], and incorporating the essential contributions of Roe and Powell [1], a new robust and accurate high-resolution MHD flow solver was developed. After a general introduction which illustrates some of the basic concepts of numerical simulation of flow problems with shocks, we give a brief but complete description of the MHD flow solver we have developed. This is the numerical code used for the simulations presented in this dissertation.

Numerical techniques similar to the one described in this Chapter are currently being used in several application codes [118, 162, 124, 117]. Not much can be found in the literature on rigorous validation of this approach, however. We have carried out our MHD code development to the point of its validation by a set of careful grid convergence studies making use of characteristic theory. These studies are reported in Chap. 5 which should be read as a complement to Chap. 4.

4.1 Upwind discretization of conservation laws in one space dimension

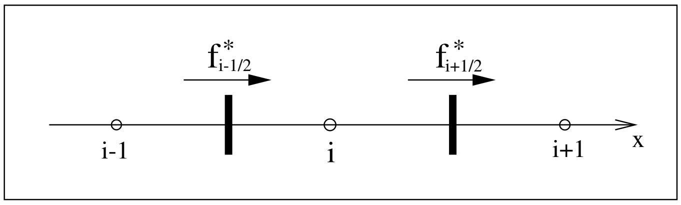

Figure 4.1: *The x-axis is divided into cells of equal length Δx for the numerical computation of the value u_i^n in every cell which approximates the solution $u(x,t)$ at discrete position $x = x_i$ and time $t = t_n$.*

In this Section we introduce some of the basic concepts used in the design of numerical schemes for equations which allow for discontinuous solutions. A good introduction to this subject can be found in [90]. It is beyond the scope of this Section to give a rigorous and complete account of this subject, but we want to give an intuitive introduction for the reader who is unfamiliar with this kind of numerical techniques, and at the same time we may remind the more knowledgeable reader of some of the basic concepts. The reader will note a general conceptual analogy between the discussion in this Section and the discussion of waves and characteristics in hyperbolic systems presented in Sec. 3.2.1. Most of the discussion in the present Section is situated in the context of *finite difference* numerical discretizations. By the end of the Section, we make the link to *finite volume* discretizations.

4.1.1 Scalar conservation laws

A *scalar* conservation law is described by

$$\frac{\partial u}{\partial t} + \frac{\partial f(u)}{\partial x} = 0, \tag{4.1}$$

in terms of scalar u and flux function $f(u)$. The *linear* scalar conservation law or linear advection equation is given by

$$\frac{\partial u}{\partial t} + a\frac{\partial u}{\partial x} = 0, \tag{4.2}$$

with linear flux function $f(u) = a\,u$ for some constant a. Let us assume for the moment that $a > 0$, such that advection proceeds from left to right. The left direction is thus called the *upwind* direction. Obtaining solutions of this equation on a computer requires *discretization* of the equation. We divide both the x and t axes in equal intervals and look for values u_i^n which approximate the solution $u(x,t)$ at discrete position $x = x_i = i\,\Delta x$ and time $t = t_n = n\,\Delta t$ (Fig. 4.1).

A natural way to discretize Eq. 4.2 is to approximate the temporal and spatial derivatives by *finite differences* in the following way

$$\frac{u_i^{n+1} - u_i^n}{\Delta t} + a\frac{u_{i+1}^n - u_{i-1}^n}{2\Delta x} = 0, \tag{4.3}$$

The temporal derivative has been taken *forward* in time, such that a value at time $t = t_{n+1}$ can be calculated from values at time $t = t_n$, leading to an *explicit* numerical scheme. In the rest of this Section we only consider explicit time integration. The *central* spatial discretization in Eq. 4.3 is an approximation of the derivative which is accurate up to second order in Δx. Stability analysis shows, however, that this central discretization results in a numerical scheme which is *numerically unstable.*

Alternatively, we can use the following *upwind* discretization for the spatial derivative

$$\frac{u_i^{n+1} - u_i^n}{\Delta t} + a\frac{u_i^n - u_{i-1}^n}{\Delta x} = 0. \tag{4.4}$$

The derivative is now approximated by a finite difference chosen on the *upwind* side of point i. Stability analysis shows that this discretization is numerically stable under the condition that

$$\Delta t < \frac{\Delta x}{a}, \tag{4.5}$$

which is called the Courant-Friedrichs-Lewy (CFL) condition. This spatial discretization is, however, accurate only to first order in Δx.

More generally, if the sign of a is not specified in advance, then the upwind discretization can be written as

$$\frac{u_i^{n+1} - u_i^n}{\Delta t} + a^+\frac{u_i^n - u_{i-1}^n}{\Delta x} + a^-\frac{u_{i+1}^n - u_i^n}{\Delta x} = 0, \tag{4.6}$$

with the definitions: $a^+ = max(0, a)$ and $a^- = min(0, a)$.

This upwind discretization can be written in *conservative form*

$$\frac{u_i^{n+1} - u_i^n}{\Delta t} + \frac{f_{i+1/2}^{n*} - f_{i-1/2}^{n*}}{\Delta x} = 0, \tag{4.7}$$

with the *numerical flux function* f^{n*} (Fig. 4.1) given by

$$f_{i+1/2}^{n*} = a^+ u_i^n + a^- u_{i+1}^n = \frac{a\, u_{i+1}^n + a\, u_i^n}{2} - \frac{1}{2}|a|(u_{i+1}^n - u_i^n). \tag{4.8}$$

The conservative form of the equations reflects on the discrete level the conservation law form of the PDE, and guarantees *discrete conservation*: $\sum_i u_i^{n+1} = \sum_i u_i^n$. This property turns out to be crucial for the numerical simulation of problems with discontinuities. Indeed, the *Lax-Wendroff theorem* guarantees that a conservative numerical scheme converges to a weak solution of the conservation law, if it converges. This is an important property, because non-conservative numerical schemes can for instance converge to solutions with shocks which propagate at wrong speeds.

The upwind discretization is attractive, but it is too *diffusive*, due to the fact that it is only first order accurate. This can be seen by rewriting Eq. 4.6 in the form

$$\frac{u_i^{n+1} - u_i^n}{\Delta t} + a\frac{u_{i+1}^n - u_{i-1}^n}{2\Delta x} - \frac{|a|\Delta x}{2}\frac{u_{i+1}^n - 2u_i^n + u_{i-1}^n}{\Delta x^2} = 0, \tag{4.9}$$

which can be interpreted to be a second order accurate discretization of the *linear advection-diffusion equation*

$$\frac{\partial u}{\partial t} + a\frac{\partial u}{\partial x} = \eta\frac{\partial^2 u}{\partial x^2}, \tag{4.10}$$

with diffusion coefficient $\eta_{num} = |a|\Delta x/2$. This *numerical diffusion* vanishes in first order in Δx, and thus makes Eq. 4.9 a first order accurate discretization of the linear advection equation 4.2. If one solves the ideal conservation law Eq. 4.1 numerically, one naturally wants to minimize the amount of numerical diffusion in the discretization. However, a certain amount of numerical diffusion is necessary to obtain a stable scheme: the second order accurate central discretization, which does not introduce any numerical dissipation, is numerically unstable. This allows us to interpret the expression for the numerical flux function in Eq. 4.8 as the sum of a term corresponding to a central second order accurate discretization without numerical diffusion, and a term proportional to $|a|$ which represents numerical diffusion.

It is also interesting to remark that the discretization Eq. 4.9 of the scalar advection-diffusion equation 4.10 is only numerically stable under the condition

$$\Delta t < \frac{(\Delta x)^2}{2\eta_{num}}. \tag{4.11}$$

The upwind scheme thus introduces the *maximal* numerical diffusion $\eta_{num} = |a|\Delta x/2$ which is dissipatively stable under the constraint of the CFL condition, in the sense that adding more (numerical) dissipation would make the dissipative time step limitation more stringent than the CFL condition.

Spurious oscillations are another point of concern. They do not arise for numerical schemes which have the property of *positivity* [7]. We discretize the spatial derivative of Eq. 4.1 on a three–point stencil and obtain as a general form

$$\frac{\partial u_i}{\partial t} = c_{i-1}\, u_{i-1} + c_i\, u_i + c_{i+1}\, u_{i+1}. \tag{4.12}$$

Because of consistency with the differential equation, it holds that $c_{i-1} + c_i + c_{i+1} = 0$, so we can rearrange Eq. 4.12 to

$$\frac{\partial u_i}{\partial t} = c_{i-1}\,(u_{i-1} - u_i) + c_{i+1}\,(u_{i+1} - u_i). \tag{4.13}$$

It is clear that a local extremum — for instance a local maximum with $u_i > u_{i-1}$ and $u_i > u_{i+1}$ — will be damped out when the coefficients c_{i-1} and c_{i+1} are both positive. A spatial discretization is called positive when the coefficients of the points in the stencil — except c_i — are positive. It can be seen from Eq. 4.6 that the upwind scheme is positive, such that spurious oscillations cannot be formed at discontinuities. Positive numerical schemes are related to *total variation diminishing* (TVD) schemes [90]. The positivity concept carries over automatically to multiple space dimensions, while the TVD concept is only well-defined in one space dimension.

The upwind scheme can be made more accurate by reducing the numerical diffusion such that $\eta_{num} \approx (\Delta x)^2$, which would mean that the scheme is second order accurate. This can be done through the technique of *linear reconstruction*, as explained in Sec. 4.2. However, *Godunov's theorem* states that a second order scheme which is linear, cannot be positive. To conserve the property of positivity, one has to consider *nonlinear schemes* which are second order away from discontinuities, but which through the action of a *nonlinear limiter* automatically add more dissipation $\eta_{num} \approx \Delta x$ at discontinuities.

The upwind scheme can be generalized to *nonlinear* scalar conservation laws by defining the numerical flux function in analogy with Eq. 4.8 as

$$f^{n*}_{i+1/2} = \frac{f(u^n_{i+1}) + f(u^n_i)}{2} - \frac{1}{2}|f'^{n*}_{i+1/2}|(u^n_{i+1} - u^n_i), \tag{4.14}$$

where $f'^{n*}_{i+1/2}$ is some approximation for the derivative of the flux at the location $x = x_{i+1/2}$. For instance, one can make the simple choice $f'^{n*}_{i+1/2} = f'((u^n_i + u^n_{i+1})/2)$, but other choices with advantageous properties are possible.

4.1.2 Systems of conservation laws

A hyperbolic *system* of conservation laws

$$\frac{\partial \mathbf{U}}{\partial t} + \frac{\partial \mathbf{F}(\mathbf{U})}{\partial x} = 0, \tag{4.15}$$

can be discretized in a way analogous to the scalar case. In case of a *linear* system with $\mathbf{F}(\mathbf{U}) = \mathsf{A} \cdot \mathbf{U}$ and $\mathsf{A} = \mathsf{R}\,\Lambda\,\mathsf{L}$ the eigenvector decomposition of A, we can decouple the equations and apply the upwind discretization technique to every decoupled equation separately, which leads to the numerical flux function

$$\mathbf{F}^{n*}_{i+1/2} = \frac{\mathsf{A}\,\mathbf{U}^n_{i+1} + \mathsf{A}\,\mathbf{U}^n_i}{2} - \frac{1}{2}|\mathsf{A}|(\mathbf{U}^n_{i+1} - \mathbf{U}^n_i), \tag{4.16}$$

where $|\mathsf{A}| = \mathsf{R}\,|\Lambda|\,\mathsf{L}$. This adds the numerical dissipation $\eta^{(k)}_{num} = |\lambda^{(k)}|$ $\Delta x/2$ to (decoupled) equation k.

For a *nonlinear* system, we have to specify an approximation for $\mathsf{A}^n_{i+1/2} = \mathbf{F}'^n_{i+1/2}$, which is the Jacobian $\partial\mathbf{F}/\partial\mathbf{U}$ of the flux at the location $x = x_{i+1/2}$. For instance, one can again make the simple choice $\mathsf{A}^{n*}_{i+1/2} = \mathsf{A}((\mathbf{U}^n_i + \mathbf{U}^n_{i+1})/2)$. The numerical flux function then reads

$$\mathbf{F}^{n*}_{i+1/2} = \frac{\mathbf{F}(\mathbf{U}^n_{i+1}) + \mathbf{F}(\mathbf{U}^n_i)}{2} - \frac{1}{2}|\mathsf{A}^{n*}_{i+1/2}|(\mathbf{U}^n_{i+1} - \mathbf{U}^n_i), \tag{4.17}$$

with $|\mathsf{A}^{n*}_{i+1/2}| = \mathsf{R}_{i+1/2}\,|\Lambda|_{i+1/2}\,\mathsf{L}_{i+1/2}$. This expression is closely related to the Roe flux function [127]. The CFL time step limitation now becomes

$$\Delta t < \frac{\Delta x}{\max_{k,i}(|\lambda^{(k)}_{i+1/2}|)}, \tag{4.18}$$

with $\max_{k,i}(|\lambda^{(k)}_{i+1/2}|)$ the largest wave speed in the system. This suggests, however, that we could simplify the numerical scheme considerably by applying the largest numerical diffusion $\eta_{num,i+1/2} = \max_k(|\lambda^{(k)}_{i+1/2}|)$ $\Delta x/2$ uniformly to *all* the equations at location $x = x_{i+1/2}$. This still guarantees numerical stability and positivity of the discretization, although it adds some excessive dissipation to some of the characteristic waves. The numerical flux function simplifies to

$$\mathbf{F}^{n*}_{i+1/2} = \frac{\mathbf{F}(\mathbf{U}^n_{i+1}) + \mathbf{F}(\mathbf{U}^n_i)}{2} - \frac{1}{2}\max_k(|\lambda^{(k)}_{i+1/2}|)(\mathbf{U}^n_{i+1} - \mathbf{U}^n_i). \tag{4.19}$$

The resulting numerical scheme is much simpler because no eigenvector decomposition is necessary, and it also turns out to be much more robust. It is called the *(local) Lax-Friedrichs scheme.*

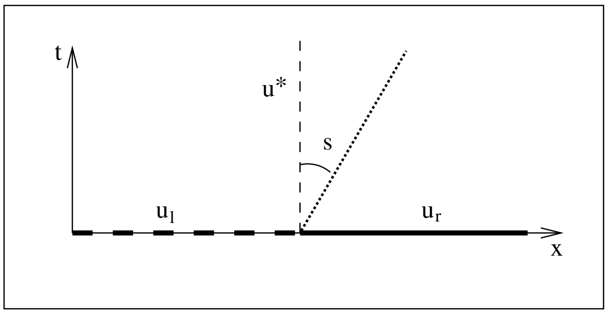

Figure 4.2: *Riemann problem for a scalar equation. In this example the solution is a shock which connects u_l with u_r and propagates with speed s.*

We can now make the link to *finite volume* discretizations [90]. To this end we first have to introduce the concept of a *Riemann problem* [90]. For simplicity we discuss the scalar case. As is shown in Fig. 4.2, a Riemann problem is an initial value problem for which the initial state is a discontinuous jump between two constant states. We have shown in Sec. 3.3.5 that the exact solution of a scalar Riemann problem is a shock (propagating with shock speed s, see Fig. 4.2) or a rarefaction — or possibly a compound shock for non-convex flux functions. For a $k \times k$ system, the solution to the Riemann problem generally consists of k shocks and/or rarefactions which propagate at different speeds. An important property of Riemann problem solutions is that they are *self-similar* in the variable x/t, such that the state $u^*(t)$ at the x-location of the initial discontinuity between u_l and u_r, is *constant in time.* In a linear system, there are only shocks and no rarefactions, and below we consider *linearized* Riemann problems.

We divide the x and t axes in *finite volume* cells with constant lengths Δx and Δt. We integrate Eq. 4.1 over a finite volume cell (Fig. 4.3) and obtain

$$(\overline{u}_i^{n+1} - \overline{u}_i^n)\,\Delta x + (\overline{\overline{f}}(u_{i+1/2}^{n*}) - \overline{\overline{f}}(u_{i-1/2}^{n*}))\,\Delta t = 0, \qquad (4.20)$$

where the overbar denotes a spatial average, the double overbar is a temporal average and $u_{i+1/2}^{n*}$ is the exact solution at $x = x_{i+1/2}$. The cell average $\overline{u}_i^n$ is stored in the center of cell i. Eq. 4.20 is exact and can be interpreted as an evolution equation for the cell averages, which change when there is a net flux through the cell interfaces. We can

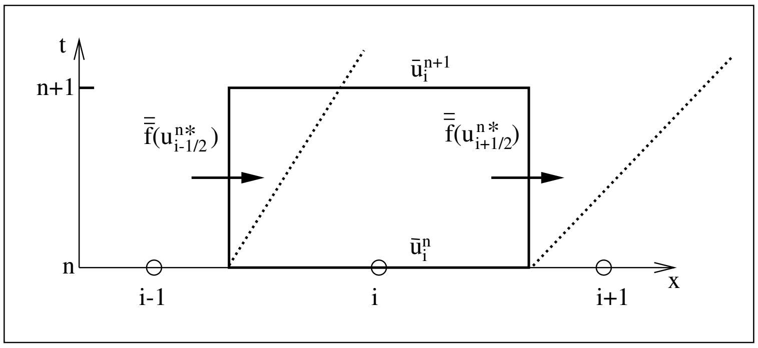

Figure 4.3: *Finite volume integration.*

now approximate $u(x,t)$ by evolving the cell averages in time using Eq. 4.20 with a certain approximation $f^{n*}_{i+1/2}$ for the flux $\overline{\overline{f}}(u^{n*}_{i+1/2})$. $f^{n*}_{i+1/2}$ is again called the *numerical flux function.* At a given time $t = t_n$, we have thus to consider the evolution of a piecewise-constant profile, which in fact is equivalent to the solution of many Riemann problems at every cell interface. The solutions u^* of these Riemann problems at the interfaces are constant in time, so we can drop the double overbar in Eq. 4.20. We can solve these Riemann problems approximately, and can for instance choose the linearized approximate Riemann solver $f^{n*}_{i+1/2}$ defined by

$$f^{n*}_{i+1/2} = \frac{f(u^n_{i+1}) + f(u^n_i)}{2} - \frac{1}{2}|f'^{n*}_{i+1/2}|(u^n_{i+1} - u^n_i), \tag{4.21}$$

where we have been inspired by the flux function used in our upwind finite difference scheme Eq. 4.14.

The reader can note the equivalence between conservative finite difference schemes (*point values* are updated using finite difference approximations of derivatives) and finite volume schemes (*cell averages* are updated using differences of fluxes through cell interfaces). For the first order schemes considered in this Section the two approaches are completely equivalent. For instance, the CFL condition can be interpreted as the condition that waves from neighboring Riemann problems do not interfere. *Upwind discretization* is equivalent to solving *Riemann problems* to determine the numerical finite volume flux. Higher order discretization of derivatives, however, is not automatically equivalent to higher order discretization of fluxes through interfaces.

4.2 Spatial discretization: finite volume schemes

In this Section we describe the spatial discretization approach adopted in our code, which leads to schemes which are first and second order accurate in space (for smooth flow). Here we only describe discretization of the *ideal* equations. It is not too difficult to discretize the dissipative terms as well [106], and the 2D numerical code used for the simulations presented in this dissertation actually is capable of performing dissipative simulations [155], but this aspect of the code is not described here. For simplicity, we start with an equi-distant spatial discretization in 1D (grid size Δx), and subsequently discuss 2D, 3D and 2D axi-symmetrical discretizations. The ideal MHD equations 3.12 can be written in the following abstract conservation law form

$$\frac{\partial \mathbf{U}}{\partial t} + \nabla \cdot \vec{\mathbf{F}}(\mathbf{U}) = \mathbf{S}^{Pow}, \tag{4.22}$$

with $\mathbf{U}$ the vector of state variables which are conserved quantities, $\vec{\mathbf{F}}$ the flux vector, and $\mathbf{S}^{Pow}$ the Powell source term (which equals zero on the PDE level because it is proportional to $\nabla \cdot \vec{B}$).

4.2.1 One–dimensional space

In every cell (i) we define the cell average of the state variable $\mathbf{U}$ as

$$\overline{\mathbf{U}}_i = \left(\int_{x_{i-1/2}}^{x_{i+1/2}} \mathbf{U}(x,t)\, dx \right) / \Delta x. \tag{4.23}$$

This cell average is stored in the center of cell (i) — leading to a *cell-centered* approach. We obtain the following time evolution equation for this average after integration of Eq. 4.22 in space over the *finite volume* cell with label i

$$\frac{\partial \overline{\mathbf{U}}_i}{\partial t} + 1/\Delta x\, (\mathbf{F}^*_{i+1/2} - \mathbf{F}^*_{i-1/2}) = 0. \tag{4.24}$$

In 1D the Powell source term is also identically zero numerically, because B_x is a constant in 1D space. $\mathbf{F}^*_{i+1/2}$ is a numerical approximation for the flux through the interface between cell (i) and cell $(i+1)$ (the *numerical flux function*).

There are many possible choices for the form of the numerical flux function, corresponding to the choice of an (approximate) Riemann solver. In Sec. 4.2.5 we discuss some possible choices and describe the numerical flux function used for the simulations presented in this paper.

Many numerical flux functions, including the Roe and Lax-Friedrichs flux functions, can be cast in the following form

$$\mathbf{F}^*(\mathbf{U}_l, \mathbf{U}_r) = \frac{\mathbf{F}(\mathbf{U}_l) + \mathbf{F}(\mathbf{U}_r)}{2} + D(\mathbf{U}_l, \mathbf{U}_r), \tag{4.25}$$

with $\mathbf{F}$ being the 1D MHD flux function of Eq. 3.76, and $\mathbf{U}_l$ and $\mathbf{U}_r$ the state variables to the left and to the right of the interface. The third term $D(\mathbf{U}_l, \mathbf{U}_r)$ is in general proportional to $\mathbf{U}_r - \mathbf{U}_l$.

Let us focus on the flux through the interface between cells i and $i+1$. A first order accurate spatial discretization is obtained if we take the left and the right state used to calculate the numerical flux, to be the cell-averages to the left and the right of the interface, viz. $\mathbf{U}_l = \overline{\mathbf{U}}_i$ and $\mathbf{U}_r = \overline{\mathbf{U}}_{i+1}$. In this picture, the solution is thought to be *piecewise-constant* in every cell. The first two terms in the right-hand side (RHS) of Eq. 4.25 correspond to a second-order accurate central space discretization of the flux terms without dissipation, and would lead to a numerically unstable scheme without the addition of dissipative terms. The third term $D(\mathbf{U}_l, \mathbf{U}_r)$ precisely adds this (numerical) dissipation with a dissipation coefficient which vanishes in first order in Δx. There are many choices for the exact form of this dissipative term, corresponding to the choice of an (approximate) Riemann solver. This is discussed in Sec. 4.2.5.

The scheme can be enhanced to second order spatial accuracy by considering *piecewise-linear* variation in a cell. For instance, $\mathbf{U}_l$ can be calculated — or *reconstructed* — as $\mathbf{U}_l = \overline{\mathbf{U}}_i + 1/2\,(\overline{\mathbf{U}}_i - \overline{\mathbf{U}}_{i-1})$, or possibly also as $\mathbf{U}_l = \overline{\mathbf{U}}_i + 1/2\,(\overline{\mathbf{U}}_{i+1} - \overline{\mathbf{U}}_i)$ or any convex combination of these two. This kind of reconstruction would lead to second order accurate schemes — the dissipation coefficient of the term $D(\mathbf{U}_l, \mathbf{U}_r)$ would vanish in second order —, but the solution near discontinuities would contain spurious oscillations. To discard these spurious oscillations, a nonlinear *slope limiter* L can be used to determine the slope of the linear reconstruction, with

$$\mathbf{U}_l = \overline{\mathbf{U}}_i + 1/2\,L(\overline{\mathbf{U}}_i - \overline{\mathbf{U}}_{i-1}, \overline{\mathbf{U}}_{i+1} - \overline{\mathbf{U}}_i). \tag{4.26}$$

Again, there are many possible choices for such a limiter [90], and we use the *minmod* limiter for our simulations. The component-wise action of the minmod function is given by

$$l(x, y) = \mathrm{sign}(x)\ \max(\,0\,, \min(\mathrm{abs}(x), \mathrm{sign}(x)\,y)\,). \tag{4.27}$$

It can easily be verified that this function selects the least steep slope for the reconstruction if the sign of the slopes is the same, and vanishes (leading to piecewise constant reconstruction and first order accuracy) when the signs of the two slopes are different, which typically is the case at discontinuities. It can be proven rigorously that this limiter function (and other similar limiter functions) effectively discards spurious oscillations [90] because it ensures positivity of the scheme. In practice we do the second order reconstruction using the primitive variables $\mathbf{W}$, and not the conservative variables $\mathbf{U}$. Experience shows that this improves the robustness and steady state convergence properties of the scheme.

4.2.2 Two–dimensional space

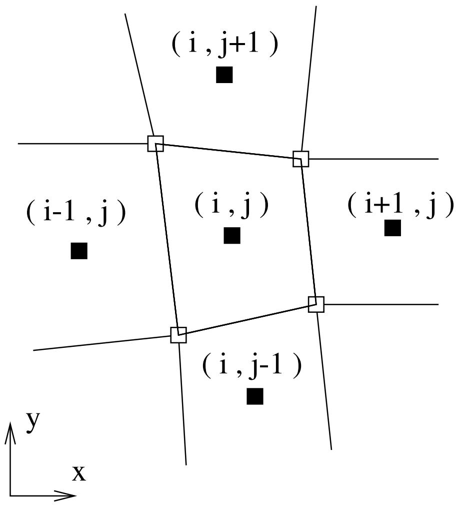

Figure 4.4: *Finite volume grid cell with label (i, j) and its nearest neighbor cells. The variables stored in the centers of a cell represent the averages of the state variables over the cell.*

Now we describe how these concepts can be extended to spatial discretization on a 2D structured body-fitted grid. We divide the computational domain in a logically rectangular structured grid of quadrilaterals (Fig. 4.4). The solution of the flow is sought in the *physical* cells, with indices in the computational domain ranging from 1 to n_i for index i, and from 1 to n_j for index j. This physical domain is surrounded by two layers of *ghost cells*, which allow for a simple implementation of boundary conditions (see Sec. 4.2.6). The cell interfaces are not constrained to be parallel to a Cartesian axis, which for instance allows to fit the grid to a curved rigid body. We integrate Eq. 4.22 formally over the *finite volume* cell with label (i, j), and obtain the following discretized equation

$$\frac{\partial \overline{\mathbf{U}}_{i,j}}{\partial t} + 1/\Omega_{i,j} \sum_{k=1}^{4} \vec{\mathbf{F}}_k^* \cdot \vec{n}_k \, \Delta l_k = \overline{\mathbf{S}}_{i,j}^{Pow}, \tag{4.28}$$

for the time evolution of the average of the state variable over cell (i, j)

$$\overline{\mathbf{U}}_{i,j} = \left(\int\!\!\int \mathbf{U}(x, y, t) \, dx \, dy \right) / \Omega_{i,j}, \tag{4.29}$$

which is stored in the center of cell (i, j). The coordinates of the cell centers are calculated as the arithmetic average of the corner point coordinates. Here $\Omega_{i,j}$ is the surface of cell (i, j), and the summation in Eq. 4.28 extends over the four sides or interfaces of cell (i, j). $\vec{\mathbf{F}}_k^*$ is a numerical approximation for the flux vector through the interface k, Δl_k is the length of interface k, and $\vec{n}_k$ is the outside unit vector normal to side k. $\overline{\mathbf{S}}_{i,j}^{Pow}$ is the cell average of the Powell source term in cell (i, j).

For each interface, we can apply the above described 1D technique to calculate the normal numerical flux $\mathbf{F}^* = \vec{\mathbf{F}}^* \cdot \vec{n}$. The 1D formulas remain valid in a coordinate system aligned with the interface. For instance, to calculate the flux between cell (i, j) and cell $(i + 1, j)$, a first order accurate scheme is obtained by taking $\mathbf{U}_l = \overline{\mathbf{U}}_{i,j}$ and $\mathbf{U}_r = \overline{\mathbf{U}}_{i+1,j}$. Appropriate rotations of vector components have to be carried out then to calculate $\mathbf{F}^*$ using Eq. 4.25. A second order accurate scheme results from taking $\mathbf{U}_l = \overline{\mathbf{U}}_{i,j} + 1/2\, L(\overline{\mathbf{U}}_{i,j} - \overline{\mathbf{U}}_{i-1,j}, \overline{\mathbf{U}}_{i+1,j} - \overline{\mathbf{U}}_{i,j})$. In practice we do the second order reconstruction using the primitive variables $\mathbf{W}$, and with vector components in the coordinate system aligned with the interface. This alignment reduces errors of the scheme at boundaries. This simple dimension-by-dimension approach turns out to work well, and it can be proven that the scheme remains second order accurate if the grid is not too much distorted [164]. In the next Chapter we present grid convergence results which confirm this. A more sophisticated approach would be to do reconstruction using estimates of gradients based on 2D interpolation [7].

We use the following discretization for the source term $\overline{\mathbf{S}}_{i,j}^{Pow}$ in cell (i, j). $\nabla \cdot \vec{B}$ is discretized as

$$(\nabla \cdot \vec{B})_{i,j} = 1/\Omega_{i,j} \sum_{k=1}^{4} \vec{B}_k \cdot \vec{n}_k \, \Delta l_k, \tag{4.30}$$

with

$$\vec{B}_k = (\vec{B}_l + \vec{B}_r)/2 \tag{4.31}$$

the average of the (reconstructed) magnetic fields on the left and the right of the interface. This discretization of $\nabla \cdot \vec{B}$ is then multiplied with the appropriate cell-averaged state variables (stored in the center of cell (i,j)) to obtain a discretization for the source term in Eq. 4.28. Experience has shown that it is important to use the *reconstructed* values of $\vec{B}$ in the discretization of $\nabla \cdot \vec{B}$ for the second order scheme, because this results in a more robust scheme.

4.2.3 Three–dimensional space

It is rather straightforward to extend the above described techniques to spatial discretization to a 3D structured body-fitted grid. We divide the computational domain in a logically rectangular structured grid of hexahedrals (cells with eight corner points and six boundary interfaces). We introduce a third index k ranging from 1 to n_k in the computational space. The physical domain is again surrounded by two layers of ghost cells.

We integrate Eq. 4.22 formally over the hexahedral *finite volume* cell with label (i,j,k), and obtain the following discretized equation

$$\frac{\partial \overline{\mathbf{U}}_{i,j,k}}{\partial t} + 1/\Omega_{i,j,k} \sum_{p=1}^{6} \vec{\mathbf{F}}_p^* \cdot \vec{n}_p \, \Delta A_p = \overline{\mathbf{S}}_{i,j,k}^{Pow}, \qquad (4.32)$$

for the time evolution of the average of the state variable over cell (i,j,k)

$$\overline{\mathbf{U}}_{i,j,k} = \left(\iiint \mathbf{U}(x,y,z,t)\, dx\, dy\, dz \right) / \Omega_{i,j,k}, \qquad (4.33)$$

which is stored in the center of cell (i,j,k). Here $\Omega_{i,j,k}$ is the volume of cell (i,j,k), and the summation in Eq. 4.32 extends over the six sides or interfaces of cell (i,j,k). $\vec{\mathbf{F}}_p^*$ is a numerical approximation for the flux vector through the interface p, ΔA_p is the surface of interface p, and $\vec{n}_p$ is the outside unit vector normal to side p. In general the four points defining a cell interface are *not* co-planar, so care has to be taken to define the cell volumes and the interface normals and surfaces in a consistent way. We have used a technique which subdivides the hexahedron in three five-sided pyramids pointing at the same vertex, as described in [106].

As in the 2D case, we can apply the above described 1D technique to calculate the normal numerical flux $\mathbf{F}^* = \vec{\mathbf{F}}^* \cdot \vec{n}$ for each interface. The 1D formulas remain valid in a coordinate system aligned with the interface. The source term is discretized in a way completely analogous to the 2D case.

4.2.4 Axial symmetry

The conservative form of the ideal MHD equations with a source term Eq. 3.12 can be written in cylindrical coordinates (x,r,θ), and by assuming *rotational or axial symmetry* around the x-axis ($\partial/\partial\theta \equiv 0$), one obtains

$$\frac{\partial(r\mathbf{U})}{\partial t} + \frac{\partial(r\mathbf{F}_x(\mathbf{U}))}{\partial x} + \frac{\partial(r\mathbf{F}_r(\mathbf{U}))}{\partial r} = \mathbf{S}^{geo}(\mathbf{U}) + r\mathbf{S}^{Pow}. \tag{4.34}$$

Here $\mathbf{U} = (\rho, \rho v_x, \rho v_r, \rho v_\theta, B_x, B_r, B_\theta, e)$ is the vector of conservative variables in the cylindrical coordinate system. $\mathbf{F}_x(\mathbf{U})$ and $\mathbf{F}_r(\mathbf{U})$ are MHD flux functions (as in Eq. 3.76) in the x and the r directions, for instance

$$\mathbf{F}_x(\mathbf{U}) = \begin{bmatrix} \rho\, v_x \\ \rho\, v_x^2 + p + B^2/2 - B_x^2 \\ \rho\, v_x v_r - B_x B_r \\ \rho\, v_x v_\theta - B_x B_\theta \\ 0 \\ B_r v_x - B_x v_r \\ B_\theta v_x - B_x v_\theta \\ (e + p + B^2/2)v_x - B_x\, (\vec{v} \cdot \vec{B}) \end{bmatrix}. \tag{4.35}$$

$\mathbf{S}^{geo}(\mathbf{U})$ is a geometrical source term reading

$$\mathbf{S}^{geo}(\mathbf{U}) = \begin{bmatrix} 0 \\ 0 \\ (\rho v_\theta^2 - B_\theta^2) + (p + B^2/2) \\ -(\rho v_r v_\theta - B_r B_\theta) \\ 0 \\ 0 \\ v_r B_\theta - v_\theta B_r \\ 0 \end{bmatrix}, \tag{4.36}$$

and $r\mathbf{S}^{Pow}$ is the Powell source term given by

$$r\mathbf{S}^{Pow} = \mathbf{D}^{Pow}\, \mathbf{W}^{Pow}(\mathbf{U}), \tag{4.37}$$

with

$$\mathbf{D}^{Pow} = \left(\frac{\partial(rB_x)}{\partial x} + \frac{\partial(rB_r)}{\partial r} \right), \tag{4.38}$$

and

$$\mathbf{W}^{Pow}(\mathbf{U}) = \begin{bmatrix} 0 \\ B_x \\ B_r \\ B_\theta \\ v_x \\ v_r \\ v_\theta \\ \vec{B} \cdot \vec{v} \end{bmatrix}. \tag{4.39}$$

We have derived these expressions following the technique proposed in [13]. We discretize these equations on a 2D structured body-fitted grid.

We integrate Eq. 4.34 formally over the cell with label (i, j), and after some approximations regarding the averaging of state variables and geometrical quantities, we obtain the following discretized equation

$$\Omega_{i,j} r_{i,j}^{center} \frac{\partial \overline{\mathbf{U}}_{i,j}}{\partial t} + \sum_{k=1}^{4} r_k^{middle} \vec{\mathbf{F}}_k^* \cdot \vec{n}_k \, \Delta l_k = \Omega_{i,j}(\mathbf{S}^{geo}(\overline{\mathbf{U}}_{i,j}) + \overline{\mathbf{D}}_{i,j}^{Pow} \mathbf{W}^{Pow}(\overline{\mathbf{U}}_{i,j})), \tag{4.40}$$

for the time evolution of the average of the state variable over cell (i, j)

$$\overline{\mathbf{U}}_{i,j} = \left(\int \int \mathbf{U}(x, r, t) \, dx \, dr \right) / \Omega_{i,j}, \tag{4.41}$$

which is stored in the center of cell (i, j). Here $\Omega_{i,j}$ is the surface of cell (i, j). $\vec{\mathbf{F}}_k^*$ is a numerical approximation for the flux vector through the interface k, Δl_k is the length of interface k, and $\vec{n}_k$ is the outside unit vector normal to side k. $r_{i,j}^{center}$ is the distance between the center of cell (i, j) and the axis of rotational symmetry, and r_k^{middle} is the distance between the middle point of the interface segment with label k and the symmetry axis. The term $\overline{\mathbf{D}}_{i,j}^{Pow}$ is discretized as

$$\overline{\mathbf{D}}_{i,j}^{Pow} = 1/\Omega_{i,j} \sum_{k=1}^{4} r_k^{middle} \vec{B}_k \cdot \vec{n}_k \, \Delta l_k, \tag{4.42}$$

with

$$\vec{B}_k = (\vec{B}_l + \vec{B}_r)/2 \tag{4.43}$$

the average of the (reconstructed) magnetic fields on the left and the right of the interface. The same numerical flux functions $\vec{\mathbf{F}}^*$ and the same second order reconstruction can be used as for the case of the 1D, 2D and 3D schemes. Actually, the 2D code based on the scheme described in Sec. 4.2.2 for planar symmetry ($\partial/\partial z \equiv 0$) can be used for axi-symmetrical simulations by a simple re-definition of the geometrical quantities $\Omega' = r^{center}\Omega$ and $\Delta l' = r^{middle}\Delta l$, and by adding the geometrical source term.

4.2.5 Numerical flux functions

Throughout the years, many interesting MHD numerical flux functions have been proposed that can be used in the type of finite volume discretization described above, most of them based on some kind of approximate Riemann solver at the interface between two cells [12, 183, 23, 24, 128, 129, 1, 118, 127, 162, 6, 7, 99, 36, 26, 111]. Many of those flux functions are designed to produce as sharp as possible shock transitions and tangential discontinuities. The Roe scheme for example, which has been very popular for hydrodynamic applications, has been extended to MHD [127, 7]. This scheme tries to minimize the numerical dissipation by decomposing the difference $\mathbf{U}_r - \mathbf{U}_l$ present in $D(\mathbf{U}_l, \mathbf{U}_r)$ in the space of the eigenvectors of the Jacobian and by applying the minimum amount of numerical dissipation to every characteristic wave separately. There remain, however, several serious problems of local numerical instability with this scheme, including the carbuncle phenomenon, as for example described by Quirk [121]. Probably because of these problems the Roe scheme is not so much used in MHD simulations these days [100, 150, 82].

Several approaches have been proposed to remedy these problems. First, different types of nonlinear flux functions are being investigated, e. g. Linde's HLLE-based solver for MHD [99], which is based on some other form for the numerical dissipation, or solvers derived from kinetic descriptions [100, 99]. These new flux functions seem to remedy some of the problems associated with the Roe solver, but more investigation is necessary to see if they can solve all the stability problems. Second, it is sometimes argued that much of the problems with finite volume schemes on structured grids are inherent to the dimension-by-dimension approach, and that many of the pathological instabilities could be removed by considering truly multi-dimensional schemes on unstructured grids [167, 22]. Third, the failure of the Roe scheme can probably be related to the fact that it is not *entropy stable* [7]. New entropy stable schemes formulated in symmetrized *entropy variables* are being developed [7] and it can be expected that they will lead to more stable numerical schemes. Also in this area a lot of research is still going on.

This short discussion indicates that there are certainly many unsolved issues regarding the choice of numerical flux functions and numerical schemes in general.

The Lax-Friedrichs flux function

The (local) Lax-Friedrichs (LF) flux function [90, 162, 6] is given by

$$\mathbf{F}^*(\mathbf{U}_l, \mathbf{U}_r) = \frac{\mathbf{F}(\mathbf{U}_l) + \mathbf{F}(\mathbf{U}_r)}{2} - (|v_n^*| + c_n^{f*})\frac{\mathbf{U}_r - \mathbf{U}_l}{2}, \tag{4.44}$$

with $|v_n^*| + c_n^{f*}$ the largest wave speed in the direction normal to the interface, determined from the arithmetic average $(\mathbf{U}_l + \mathbf{U}_r)/2$ on the interface. This is sometimes also called the Rusanov flux function. The Lax-Friedrichs flux function applies to all characteristic waves the same numerical dissipation, determined by the maximum wave speed, which makes it more dissipative than the Roe scheme for instance, but much more robust and less prone to local numerical instabilities. The Lax-Friedrichs flux function is probably the most robust numerical flux function. Because it is simple and robust, its use in applications is often advocated [162, 6, 150, 82]. Stationary shock profiles are actually captured surprisingly well with this Lax-Friedrichs scheme [6, 162], but tangential discontinuities are smeared out. We show in the next Chapter that we obtain satisfactory grid convergence results using this numerical flux function. For most of the simulations to be described in this dissertation, we use the LF flux function.

The Roe flux function

The Roe scheme has been extended to MHD, and the details of the eigenvector decomposition can be found in [127, 7]. We have certainly tried to use the Roe scheme for our simulations of bow shock flows, but the Roe scheme has turned out to be not reliable enough. For instance, the carbuncle phenomenon [121] was often encountered at the nose of bow shocks. We illustrate this in Chap. 9.

The MHD HLLE flux function

Linde's extension of the HLLE flux function to MHD [99] seems to be more reliable than the Roe scheme. The carbuncle phenomenon did not seem to show up in our 2D simulations when we used this flux function, but we observed other instabilities which prevented convergence to a steady state, as is illustrated in Chap. 9. In 2D we were able to choose the resolution of the grid high enough to get good results with the LF scheme. In 3D, however, we sometimes had to use Linde's HLLE scheme to obtain flow solutions with reasonable detail.

4.2.6 Boundary conditions

Most of the simulations presented in this dissertation were performed using boundary conditions implemented with two layers of *ghost cells* (e.g. [91]). This allows us to use the same algorithm to update all the cells in the physical simulation domain, also the ones close to the boundary. Superfast inflows and outflows and perfectly conducting walls can easily be modeled by this technique. For subfast inflows and outflows, however, we have used boundary conditions based on direct specification of the numerical flux on the boundary. We discuss the boundary conditions for the case of two spatial dimensions. The 3D case is completely analogous.

Boundary conditions using ghost cells

The following three types of boundary conditions can easily be specified using the ghost cell approach. Let us focus on a boundary to the right of cell $(i = n_i, j = j^*)$, which is the last *physical* cell in the i direction with the second coordinate j equal to a certain j^* in the computational space.

First, at perfectly conducting walls, the magnetic and the velocity fields have to be tangent to the wall. This is implemented by copying the cell-averaged state of (n_i,j^*) into the first ghost cell (n_i+1,j^*), except for the components of the magnetic and velocity fields perpendicular to the interface between cells (n_i,j^*) and (n_i+1,j^*), which are copied with a change in sign. For the second order scheme, the cell-averaged state of $(n_i\text{-}1,j^*)$ is copied into the second ghost cell (n_i+2,j^*), except again for the components of the magnetic and velocity fields perpendicular to the interface between cells (n_i,j^*) and (n_i+1,j^*), which are copied with a change in sign. This procedure guarantees that the value of $(\mathbf{U}_l + \mathbf{U}_r)/2$ for the normal components of the fields vanishes exactly on that interface, also for the second order scheme with minmod reconstruction in a coordinate system aligned with the interface.

Second, at free outflows, where the normal outward plasma velocity is larger than the normal fast MHD wave speed and all the characteristic information thus propagates outward of the physical domain, the state variables of the last two physical cells are used to extrapolate linearly into the two layers of ghost cells, for instance $\overline{\mathbf{U}}_{n_i+2,j^*} = \overline{\mathbf{U}}_{n_i,j^*} + 2\,(\overline{\mathbf{U}}_{n_i,j^*} - \overline{\mathbf{U}}_{n_i-1,j^*})$.

Third, at free inflows, where the normal inward plasma velocity is larger than the normal fast MHD wave speed and all the characteristic information thus propagates into the physical domain, we impose the value of $\mathbf{U}_{in} = (\mathbf{U}_l + \mathbf{U}_r)/2$ on the boundary interface, and use this and the state of the last physical cell to calculate the value in the first ghost cell. In our example, $\overline{\mathbf{U}}_{n_i+1,j^*} = 2\,\mathbf{U}_{in} - \overline{\mathbf{U}}_{n_i,j^*}$. The value in the second ghost cell $\overline{\mathbf{U}}_{n_i+1,j^*}$ follows from linear extrapolation of $\overline{\mathbf{U}}_{n_i,j^*}$ and $\overline{\mathbf{U}}_{n_i+1,j^*}$. For the free inflows and outflows, an even simpler but often satisfactory approach is to use constant extrapolation of the solution.

Although these boundary conditions are based on a simple dimension-by-dimension extrapolation, they turn out to work well, as is proven in the next Chapter.

Flux boundary conditions

Characteristic boundary conditions [7] are implemented by directly specifying the flux as follows. At the boundary interface to the right of cell $(i = n_i, j = j^*)$, one determines the state $\mathbf{U}^*$ which is the approximate solution of the Riemann problem with left state the interpolated state $\overline{\mathbf{U}}_l = \overline{\mathbf{U}}_{n_i,j^*} + 1/2\,(\overline{\mathbf{U}}_{n_i,j^*} - \overline{\mathbf{U}}_{n_i-1,j^*})$, and right state a specified *free flow state* $\mathbf{U}_r = \mathbf{U}_\infty$. In bow shock flows, this free flow state is typically the state far upstream of the object. $\mathbf{U}^*$ can for instance be determined using the Roe linearized Riemann decomposition. The numerical flux is then given by $\mathbf{F}^* = \mathbf{F}(\mathbf{U}^*)$. For superfast inflow and outflow, this results in a boundary condition which is very close to the above described ghost cell approach. For subfast flow, however, some characteristic information flows into the physical domain, and other information flows out. It is generally hard to translate this to specifying some of the primitive variables externally, and extrapolating the others from the physical domain, because there is a complicated nonlinear and state-dependent relationship between the characteristic variables carrying the wave information and the primitive variables. The solution of the Riemann problem *automatically* selects the necessary amount of information from the state in the physical domain and the externally specified free flow state [7].

4.3 Temporal discretization: explicit Runge-Kutta schemes

In this Section we discuss the time integration strategy used in our simulation code. We situate the discussion in the context of the 2D code, but the 1D and 3D cases are completely analogous. An equation for the time evolution of the cell average in cell (i, j) can be written in the following general form

$$\frac{\partial \overline{\mathbf{U}}_{i,j}}{\partial t} = \mathbf{R}_{i,j}^{(1),(2)}(\overline{\mathbf{U}}), \tag{4.45}$$

with $\mathbf{R}_{i,j}^{(1),(2)}$ a first or second order accurate discretization of the *residual* in cell (i, j), containing the spatial discretization of the divergence term in Eq. 4.22, and the discretization of the source term. An explicit first-order accurate time integration is obtained by simply approximating the time derivative by a forward finite difference,

$$\overline{\mathbf{U}}_{i,j}^{t+\Delta t} = \overline{\mathbf{U}}_{i,j}^{t} + \mathbf{R}_{i,j}^{(1)}(\overline{\mathbf{U}}^t)\,\Delta t. \tag{4.46}$$

An explicit second-order accurate time integration is obtained by applying the following two-stage Runge-Kutta integration,

$$\begin{aligned} \overline{\mathbf{U}}_{i,j}^{*} &= \overline{\mathbf{U}}_{i,j}^{t} + \mathbf{R}_{i,j}^{(2)}(\overline{\mathbf{U}}^t)\,\Delta t/2 \\ \overline{\mathbf{U}}_{i,j}^{t+\Delta t} &= \overline{\mathbf{U}}_{i,j}^{t} + \mathbf{R}_{i,j}^{(2)}(\overline{\mathbf{U}}^*)\,\Delta t. \end{aligned} \tag{4.47}$$

The time step Δt is derived from the following CFL-like time step limitation [106]

$$\Delta t = c_{CFL}\ \min_{i,j}\left[\frac{\Omega_{i,j}}{\sum_{k=1}^{4}\ \max(0, (\vec{v}_{i,j}\cdot\vec{n}_k + c_{k,i,j}^f))\,\Delta l_k}\right], \tag{4.48}$$

with $c^f_{k,i,j}$ the fast MHD wave speed in the direction of $\vec{n}_k$ calculated with the cell-averaged state values stored in cell (i, j). The constant c_{CFL} has to be chosen smaller than one for the first order scheme, and may be chosen slightly larger than one for the second order scheme. We generally use $c_{CFL} = 0.8$ for first order calculations, and $c_{CFL} = 1.2$ for second order simulations.

We use these general time-accurate integration methods to calculate the stationary flow solutions to be described further on in this dissertation. In general, we start from a uniform initial flow condition and we evolve the flow in time until vanishing of the residuals $\mathbf{R}$ shows that a steady state has been reached. We use the following quantity based on the density residual to measure the convergence to a steady state at iteration m

$$\overline{R}(m) = \log \left(c_{norm} \sqrt{\frac{\sum_{i,j} (R^{\rho}_{i,j}(m))^2}{n_i n_j}} \right) \tag{4.49}$$

with n_i and n_j the number of cells in the i and the j direction, and the normalization constant c_{norm} chosen in such a way that $\overline{R}(0) = 0$. We routinely achieve convergence of 15 orders of magnitude, which means that the residuals are driven to machine zero. Throughout this dissertation we mean the base 10 logarithm when we use 'log' in convergence measures and on plots.

It would be possible to obtain convergence to a steady state more efficiently, and a whole scala of convergence acceleration methods of varying complexity could be tried out, ranging from simple local time stepping over implicit residual smoothing and multigrid, to fully implicit time integration [106, 161, 83, 22]. We have, however, not attempted any convergence acceleration technique for the simulations presented in this dissertation.

4.4 Enforcing the $\nabla \cdot \vec{B}$ constraint in MHD

The numerical enforcement of the $\nabla \cdot \vec{B}$ constraint is an important and much debated problem for numerical MHD codes. The $\nabla \cdot \vec{B} = 0$ condition is an initial condition, which is exactly preserved in time by the partial differential equations (PDEs) of MHD, but which is not always exactly preserved after discretization of the equations. Various strategies have been proposed to deal with the $\nabla \cdot \vec{B}$ constraint. We do not intend to give a full discussion of this subtle subject here, but we find it useful to give a brief overview of the various approaches to this problem.

The equations can be formulated in terms of a vector potential, which automatically assures divergence free magnetic fields. This approach is not always very practical and leads to difficulties near sharp gradients due to the presence of second order derivatives of the vector potential in the equations (see e.g. [33, 158]). Staggered grid approaches store different state variables on different positions of the grid, in such a way that the discrete time evolution of the magnetic field automatically conserves the divergence free condition (e.g. [33, 28, 158, 26]). They require, however, extra interpolations to be performed, and the interpolated magnetic field is not necessarily divergence free. Projection scheme approaches solve an elliptic equation in every time step and add a computed correction to the magnetic fields in order to achieve divergence free fields [10, 183, 129, 162]. Solution of the elliptic equation may take considerable computing time, and spurious oscillations can be generated, also in supersonic regions that should not be affected because they can theoretically not be reached by wave perturbations in the hyperbolic system.

Recently a new approach has been presented by Powell [118]. He proposes to add a source term proportional to $\nabla\cdot\vec{B}$ to the conservative form of the MHD equations (Eq. 3.12). Discretization of this Galilean invariant symmetrizable form of the equations with a source term [52, 118, 7] (see Sec. 4.2.2) leads to a stable numerical scheme. The $\nabla\cdot\vec{B}$ constraint is not enforced strongly and $\nabla\cdot\vec{B}$ can sometimes be substantially different from zero, but because of the presence of the source terms the dynamical effect of the $\nabla\cdot\vec{B}$ errors is largely neutralized and $\nabla\cdot\vec{B}$ errors can be shown to be advected away with the plasma flow. Although this approach seems to work well [118, 162, 100, 99, 124, 149, 151, 7, 22] and has several conceptual advantages over other techniques because of its simplicity and consistency with the hyperbolic nature of the MHD equations, not much can be found in the literature about rigorous validation of this approach, and consequently this approach is still heavily disputed in discussions often dominated by dogmatic arguments.

In this dissertation we generally employ the Powell source term technique to control $\nabla\cdot\vec{B}$. In the Sections above, we have described how we discretize the Powell source term. We have found that this technique leads to consistent solutions, and in the next Chapter we prove by formal grid convergence studies of magnetic flux conservation and other flow quantities, that this approach is valid, at least for the class of stationary flow problems that we consider. It is sometimes argued that for some problems, for which the conservation of magnetic flux up to very high accuracy is crucial, the source term technique could turn out to be insufficient. We are not aware of any clear examples which would confirm this, however.

For some flow problems, we have explicitly compared the Powell source term technique with a projection scheme technique. In the projection scheme approach, one calculates a correction $\vec{B}_{corr}=-\nabla\Phi$ to the magnetic field after every time step, such that $\nabla\cdot(\vec{B}+\vec{B}_{corr})=0$

or $\nabla \cdot (\nabla \Phi) = \nabla \cdot \vec{B}$. Discretization of this Poisson equation leads to a large linear system, and care has to be taken to formulate the boundary conditions of this Poisson equation consistently with the boundary conditions of the hyperbolic MHD system. We have discretized the Poisson equation as proposed in [129, 161]. As is shown in Chap. 9, the Powell approach and the projection approach produce very similar results. Only near a stagnation point have we found the Powell technique to be less accurate than projection. The Powell technique is much faster and deals with the $\nabla \cdot \vec{B}$ constraint in a more consistent hyperbolic way, whereas the projection technique introduces contamination of upstream flow regions, which in the case of our projection scheme implies upstream oscillations due to *mode decoupling*. The projection scheme technique is not easily parallelizable, because it involves the global solution of a linear system. For all these reasons we prefer to use the Powell technique for most of our simulations.

4.5 Implementation on massively parallel computers

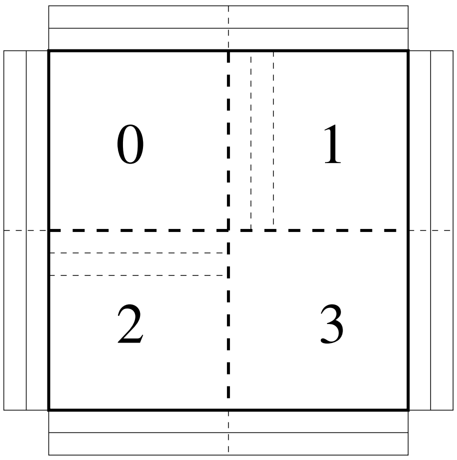

Figure 4.5: *Parallelization strategy to solve a flow problem in a given physical domain (thick solid) on four processors by dividing the domain in four sub-domains (thick dashed). The thin lines represent ghost cell layers.*

The algorithm described above has been implemented to run on *massively parallel* computers with *distributed memory.* Such computers consist of several processors connected by a fast network, and every processor has its own memory which can not directly be accessed by the other processors. The processors can communicate by sending *messages*. It is relatively straightforward to implement our numerical scheme with explicit time integration on a parallel computer, for instance using the Message Passing Interface (MPI) communication library [60]. Indeed, the algorithm is *inherently parallel* because for the update of a given cell only the values stored in its immediate neighbor cells are needed.

We illustrate our approach for the 2D case in Fig. 4.5. Suppose we want to calculate a flow problem in a given physical domain (thick solid) on four processors. We cover the physical domain by a logically rectangular structured grid, and add two layers of ghost cells (thin solid). We divide the domain in four equally-sized sub-domains (thick dashed) and associate one processor to every sub-domain. We store the flow variables of all the cells in sub-domain 0 in the memory of processor 0, and add two layers of ghost cells (thin dashed). Only the ghost cells for processor 0 are shown on the Figure. In every time step, the internal cells of sub-domain 0 can be updated by processor 0 with information available in the memory of processor 0. For the cells close to the boundary (thick dashed), we use the information in the ghost cells. After every time step, the ghost cells which correspond to physical boundaries (thin solid), are updated using the physical boundary conditions. The ghost cells corresponding to sub-domain boundaries, however, are updated by exchanging messages between neighboring processors. Every processor thus executes the same algorithm, which is very similar to the serial algorithm, except for the update of the ghost cells. Only the time step Δt has to be communicated globally in every iteration.

For an inherently parallel algorithm it is expected that a given problem executes two time faster on $2n$ processors than on n processors. We say that the theoretical *speedup* is 2 in this case. In practice, however, this theoretical speedup is rarely achieved, because for an increasing number of processors, more and more information has to be exchanged via messages for a given problem size, such that the *communication overhead* may become significant enough to reduce the speedup. The relative communication overhead is generally smaller for larger problems. Also, the influence of *serial bottlenecks* — small portions of the program which are not parallelized— becomes more significant for high processor numbers. In some cases the theoretical speedup can be exceeded, for instance because of hardware cache effects.

It is difficult to measure the execution speed of parallel programs in a consistent way, for instance because of variability in system load. In Fig. 4.6 we show the speedup for the simulation of a 2D bow shock flow with our parallel code. The theoretical speedup is given by the solid line. The dashed line with asterisks shows the speedup curve for

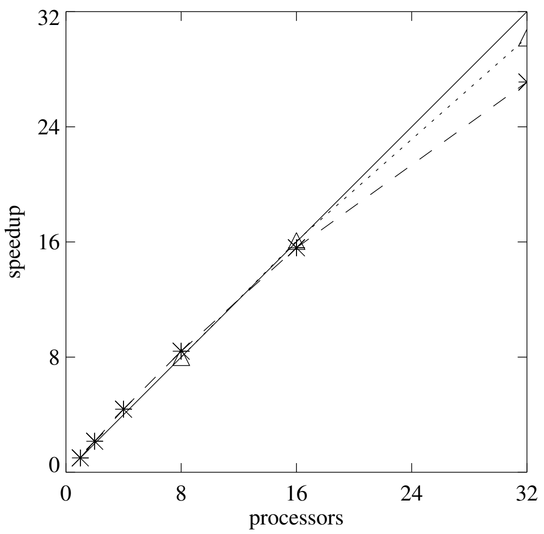

Figure 4.6: *Speedup for the simulation of a 2D bow shock flow with our parallel code on a relatively coarse grid* (80×80, *dashed with asterisks) and on a slightly finer grid* (160×160, *dotted with triangles). The theoretical speedup is given by the solid line.*

simulation on a relatively coarse grid (80×80). For $n_{proc} = 32$ the communication overhead starts to become important. For a slightly finer grid (160×160, dotted with triangles), however, the theoretical speedup is almost achieved. These curves show that our parallel code scales satisfactorily with the number of processors used. Good parallel scaling is an advantage of the explicit time integration strategy, and parallel codes based on implicit time integration scale generally less favorably [167] because matrix inversion is a global process.

Chapter 5

MHD model flows with shocks: characteristic analysis and grid convergence study

In this Chapter we present five model flows of increasing complexity belonging to the class of stationary 2D planar field-aligned MHD flows. The purpose of this Chapter is two-fold. First, we analyze the physical properties of these five flows using characteristic theory. This illustrates the characteristic theory derived in Chap. 3 and how this theory can be used to interpret MHD flows. Second, we derive grid convergence criteria for flows belonging to this class from characteristic theory, and grid convergence is demonstrated for the numerical simulation of the five model flows with our numerical MHD code using the Lax-Friedrichs scheme. It is investigated, by formal grid convergence studies of magnetic flux conservation and other flow quantities, whether the Powell source term approach to control the $\nabla \cdot \vec{B}$ constraint leads to correct results for this class of flows. This grid convergence study is important because it constitutes the validation of the numerical technique used in this dissertation. In the Appendix a model flow is presented which is not field-aligned, and it is discussed how grid convergence can be studied for this flow.

The main content of this Chapter will appear in [148].

5.1 Introduction

We present five field-aligned model flows, with increasing complexity in terms of wave features present in the flow: a fully smooth radial outflow, an expanding tube flow with a weak discontinuity, a wedge flow with a plane fast shock, a bow shock flow with a curved fast shock, and a nozzle flow with reflecting fast shocks. These model flows describe various nonlinear wave phenomena in their most basic form. The corresponding Euler flows have been described and used many times, but in the numerical MHD literature these basic flows have not received much attention yet. We show that this set of model problems is well suited to test grid convergence of MHD codes, and to study in detail how the behavior of numerical schemes changes when increasingly complex wave structures are present in the flow. Characteristic analysis reveals basic invariants of the flow, and these invariants can be used to test grid convergence as they lead to analytical solutions for some combinations of the flow variables if the incoming flow is uniform. Characteristic analysis also provides a clear insight into the physical properties of the model flows and into the stationary wave features present in the flows.

Although these five model problems exhibit quite a variety of flow features, they all belong to the sub-class of stationary planar 2D field-aligned MHD flows. Stationary flow has important applications [159, 55, 56, 150, 93, 53, 100] and any stationary 2D problem where ideal wall boundary conditions are present automatically leads to a solution where the magnetic field is aligned to the velocity field in the whole simulation domain. Hence the class of stationary field-aligned flow is an important class of MHD flows. One could even argue that 2D stationary flow problems in a finite domain with the magnetic field *not* aligned to the plasma flow are rare [61, 93, 53]. It is hard to define the boundary conditions consistently in that case. However, it is important to test MHD codes also for non-field-aligned flow. Therefore we include one model problem for which the magnetic field is not aligned to the plasma flow. This model flow is constructed in a special way; the fields are actually aligned in a rotating frame, but not in the rest frame. The analysis of this model problem is substantially different from the analysis of the field-aligned problems, so we prefer to present and analyze this non-field-aligned flow problem in an Appendix, while the grid convergence results for this flow are integrated in the discussion in the main text.

Although most model problems presented in the MHD literature only allow for qualitative comparison and cannot be used for formal accuracy testing, a very limited number of (mostly 1D) test problems have been described which allow for some degree of formal accuracy testing. Stone et al. [157, 158] present 1D model problems including stellar wind flows and obtain grid convergence which is satisfactory for most cases. Ryu et al. [129] show that the numerical dissipation of their scheme vanishes in second order as a function of grid resolution. Vanden Abeele and Deconinck [1] show how the conservation of magnetic flux in a flux tube can be used as a measure of improved accuracy as a function of grid resolution. Barth [7] obtains 'optimal' grid convergence for the $\nabla \cdot \vec{B}$ constraint in a continuous Prandtl-Meyer flow with an added magnetic field. The most interesting approach to grid convergence studies of MHD codes to date can probably be found in Linde's PhD thesis [99]. This author describes briefly a wedge flow and a stellar wind flow, and obtains satisfactory grid convergence. Although we have made use of some of the ideas presented in the above cited articles, the variety of problems presented in this Chapter, and especially the firm grounding of convergence study on the rigorous and complete characteristic analysis of the model flows, are new in the grid convergence study of MHD codes.

The numerical enforcement of the $\nabla \cdot \vec{B}$ constraint is an important and much debated problem for numerical MHD codes. In Chap. 4 a new approach to control $\nabla \cdot \vec{B}$ presented by Powell [118] has been described. In this Chapter we employ the Powell source term technique and we investigate by formal grid convergence studies of magnetic flux conservation and other flow quantities, if this approach is valid, at least for the class of stationary flow problems that we consider. Linde [99] and Barth [7] carry out a similar study and confirm the validity of the Powell source term approach, but their investigation is less complete and systematic than ours, and is carried out on adaptively refined Cartesian grids [99] or on unstructured grids [7], and not on the body-fitted structured grids used in our numerical approach.

In the next Section we present the five field-aligned model flows and their analysis in terms of stationary characteristics. In Sec. 5.3 we discuss grid convergence criteria. Sec. 5.4 contains the results of the grid convergence study of the five field-aligned model flows and one non-field-aligned model flow, which is presented and analyzed in the Appendix.

5.2 Characteristic analysis of model flows

5.2.1 Cylindrical expansion flow

The first model flow (Fig. 5.1) is a stationary cylindrical expansion flow in the domain ($r \in [1, 2]$, $\theta \in [0°, 30°]$) with planar symmetry ($\partial/\partial z \equiv 0$). All the figures shown in this Section represent simulation results obtained with our numerical MHD code using a second order Lax-Friedrichs scheme. In Fig. 5.1, a uniform superfast inflow with radial magnetic field is imposed at the $r = 1$ boundary, with $\rho = 1$, $p = 1$, $v_r = 3$ and $B_r = 1$. The sonic and Alfvénic inflow Mach numbers are thus $M = 3\sqrt{3}/\sqrt{5}$ and $M_A = 3$. The plasma is allowed to flow out freely at $r = 2$. For

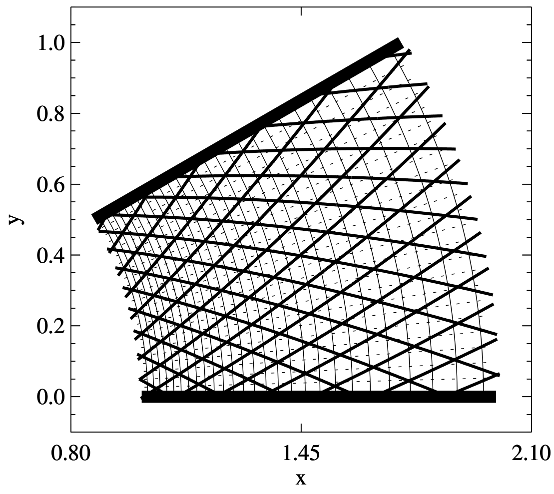

Figure 5.1: *The cylindrical expansion flow* (70 × 70 *grid). Density contours (thin solid) and streamlines (thin dotted) are shown. The streamlines are also magnetic field lines. The thick solid lines represent simulation domain boundaries with ideal wall symmetry. The flow is hyperbolic in the whole simulation domain. Two families of fast characteristics (thick solid) make equal angles with the streamlines. The flow is smooth in the whole simulation domain.*

$r > 1$, a stationary completely smooth radial expansion profile with variables only changing as a function of r results. This flow is thus strictly speaking a 1D flow.

In Fig. 5.1 and the subsequent figures, density contours are shown as thin solid lines, and streamlines as thin dotted lines. The streamlines are also magnetic field lines. The streamlines are threefold-degenerate characteristics with s, h_s and ρ/α as associated RIs. The thick solid lines represent simulation domain boundaries with ideal wall symmetry. Two families of fast characteristics (thick solid) make equal angles with the streamlines in hyperbolic regions.

As the inflow in Fig. 5.1 is uniform and every streamline thus carries the same values for the RIs s, h_s and ρ/α, those RIs are global invariants over the whole flow domain. $\nabla\cdot\vec{B} = 0$ and $B_r(1) = 1$ imply that $B_r(r) = 1/r$. The four state variables ρ, p, B_r and v_r can thus be determined as a function of r from $B_r(r) = 1/r$ and the three global invariants, which establishes the exact analytical solution of this flow problem. The flow is hyperbolic Hf1 (Fig. 3.4) everywhere, so the two (generalized) Mach characteristics exist. This flow is smooth everywhere, and this is the property which distinguishes it from the model flows to be presented next, which contain increasingly complex (weakly) discontinuous flow features. This flow is related to the stellar outflow problems discussed in [131, 157, 158, 99, 82]. By giving the flow a rotational component at the inflow boundary, we obtain a non-field-aligned model problem describing radial outflow from a rotating object [131, 82]. This rotating outflow problem is described and analyzed in the Appendix.

5.2.2 Expanding tube flow

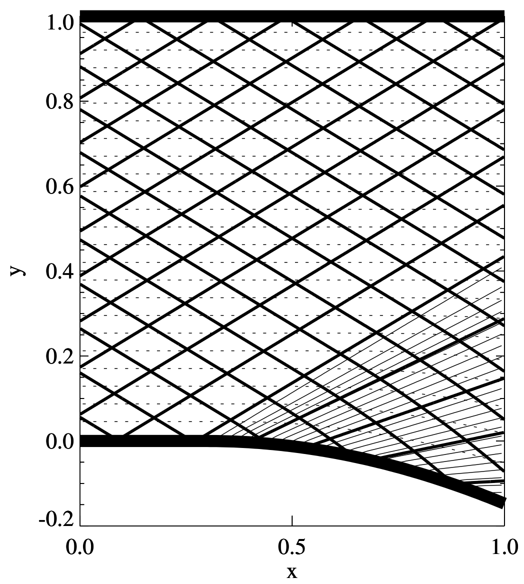

Figure 5.2: *The expanding tube flow (75 × 125 grid). The flow is hyperbolic in the whole simulation domain. A weak discontinuity detaches from the lower wall where the tube starts to expand. This weak discontinuity is a fast characteristic, and is followed by a simple wave rarefaction region. One family of characteristics consists of straight lines in the simple wave region. The simple wave is not centered.*

In Fig. 5.2 we show a stationary expanding tube flow in the domain $(x \in [0,1], y \in [y_0(x), 1])$, with $y_0(x) = 0$ for $x \in [0, 0.3]$ and $y_0(x) = -1 + \cos(\pi/4 * (x - 0.3))$ for $x \in [0.3, 1]$. A uniform superfast horizontal inflow with horizontal magnetic field is imposed at the $x = 0$ boundary, with $\rho = 1$, $p = 1$, $v_x = 8$ and $B_x = 4$. The sonic and Alfvénic inflow Mach numbers are thus $M = 8\sqrt{3}/\sqrt{5}$ and $M_A = 2$. The plasma is allowed to flow out freely at $x = 1$, where the flow remains superfast. At $y = y_0(x)$ and $y = 1$ we impose ideal wall symmetry conditions. A stationary expanding flow results, as shown by the density contours of Fig. 5.2.

The flow is hyperbolic Hf2 (Fig. 3.4) in the whole simulation domain, such that two families of fast characteristics exist. As long as the lower wall is straight, the flow is uniform. When the wall starts to curve $(x = 0.3)$, this acts as a (wave-like) perturbation, which can only propagate downstream along the characteristics. This means that the flow is non-uniform only below the upward fast characteristic which originates from the lower boundary at $(x = 0.3)$ with an angle of $\theta = 31.276°$, as can be calculated from Eq. (3.68). This fast characteristic thus separates a uniform flow region from a perturbed region, and is thus necessarily a *weak discontinuity* [20, 21]. At a weak discontinuity, the spatial derivative of the flow variables in a direction perpendicular to the weak discontinuity characteristic, is discontinuous. However, the flow variables themselves are continuous, and the entropy is thus also conserved on streamlines across weak discontinuities. A weak discontinuity thus detaches from the lower wall where the tube starts to expand.

This weak discontinuity is followed by a simple wave [20, 21, 151] rarefaction region. This rarefaction is called a (stationary) simple wave because it carries a variation in only one MHD wave family. It is a property of simple waves that one family of characteristics consists of straight lines, and that the flow variables are constant along these characteristics, which makes the characteristics parallel to the contour lines of flow variables, e. g. the density, as can be seen in Fig. 5.2. In the present flow, these straight line characteristics do not converge in one point, so this simple wave is not centered. Centered simple waves exist in rarefaction flows around sharp corners, like the well-known Prandtl-Meyer flow [7]. Such a sharp corner is a geometrical singularity in the boundary and this can complicate grid convergence studies, as is explained in the next Section. For this reason, we have chosen to present model flows with smooth boundaries in this Chapter. A simple wave, also if it is non-centered, can be described mathematically as a function of only one spatial parameter, so strictly speaking this flow is 1D. As the inflow is uniform, every streamline throughout the whole domain carries the same values for RIs h_s and ρ/α, and also for s as the flow does not contain strong discontinuities. These RIs are thus global invariants over the whole flow domain.

This flow contains a weak discontinuity, and this is the property which distinguishes it from the fully smooth model flow discussed in Sec. 5.2.1.

5.2.3 Wedge flow

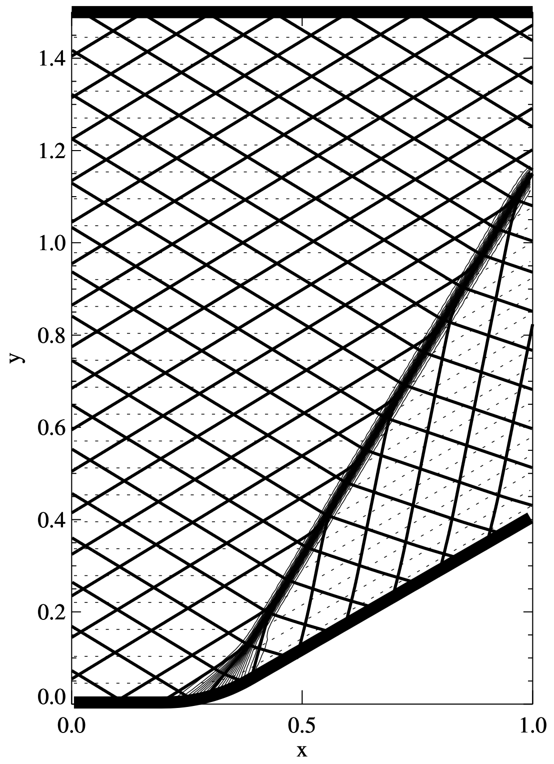

Figure 5.3: *The wedge flow (*100×200 *grid). The flow is hyperbolic in the whole simulation domain. A plane fast MHD shock is formed where characteristics start to intersect near the lower wall. This discontinuity stretches out upwards in a straight line.*

In Fig. 5.3 we show a stationary wedge flow in the domain ($x \in [0, 1]$,

$y \in [y_0(x), 1.5]$). The lower simulation domain boundary has the form of a wedge with angle $\theta = 30°$.

A uniform superfast horizontal inflow with horizontal magnetic field is imposed at the $x = 0$ boundary, with $\rho = 1$, $p = 1$, $v_x = 8$ and $B_x = 4$. The sonic and Alfvénic inflow Mach numbers are thus $M = 8\sqrt{3}/\sqrt{5}$ and $M_A = 2$. At $y = y_0(x)$ and $y = 1$ we impose ideal wall symmetry conditions. The wedge geometry causes the formation of a fast MHD shock, as shown by the accumulation of density contours in a solid line. At the shock, the magnetic field lines are refracted away from the shock normal in going from upstream to downstream, which shows that this is a fast MHD shock. The plasma is allowed to flow out freely at $x = 1$, where the (normal) flow is superfast.

As the inflow is uniform, every streamline throughout the whole domain carries the same values for h_s and ρ/α, but not for s since the flow does contain a strong discontinuity where the entropy increases discontinuously. Only the RIs h_s and ρ/α are thus global invariants over the whole flow domain. The flow is hyperbolic Hf2 (Fig. 3.4) everywhere, so the two (generalized) Mach characteristics exist.

We have to remark that the two straight 'legs' of the wedge could be connected at $x = 0.3$, but that we have again chosen for a smooth boundary with the wedge corner smoothed out by a circular profile. The lower boundary is described by $y_0(x) = 0$ for $x \in [0, 0.2]$ and $y_0(x) = \tan(30°) * (x - 0.3)$ for $x \in [0.3 + 0.1 * \cos(30°), 1]$. A segment of a circle with center point $(0.2, 0.1 * (1 + \cos(30°))/\sin(30°))$ and radius $r = 0.1 * (1 + \cos(30°))/\sin(30°)$, which is tangent to the two 'legs' of the wedge, then replaces the corner singularity of the wedge with a smooth profile. Close to the lower boundary our wedge flow with smooth boundaries is thus slightly different from a wedge flow with a sharp corner, and one can see a small compressional wave region with converging characteristics in the corner region on Fig. 5.3 [160], but above the point where those characteristics converge and the shock is formed, this flow is identical to the wedge flow with a sharp corner.

The wedge flow described in this Section contains a plane strong discontinuity, and this is the property which distinguishes it from the flows discussed earlier. MHD wedge flows have also been discussed in [99].

5.2.4 Bow shock flow

In Fig. 5.4 we show a stationary bow shock flow in the domain ($r \in [r_0(\theta), 0.125]$, $\theta \in [90°, 180°]$), with $r_0(\theta) = 0.75 - 0.45\,(\theta - 90)/90$. The bow shock is formed by the obstruction of a uniform incoming flow by a rigid perfectly conducting circular cylinder with $r = 0.125$. A uniform superfast horizontal inflow with horizontal magnetic field is imposed at

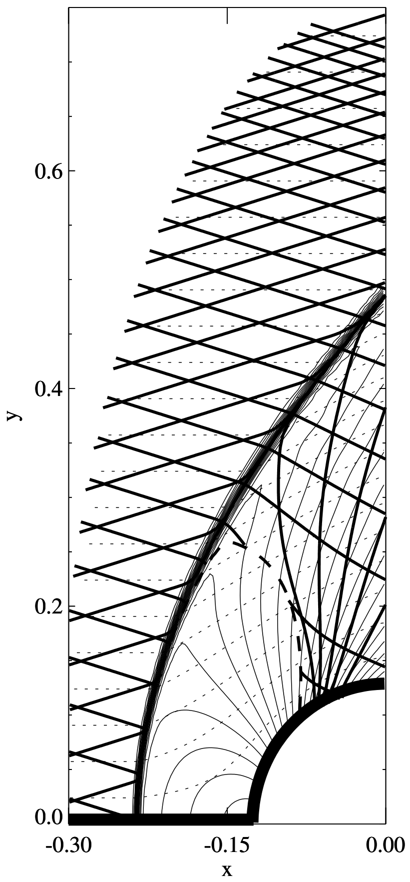

Figure 5.4: *The bow shock flow (80×80 grid). A fast MHD bow shock is formed in front of the cylindrical obstacle. The flow is hyperbolic in front of this bow shock, and also behind the shock front sufficiently far upward from the horizontal x-axis. The region behind the shock front and close to the horizontal x-axis, is an elliptic region, in which real fast characteristics do not exist. This elliptic region is separated from the upward hyperbolic region by the $M = 1$ contour (dashed).*

the $r = r_0$ boundary with $\rho = 1$, $p = 0.2$, $v_x = 2$, and $B_x = 0.1$. The sonic and Alfvénic inflow Mach numbers are thus $M = 2\sqrt{3}$ and $M_A = 20$. At $y = 0$ and $r = 0.125$ we impose ideal wall symmetry conditions. The plasma is allowed to flow out freely at $x = 0$, where the (normal) flow is superfast. A curved fast MHD bow shock is formed, as shown by the accumulation of density contours. At the shock, the magnetic field lines are refracted away from the shock normal in going from upstream to downstream, which shows that this is a fast MHD shock.

As the inflow is uniform, every streamline throughout the whole domain carries the same values for h_s and ρ/α, but not for s as the flow does contain a strong discontinuity. Only the RIs h_s and ρ/α are thus global invariants over the whole flow domain. The flow is hyperbolic Hf1 (Fig. 3.4) in the upstream region and in the part of the downstream region above the dashed line (the $v^2 = c^2$ or $M = 1$ contour). In these hyperbolic regions the two (generalized) Mach characteristics exist. The downstream region below the $M = 1$ contour is of elliptic type Efs1, and real characteristics do not exist in this region.

The bow shock flow described in this Section contains a curved strong discontinuity and an elliptic region, and these properties distinguish it from the flows discussed earlier. MHD bow shock flows have been discussed before in [1, 150, 161, 7, 151]. In Chap. 6 we describe the characteristic analysis of a complex MHD bow shock flow which contains interacting fast and intermediate shocks and tangential discontinuities, and several alternating regions of the different hyperbolic and elliptic types of Fig. 3.4.

5.2.5 Nozzle flow

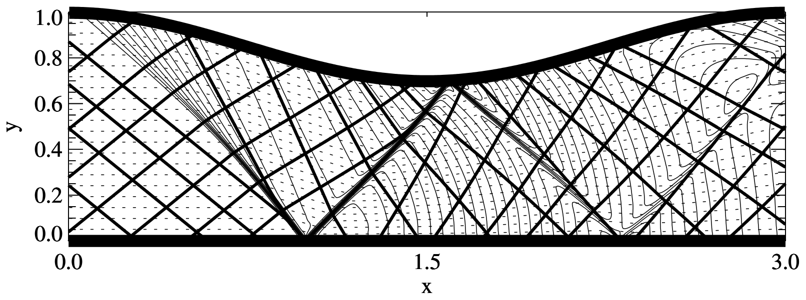

Figure 5.5: *The nozzle flow (*480×160 *grid). The flow is hyperbolic in the whole simulation domain. A fast MHD shock is formed where characteristics start to intersect. This shock is reflected by the lower wall, by the upper wall, and again by the lower wall, before it leaves the simulation domain. Throughout these reflections, the shock front remains nearly plane and the shock remains of the fast type.*

In Fig. 5.5 we show a stationary nozzle flow in the domain ($x \in [0,3]$, $y \in [0, y_1(x)]$), with $y_1(x) = 1 - 0.3 * \sin^2(\pi/3 * x)$. A uniform superfast horizontal inflow with horizontal magnetic field is imposed at the $x = 0$ boundary with $\rho = 1$, $p = 1$, $v_x = 3.5$, and $B_x = 2$. The sonic and Alfvénic inflow Mach numbers are thus $M = 3.5\sqrt{3}/\sqrt{5}$ and $M_A = 1.75$. At $y = 0$ and $y = y_1$ we impose ideal wall symmetry conditions. The plasma is allowed to flow out freely at $x = 3$, where the (normal) flow is superfast. A fast MHD shock is formed near the upper wall because of the curvature of this wall, as shown by the accumulation of density contours. At the shock, the magnetic field lines are refracted away from the shock normal in going from upstream to downstream, which shows that this is a fast MHD shock. This shock reflects several times from the rigid ideal walls $y = 0$ and $y = y_1(x)$.

As the inflow is uniform, every streamline throughout the whole domain carries the same values for h_s and ρ/α, but not for s as the flow does contain strong discontinuities. Only the RIs h_s and ρ/α are thus global invariants over the whole flow domain. The flow is hyperbolic Hf2 (Fig. 3.4) everywhere, and two (generalized) Mach characteristics exist.

The nozzle flow described in this Section contains strong discontinuities which are reflected by ideal walls, which distinguishes it from the flows discussed earlier. MHD nozzle flows have been discussed before in [1].

5.3 Grid convergence criteria

In this Section we define grid convergence criteria for stationary model flows, but first we discuss what kind of convergence order we can expect for model flows simulated with the numerical techniques discussed in Chap. 4.

Formal grid convergence

The basic idea of grid convergence is that for smooth flow (see below), some measure of the error of the simulation result should decrease as a function of the resolution with an order which is the formal order of accuracy of the scheme. Formal Taylor series expansion of the numerical schemes presented in Chap. 4 would show that for a stationary solution

$$E = ||\mathbf{U} - \overline{\mathbf{U}}|| = c\ (1/n)^p, \tag{5.1}$$

with $\mathbf{U}$ the exact solution, $\overline{\mathbf{U}}$ the numerical solution, E the error in some norm, c a constant, n the number of cells in a certain direction — where it is understood that the resolution is changed proportionally in all directions —, and p the order of the method (1 or 2 for the schemes discussed in Chap. 4). On logarithmic axes this would lead to grid convergence curves which are straight lines with slope 1 or 2

$$\log(E) = \log(c) - p\log(n). \tag{5.2}$$

All state variable quantities are expected to be calculated with the accuracy of the scheme. It is important to remark here, however, that the $\nabla \cdot \vec{B}$ quantity ('magnetic flux production per unit volume') with discretization given by Eq. 4.30, is a sum of derivatives of the magnetic field state variables, and can thus be expected to converge more slowly than the state variables, in the worst case with one order less [33, 7]. Probably for this reason, Linde [99] proposes to measure magnetic flux conservation in a different way. The following alternative quantity

$$F_{i,j} = \frac{\sum_{k=1}^{4} \vec{B}_k \cdot \vec{n}_k \, \Delta l_k}{\sum_{k=1}^{4} \Delta l_k}, \tag{5.3}$$

is a measure of magnetic flux conservation ('flux production per unit length') which should converge at least with the same order as the state variables. We investigate how these two measures of flux conservation behave for the numerical simulation of our five model flows.

The actually observed convergence order for a numerical simulation can be lower than the formal order of accuracy of the scheme because of several reasons. We discuss in short five possible reasons of convergence degradation. The first two reasons are related to the analytical properties of fluid flows, viz. to the *regularity* of flows. The latter three reasons for convergence degradation are more related to the details of the numerical scheme.

First, when the analytical solution to a flow contains (weak) discontinuities, then the derivatives in the above mentioned Taylor expansion do not exist everywhere, which means that the convergence order result derived using the Taylor expansion is not valid. In general it can be expected that the convergence order for a numerical scheme is lower for a solution containing discontinuities. Leveque [90] gives an example where the convergence order of an approximation degrades by 0.5 for a solution containing a discontinuity.

Second, near geometrically singular points on boundaries, the analytical solution to the flow problem is generally not smooth, with similar consequences of convergence order degradation [135]. These effects can be reduced by choosing smooth boundaries, as we have done for all our model flows, but even then the finite grid resolution leads to singular corners at curved boundaries. The effects of these singularities can be reduced by a careful geometrical refinement of the grid near the boundary [135]. Barth [7] reports improved grid convergence if interpolation at the boundary interfaces is done with higher order polynomials than inside the domain (so-called *iso-parametric* boundaries), in the context of finite element methods which allow for more flexibility than our finite volume schemes.

Third, the choice of numerical flux function seems to be important for the errors induced at boundaries. For instance, it is well-known that the Roe scheme can lead to the problem of *wall-heating* at perfect wall boundaries [91]. It seems that our choice of the Lax-Friedrichs flux function in general performs better in such situations, and our grid convergence results seem generally to be satisfactory. We have thus not adopted the strategy to exclude physical cells close to the boundaries from our error norm calculations [157, 158], because we think that this process is somewhat artificial and arbitrary, and because we want to prove grid convergence of our numerical scheme with the boundary treatment included. We have to admit, however, that the errors are often large not only at discontinuities, but also at the boundaries.

Fourth, near discontinuities our second order scheme switches to first order accuracy due to the action of the nonlinear limiter. In error norms calculated over the whole simulation domain, these local first order errors dominate the second order errors in smooth parts of the flow, resulting in convergence degradation to first order.

Fifth, simulations on highly distorted grids, with angles in cells substantially deviating from $90°$ or with cells highly elongated, may show degraded convergence rates [164].

Practical grid convergence criteria

For the model flows we propose in this Chapter, the analytical solution is generally not known. How can we carry out grid convergence studies then? We do not engage in the use of 'self-convergence' criteria [157, 158], because they do not easily lead to rigorous conclusions.

But even when the analytical solution is not known, we can formulate grid convergence criteria. In general we can distinguish three classes of grid convergence criteria.

The first class of criteria follows directly from the divergence nature of the steady conservation law (Eq. 3.12 with vanishing time derivative) and the $\nabla \cdot \vec{B}$ constraint. These laws basically state that the divergence of a flux vanishes. This leads to grid convergence criteria in two ways.

First, over the whole physical domain, the integrated form of the divergence law shows that the line integral of the normal flux through the circumference of the physical domain has to vanish. For instance, in a steady flow the net flux of density (the momentum) through the boundaries has to vanish, and numerically this net flux has to converge to zero as a function of resolution. This, however, merely checks global conservation and only gives a very global measure of accuracy as internal errors can cancel out. This grid convergence measure is not further exploited in this Chapter.

Second, when the flux vectors are aligned with a boundary at two opposing boundaries of the simulation domain, and the boundaries thus form *flux tubes*, then the flux through any line connecting the two boundaries has to be the same. This can be tested along lines consisting of cell interfaces. We use this observation extensively to verify if the magnetic and momentum fluxes through sections of flux tubes are constant along the flux tube. This leads to a more local measure of accuracy. Suppose for instance that the boundaries below $j = 1$ and above $j = n_j$ are perfect walls, then we can calculate the (magnetic or momentum) flux $\Phi_{i+1/2}$ through every line formed by interfaces between cells with equal coordinates i and $i + 1$, using the reconstructed $\mathbf{U}_l$ and $\mathbf{U}_r$ in the average $(\mathbf{U}_l + \mathbf{U}_r)/2$ at every interface, and with i running from 0 to n_i. Then an L1 error measure can be defined as

$$E_\Phi^{B,m} = \frac{\sum_{i=0}^{i=n_i} \text{abs}(\Phi_{i+1/2} - \Phi_{theor})}{n_i + 1} \tag{5.4}$$

with Φ_{theor} being the known theoretical value of the flux, and E_Φ^B and E_Φ^m the magnetic and momentum flux error measure respectively. Flux conservation criteria like this have been used before to investigate the accuracy of MHD simulations as a function of resolution [157, 158, 1, 99].

The second class of grid convergence criteria follows from the rigorously defined characteristic properties of the class of flows under consideration, and leads to measures of true local grid convergence in every cell of the simulated flow. There can be up to four global invariants for stationary planar field-aligned flow, as follows from characteristic analysis. The angle θ between the magnetic and the velocity fields has to vanish everywhere. In the case of uniform inflow, Riemann invariants ρ/α and h_s are global invariants. If the flow is additionally smooth, then Riemann invariant s is a fourth global invariant. An L1 error measure for these invariants I can be defined as

$$E_I = \frac{\sum_{i,j} \text{abs}(\overline{I}_{i,j} - I_{theor})\,\Omega_{i,j}}{\sum_{i,j} \Omega_{i,j}} \tag{5.5}$$

with I_{theor} being the known theoretical value of the invariant. Note that we actually calculate the difference between the cell-averaged numerically calculated values of the invariant and the cell-average of the theoretical value of the invariant (which, of course, is the invariant itself). Global grid convergence criteria based on characteristic invariants have to our knowledge not been used before to investigate the accuracy of 2D MHD simulation results as a function of resolution. The s and h_s quantities keep their invariant properties in stationary Euler flow, so this type of grid convergence study can also be carried out for that case, as is well-known. Finally, we should mention that $\nabla \cdot \vec{B}$ should vanish in theory for every MHD flow, so this can easily be tested using the same expression to calculate the error.

The third class of grid convergence criteria follows from the RH jump relations. If sufficient information is available in terms of imposed upstream flow conditions and geometrical constraints, then the remaining unknown values can be calculated from Eq. 3.75 with high accuracy, and in some cases analytical solutions can be found. These values can then be compared with the values resulting from full 2D numerical simulations of the flow, and grid convergence can be investigated.

In practice, we measure the simulation error using the above given expressions E as a function of the number of grid cells in a certain direction n, and determine the numerical convergence order by a least-squares fit of the $\log E$–$\log n$ curve with generally four data points.

5.4 Grid convergence study of model flows

In this Section we discuss numerical simulation aspects of the model flows presented in Sec. 5.2 and the non-field-aligned flow presented in the Appendix, and we present grid convergence results obtained with the criteria discussed in Sec. 5.3.

5.4.1 Numerical simulation aspects

The steady state simulation results shown in Figs. 5.1–5.5 were obtained via time-accurate relaxation starting from uniform initial states. Fig. 5.6 shows the convergence of the logarithm of the density residual $\overline{R}(m)$ (Eq. 4.49) towards a steady state in function of the number of time steps. We can observe that the steady state convergence of our numerical scheme is extremely well behaved. For all simulations we obtain convergence up to machine accuracy both using the first order scheme (solid) and the second order scheme (dash-dotted). The number of time steps needed to obtain convergence is mostly similar for the first and the second order schemes. We used the same CFL number for the first and the second order scheme. The computational cost per time step is, however, about three times higher for the second order scheme. The number of time steps is much higher for the bow shock flow than for the other flows, because of the low velocities in the elliptic region near the stagnation point.

Fig. 5.7 shows the simulation grids used for the numerical results presented in this Chapter. The grids are nearly uniform and the grid cells are mostly quite regular, except perhaps for some strongly deformed cells in the bow shock grid. For the cylindrical expansion problem and the

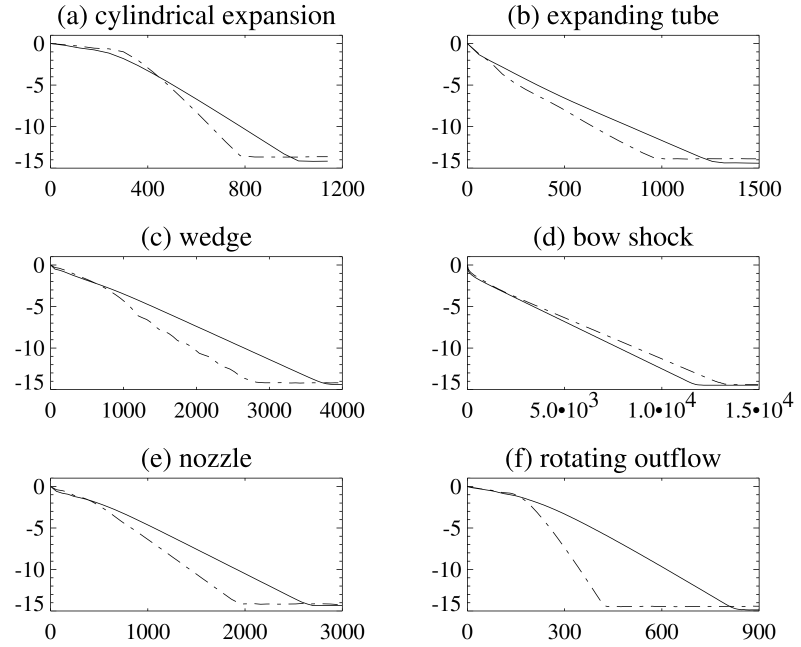

Figure 5.6: *Convergence of the logarithm of the density residual towards a steady state, as a function of the number of time steps. First order (solid) and second order (dash-dotted) numerical schemes.*

rotating outflow problem the grid convergence has been studied making use of simulations on 40×40, 50×50, 60×60 and 70×70 grids. The expanding tube problem has been simulated on 30×50, 45×75, 60×100 and 75×125 grids, and the wedge problem on 40×80, 60×120, 80×160 and 100×200 grids. Grid convergence for the bow shock flow has been studied making use of simulations on 20×20, 40×40, 60×60 and 80×80 grids, and the nozzle simulations were performed on 48×16, 72×24, 96×32 and 120×40 grids.

5.4.2 Grid convergence results for flux conservation

The cylindrical expansion flow, the expanding tube flow, the wedge flow and the nozzle flow all have opposed simulation domain boundaries which are ideal walls and thus define a flux tube. We can study grid convergence of the magnetic and momentum flux through these flux tubes. The rotating outflow problem described in the Appendix has the property of radial conservation of magnetic and momentum flux. Fig. 5.8 shows the

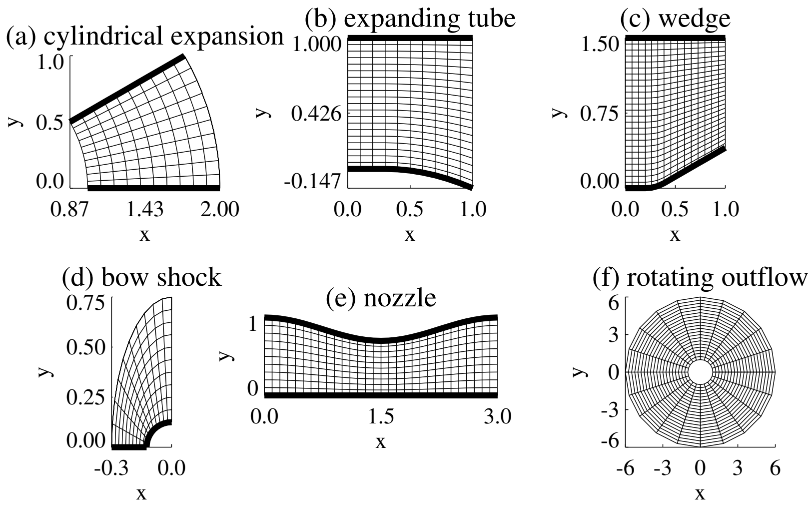

Figure 5.7: *Finite volume simulation grids. Successive conformal refinements of these grids have been used for grid convergence study.*

grid convergence behavior of the fluxes for these five test cases.

The first row of the figure shows the normalized magnetic flux through vertical or radial sections as a function of the vertical or radial coordinate. Every panel contains eight curves, four for the first order scheme (dotted) for increasing grid resolution, and four for the second order scheme (dashed). We see that in all cases the normalized magnetic flux approaches the value of unity nicely, and that the flux conservation is much more accurate for the second order results than for the first order results.

The second row of the figure shows the normalized momentum flux through the vertical or radial sections. Every panel again contains eight curves, four for the first order scheme (dash-dotted) for increasing grid resolution, and four for the second order scheme (dash-dot-dot-dotted). We again see that in all cases the normalized momentum flux approaches the value of unity nicely, and that the flux conservation is much more accurate for the second order results than for the first order results.

The shape of the momentum flux curves is generally similar to the shape of the magnetic flux curves, and this is no surprise for field-aligned flow. Only for the non-field-aligned rotating outflow (Fig. 5.8e) are the curves markedly different in shape.

The third row shows the ten logarithm of the L1 norm of the errors of the magnetic and momentum flux curves, as a function of the grid

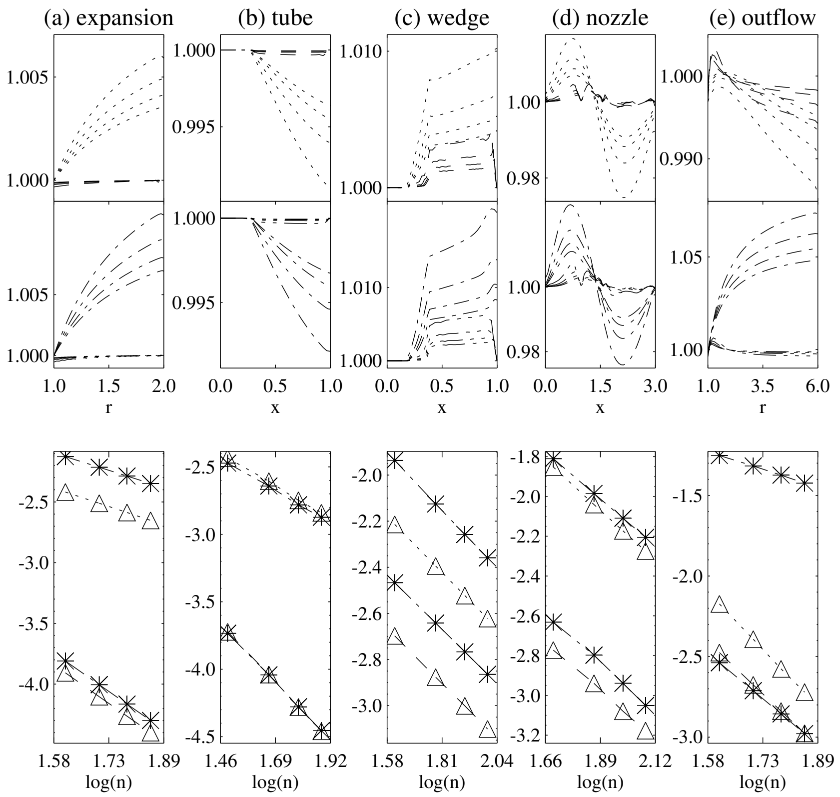

Figure 5.8: *Grid convergence behavior of the magnetic and momentum flux conservation for five test cases. The first row shows the normalized magnetic flux through vertical or radial sections as a function of the vertical or radial coordinate for four different grid resolutions, both for the first order scheme (dotted) and the second order scheme (dashed). The second row shows the normalized momentum flux profiles for the first order scheme (dash-dotted) and the second order scheme (dash-dot-dot-dotted). The third row shows the ten logarithm of the L1 norm of the errors of the magnetic flux (triangles, first order dotted and second order dashed) and momentum flux (asterisks, first order dash-dotted and second order dash-dot-dot-dotted), as a function of the grid resolution (ten logarithm of* n*, the number of grid cells in the* i *direction).*

resolution (ten logarithm of n, the number of grid cells in the i direction). The magnetic flux conservation for the first order scheme is indicated by a dotted line with triangles, and by a dashed line with triangles for the second order scheme. The momentum flux conservation for the first order scheme is indicated by a dash-dotted line with asterisks, and by a dash-dot-dot-dotted line with asterisks for the second order scheme. We observe that in all cases the convergence curves follow a straight line, which indicates convergence with a well-defined order. The fitted slope coefficients for these lines are presented in Table 5.1.

The cylindrical expansion flow and the expanding tube flow are both smooth flows. The fluxes both converge with the expected slope close to -1 for the first order scheme, and close to -2 for the second order scheme. The wedge flow contains a strong discontinuity, and due to the action of the nonlinear limiter, the second order scheme converges only with a slope close to -1, like the first order scheme. The second order results are more accurate, however. The nozzle flow contains shocks as well, and also shows first order convergence both for the first and the second order scheme. The rotating outflow problem is smooth, and shows the expected second order convergence for the second order scheme. For the first order scheme, the momentum flux converges with an order which is lower than first order, but, remarkably, the magnetic flux converges with slope -2.3.

The main conclusions to be drawn from this grid convergence study for magnetic and momentum flux conservation, is that the experimentally obtained grid convergence orders are very close to the theoretically expected orders. The numerical schemes seem thus to behave extremely well. The excellent conservation of magnetic flux indicates strongly that the Powell source term approach to control $\nabla \cdot \vec{B}$ produces valid results.

5.4.3 Grid convergence results for global invariants

Table 5.1 contains the fitted slopes of the grid convergence curves for the global invariants entropy s, stagnation enthalpy h_s, ρ/α and θ. The entropy s is not a global invariant when shocks are present. In the case of the rotating outflow, the invariants are entropy s, Bernoulli function h, angular momentum L and electric field E_z, as discussed in the Appendix. Note that no error slope has been given for the grid convergence of the angle θ between the magnetic and velocity field for the case of the cylindrical expansion. In the initial condition the fields are aligned perfectly up to the machine error induced by a rotation, and this property is conserved throughout the time relaxation as the flow is perfectly radial. These rotational machine errors are very small — much smaller than the errors in the other global RIs — and do of course not depend on resolution, such that for this case grid convergence of θ is not relevant. The *first order scheme* produces grid convergence orders which are generally close to the theoretically expected slope of -1. For some model problems

Table 5.1: *Grid convergence order of several invariant quantities for the model flows discussed in this Chapter. The fitted slope of the ten logarithm of the L1 norm of the error as a function of the ten logarithm of the number of grid cells in the i direction, is shown. For the values marked with an asterisk, the rotating outflow grid convergence is measured using slightly different invariant quantities than for the other flows. The results show that the presence of discontinuities (in the wedge, bow shock, and nozzle flows) consistently degrades the convergence for the second order numerical scheme to first order due to the action of the nonlinear limiter. Analytical singularities or numerical inaccuracies at boundaries and grid distortion may further degrade the convergence. Such additional convergence degradation can be observed for the values that are italicized. Overall, a satisfactorily consistent grid convergence behavior is obtained.*

	expans.	**tube**	**wedge**	**shock**	**nozzle**	**outflow**
1st order						
Φ_B	-0.98	-1.05	-1.04		-1.08	-2.30
Φ_m	-0.93	-1.04	-1.08		-1.01	*-0.72*
s	-0.93	-0.87				-0.81
h_s	-0.82	-1.04	-1.15	-0.86	-0.91	*-0.58**
ρ/α	-0.87	-0.99	-0.97	*-0.72*	*-0.70*	-0.82*
θ		-0.99	-1.06	*-0.60*	*-0.73*	-0.84*
$\nabla \cdot \vec{B}$	-0.98	-0.92	-0.79	-0.59	-0.90	-1.33
F	-1.98	-1.92	-1.79	-1.55	-1.90	-2.36
2nd order						
Φ_B	-2.06	-1.90	-1.03		-1.04	-2.10
Φ_m	-2.06	-1.86	-1.02		-1.07	-1.85
s	-1.96	-1.74				*-1.28*
h_s	-1.91	*-1.10*	-1.01	-0.90	-0.87	-1.92*
ρ/α	-2.07	*-1.44*	-0.82	-1.07	-0.97	-1.71*
θ		-1.78	-0.99	-0.85	-1.01	-1.89*
$\nabla \cdot \vec{B}$	-1.96	-1.38	-0.22	-0.55	-0.42	-1.79
F	-2.95	-2.39	-1.22	-1.53	-1.43	-2.83

and for some invariants, the convergence order is smaller than 1. In this case the slopes are shown in *italics*, where we have (arbitrarily) put the limit of expected behavior at 80% of the theoretical values. Convergence degradation seems to be most severe for the bow shock and nozzle flows, and detailed study of the simulation results shows that this can mainly be attributed to the interaction of the shocks with the boundaries. Overall, however, the results are quite consistent with the order of the scheme. For the smooth flow problems, the *second order scheme* produces grid convergence orders which are generally close to the theoretically expected slope of -2, except for the values in italics. For the expanding tube flow, careful study shows again that convergence degradation can be attributed to inaccuracies at the (not perfectly smooth) boundary. The model problems with shocks show consistent first order convergence behavior, again due to the limiter.

Table 5.1 also shows grid convergence slopes for $\nabla \cdot \vec{B}$ and Linde's quantity F. For the first order scheme, we see that $\nabla \cdot \vec{B}$ converges with an order not too far from the expected convergence order for state variables, although it is a quantity obtainable from the magnetic field through derivation. The reason may be that the numerical scheme treats $\nabla \cdot \vec{B}/\rho$ as a passive scalar [118]. Linde's quantity F indeed converges one order faster than $\nabla \cdot \vec{B}$. The second order scheme produces satisfactory grid convergence behavior for the $\nabla \cdot \vec{B}$-related quantities as well, except for the wedge, the bow shock and the nozzle. Again the convergence degradation there can be traced back to errors at (not perfectly smooth) boundaries and shock-boundary interactions. Our results on $\nabla \cdot \vec{B}$ convergence for a broad set of model problems confirm the results reported by Linde [99] and Barth [7] for smaller sets of model problems.

To conclude this section about the grid convergence study for global invariants, we can say that the experimentally obtained grid convergence behavior is satisfactorily consistent with the theoretically expected behavior. Some convergence degradation can be observed at (not perfectly smooth) boundaries and shock-boundary interactions, but this is not unexpected, given the discussion on convergence degradation in Sec. 5.3. The fluxes discussed in the previous Section, which can be considered as one-time-integrated quantities, seem to be less sensitive to boundary effects. The results discussed in this Section thus confirm again the validity of the numerical approach and the source term technique to control $\nabla \cdot \vec{B}$.

5.4.4 Grid convergence results for Rankine-Hugoniot relations

For the wedge flow, the inflow quantities and the wedge angle completely determine the angle and the downstream quantities of the fast MHD shock. The algebraic equations of the MHD RH relations 3.75

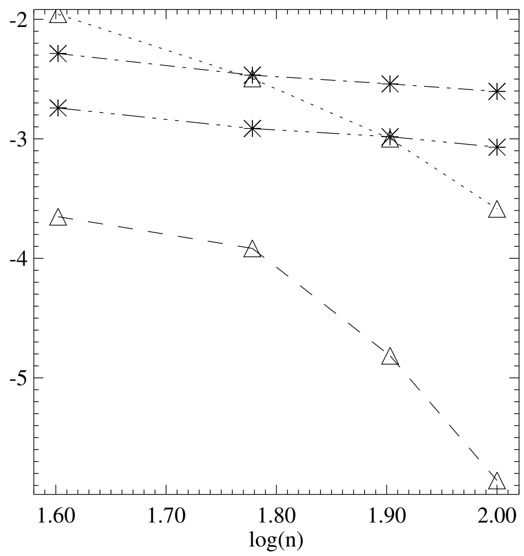

Figure 5.9: *The wedge flow. Grid convergence of the Rankine-Hugoniot relations. Ten logarithm of the relative errors of the downstream density and velocity at ($x = 0.96, y = 0.87$), as a function of the grid resolution. The density (first order scheme, dotted, triangles, and second order scheme, dashed, triangles) does converge, but not with a well-defined order. The velocity converges with $a = -0.79$ (first order scheme, dash-dotted, asterisks), and with $a = -0.80$ (second order scheme, dash-dot-dot-dotted, asterisks).*

can be solved numerically up to a very high accuracy, using for instance standard iterative methods provided in software for symbolical calculations. Following such a procedure, we have obtained the (nearly) exact downstream density and velocity field magnitude to be $\rho = 2.00060295$ and $v = 7.04956575$. In Fig. 5.9 we investigate grid convergence of the Rankine-Hugoniot relations. The ten logarithm of the relative errors of the downstream density and velocity at ($x = 0.96, y = 0.87$) is shown, as a function of the grid resolution. First of all we can say that our numerical scheme calculates a solution which closely matches the RH relations. The errors are 1% and lower. The velocity seems to converge linearly with a slope close to the theoretically predicted one, but the density seems to behave more erratically. Fig. 5.10a indicates a reason for this. MUSCL finite volume schemes have the well-known defect that they produce grid-related entropy oscillations in a direction parallel to a shock, and these entropy errors are advected downstream along the streamlines. This generates small ripples in the downstream solution which should be uniform. The value of the downstream density, for instance, thus depends of the location and on the grid resolution, and this degrades pointwise convergence. The entropy oscillations are quite small with the Lax-Friedrichs scheme, and would be much larger when using the Roe scheme. Due to the inherent defect of finite volume schemes, we can not prove proper grid convergence of the RH relations, but we can see that the RH relations are generally well satisfied, and that the tendency is that they are better satisfied on finer grids. It will be interesting to see [22] if new MHD schemes based on multi-dimensional approaches will reduce or eliminate the downstream entropy contamination typical for finite volume approaches.

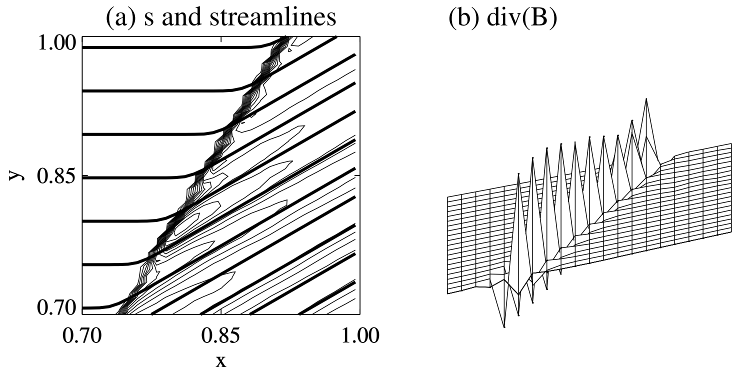

Figure 5.10: *The wedge flow. (a) Entropy contours (15 contours between $s = 2.43$ and $s = 2.45$, thin) and streamlines (thick) in a small region which contains the shock. Small errors in the entropy generated at the shock are convected away downstream parallel to the streamlines, generating small ripples in the downstream region which should be uniform. (b) Divergence of the B field in a small region containing the shock ($x \in [0.6, 0.8]$, $y \in [0.55, 0.75]$). $\nabla \cdot \vec{B}$ is strongly non-zero in a small layer around the shock. Negative and positive $\nabla \cdot \vec{B}$ peaks cancel each other out, such that on a slightly more global scale, magnetic monopoles are not present. $\nabla \cdot \vec{B}$ reaches values from -3.36 to 6.76 in the region shown.*

It is interesting here to investigate more closely what happens with the $\nabla \cdot \vec{B}$ constraint at a strong discontinuity. Fig. 5.10b shows the divergence of the B field in a small region containing the shock ($x \in$

$[0.6, 0.8]$, $y \in [0.55, 0.75]$). $\nabla \cdot \vec{B}$ is strongly non-zero in a small layer around the shock. $\nabla \cdot \vec{B}$ reaches values from -3.36 to 6.76 in the region shown. Actually, an upper bound for $\nabla \cdot \vec{B}$ can be given by $\nabla \cdot \vec{B} = |\Delta B|/\Delta x$, with $|\Delta B|$ the jump in the magnitude of the magnetic field vector across the shock, and Δx a 1D measure of grid spacing. As in the MUSCL schemes discussed above, a stationary shock is generally captured with a constant number of intermediate cells which does not depend on the resolution, and as $|\Delta B|$ is independent of the resolution, this means that $\nabla \cdot \vec{B}$ peaks near shocks grow without bounds as $1/\Delta x$ as a function of the grid resolution. Since second order schemes produce sharper shocks, the $\nabla \cdot \vec{B}$ peaks are larger when using a second order scheme than when using a first order scheme, and our simulation results clearly confirm that (not shown). The Roe scheme, which produces sharper shocks than the Lax-Friedrichs scheme, also produces larger $\nabla \cdot \vec{B}$ peaks at shocks. The Powell source term approach takes into account these $\nabla \cdot \vec{B}$ peaks consistently and the source term precisely neutralizes the dynamical effect of the $\nabla \cdot \vec{B}$ peaks. It is important to note that the exact location and magnitude of the $\nabla \cdot \vec{B}$ peaks changes when a different discretization is chosen for $\nabla \cdot \vec{B}$, and even in numerical schemes which guarantee $\nabla \cdot \vec{B}$ to vanish with machine precision in a certain discretization, it is clear that $\nabla \cdot \vec{B}$ peaks are present as soon as one looks at $\nabla \cdot \vec{B}$ in a different discretization. $\nabla \cdot \vec{B}$ peaks are an unavoidable consequence of our attempt to represent discontinuities on grids with a finite spatial resolution. All this seems to be quite worrisome, given the fact that magnetic monopoles do not exist in nature, but in practice correct results seem to be produced by numerical schemes on discrete grids. How is this possible? As noted by Linde [99], discretization of $\nabla \cdot \vec{B}$ near shocks has a 'telescoping' property, which can be described as follows. Negative and positive $\nabla \cdot \vec{B}$ peaks cancel each other out, such that on a slightly more global scale, magnetic monopoles are not present. This alternation of positive and negative $\nabla \cdot \vec{B}$ peaks can be seen clearly on Fig. 5.10. This is not a proof that the Powell approach produces valid results. A convincing proof of the validity of Powell's source term approach is given by the results of our grid convergence studies. Table 5.1 shows that the measure of flux conservation F converges faster than the state variables, and thus faster than predicted. Fig. 5.9 shows that the numerical solution satisfies the MHD RH relations up to high precision. Most convincingly, Fig. 5.8 shows clearly that the magnetic flux through flux tubes which may contain fast shocks is conserved and that flux conservation converges with the theoretically predicted order.

For the bow shock flow, we can investigate grid convergence of the solution at the stagnation point. On the stagnation streamline, the RH relations lead to an analytical solution for the state variables downstream of the shock, and using the conservation of s and h_s on the stagnation

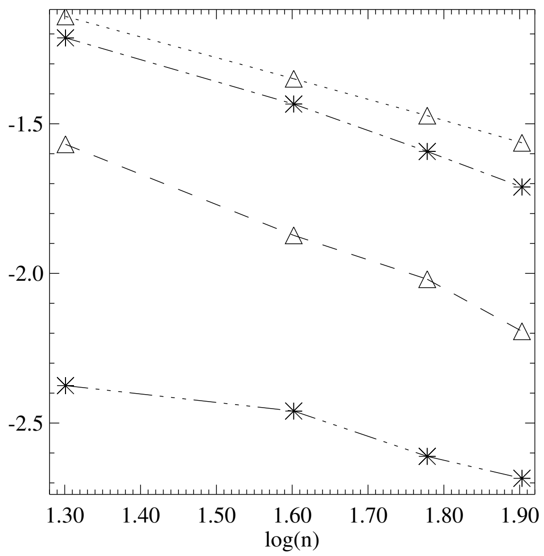

Figure 5.11: *The bow shock flow. Grid convergence of the stagnation point values. Ten logarithm of the relative errors of the stagnation point density and pressure, as a function of the grid resolution. The density converges with $a = -0.70$ (first order scheme, dotted, triangles), and with $a = -1.01$ (second order scheme, dashed, triangles). The pressure converges with $a = -0.82$ (first order scheme, dash-dotted, asterisks), and with $a = -0.52$ (second order scheme, dash-dot-dot-dotted, asterisks).*

streamline, the exact analytical solution of the stagnation point quantities in terms of the upstream flow quantities can be obtained [114]. For the inflow values of our bow shock model problem $\rho_{stag} = 3.61528$ and $p_{stag} = 3.61528$. Fig. 5.11 shows grid convergence of the stagnation point values. Although the grid convergence orders are not all close to the theoretical value of one, there is a clear trend of grid convergence to the correct values, and this is a remarkable result, given the well-known problems of many finite volume schemes with 'wall-heating' at perfect walls [91].

5.5 Conclusion

In this Chapter we have studied the grid convergence behavior of our numerical code for six model flows. We did not always obtain grid convergence orders completely consistent with theoretical expectations. Such degradation of convergence can mostly be attributed to analytical singularities or numerical inaccuracies at boundaries, to complex behavior at discontinuities, and to the distortion of the grid. However, in general we *did* obtain satisfactory grid convergence for most properties. The conservation of magnetic and momentum flux in flux tubes behaved especially well (see Table 5.1). All these results give us strong indications that we have calculated the physically correct solution to the flow problems, and that we could improve the accuracy by refining the grid. It is important to establish such formal accuracy tests for MHD simulations, and this is certainly not trivial given the lack of analytical solutions for 2D MHD problems. More advanced schemes and boundary treatment may lead to more completely consistent grid convergence results.

We have investigated by formal grid convergence studies of magnetic flux conservation and other flow quantities, whether the Powell source term approach to control the $\nabla \cdot \vec{B}$ constraint leads to correct results for this class of flows. Our grid convergence results show clearly that this method leads to correct solutions for the transonic problems we considered, although it remains difficult to grasp all the subtle details of how this correct result is obtained. It may also be, that for some problems, for which the conservation of magnetic flux up to very high accuracy is crucial, the source term technique would turn out to be insufficient.

Although the model problems presented in this Chapter exhibit quite a variety of flow features, they all belong to the sub-class of stationary planar 2D MHD flows. Stationary flow has important applications, and in this Chapter we have taken a first important step to prove grid convergence for model problems belonging to this important sub-class of flows. It would certainly be useful to develop more general test problems allowing for grid convergence studies, which, for instance, would also investigate the accuracy of time integration. Self-similar MHD flows are probably good candidates for this. Fully 3D test problems should be considered as well. In 3D, when the magnetic field is not aligned to the flow, many of the invariants used in this Chapter to prove grid convergence, cease to be invariant (Chap. 3), so it is to be expected that it will be more difficult to formulate 3D MHD model flow problems which allow for grid convergence study. For the time being, however, we can reassure ourselves by realizing that many 3D algorithms are straight extensions of their 2D counterparts, so it can be expected that the 3D algorithms perform similarly to the 2D algorithms in terms of accuracy.

Appendix: Radial outflow from a rotating cylindrical object

In this Appendix we describe and analyze a model problem describing radial outflow from a rotating cylindrical object. The grid convergence study for this problem is integrated in the discussion in Sec. 5.4.

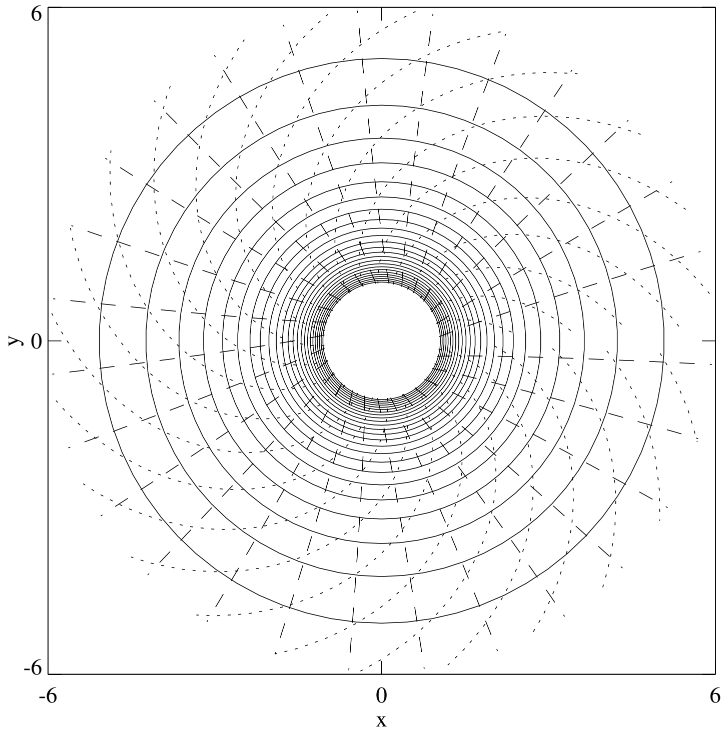

Figure 5.12: *The rotating outflow problem (70 × 70 grid). Density contours (thin solid), streamlines (dashed) and magnetic field lines (dotted) are shown. The magnetic and velocity fields are not aligned. The flow is smooth in the whole simulation domain.*

We start from the cylindrical expansion flow described in Sec. 5.2.1. We take the same inflow conditions and keep $\gamma = 5/3$, but add a rotational velocity component $v_\theta = 1$ in the anti-clockwise direction. The magnetic field remains radial at the boundary $r = 1$. We extend the simulation domain up to $r = 6$ and $\theta = 360°$. The resulting smooth stationary flow is shown in Fig. 5.12. The magnetic field lines (dotted) are clearly not aligned with the streamlines (dashed). If we transform to a coordinate frame rotating rigidly around the origin with angular velocity $\Omega = -1$, the velocity becomes radial, and thus parallel to the magnetic field (which is not changed by the coordinate transformation). It can be proved that in this rotating frame the magnetic field and the velocity field are aligned everywhere, if they are aligned at the boundary and if the flow is stationary. This is again just a consequence of the MHD frozen-in condition. In the rest frame, however, the flow is not field-aligned, as can be seen in Fig. 5.12. This flow can thus be interpreted as a field-aligned radial outflow from a rotating object, and is related to flows studied in the context of stellar winds [131, 82].

We want to study the grid convergence behavior of this non-field-aligned flow, but cannot directly use the characteristic invariants derived for field-aligned flow. Fortunately, related invariants can be found for this effectively 1D rotating flow [131, 82], as is briefly reviewed next.

The rotating outflow is completely specified when the six constants s, f_m, f_B, Ω, r_A and h are chosen in

$$\begin{aligned} s &= \frac{p}{\rho^\gamma} \\ f_m &= \rho v_r\, r \\ f_B &= B_r r \\ (v_\theta - \Omega\, r)\, B_r - v_r B_\theta &\equiv E_z \equiv 0 \\ \Omega\, r_A^2 &= r\left(v_\theta - \frac{B_r B_\theta}{\rho v_r}\right) \equiv L \\ h = \frac{1}{2}\, v_r^2 + \frac{1}{2}\,(v_\theta - \Omega\, r)^2 + \frac{\gamma}{\gamma-1}\frac{p}{\rho} &- \frac{1}{2}\,\Omega^2\, r^2. \end{aligned} \tag{5.6}$$

Here s is the entropy, f_m and f_B are the radial momentum flux and magnetic flux, Ω is the angular speed of the rotating object, r_A is the *Alfvén radius* and h is the *Bernoulli constant.* E_z is the electrical field in the z direction, and L is the angular momentum density. The invariants defined in Eq. (5.6) are used to study grid convergence for the rotating outflow problem in Sec. 5.4.

Following Sakurai [131], we derive the *Bernoulli function* $H(r, \rho)$

$$H(r,\rho) = \frac{f_m^2}{2\rho^2 r^2} + \frac{1}{2} r_A^2 \Omega^2 \left(\frac{r_A/r - r/r_A}{1 - \rho f_B^2/f_m^2}\right)^2 + \frac{\gamma}{\gamma-1} s\rho^{\gamma-1} - \frac{1}{2}\Omega^2 r^2. \tag{5.7}$$

For given constants s, f_m, f_B, Ω and r_A we can implicitly describe the *orbits* $\rho(r)$ as level curves of the Bernoulli function $H(r, \rho) = h$ for varying h. Fig. 5.13 shows these orbits (dotted) for the values of s, f_m,

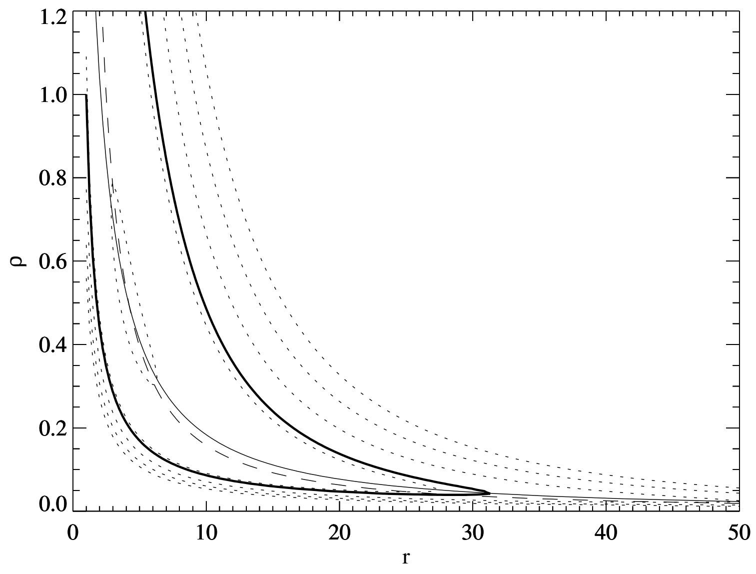

Figure 5.13: *Critical point analysis for the rotating outflow problem. The dotted lines are solution orbits. The thick solid line is the orbit corresponding to the flow shown in Fig. 5.12. The thin solid line is the fast/slow critical curve, and the dashed line is the 'throat' curve. There is one finite critical point (of O-type) where these two curves intersect. The outer radius of the simulation domain has to be chosen smaller than approximately $r = 30$ to obtain a continuous stationary solution. Indeed, at the point where the orbit and the fast/slow line cross, the flow becomes subfast. The continuous orbit becomes multi-valued, which means that there is no continuous solution, but a (non-stationary) shock would be formed.*

f_B, Ω and r_A corresponding to the simulation shown in Fig. 5.12. The thick solid orbit corresponds to the value of the Bernoulli constant h of the simulation. Two other curves of interest are the *fast/slow Mach curve* defined by $\partial H/\partial\rho = 0$ (thin solid) and the *throat curve* defined by $\partial H/\partial r = 0$ (dashed). Orbits are vertical where they cross the fast/slow Mach curve, and horizontal where they cross the throat curve. The fast/slow Mach curve and the throat curve cross in an *O-type critical point.* This critical point analysis is instructive because it shows that the outer radius of the simulation domain has to be chosen smaller than approximately $r = 30$ to obtain a continuous stationary solution. Indeed, at the point where the orbit and the fast/slow line cross, the flow becomes subfast. The continuous orbit becomes multi-valued, which means that there is no continuous solution, but a (non-stationary) shock would be formed. The model problem of Fig. 5.12 does thus not constitute an example of a smooth outflow in an infinite domain. In an appropriately chosen finite domain, however, this problem describes a valid MHD flow with well-defined boundary conditions (the flow remains superfast at the outer boundary), and is thus perfectly suitable for the purpose of testing a numerical MHD code through grid convergence study.

To conclude, we can remark that this non-field-aligned model problem is really a very special case. It could be constructed from the cylindrical expansion flow by rotation because the cylindrical expansion problem has the peculiar property that the flow, the boundary shapes and the boundary conditions themselves are all rotationally invariant. We anticipate that it is very difficult to find stationary 2D non-field-aligned model problems without such special symmetries.

Chapter 6

Magnetically dominated MHD bow shock flows: symmetrical two-dimensional flow around a cylinder

In this Chapter we present numerical simulation results of planar ($v_z \equiv B_z \equiv 0$) field-aligned MHD bow shock flows with top-bottom symmetry around perfectly conducting rigid cylinders.

Fig. 6.1a shows that in the case of hydrodynamic flow ($\vec{B} \equiv 0$) a single shock front is obtained with a concave-inward — towards the cylinder — shape. This topology is also found in experiments of hydrodynamic bow shock flows (Fig. 2.3). As long as the upstream magnetic field strength is small and thermal or dynamic pressure effects dominate, MHD bow shock flows have the same topology as hydrodynamic bow shock flows. An example is shown in Fig. 6.1b. A single-front bow shock with a concave-inward shape is obtained which is entirely of fast 1–2 MHD shock type. It was generally believed until recently that all MHD bow shocks and all bow shocks in space physics plasmas have this topology.

The main result presented in this dissertation is that MHD bow shock flows exhibit an entirely different topology when the upstream magnetic field strength is high and magnetic effects dominate over thermal and dynamic pressure effects such that the intrinsically magnetic phenomena of switch-on shocks and intermediate shocks arise. Because of the peculiar geometrical properties of these types of shocks a complex bow

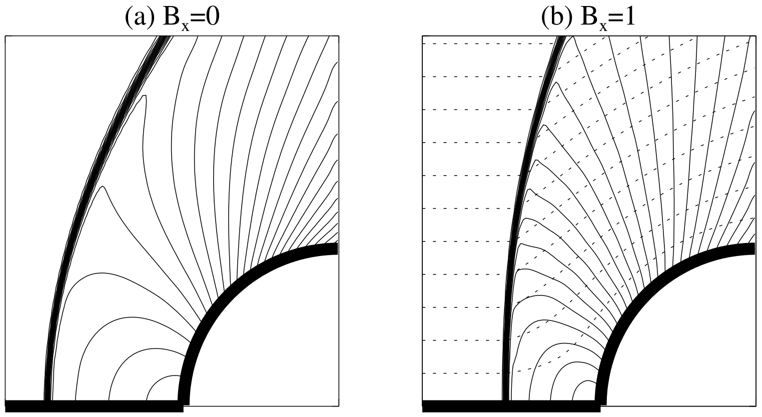

Figure 6.1: *Symmetrical bow shock flows around a cylinder (thick solid) with standard concave-inward topology. The flow comes in from the left. Density contours (thin solid) pile up in the bow shock. Magnetic field lines are dotted. The thick solid horizontal line is a line of symmetry. (a) Hydrodynamic flow: $B_x = 0$, $M = 3.46$. (b) Pressure-dominated MHD flow: $B_x = 1$, $M = 3.46$, $\beta = 0.4$.*

shock topology is needed to channel the flow around the obstacle in this magnetically dominated parameter regime. An example of a bow shock flow with this new topology is shown in Fig. 6.2. The new topology involves several consecutive shock fronts of various MHD shock types. It is not really a surprise that several shock transitions occur, because MHD allows for three anisotropic linear wave modes, and the transition from hyperbolic flow far upstream to elliptic flow in front of an obstacle can thus in principle be made through a succession of several shocks of different MHD shock type.

This Chapter is organized as follows. In Sec. 6.1 we explain in terms of the geometrical properties of MHD shocks why the complex bow shock topology of Fig. 6.2 arises when the upstream flow is magnetically dominated and switch-on shocks occur. In Sec. 6.2 we give a detailed interpretation and identification of discontinuities in one example of a complex bow shock flow with the topology of Fig. 6.2. Sec. 6.3 contains a parameter study of symmetrical bow shock flows, which clearly shows that the parameter regime in which the complex bow shock topology arises corresponds to the magnetically dominated regime for which switch-on shocks occur. In Sec. 6.4 we use characteristic analysis to study the complex stationary wave structures present in the magnetically dominated

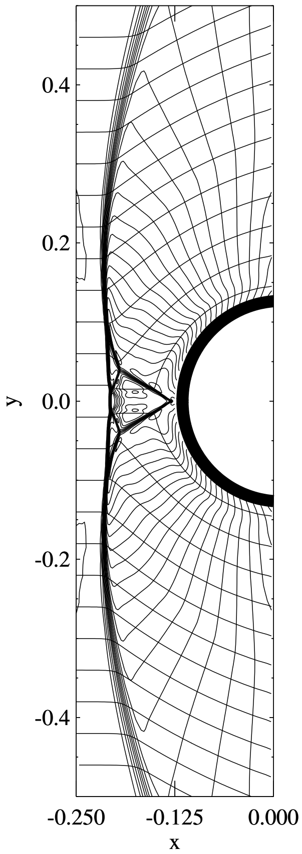

Figure 6.2: *Global view of a magnetically dominated MHD bow shock flow around a cylinder (thick) with upstream parameters* $M_x = 1.5\sqrt{3}$ *and* $\beta = 0.4$. *We show density contours (piling up in the shocks) and magnetic field lines (coming in horizontally on the left). The flow comes in from the left. The leading shock front is slightly dimpled. The upper and lower parts of this front are of the fast type. In the central part of the flow, a second front has separated and is trailing the leading front. Additional discontinuities can be seen in the central interaction region.*

bow shock flows and to identify steady compound shocks. In Sec. 6.5 we discuss the stability of the symmetrical bow shock flow solutions against non-symmetrical perturbations. We conclude briefly in Sec. 6.6.

The results presented in this Chapter have been reported in [150, 149, 151, 152].

6.1 Topology of magnetically dominated bow shock flows

In this Section we discuss the topology of symmetrical field-aligned MHD bow shock flows with magnetically dominated upstream parameters for which switch-on shocks occur. We make extensive use of the properties of MHD shocks which were discussed in Sec. 3.3.2. The discussion is placed in a planar ($v_z \equiv B_z \equiv 0$) 2D context, but most conclusions are equally valid for the 3D case, as is discussed in the next Chapter. Part of our reasoning is similar to the reasoning presented in [147].

6.1.1 The switch-on regime

Switch-on shocks (Fig. 3.8d) can only occur when in the upstream flow

$$B^2 > \gamma p \tag{6.1}$$

and

$$\rho v_x^2 > B^2 > \rho v_x^2 \frac{\gamma - 1}{\gamma(1-\beta)+1}, \tag{6.2}$$

with v_x the velocity along the magnetic field. When the magnetic field strength is small and thermal and dynamical pressure effects dominate, switch-on shocks and intermediate shocks do not occur (e.g. Fig. 3.11). For stronger magnetic fields, however, the intrinsically magnetic phenomena of switch-on shocks and intermediate shocks arise (e.g. Fig. 3.9). Equivalent conditions for the occurrence of switch-on shocks are that the upstream plasma $\beta < 2/\gamma$ and

$$1 < M_{Ax} < \sqrt{\frac{\gamma(1-\beta)+1}{\gamma - 1}}. \tag{6.3}$$

The parameter regime for which magnetic effects dominate and switch-on shocks occur is represented in the $\beta - M_{Ax}$ plane in Fig. 6.3. Because there is a fixed relationship between M_{Ax} and M_x which only involves β and γ, viz. $M_x^2/M_{Ax}^2 = c_{Ax}^2/c^2 = 2\beta/\gamma$, we can also represent the switch-on parameter domain in the $\beta - M_x$ plane, as is done in Fig. 6.3b. Remember from Sec. 3.1.3 that only two non-dimensional numbers are required to parametrize the scales of a given stationary ideal MHD problem, for instance either M_x and β, or M_{Ax} and β.

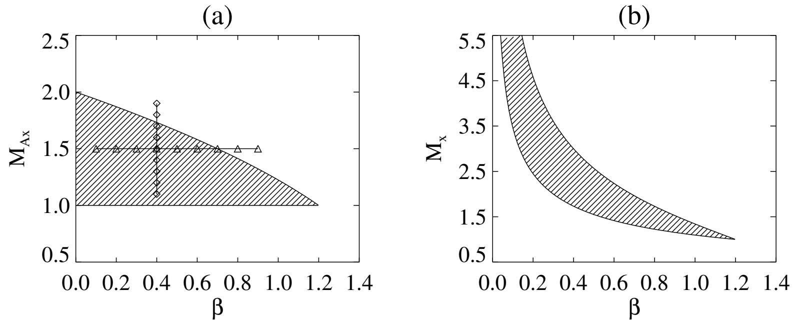

Figure 6.3: *Parameter domain for which states are magnetically dominated and switch-on shocks occur. For $\gamma = 5/3$, switch-on shocks are possible for upstream values of β and M_{Ax} (a) and β and M_x (b) which are located in the shaded regions. In Sec. 6.3, numerically obtained bow shock flows are presented for inflow quantities with fixed $\beta = 0.4$ and M_{Ax} varying from 1.1 to 1.9 (the diamonds on the vertical line in (a)), and with fixed $M_{Ax} = 1.5$ and β varying from 0.1 to 0.9 (the triangles on the horizontal line).*

6.1.2 Shock configurations at perpendicular points

We discuss now what the occurrence of switch-on shocks in magnetically dominated regimes implies for the topology of bow shocks. Two general considerations are important guidelines in our discussion. First, when the upstream flow is magnetically dominated and intermediate shocks can exist, the shock transition from a superfast upstream state of type 1 to a subfast downstream state at the leading front of a bow shock is not necessarily a 1–2 fast shock, but can as well be a 1–3 or a 1–4 intermediate shock. Second, downstream of a leading 1–2 fast shock secondary shocks of slow or intermediate type can in principle be formed, because the downstream state 2 is super-Alfvénic and superslow.

In order to understand the topology of magnetically dominated bow shock flows, it is useful to consider points on shock fronts where the magnetic field is perpendicular to the shock front. We call such points perpendicular points. In Fig. 6.4a we investigate if a shock front which contains a perpendicular point B, can entirely be of the 1–2 fast shock type. When the upstream flow is magnetically dominated (switch-on shocks occur), the 1–2 shock at a perpendicular point has to be a 1–2=3 switch-on shock. Suppose that the switch-on shock at perpendicular point B in Fig. 6.4a deflects the magnetic field upwards. The shock

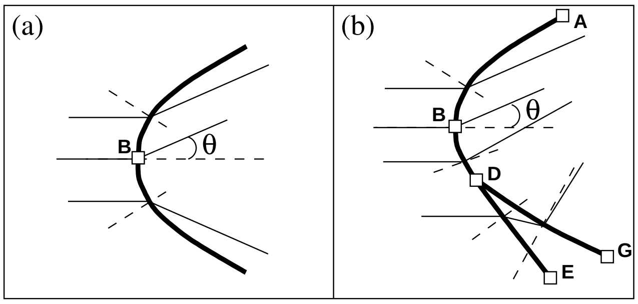

Figure 6.4: *Two proposed topologies for a shock front with a switch-on shock at perpendicular point B for the case of a magnetically dominated upstream flow. Thick lines are shock fronts, thin lines are magnetic field lines, and shock normals are dashed. Point B is a perpendicular point, where the magnetic field is normal to the shock front. The shock at point B is a switch-on shock, which deflects the magnetic field with downstream angle θ. (a) The shock front cannot entirely be of the 1–2 fast type. (b) A complex shock topology is necessary to channel the flow. Shock segment AB is of 1–2 fast type, BD is 1–3 intermediate, DE is 1–2 fast, and DG is 2–4 intermediate, evolving into 2=3–4 switch-off and 3–4 slow along the front.*

segment above point B can entirely be of 1–2 type. Indeed, a fast 1–2 shock deflects the magnetic field away from the normal (Fig. 3.8a), which means upward for this shock segment. If we move downward along this segment towards point B, then the deflection of the magnetic field continuously evolves into a 1–2=3 switch-on shock with upward deflection at point B. The shock segment below point B, however, cannot be of fast 1–2 type, because the magnetic field would be deflected away from the shock normal and thus downward. A 1–2 shock segment can thus not continuously be linked from below to the switch-on shock with upward deflection at point B. The topology of Fig. 6.4a, with a shock entirely of 1–2 type, is thus not possible at a perpendicular point. The question thus arises which shock configurations are possible at a perpendicular point.

Fig. 6.5 shows several allowed shock configurations at a perpendicular point with a superfast upstream state of type 1. In the first row (Fig. 6.5a–d) we show the possibilities for the case that the shock at the perpendicular point is a switch-on shock with upward deflection of the magnetic field. Fig. 6.5a shows that a upper segment of 1–2 fast type can be linked continuously to a lower segment of 1–3 intermediate type in the perpendicular point. Indeed, the 1–2=3 switch-on shock with

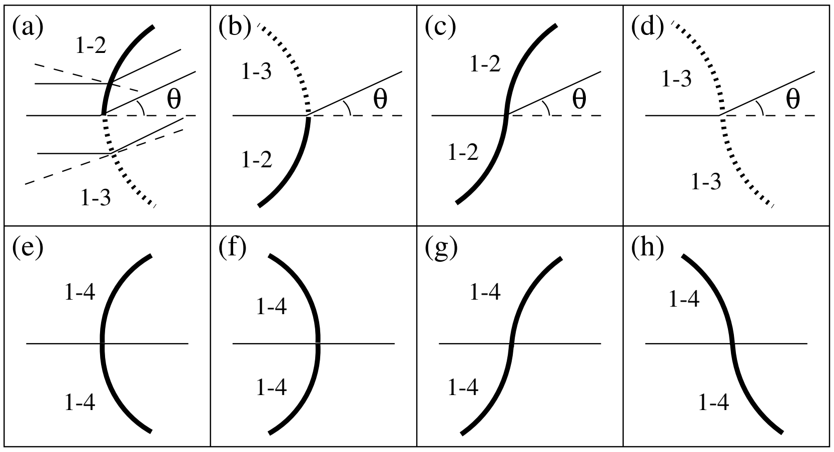

Figure 6.5: *Allowed MHD shock configurations near perpendicular points with magnetically dominated superfast upstream state (switch-on shocks can occur). Magnetic field lines are thin solid, shocks are thick and shock normals are dashed.*

upward deflection is a limit of both the 1–2 fast shock and the 1–3 intermediate shock (see also Fig. 3.9). Fig. 6.5b–d shows other possibilities for the case of a switch-on shock at a perpendicular point.

In the second row of Fig. 6.5 we show the possibilities for the case that the shock at the perpendicular point is a 1–4 hydrodynamic shock (Fig. 3.8f) which does not deflect the magnetic field. The 1–4 hydrodynamic shock is a limit of 1–4 shocks which deflect the magnetic field (see Fig. 3.9), so only 1–4 shock segments can be linked continuously to the 1–4 hydrodynamic shock.

All the configurations of Fig. 6.5 are thus possible near perpendicular points. However, the curved 1–3 and 1–4 intermediate shock segments in Fig. 6.5 can only have a limited extent, because intermediate shocks can only exist for a limited angle between the magnetic field and the shock normal. For the parameter values of Fig. 3.9, for instance, this maximum angle is 16°.

6.1.3 Topology of symmetrical bow shock flows

How can we use the pieces presented in Fig. 6.5 to solve the puzzle of symmetrical bow shock topology in the switch-on regime? Fig. 6.6 proposes two possible topologies for the field-aligned flow around a cylinder. The flow comes in horizontally from the left. The horizontal line through the center of the cylinder is called the stagnation streamline, because the

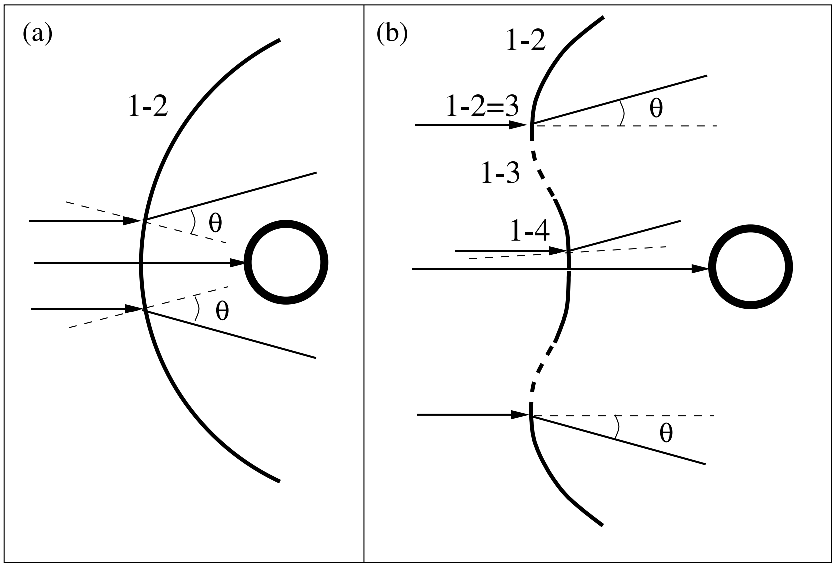

Figure 6.6: *Two proposed symmetrical bow shock topologies for a uniform magnetically dominated flow coming in from the left and obstructed by a conducting cylinder. Magnetic field lines have arrows and shock normals are shown as dashed lines. The horizontal field line terminating on the cylinder is the stagnation streamline. (a) Concave-inward (to the cylinder) shape. The whole shock front (thick line) is of the fast 1–2 type. (b) Dimpled shape proposed by Steinolfson and Hundhausen [147]. Starting from above, the front is first of the fast 1–2 type. At the nose, a 1–2=3 switch-on shock refracts the horizontal incoming magnetic field upward with a finite angle θ. Under the nose the shock front is first of the 1–3 intermediate type, and is then linked to a 1–4 intermediate shock part.*

fluid velocity vanishes on this line at the cylinder. The specification of this flow problem is symmetrical relative to the stagnation streamline. Consequently we expect a flow solution with top-bottom symmetry, and we discuss the topology of such a symmetrical flow here.

On the stagnation line the magnetic field cannot be deflected due to symmetry. This observation immediately rules out the topology of Fig. 6.6a with a single shock front entirely of 1–2 type for magnetically dominated upstream flows. Indeed, a 1–2 shock necessarily has to become a switch-on shock at a perpendicular point, and this is not allowed due to symmetry. This explains why magnetically dominated MHD bow shock flows cannot have the topology of pressure-dominated bow shock flows

(Fig. 6.1) with a single concave-inward shock front of fast 1–2 type! In contrast, for pressure-dominated upstream parameters switch-on shocks do not occur and the angle θ in Fig. 6.6a vanishes at the perpendicular point, such that the bow shock can entirely be of 1–2 fast type.

At the line of symmetry the magnetic field cannot be deflected, so the shock configuration can only be the configuration of either Fig. 6.5e or f. The 1–4 intermediate shock segments can only have a limited extent, however, because for increasing angle between the magnetic field and the shock normal, the 1–4 shock first becomes a 1–3=4 shock and then ceases to exist (Fig. 3.9). Steinolfson and Hundhausen [147] proposed the topology of Fig. 6.6b in the context of their analysis of propagating shocks induced by fast solar Coronal Mass Ejections (CMEs). This topology contains the configuration of Fig. 6.5f near the stagnation line. The configuration of Fig. 6.5a is then linked to the 1–4 shock at the point where the 1–4 shock becomes a 1–3=4 shock (Fig. 3.9). In this configuration the shock front adopts a shape with a *concave-outward dimple* in the central part of the front. The proposed dimple topology contains three perpendicular points, two at the two nose points and one central perpendicular point on the stagnation line. Approaching the top perpendicular point from above, the shock front is first fast 1–2, and becomes 1–2=3 switch-on at the perpendicular point. Going further down, this 1–2=3 shock can continuously evolve into a 1–3 intermediate shock segment. For increasing angle between the magnetic field and the shock normal, the shock type evolves to 1–3=4. Beyond this point the shock becomes 1–4 and concave-outward. At the central perpendicular point the shock becomes a 1–4 hydrodynamic shock.

This proposed solution contains two quite revolutionary ideas: first, the shock front contains a concave-outward part, and second, it is composed of segments of various MHD shock types, which can be linked together in a continuous way. Time-dependent 2D MHD simulations [147, 146] partially confirmed this picture (a dimpled shock front was obtained), and dimpled fronts were also observed in coronagraph images of fast moving CMEs [147, 146, 68].

However, Steinolfson and Hundhausen's time-dependent 2D simulation results for a uniform upstream field did not fully confirm the hypothetical shock geometry of Fig. 6.6b. In their numerical results they found several features for which they could not provide a clear interpretation, including traces of slow shocks, an unusual 'tube' configuration near the symmetry line, and a possible singular point where four shock branches would interact [147].

In our simulation results of stationary bow shock flows with magnetically dominated upstream parameters (Fig. 6.2) we do not find the topology of Fig. 6.6b, although we recover some of its constituting elements. We do find a topology with three perpendicular points. The

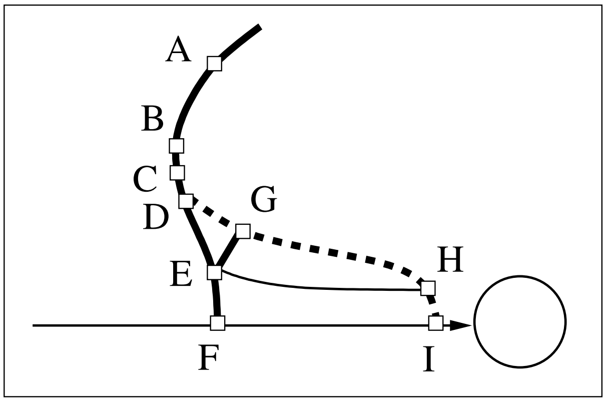

Figure 6.7: *Sketch of the complex multiple-front bow shock topology. In the leading front, shock AB is a 1—2 fast shock, BCD is 1—3 intermediate, DE is 1—2 fast, and EF is 1—4 hydrodynamic. The second front DGHI is 2—4 intermediate (2=3—4 slow switch-off or 3–4 slow at places). EG is a 1=2—3=4 intermediate shock which is sonic both upstream and downstream. EH is a tangential discontinuity, and tangential discontinuities also stretch out from points D, G, and H, along the streamlines towards infinity. At perpendicular point B the shock is a 1–2=3 switch-on shock, at points D and E the shock is of 1–3=4 intermediate type, and at perpendicular point F the shock is 1–4 hydrodynamic. The topology near the perpendicular point B is the topology of Fig. 6.4b.*

topology of the numerically obtained flow pattern (top half) is sketched in Fig. 6.7. Throughout this Chapter we refer to the lettering labels of this Figure for the identification of shock parts. Above the top perpendicular point the shock is indeed of fast 1–2 type, and below this point the shock is of 1–3 type, like in Fig. 6.6b. At the point where the 1–3 shock ceases to exist, however, the shock front splits up into two consecutive shock fronts. This is sketched in Fig. 6.4b. The leading shock segment DE is of the 1–2 fast type, and analysis of the simulation result of Fig. 6.2 learns that the secondary shock segment DG is 2–4 intermediate, evolving into 2=3–4 switch-off and 3–4 slow along the front. The combination of the fast and the intermediate shock can deflect the magnetic field such that field lines merge continuously downstream of the so-called λ-point D where the three shock segments meet.

Near the stagnation line in Fig. 6.2 we find the configuration of Fig. 6.5e. At the point where the 1–4 shock ceases to exist, it splits up into a fast 1–2 shock followed by a 1=2–3=4 intermediate shock. This cannot be seen very clearly in Fig. 6.2, but shock segments are clearly identified in the next Section. In general it seems that the leading shock front splits into two consecutive fronts at 1–3=4 points beyond which intermediate shocks can no longer exist.

In this Chapter we present simulations of the 2D steady state MHD bow shock problem with magnetically dominated upstream flow (switch-on shocks occur). In contrast to the time-dependent flows considered by Steinolfson and Hundhausen [147], our bow shock solutions are stationary in time, which allows for higher grid resolution and greatly facilitates a clear interpretation. The topology we obtain in our simulation results contains some elements of the topology proposed in Fig. 6.6b, but the resulting bow shock flow is quite more complicated than could be anticipated from the important earlier work of Steinolfson and Hundhausen [147]. The leading shock front is followed by a second shock front, and other discontinuities can be identified between the two fronts. Our solution reveals and explains much richer and more complex physics not anticipated in the work of Steinolfson and Hundhausen [147]. Clearly an additional level of complexity is present: not only do shocks of several different types form in the leading front, but multiple shock fronts are necessary to channel the magnetically dominated flow around the obstacle. It is conceivable that our results on shock topology in stationary magnetically dominated flows can also be important for shock propagation in time-dependent flows in this parameter regime.

6.2 Detailed interpretation and identification of discontinuities in a magnetically dominated bow shock flow

In this Section we analyze in detail the flow of a planar ($v_z \equiv B_z \equiv 0$) superfast MHD fluid around a perfectly conducting rigid cylinder for magnetically dominated upstream parameters (switch-on shocks occur). The angle between the magnetic field and the velocity field cannot be varied because the flow is necessarily field-aligned, so the problem of stationary 2D MHD flow around a perfectly conducting cylinder has only two free parameters which parametrize the scales, for instance β and M_A or β and M. The analogous hydrodynamic problem has only one free parameter, for instance M.

For the incoming flow we choose $\beta = 0.4$, which implies a critical Alfvénic Mach number $M_{Ax,crit} = 1.732$ (Eq. 6.3). We choose the Alfvénic Mach number of the incoming flow $M_{Ax} = 1.5$, such that the upstream flow is magnetically dominated and allows for switch-on shocks (see also Fig. 6.3a). The x axis being horizontal, we can choose $\rho = 1$

and $B_x = 1$ (implying that the Alfvén speed $c_{Ax} = 1$). The pressure and velocity can then be determined from β and M_{Ax}, yielding $p = 0.2$ and $v_x = 1.5$ (such that the acoustic Mach number $M_x = 1.5\sqrt{3}$). Finally, we take $B_y = 0$ and $v_y = 0$. As the resulting stationary ideal MHD flow is scale invariant, we can freely choose the radius of the cylinder. We take $r = 0.125$ and the cylinder is placed at the origin of the coordinate system.

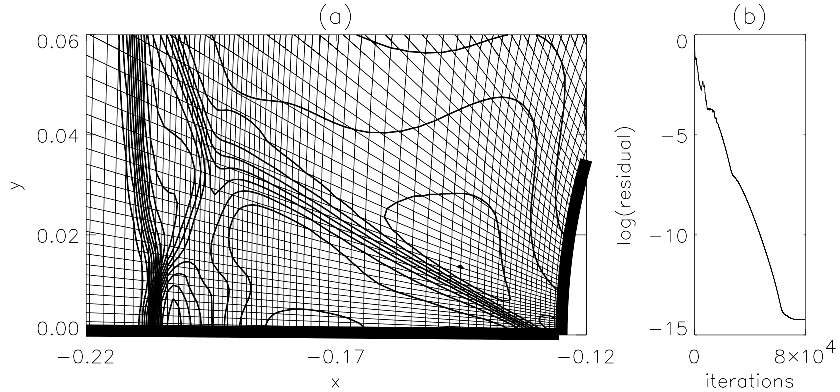

Figure 6.8: *(a) Detail of the simulation grid (*80×80*) with density contours. The thick solid lines represent simulation domain boundaries with ideal wall symmetry. (b) Convergence of the simulation to a steady state. The logarithm of the root mean square of the density residual is shown as a function of the number of iterations.*

The numerically computed stationary solution of Fig. 6.2 is obtained through time relaxation starting from a uniform initial condition, which is taken to be the above described uniform inflow. We look for a stationary solution, and the steady flow necessarily has to be field-aligned. The complete setup of this problem — initial condition, boundary conditions and the MHD equations — satisfies top-bottom symmetry relative to the stagnation line. We thus expect a stationary solution which satisfies this top-bottom symmetry as well. In our numerical simulations we explicitly impose this symmetry by performing the calculations only in the upper left quadrant bounded from below by the stagnation streamline, and by specifying symmetry boundary conditions on this lower boundary. These boundary conditions are the same as for a perfectly conducting wall. The simulated bow shock flow in the upper quadrant can thus also be thought of as a 2D model flow over a perfectly conducting plate (the stagnation line) with a semi-circular bump or corner. In the case of the full flow around the cylinder, the question of the stability of the symmetrical solution against non-symmetrical perturbations turns out to be important, as is discussed in Sec. 6.5.

We simulate the flow in the upper left quadrant, on a 120×120 stretched elliptic polar-like structured grid, extending to $x = -0.35$ on the x axis, and to $y = 1.4$ on the y axis. Part of the simulation grid is shown in Fig. 6.8a. The grid resolution is increased near interesting features of the flow by accumulating or clustering grid points. This grid accumulation is done in a dimension by dimension way. In the i direction, the grid is clustered near the perpendicular point on the leading shock front, and near the stagnation point. In the j direction, the grid is clustered near the stagnation line. We use ghost cells to specify the boundary conditions (Sec. 4.2.6). On the left, we impose the uniform superfast incoming flow. The cylinder wall is an ideally conducting rigid wall. The lower border of the simulation domain satisfies ideal wall symmetry as mentioned above. The right outflow condition is superfast, so there we extrapolate all quantities to the ghost cells. The flow evolves in time until a converged steady state bow shock solution is obtained, and Fig. 6.8b shows the convergence of the density residual.

For our present simulations, we use the second order scheme with Lax–Friedrichs numerical flux function (Sec. 4.2.5). In Chap. 9 we report on our experience with other numerical flux functions for this bow shock problem. We use Powell's source term technique to keep the $\nabla \cdot \vec{B} = 0$ constraint satisfied (Sec. 4.4), and in Chap. 9 we show that a projection scheme leads to essentially the same results.

We now show how the types of all MHD discontinuities arising in the flow of Fig. 6.2 can be clearly determined.

In Fig. 6.9 we show a detailed section of the computed flow in the half plane above the stagnation streamline. D–E is a fast shock with $B_{y,1}$ almost vanishing upstream, so it is almost a fast switch-on shock. E–F is a 1–4 intermediate shock. It is probably slightly concave-inward at locations on the front away from point F, like in Fig. 6.5e, and thus unlike the concave-outward 1–4 central part in Steinolfson and Hundhausen's proposed solution (Fig. 6.6b). At the resolution of our simulations, however, no definite conclusions can be made about this orientation.

At point F, the shock is definitely of the hydrodynamic 1–4 type. E–G is an intermediate shock, because it clearly contains the dashed $M_A = 1$ contour (showing that the flow goes from super-Alfvénic to sub-Alfvénic upon passing through the shock), and because the field lines are flipped over the normal. Bear in mind that the Alfvénic Mach number M_A does not depend on the direction for the case of field-aligned flow. Below it is shown that shock E–G is a 1=2–3=4 intermediate shock.

D–G–H–I is an intermediate shock with an upstream Alfvénic Mach number (slightly) greater than one, and with magnetic field lines that

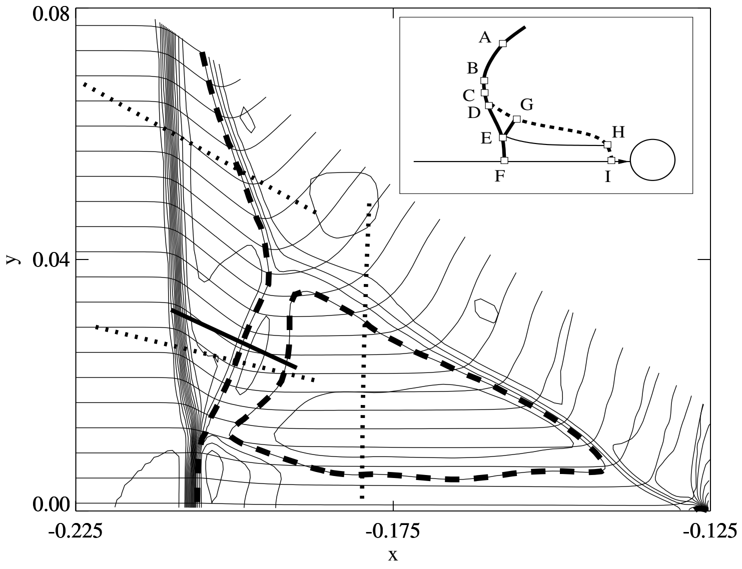

Figure 6.9: *Detail of the solution in the half plane above the stagnation streamline. We show Alfvénic Mach number contours (piling up in the shocks) and magnetic field lines (coming in horizontally on the left). The dashed line is a contour where the Alfvénic Mach number exactly equals one. This information together with the refraction of the field lines serves to identify the shocks as fast, hydrodynamic, and intermediate (see the text).*

are flipped over the normal. At various places along the shock front, the upstream intermediate Mach number approaches one and the downstream magnetic field becomes normal to the front, meaning that the shock becomes 2=3–4 slow switch-off and even 3–4 slow at places.

E–H is a tangential discontinuity. Other tangential discontinuities are stretching out from points D, G, and H along the streamlines to infinity.

E–F is very reminiscent of a Mach stem as it occurs in Hydrodynamic shock reflection [169]. A priori the point E could lie on the stagnation streamline, in which case this point would be a singular point on this streamline where four shock branches interact. In such a situation, the stagnation streamline would not be a shock normal. In such a hypothetical singular point, the $\nabla \cdot \vec{B} = 0$ constraint could be satisfied if the jump in B_y in the y direction is exactly the same (with opposite sign) as the jump in B_x in the x direction. A solution with such a singular point is found for simulation on a grid with low spatial resolution. With sufficient resolution however, the shock part E-F appears, reducing the singularity to three branches interacting in point E. An interaction point where four branches meet, seems thus to be avoided. This may be a more general feature of MHD shock interaction.

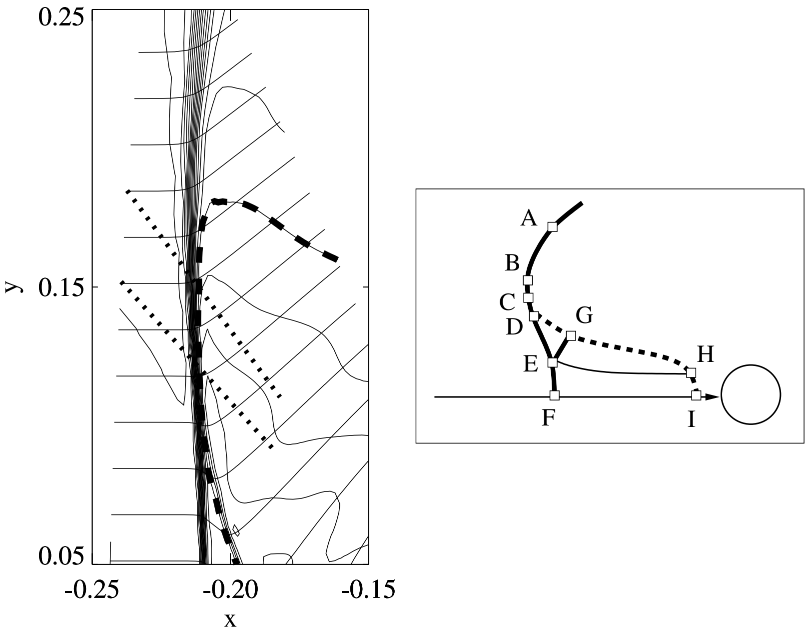

Figure 6.10: *Detail of the solution close to the 'nose'. We show Alfvénic Mach number contours and magnetic field lines. The dashed line is a contour where the Alfvénic Mach number exactly equals one. This information together with the refraction of the field lines serves to identify the shocks as fast and intermediate (see the text).*

In Fig. 6.10 we show a detail of the region close to the 'nose' point B. The refraction of the field lines (away from the shock normal) above point B shows that this part of the shock is a fast shock. The shock at point B is a 1–2=3 fast switch-on shock, because the tangential field component is switched on, and because the downstream Alfvénic Mach number equals one. B–C–D is an intermediate shock, because it clearly contains the dashed $M_A = 1$ contour, and because the field lines are flipped over the normal. Shock B–C–D is of the 1–3 type, which can be merged continuously with the fast 1–2=3 switch-on shock in point B.

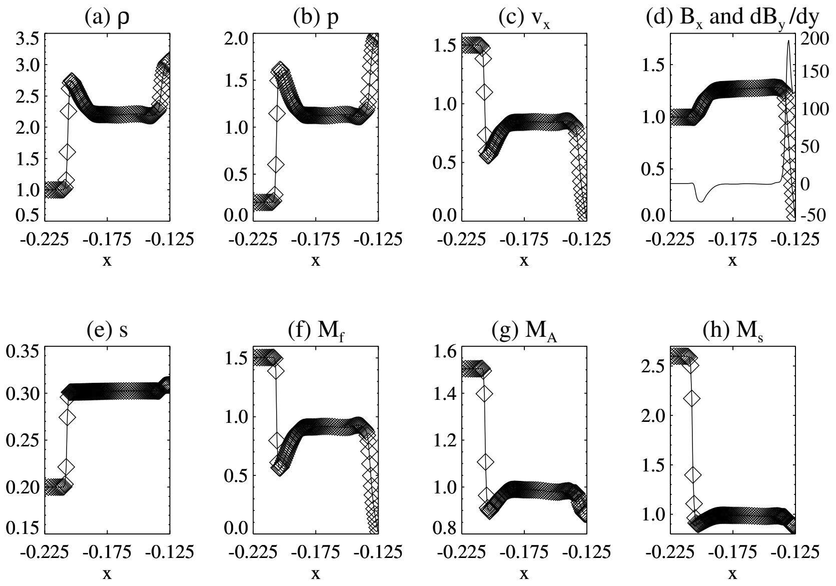

Figure 6.11: *Plots of the variables along the stagnation streamline. From left to right, the uniform incoming flow first jumps in the hydrodynamic shock, followed by a slow rarefaction, which brings the flow back to uniform. Close to the cylinder we pass the intermediate shock. The flow is then brought to the stagnation point in a continuous diverging compression. The variation of $\partial B_y/\partial y$ in (d) (thin line, axis on the right) shows that the flow is effectively 2D at various locations on the stagnation line.*

In Fig. 6.11 we show plots of the variables along the stagnation streamline. The simulation results presented in this plot were obtained using a projection method, because the Powell approach computes slightly inaccurate values near the stagnation point (see Chap. 9). The first feature we encounter when we go from left to right, is a discontinuity which corresponds to the hydrodynamic shock at point F. The RH relations for the shock on the stagnation streamline are simple and can be solved easily [114], resulting in downstream quantities $p = 1.64$, $\rho = 2.77$, $v_x = 0.542$, and $s = 0.300$. The jumps of the density, pressure, velocity, and entropy in Fig. 6.11 agree well with the jumps calculated from the

RH relations. The fast, Alfvénic and slow Mach number all jump from above one to under one, indicating a 1–4 intermediate shock. The magnetic field does not show a jump, consistent with a purely hydrodynamic shock.

Going further to the right, we see that we pass through a rarefaction to reach a constant state. This slow rarefaction converges the flow slightly towards the stagnation streamline. Although the flow near the stagnation line may appear to be close to a 1D flow in Fig. 6.9, the flow is in fact 2D at various places along the stagnation line. In Fig. 6.11d we plot $\partial B_y/\partial y$ (thin line), indicating that the flow is 2D in this rarefaction region. The density decreases in the main direction of the converging flow on the stagnation line, because the velocity (v_x) is increasing and $\nabla \cdot (\rho\vec{v}) = 0$. B_x is not significantly influenced by the increasing v_x because the field is aligned to the flow. However, B_x increases along the flow because of the 2D effect of converging flow in the y direction perpendicular to the stagnation line. This flow component causes the field lines to converge towards the stagnation line, as can be seen in Fig. 6.11d: $\partial B_x/\partial x$ balances $\partial B_y/\partial y$ such that $\nabla \cdot \vec{B} = 0$.

Going further to the right, we pass a region where the flow is uniform. The flow becomes 2D again as we approach the stagnation point at the cylinder, as can be seen in Fig. 6.11d. This is no surprise, because in general every stationary stagnation point flow is necessarily 2D due to the requirement of mass conservation ($\nabla\cdot(\rho\vec{v}) = 0$). Indeed, a stagnation point can clearly not be reached by means of a stationary 1D flow (neither a shock nor a continuous flow), because a 1D flow can not bring ρv_x down from a finite value to a value of zero at the stagnation point.

As an illustrative example of a stationary 2D stagnation point flow, we show in Fig. 6.12 how a stagnation point is reached in a traditional pressure-dominated single-front MHD bow shock flow, which is obtained by choosing the inflow velocity outside of the switch-on region (Eq. 6.3): $\rho = 1$, $p = 0.2$, $v_x = 2$, $v_y = 0$, $B_x = 1$, and $B_y = 0$ at the inflow, resulting in inflow Mach numbers $M_{Ax} = 2$ and $M_x = 2\sqrt{3}$ ($\beta = 0.4$). The stagnation point is reached in a continuous (constant-entropy) 2D compressive diverging flow region behind the shock front.

In our simulation, the 2D stagnation point flow is complicated by the presence of intermediate shock D–G–H–I. Fig. 6.2 shows that point I lies very close to the cylinder. In this small region between point I and the cylinder we expect the 2D stagnation point flow. Because this region is extremely small compared to the dimensions of the other features in our simulation, we could not avoid a comparatively low numerical resolution in this region. Moreover, the curvature of the intermediate shock front at point I is very large and may even be singular, which makes the post-shock flow 2D and complicates the interpretation of the shock as a 1D shock.

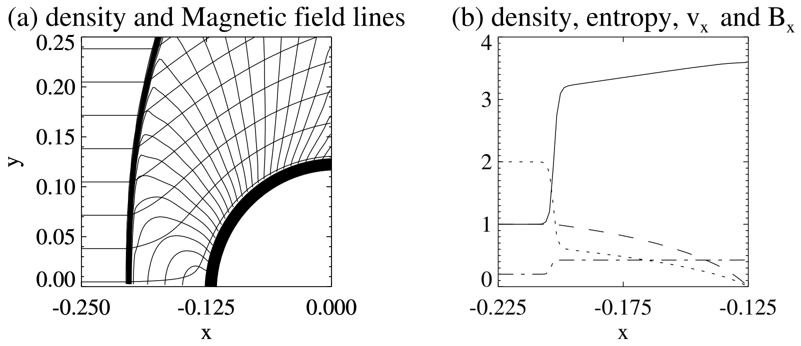

Figure 6.12: *Simulation of a pressure-dominated MHD flow with a single-front bow shock (inflow Mach numbers $M_{Ax} = 2$ and $M_x = 2\sqrt{3}$, and $\beta = 0.4$). (a) Flow near the cylinder. (b) Stagnation line variables. Behind the shock, the flow variables are brought to their stagnation point values in a continuous compressive diverging flow. B_x is dashed, v_x dotted, s dash–dotted, and ρ full.*

All these complications make the interpretation of the simulation results near the cylinder quite difficult. However, we can propose the following possible interpretation for the variation of the flow variables near the cylinder in Fig. 6.11.

The location of the small jump in entropy in Fig. 6.11e close to the cylinder can reasonably be identified with the point I of Fig. 6.9, where the intermediate shock D–G–H–I intersects the stagnation line. This entropy jump is located at a finite distance from the cylinder, which means that there is a small but finite standoff distance between the shock and the cylinder. In the small constant-entropy region between point I and the cylinder, we can expect a continuous 2D stagnation point flow analogous to the flow in Fig. 6.12. The variation of ρ, v_x, and B_x close to the cylinder in Fig. 6.11 appears to be consistent with the continuous variation of these quantities in the stagnation point flow of Fig. 6.12.

Although not conclusively proven, this interpretation of the flow near the cylinder in Fig. 6.11 as a weak shock followed by a 2D compressive diverging stagnation point flow is physically reasonable since it is consistent with the simulation data and since it establishes a clear analogy with less complicated stagnation point flows. It will be interesting to see if future simulations with more powerful numerical techniques will confirm all the details of this interpretation of the highly complicated stagnation point flow.

In Fig. 6.13 we show plots of some variables along several instruc-

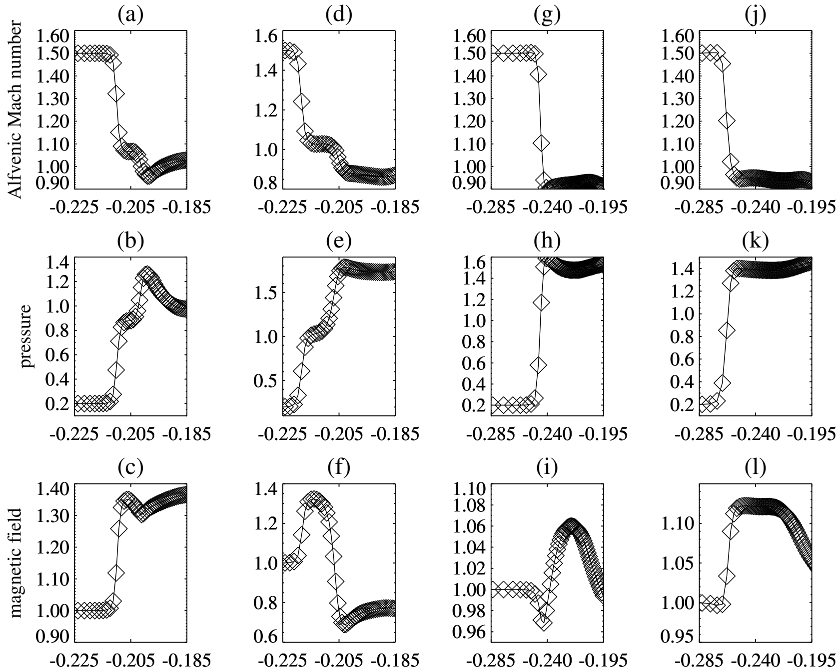

Figure 6.13: *Alfvénic Mach number (a,d,g,j), pressure (b,e,h,k), and magnetic field (c,f,i,l) along various cuts through the simulation domain. (a-c) Cut along the lower dotted line cutting the leading front in Fig. 6.9. (The lower axis shows the distance to the center of the cylinder.) We pass the fast shock, and then the intermediate shock followed by a rarefaction. (d-f) Cut along the upper dotted line cutting the leading front in Fig. 6.9. We pass the fast shock, and then the intermediate shock. (g-i) Cut along the lower dotted line cutting the leading front in Fig. 6.10. We cross the intermediate shock. (j-l) Cut along the upper dotted line cutting the leading front in Fig. 6.10. We cross the intermediate shock.*

tive 1D cuts. Figs. 6.13a-c show a cut along the lower dotted line cutting the leading front in Fig. 6.9 under an angle of $\theta = 13.82$ degrees. First we cross the fast shock. Then the intermediate shock brings the Alfvénic Mach number from above one to under one. Figs. 6.13d-f show a cut along the upper dotted line cutting the leading front in Fig. 6.9 ($\theta = 29.25$). Again we cross the fast shock first. Then we cross the intermediate shock, with the upstream Alfvénic Mach number close to one. Figs. 6.13g-i show a cut along the lower dotted line cutting the leading front in Fig. 6.10 ($\theta = 47.66$). We cross only one shock, which is of the intermediate type, because it brings the Alfvénic Mach number from above one to under one. Figs. 6.13j-l show a cut along the upper dotted line cutting the leading front in Fig. 6.10 ($\theta = 53.40$). We cross the same intermediate shock.

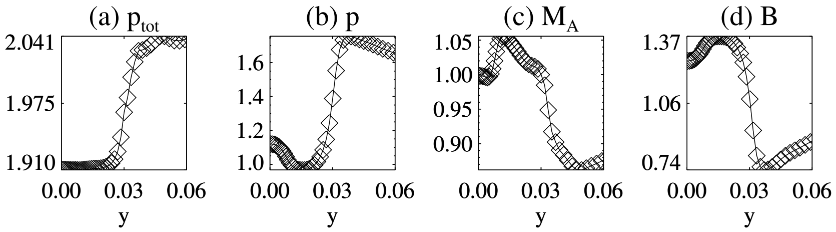

Figure 6.14: *Cut along the vertical dotted line in Fig. 6.9. We first cross the tangential discontinuity, with a jump in pressure but not in total pressure. Then we pass the intermediate shock.*

In Fig. 6.14 we show plots of some variables along the vertical dotted line in Fig. 6.9. Where the pressure jumps for the first time, we pass through the tangential discontinuity (a little more smeared out than the shocks), as is proved by the continuity of the total pressure here. The next jump is the intermediate shock, with an upstream Alfvénic Mach number close to one. (This profile is a little smeared out because we cross it at a large angle).

It is interesting to look for the presence of 1=2–3 and 2–3=4 sonic intermediate shocks in our 2D simulation results, as they are a manifestation of the non-convex nature of the MHD equations, as was explained in Sec. 3.3.5. Bear in mind that we call a shock 'sonic' whenever the normal plasma speed equals any of the MHD wave speeds on the upstream or the downstream side. We look for shocks with a conspicuous rarefaction attached, as seen in compound shocks of the time-dependent non-convex MHD system, and investigate if the shock is sonic where the rarefaction is attached.

Let us first consider the 1–4 hydrodynamic intermediate shock on the stagnation streamline. It is followed by a slow rarefaction (Fig. 6.11), but Fig. 6.11f-h shows clearly that the flow is not sonic where the rarefaction is attached to the shock. This shock is thus not of the sonic type, and in this example the rarefaction is a 2D effect, as noted before. It serves to bring the Alfvénic Mach number from its downstream value lower than one to a value close to one, necessary for the shock at point I.

Intermediate shock C–D (Fig. 6.13h-i) is followed by a rarefaction, in contrast to intermediate shock B–C (Fig. 6.13k-l; the different behavior of the post-shock magnetic field is striking). Shock D–G–H–I seems to be followed by a rarefaction as well (Figs. 6.13e-f, 6.14d). For all of these structures, the flow is, however, not sonic where the rarefaction is attached to the shock.

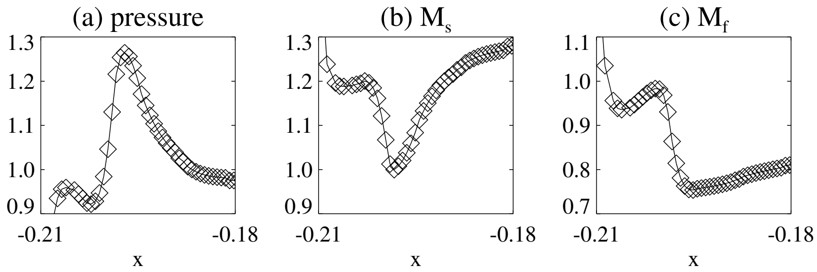

Figure 6.15: *Cut along the solid line normal to the intermediate shock E–G in Fig. 6.9. The intermediate shock is preceded and followed by rarefaction regions. The normal fast Mach number equals one where the upstream (left) rarefaction is attached to the shock. The normal slow Mach number equals one where the downstream rarefaction is attached to the shock. The intermediate shock is thus a 1=2–3=4 shock.*

Finally intermediate shock E–G remains to be investigated. This shock is followed by a distinct rarefaction and preceded by another (weak) rarefaction (Fig. 6.13b-c and Fig. 6.15a). A detailed analysis of the speeds along the solid line normal to shock E–G in Fig. 6.9 shows that the intermediate shock is a 1=2–3=4 shock, as the downstream normal slow Mach number and the upstream normal fast Mach number are both equal to one (Fig. 6.15b-c). The flow is thus sonic on both sides of the shock. This is a clear manifestation of the non-convexity of the MHD equations in a steady state 2D flow.

It has been shown recently by Myong and Roe [109, 110] that this type of 1=2–3=4 shock can be present in the analytical solution of planar xt Riemann problems, embedded in a double xt compound wave. The stationary 2D rarefaction–shock–rarefaction structure of our xy simulation result could be more closely related to this double xt compound wave, if the steady state rarefactions preceding and following the sonic shock are simple waves, and not merely 2D effects similar to the rarefaction following the hydrodynamic shock on the stagnation line. To investigate this, it is interesting to compare the characteristic structure of this 2D stationary structure in the xy plane to the characteristic structure of the double compound wave in the xt plane, which has simple wave rarefactions. This is investigated in Sec. 6.4 using the characteristic properties of the steady state MHD equations. There it is shown that shock E–G is a genuine stationary double compound shock, mathematically completely analogous to the time-dependent double compound shock analyzed by Myong and Roe.

6.3 Parameter study of symmetrical bow shock flows

In this Section we report on a detailed parameter study of symmetrical field-aligned bow shock flows around a cylinder. We study how the shape and topology of the bow shock solution which was presented in the previous Section for one particular set of parameter values in the switch-on domain, changes when parameters are varied within the switch-on domain and when parameters are taken outside the switch-on domain. We present numerical simulation results for the values of the parameters β and M_{Ax} which are indicated by the triangles and diamonds in Fig. 6.3a.

Fig. 6.16 shows global views of the bow shock solutions for a fixed $\beta = 0.4$ with M_{Ax} varying from 1.1 to 1.9. We take $c_{Ax} = 1$ in the inflow, such that $M_{Ax} = v_x$. It follows from Eq. 6.3 that the critical Alfvénic Mach number under which switch-on shocks can exist is $M_{Ax} = 1.732$. For inflow speeds much faster than the Alfvén speed ($c_{Ax} = 1$), the upstream flow is pressure-dominated (no switch-on shocks). For pressure-dominated upstream parameters the bow shock has the traditional single-front topology that is also encountered in hydrodynamic bow shocks. When the inflow speed drops below 1.732, however, the flow becomes magnetically dominated (switch-on shocks occur). A concave-outward dimple forms in the leading shock front and a second shock front appears. This change in shape and topology of the bow shock flow thus happens exactly when the inflow speed becomes lower than the critical speed under which switch-on shocks are possible.

Fig. 6.17 shows a detailed representation of the flow near the stagnation streamline for the bow shock solutions with varying inflow speed of Fig. 6.16. For inflow velocities below the critical switch-on value for the inflow speed ($M_{Ax} < 1.732$), the leading shock front has a dimpled shape. The dimpling becomes much more pronounced as the inflow velocity decreases. Below the critical inflow speed, a second shock front appears which trails the leading shock front, and additional discontinuities are present between the two shock fronts. All the shocks and discontinuities present in the topology sketch of Fig. 6.7 seem to be present in all the flows. Inspection of the way in which the field lines are refracted when they pass the shocks, reveals that the shocks in all the flows are of the same type as the shocks in the model flow of Fig. 6.2 which was discussed in detail in Sec. 6.2, and this conclusion is confirmed

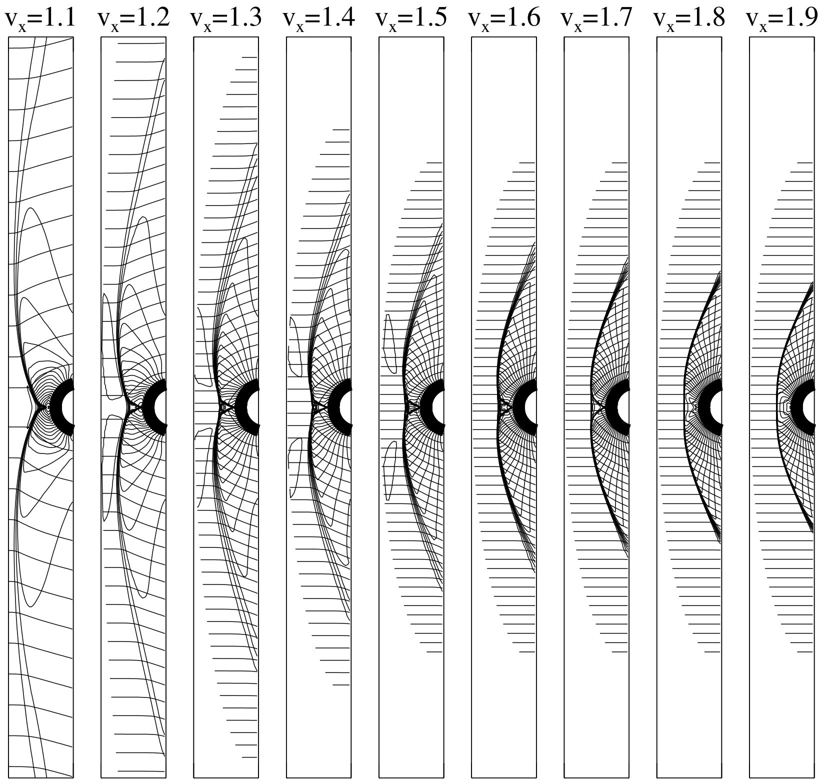

Figure 6.16: *Stationary bow shock solutions for fixed* $\beta = 0.4$ *and for varying inflow speeds* (80×80 *grids,* $x \in [-0.35, 0]$, $y \in [-2, 2]$)*. Density contours pile up in shocks, and streamlines come in horizontally from the left. For inflow speeds much faster than the Alfvén speed* ($c_{Ax} = 1$)*, the upstream plasma is pressure-dominated (no switch-on shocks), and the bow shock has the traditional single-front topology that is also encountered in hydrodynamic bow shocks. When the inflow speed drops below* 1.732 *however, the inflow becomes magnetically dominated, which means that switch-on shocks occur. For these magnetically dominated inflows a concave-outward dimple forms in the leading shock front and a second shock front appears.*

by detailed analysis of upstream and downstream Mach numbers, along the lines of the detailed analysis in the previous Section. For smaller inflow velocities, the central interaction region becomes smaller and the leading shocks become weaker while the trailing shock becomes stronger.

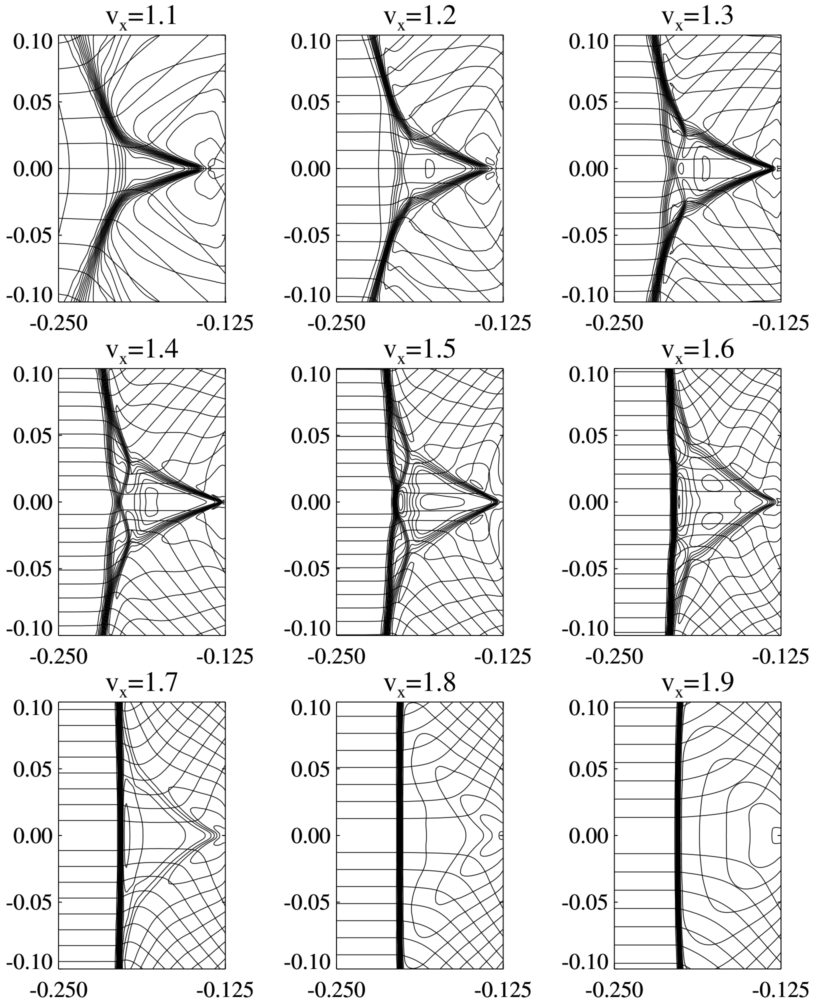

Figure 6.17: *Detailed representation of the flow near the stagnation streamline for the bow shock solutions with varying inflow speed and fixed* $\beta = 0.4$ *(*80×80 *grids). Density contours pile up in shocks, and streamlines come in horizontally from the left. When the upstream flow is magnetically dominated, the leading shock front dimples and a second shock front appears. Additional discontinuities can be seen between the two shock fronts.*

As a consequence, the shock E–G of Fig. 6.7 can not be identified for the flow with $v_x = 1.1$ with the resolution of Fig. 6.17. More detailed simulations and plots (not shown) do, however, show that shock E–G is present also for the flow with $v_x = 1.1$. For inflow velocity $v_x = 1.7$, close to the critical velocity of $v_x = 1.732$, the secondary shock fronts become weak and shock E–G can hardly be identified with the resolution of Fig. 6.17. For $v_x = 1.8$ the secondary (stationary) waves are still present, but they have not steepened into shocks any more. The secondary waves have disappeared almost completely for $v_x = 1.9$, and the simple single-front bow shock topology of Fig. 6.6a is recovered. We can thus conclude that for all the flows with magnetically dominated upstream parameters ($1 < M_{Ax} < 1.732$), the topology of Fig. 6.7 is a universal feature. The shapes, sizes and shock strengths of the shock parts present in the topology of Fig. 6.7, vary when M_{Ax} is varied within the switch-on region.

The dimple effect is more pronounced for smaller inflow Alfvénic Mach number M_{Ax}. This can be explained by the fact that when for magnetically dominated upstream flows v_x is increased towards v_{crit}, the maximum angle between the upstream magnetic field and the shock normal for which intermediate shocks can occur decreases. This means that for faster upstream flows, point D in Fig. 6.7, where the shock is of 1–3=4 type and beyond which the shock front splits up, lies closer to the perpendicular nose point B. The 1–3 intermediate shock segment which forms part of the dimple, is thus shorter and less deep for higher v_x. For instance, Figs. 3.9 and 3.10 show that for $v_x = 1.2$ the angle between the horizontal and the 1–3 shock front at point D is approximately 16°, whereas for $v_x = 1.5$ this angle is only 3°. This expected behavior is indeed observed in Figs. 6.16 and 6.17.

Above we discussed how the flow manages to go around the obstructing cylinder by adjusting the bow shock shape and topology to the inflow Alfvénic Mach number. Hereby the plasma β value was fixed to 0.4. Below we fix the inflow Alfvénic Mach number and verify how the flow modifies the geometrical structure of the bow shock when the value of the plasma β is varied.

In Fig. 6.18 we show global views of the bow shock solutions for a fixed $M_{Ax} = 1.5$ and β varying from 0.1 to 0.9. It follows from Eq. 6.3 that the critical plasma β under which switch-on shocks can exist is $\beta = 0.7$. For plasma β values larger than the critical value of $\beta = 0.7$, the upstream flow is pressure-dominated and the bow shock has the traditional single-front topology that is also encountered in hydrodynamic bow shocks. When the plasma β drops below 0.7, however, the inflow becomes magnetically dominated. A concave-outward dimple forms in the leading shock front and a second shock front appears. This second shock front thus appears precisely when the plasma β becomes lower than the critical plasma β under which switch-on shocks are possible.

Fig. 6.19 shows a detailed representation of the flow near the stag-

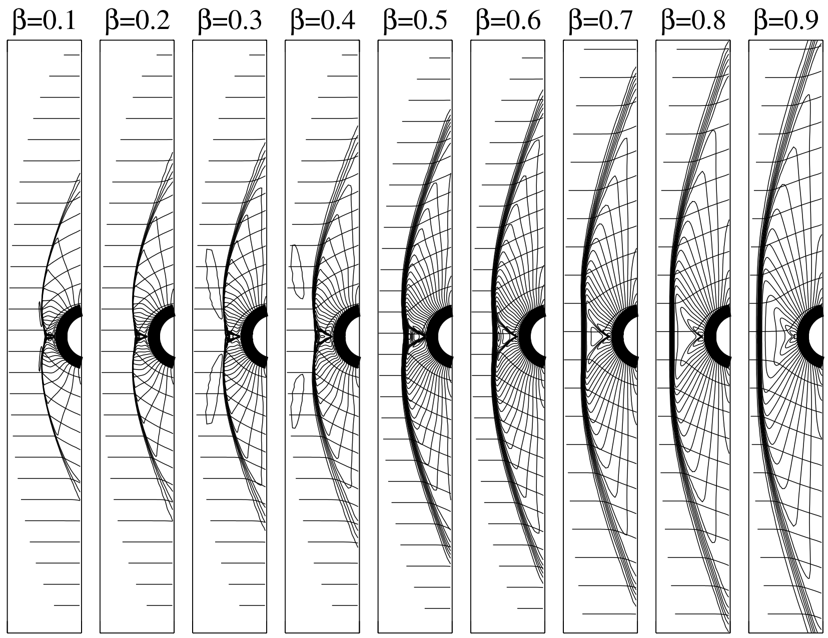

Figure 6.18: *Stationary bow shock solutions for fixed* $M_{Ax} = 1.5$ *and for varying plasma* β *(*80×80 *grids,* $x \in [-0.35, 0]$, $y \in [-1.4, 1.4]$*). Density contours pile up in shocks, and streamlines come in horizontally from the left. For plasma* β *values larger than the critical value of* $\beta = 0.7$ *the upstream flow is pressure-dominated, and the bow shock has the traditional single-front topology that is also encountered in hydrodynamic bow shocks. When the plasma* β *drops below* 0.7 *however, the upstream flow becomes magnetically dominated (switch-on shocks occur). A concave-outward dimple forms in the leading shock front and a second shock front appears.*

nation streamline for the bow shock solutions with varying plasma β of Fig. 6.18. We find again that the topology of Fig. 6.7 is universal for flows with plasma β values below the critical switch-on value ($\beta < 0.7$). The dimpling becomes more pronounced as the plasma β is decreased. For smaller plasma β values, the central interaction region in front of the cylinder becomes smaller. As a consequence, the shock E–G of Fig. 6.7 can not be identified for the flow with $\beta = 0.1$ with the resolution of Fig. 6.19. More detailed plots (not shown) do, however, show that shock E–G is present also for the flow with $\beta = 0.1$. For plasma

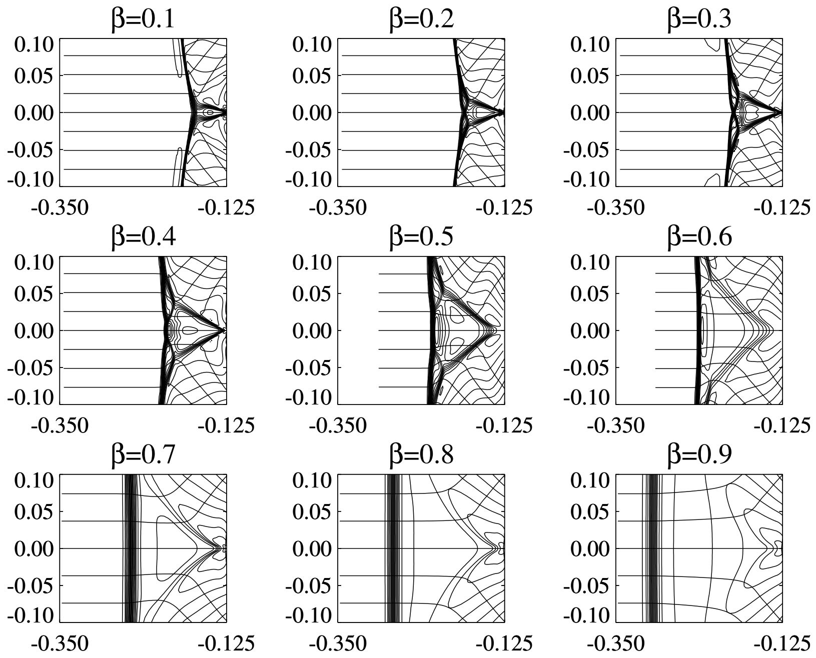

Figure 6.19: *Detailed representation of the flow near the stagnation streamline for the bow shock solutions with varying plasma* β *and for fixed* $M_{Ax} = 1.5$ *(*80×80 *grids). Density contours pile up in shocks, and streamlines come in horizontally from the left. Under the critical switch-on value for the plasma* β*, the leading shock front dimples and a second shock front appears. Additional discontinuities can be seen between the two shock fronts.*

$\beta = 0.7$, which is the critical value, the secondary (stationary) wave has only nearly steepened into a shock. Shock E–G can not be identified for this critical value of the parameters. For $\beta = 0.8$ the secondary waves are still present, but they have not steepened into shocks any more. The secondary waves are even weaker for $\beta = 0.9$, and the simple single-front bow shock topology of Fig. 6.6a is recovered. We can thus conclude that for all the flows with magnetically dominated upstream states ($\beta < 0.7$), the topology of Fig. 6.7 is recovered. The shapes, sizes and shock strengths of the shock parts present in the topology of Fig. 6.7, vary when β is varied in the switch-on regime. The dimple effect is more pronounced for smaller β.

As a remark, we can say that in the parameter regime under consideration, the stand-off distance of the bow shocks on the stagnation line [114] does not seem to be influenced by changing M_{Ax} while keeping β constant (Fig. 6.17), whereas the stand-off distance increases for increasing β while M_{Ax} is kept constant (Fig. 6.19). This is consistent with observations of planetary bow shocks [114].

The main conclusion from the parameter study described in this Section is that there are two basic topologies for symmetrical 2D MHD bow shock flows. When the magnetic field is strong enough for the intrinsically magnetic effect of switch-on shocks to occur, we call the upstream flow magnetically dominated. When the magnetic field is too weak for switch-on shocks to occur, we call the upstream flow pressure-dominated. For pressure-dominated upstream flows a single-front topology is obtained which is the same as the well-known topology of hydrodynamic bow shock flows. We call this topology the pressure-dominated MHD bow shock topology, and we say that the MHD bow shock flow is pressure-dominated. For magnetically dominated upstream flows, we find the complex bow shock topology sketched in Fig. 6.7. We call this topology the magnetically dominated MHD bow shock topology, and we say that the MHD bow shock flow is magnetically dominated. The bifurcation between the two basic topologies occurs precisely on the border between the pressure-dominated and magnetically dominated parameter regimes as defined in terms of the occurrence of switch-on shocks. The complexity of the magnetically dominated MHD bow shock topology is due to intrinsically magnetic effects. The magnetically dominated MHD bow shock topology was previously unknown.

The existence of two basic MHD bow shock topologies proven in this Section is an *a posteriori* justification for the terminology of magnetically dominated versus pressure-dominated upstream states, bow shock flows and bow shock flow topologies which we have been using since the Introductory Chapter. In the next Chapter we show, although less extensively than for the 2D case, that the 3D flow of a superfast MHD plasma over a sphere also exhibits two basic bow shock topologies, with a clear bifurcation again arising precisely on the border between the pressure-dominated and magnetically dominated parameter regimes. The terminology we use to refer to these two basic bow shock flow topologies is thus universally valid for MHD bow shock flows in 2D and in 3D.

6.4 Characteristic analysis and steady compound shocks

In the present Section we further investigate the complicated magnetically dominated bow shock flow discussed in Sec. 6.2 using the characteristic properties of the steady MHD equations in two space dimensions (in the xy plane). The theory of MHD characteristics described in Sec. 3.2 is used extensively. A geometric view of this steady flow is presented in terms of transition lines, cusping of characteristics, limiting lines, and elliptic and hyperbolic regions in the flow. This analysis yields a clear insight into a complicated nonlinear MHD flow with interacting shocks, and the consistency of the interpretation in terms of characteristics further validates the numerical results discussed above. In the recent literature, characteristic analysis of steady MHD flows has been applied to the study of astrophysical flows [62, 131, 163, 19] and stationary symmetric and transonic flows [93, 53]. In these papers analytical solutions of the steady MHD equations in two dimensions (2D) are obtained under various assumptions of self-similarity. The presence of shocks and the absence of any self-similarity assumption in the bow shock flows to be analyzed in this Section are new elements not treated in earlier characteristic analysis of MHD flows [62, 131, 163, 19, 93, 53].

In Sec. 6.2, the planar magnetically dominated bow shock solution was shown to contain an intermediate shock which is preceded and followed by steady rarefactions with the particular property that the normal plasma velocity is equal to a normal characteristic speed at the points where the rarefactions are attached to the shock (Fig. 6.15). This is one of the basic properties of an xt compound shock [90, 12] (see Sec. 3.3.5). However, the correspondence between xt compound shocks (with an attached simple wave rarefaction which is continuously expanding in time), and steady wave structures in two space dimensions (xy), is not immediately clear and does not follow trivially from the respective governing equations, although a general conceptual analogy can be expected between wave structures in the xt and the xy planes, such as demonstrated for compressible fluid dynamics [160]. Such a correspondence has also been worked out analytically for simple MHD waves in the xt and the xy planes [85]. In the present Section we explore the correspondence between complex wave patterns in the xt and the xy planes using characteristic properties of the steady MHD equations in two space dimensions (xy).

The characteristic analysis of the magnetically dominated multiple-front MHD bow shock flow is quite complicated, so it is useful to gain some insight from more simple configurations first. We start out with the simple case of a traditional hydrodynamic bow shock flow, followed by a discussion of the characteristic analysis of a pressure-dominated single-front planar MHD bow shock flow, before we proceed with the case of the magnetically dominated multiple-front planar MHD bow shock flow. We relate the results of the analysis of this flow to recent findings on stationary symmetric flows [53] and on xt MHD compound shocks [12, 110].

6.4.1 Hydrodynamic bow shock

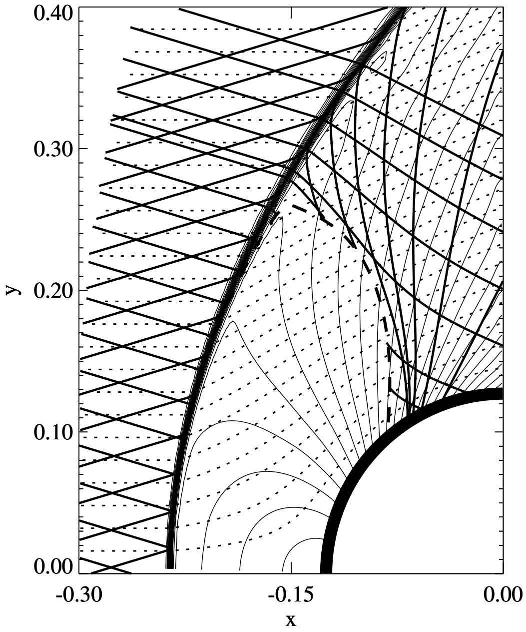

Figure 6.20: *Bow shock flow for the hydrodynamic case* ($v_x = 2,\ B_x = 0$).

Fig. 6.20 shows the simulation result of a hydrodynamic bow shock with $v_x = 2$ and $B_x = 0$ for the incoming flow. We take $\rho = 1$ and $p = 0.2$ for the inflow of all the bow shock flows presented in Sec. 6.4. The shock is clearly seen where the density contours (thin solid lines) are piling up. The streamlines (dotted) are double characteristics, and s and h_s are the corresponding Riemann Invariants along these characteristics. The thick solid lines are the two families of hydrodynamic characteristics (Mach lines [20]) making equal angles ψ with the streamlines. The thick dashed transition line is the $M = 1$ contour, separating the subsonic elliptic region close to the cylinder from the rest of the flow, which is supersonic and thus hyperbolic. The Mach lines are perpendicular to the streamlines at the transition line, corresponding to case (b) of Fig. 3.5.

Limiting characteristics [20, 53] (or limiting lines) are the convex hulls of characteristics which appear when characteristics of one family start to pile up and develop those convex hulls. Limiting characteristics can not exist in real flows, unless they are perpendicular to the streamlines. They are generally avoided through the appearance of shocks [20, 53], because at the location of the limiting characteristic the solution would be multi-valued. In the bow shock flow of Fig. 6.20 it is indeed seen that limiting lines are not present, but that shocks bring the flow from the upstream supersonic state to a downstream elliptic (close to the stagnation point) or hyperbolic (further away from the stagnation point) state [53].

6.4.2 Pressure-dominated MHD bow shock

In Fig. 3.6 we have shown the simulation result of a pressure-dominated fast MHD bow shock with $v_x = 2$ and $B_x = 1$ for the incoming flow. The inflow plasma β is low, but these inflow parameters do not allow for switch-on shocks, so that we get a simple traditional single-front MHD bow shock. The characteristic structure of this flow, which was discussed in Sec. 3.2, is very similar to the structure of the hydrodynamic flow. The angle ψ is a little larger, such that the bow shock and the characteristics are opened up a little compared to the hydrodynamic case. The influence of the magnetic field on this angle is clear: the angle is always larger than the corresponding hydrodynamic angle ($B_x = 0$), as

$$\sin^2 \psi_{MHD} = \frac{M^2 + M_A^2 - 1}{M^2 M_A^2} \geq \sin^2 \psi_{HD} = \frac{1}{M^2} \tag{6.4}$$

for supersonic flow ($M^2 \geq 1$). The comments regarding limiting characteristics that were given in the hydrodynamic case, also apply to this fast MHD bow shock flow.

6.4.3 Magnetically dominated MHD bow shock

Fig. 6.21 shows the simulation result of a magnetically dominated MHD bow shock flow with $v_x = 1.5$ and $B_x = 1$ for the incoming flow. This is the flow discussed in Sec. 6.2. The angle ψ in the upstream part is larger than in the single-front case of Sec. 6.4.2. The bow shock is opened up even more and a 'dimple' appears in the shock front near the stagnation streamline, where the front is now curved convex outward from the cylinder. A second shock front is seen to have separated from the leading shock front. Additional discontinuities can be seen between these two shock fronts.

These complex shock interaction phenomena lead to a flow which is quite a bit more complicated in terms of characteristic analysis. The dotted lines again indicate the streamlines, and the thick solid lines

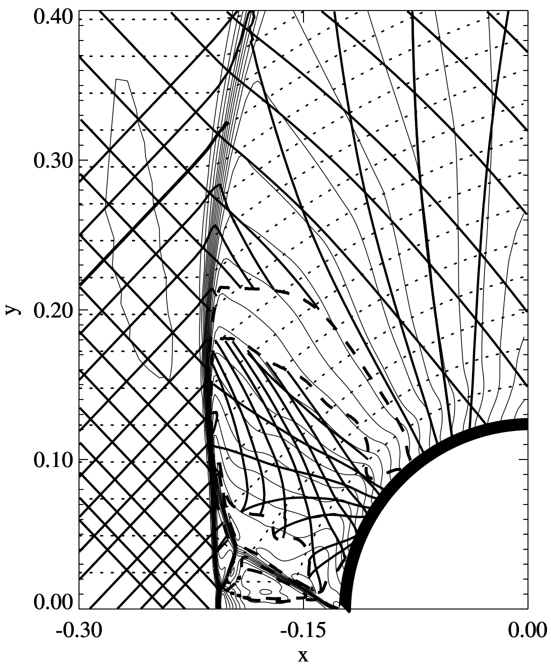

Figure 6.21: *Magnetically dominated MHD bow shock flow ($v_x = 1.5$, $B_x = 1$). Density contours (thin solid lines) pile up in the shocks. The streamlines (which are also magnetic field lines) are dotted. The thick solid lines are two families of fast characteristics making equal angles with the streamlines. Several elliptic and hyperbolic regions are present.*

indicate the two families of characteristics which are of the slow or fast type depending on the location in the flow. Several separate elliptic regions can be seen.

Fig. 6.22 presents an analysis of the hyperbolicity of the flow. The thick solid line is the $\beta^* = 1$ contour. The $M = 1$ contour (thick dashed), the $M_A = 1$ contour (thick dotted), and the $M_{cusp} = 1$ contour (thick dash-dotted), are the transition lines between elliptic an hyperbolic regions. We can label the regions according to the classification of Fig. 3.4. The incoming flow is hyperbolic of the type Hf2. Downstream of

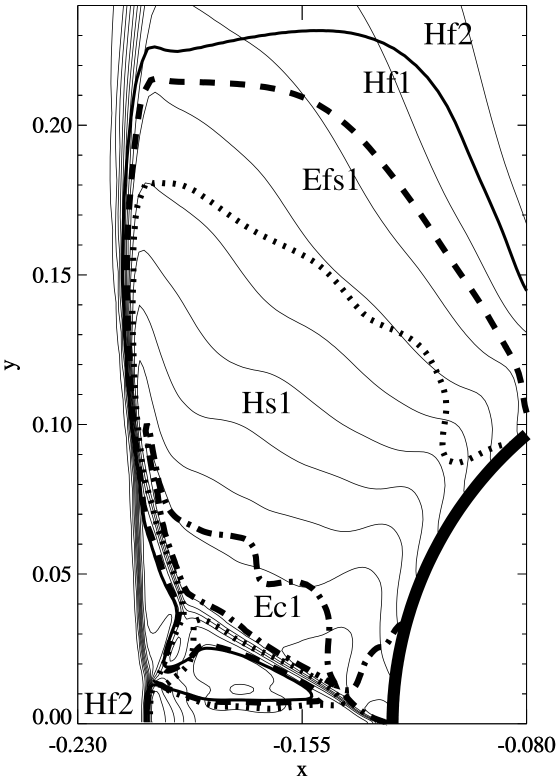

Figure 6.22: *Elliptic and hyperbolic regions in the bow shock flow. Density contours (thin solid lines) pile up in the shocks. The $\beta^* = 1$ contour (thick solid), the $M = 1$ contour (thick dashed), the $M_A = 1$ contour (thick dotted), and the $M_{cusp} = 1$ contour (thick dash-dotted) separate the different regions.*

the leading and the second shock fronts, and starting from above, the flow is first hyperbolic of the type Hf2, and becoming hyperbolic of the type Hf1 as the $\beta^* = 1$ contour is crossed. Crossing the $M = 1$ contour brings us into an elliptic region of type Efs1, followed by a hyperbolic region of type Hs1 when the $M_A = 1$ contour is crossed. In Fig. 6.21

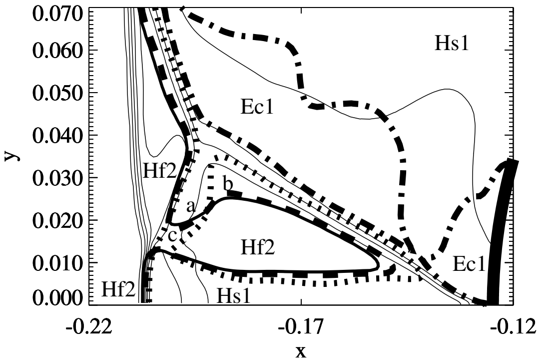

Figure 6.23: *Elliptic and hyperbolic regions in the bow shock flow near the stagnation streamline. Density contours (thin solid lines) pile up in the shocks. The $\beta^* = 1$ contour (thick solid), the $M = 1$ contour (thick dashed), the $M_A = 1$ contour (thick dotted), and the $M_{cusp} = 1$ contour (thick dash-dotted) separate the different regions. Region a is Hs1, region b is Efs1, and region c is Efs2.*

we see that the characteristics are perpendicular to the streamlines at these transition lines. Further down, we reach the elliptic region of type Ec1 as the $M_{cusp} = 1$ contour is crossed. At this transition line, the characteristics show the expected cusping behavior of Fig. 3.5c, as can be seen in Fig. 6.21.

In Fig. 6.23 we show a more detailed plot of the interaction region near the stagnation streamline. The incoming flow is Hf2, and it remains Hf2 through the fast shock DE. Shock EG brings the flow into a Hs1 region (region a), as we cross the $\beta^* = 1$, $M = 1$, and $M_A = 1$ contours simultaneously. From region a, crossing the $M_A = 1$ contour leads us to a Efs1 region (region b), and crossing the $\beta^* = 1$ and $M = 1$ contours leads to a Efs2 region (region c). Near the stagnation streamline at the bottom, shock EF brings the flow into a Hs1 region, as the $\beta^* = 1$, $M = 1$, and $M_A = 1$ contours are crossed simultaneously. Enclosed between regions c, b, and the Hs1 region at the bottom, we find a Hf2 region.

As could be expected, we do not encounter limiting lines in this flow, but instead we find shocks. Shock transitions exist between two hyperbolic regions (for example, from Hf2 to Hf2 through shock DE, and from Hf2 to Hs1 through shocks EG, EF, and BD), between a hyperbolic and an elliptic region (for example, from Hf2 to Efs1 above point B ($M_A = 1$

downstream of point B), and from Hf2 to Ec1 through shock DG), and apparently also between elliptic regions of different types (from region b (Efs1) to Ec1 through shock GH), although we have to remain careful with our conclusions as the numerical resolution is not very high in this small region. This last type of shock transition from elliptic to elliptic may be surprising at first sight, but a similar theoretical result has recently been reported, based on explicit solutions for stationary symmetric self-similar MHD flows, stating that this type of shock transition is possible [53]. We can conclude that the flow configuration, characteristic analysis, and types of shock transitions of our interacting bow shock solution are illustrations and 2D extensions of many of the recent theoretical results obtained from analysis of stationary symmetric self-similar MHD flows [53].

We now investigate if we can identify steady compound shocks in the complex bow shock flow. A steady compound shock should have the following properties, based on carrying over the geometry of characteristics from the xt case to the xy case. First, the flow should be hyperbolic on the two sides of the shock. Second, the shock should have a rarefaction attached to it which is a simple wave with one family of characteristics consisting of straight lines. Third, the xy characteristics should be parallel to the shock in the xy plane, such that the flow is sonic in the xy plane where the shock is attached to the rarefaction. We now analyze several wave structures in the simulated bow shock flow to see if they fulfill these criteria.

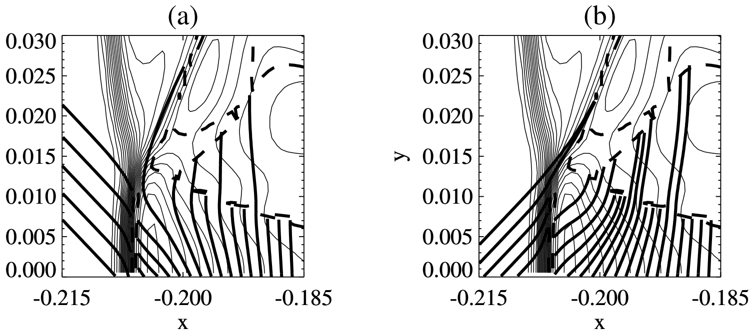

Figure 6.24: *Two families of characteristics (thick solid) near the shock EF. The thin lines are density contours. The characteristics enter the shock, so this is not a compound shock.*

We start with the leading shock at the stagnation streamline. Fig. 6.11a suggests that this could be a steady compound shock. Fig. 6.23

confirms that the flow is hyperbolic on both sides of the shock, but the behavior of the two characteristic families in Fig. 6.24 shows that this is not a steady compound shock as we have defined above. Neither of the characteristics is parallel to the shock where the rarefaction is attached to the shock, and the two families are not straight but interact in the rarefaction which is thus not a simple wave. This conclusion is consistent with the discussion in Sec. 6.2, where it was shown that this rarefaction is of a different physical origin, being a 2D effect associated with the converging flow behind the shock. The plasma speed equals neither of the wave speeds where the rarefactions are attached to the shock, as was shown in Fig. 6.11f–h.

Fig. 6.24 also reveals another interesting phenomenon. As the pressure in the rarefaction in Fig. 6.11b drops when going to the right, the characteristics in 6.24 straighten and form one coinciding limiting characteristic where the pressure reaches a constant state after the rarefaction (at approximately $x = -0.185$). This limiting characteristic is allowed because the streamlines are perpendicular to it. This limiting line is a locus of weak discontinuity, where the pressure is continuous, but the slope of the pressure has a discontinuity. This weak discontinuity connects the rarefaction region with the uniform flow region behind it, and Fig. 6.11h shows that the flow is indeed sonic at the location of this weak discontinuity. The rarefaction region bordering the uniform region is, however, not a simple wave region, such that this special configuration with a limiting characteristic seems to be an exception to the rule that a uniform region in a stationary 2D flow can only be bordered by a simple wave region [20].

We now turn our attention to intermediate shock EG. Fig. 6.15 suggests that this could be a steady compound shock with an embedded 1=2—3=4 intermediate shock. The behavior of the two characteristic families shown in Fig. 6.25, shows that the flow is hyperbolic on both sides of the shock. The second family of characteristics (Fig. 6.25b) is parallel to the shock on the right, and goes into the shock on the left. The characteristics of this family are straight on the right of the shock, indicating a simple centered slow rarefaction wave with the characteristics apparently converging in point G. The first family of characteristics (Fig. 6.25a) is parallel to the shock on the left, and goes into the shock on the right. The characteristics of this family are straight on the left of the shock. The intermediate shock is thus preceded and followed by simple rarefaction waves which are sonic at the point where they are attached to the shock. This rarefaction-shock-rarefaction structure has thus all the defining properties of a compound shock. This compound shock is sonic on the two sides, so we can call this newly identified steady wave structure a *double steady compound shock* (Fig. 6.26b). The analogous xt structure has been predicted theoretically recently in the context of xt

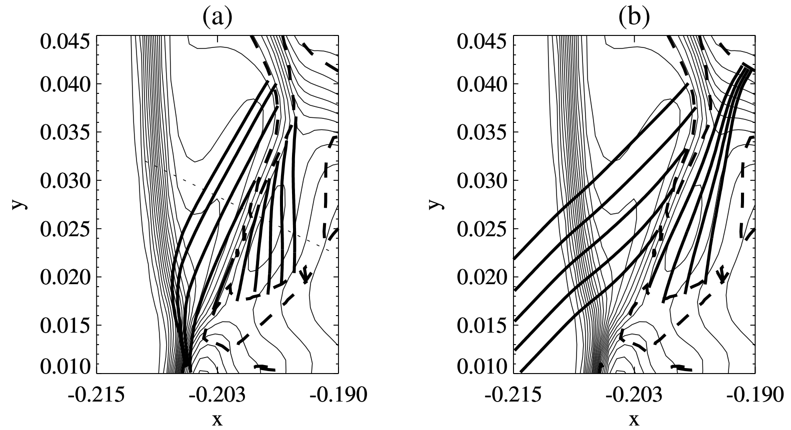

Figure 6.25: *Two families of characteristics (thick solid) near the intermediate shock EG. The thin lines are density contours. On each side of the shock, the characteristics of one family are straight lines and become parallel to the shock, so this is a double compound shock.*

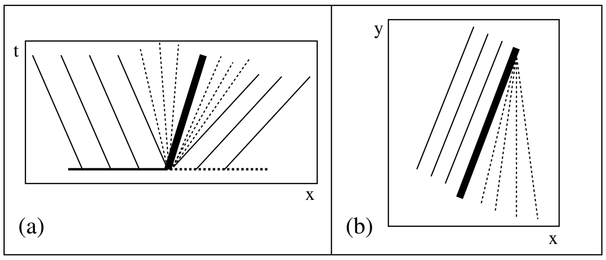

Figure 6.26: *(a) Sketch of the recently theoretically predicted double xt compound shock. The shock (thick) is preceded and followed by rarefactions (thin dotted), which are attached to the shock with characteristics parallel to the shock. (b) Sketch of the topology of the characteristics near the double xy compound shock which is present in our simulation results. The shock (thick) is preceded and followed by simple wave rarefaction regions, which are attached to the shock with straight characteristics parallel to the shock.*

compound shocks [110] (Fig. 6.26a). It has not been identified yet in xt simulations, but it is noteworthy that we encounter the analogous steady xy structure in our 2D simulation results. This new steady structure is a manifestation of the non-convex nature of the MHD equations, just like the sonic intermediate shocks embedded in xt time-dependent compound shocks are a manifestation of this property. We have thus established by explicit example a remarkably complete analogy between the characteristic structure of time-dependent compound waves in the xt plane and the characteristic structure of steady compound waves in the xy plane. Following Myong and Roe [110], we argue that this steady compound shock occurs as a substitute for a 2—3 intermediate shock which is undercompressive and inadmissible in the planar case (see Chap. 9).

We suggest the following physical relationship between the two kinds of compound shocks, those of time-dependent flows in the xt plane and those of steady flows in the xy plane. If an initial plane compound shock taken in the time-dependent sense and moving in xyt space with a sonic fast rarefaction (which is expanding in time) attached to it, were to slow down and become steady, then such a structure could conceivably retain the property that the now steady rarefaction is sonic ($v_\perp = c_{f\perp}$) at the point where it is attached to the shock. This is precisely the defining property of a fast characteristic in steady xy space (see Sec. 3.2), which means that all the points at the locus where the rarefaction is attached to the shock with a sonic speed, lie on a steady xy characteristic parallel to the shock, thus explaining that the steady xy characteristic is parallel to the shock where the rarefaction is attached to it. This observation clarifies a natural relationship between xt and xy compound shocks, which could possibly be further explored by explicit numerical simulation of the above proposed scenario. It also explains why the flow in terms of xt wave speeds is sonic where the rarefactions are attached to the shocks in steady compound shocks, as can be seen in Fig. 6.15bc.

6.5 Symmetry and stability

In this Section we investigate the global stability against perturbations of the symmetrical magnetically dominated bow shock solutions discussed in the previous sections.

All the simulation results shown in this Chapter up till now were calculated on a grid restricted to the upper left quadrant with the top-bottom symmetry explicitly imposed. As mentioned before, this flow in the upper quadrant can be interpreted physically as the flow over a perfectly conducting plate with a semi-circular bump or corner. The numerical results seemed to indicate that the obtained flow topology is stable against perturbations, and in this Section we give some more elements to support this.

The full problem of a flow around a cylinder should in theory have the same symmetrical solution, because the initial condition and the

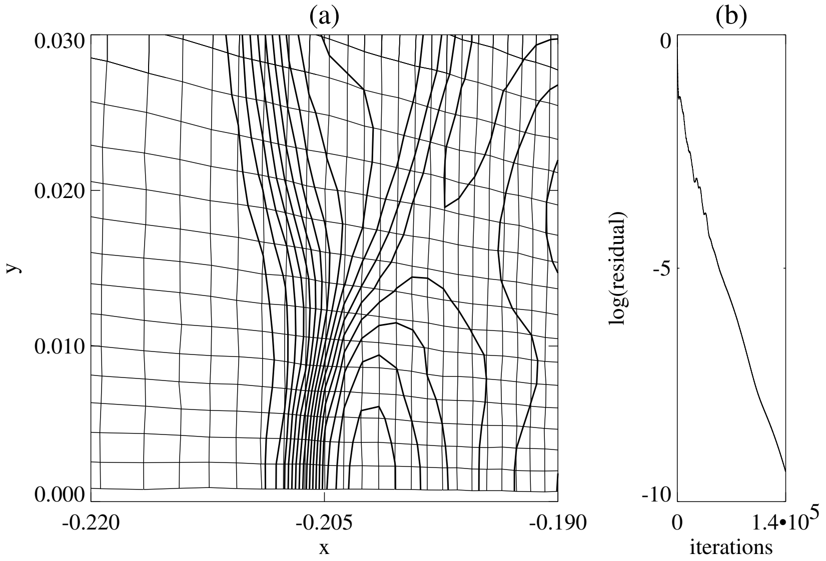

Figure 6.27: *LF flow solution and convergence for the symmetrical bow shock problem on a randomly perturbed grid* (80×80)*. The grid shown in (a) is a grid of cell centers.*

boundary conditions are symmetrical, and the MHD equations should conserve this symmetry. However, the stationary solution and its topology may be globally unstable against non-symmetrical perturbations. Such an instability might be triggered by explicit non-symmetrical perturbations, but also by non-symmetrical grids or a numerical code which is not perfectly symmetrical.

Fig. 6.27 shows that we obtain the complex bow shock topology for a flow restricted to the upper quadrant when we perturb the corner points of the finite volume cells in a random way, and that the solution converges to a perfect steady state. The corner points which lie on the boundary of the simulation domain were not perturbed. Fig. 6.28, however, shows that the full problem of the magnetically dominated flow around a cylinder in the switch-on regime without imposed symmetry leads to a very a-symmetrical unsteady flow when the grid is randomly perturbed. This is an indication that the symmetrical solution is unstable against non-symmetrical perturbations, although it is not a proof.

Another indication is given by the following observations. We consider the flow around a cylinder and also simulate the flow behind the cylinder. Fig. 6.29 shows the bow shock flows for inflow parameters

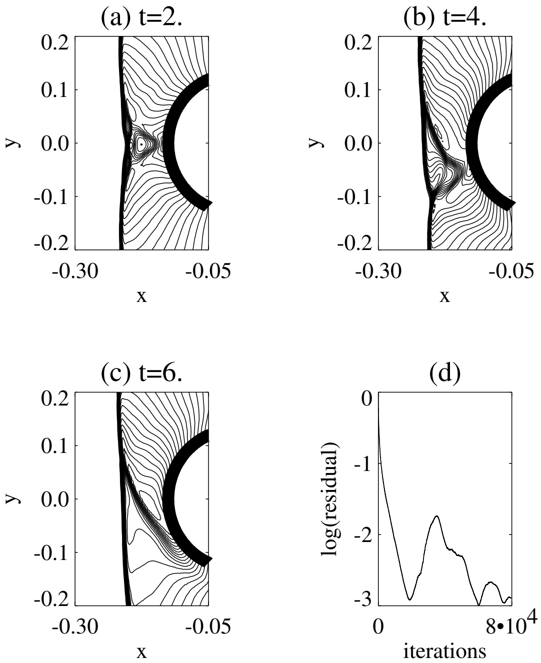

Figure 6.28: *LF flow solution* (120×240 *grid) and convergence for the magnetically dominated bow shock problem on a randomly perturbed full grid without explicitly imposed symmetry.*

$\rho = 1$, $p = 0.2$ and $v_x = 1.5$, simulated on the whole domain. The flow in the wake of the cylinder is subfast, so we use the characteristic boundary conditions described in Sec. 4.2.6 for the outer boundary. Fig. 6.29a shows the hydrodynamic case ($B_x = 0$), and Fig. 6.29b shows the case of a pressure-dominated MHD bow shock ($B_x = 0.5$). The two flows show the traditional pressure-dominated concave-inward bow shock shape and topology. We have investigated the stability of these flows against non-symmetrical perturbations by adding a small uniform upward or downward vertical velocity $v_y = \pm 0.01$ to the initial condition or by restarting the simulation from the stationary solutions of Fig. 6.30 perturbed by such a vertical velocity. In all these cases the flow returned to the stationary solutions of Fig. 6.29, which indicates that these traditional bow shock topologies are stable against non-symmetrical perturbations.

Fig. 6.30 shows the bow shock flows for magnetically dominated inflow parameters $\rho = 1$, $p = 0.2$, $v_x = 1.5$ and $B_x = 1$, such that

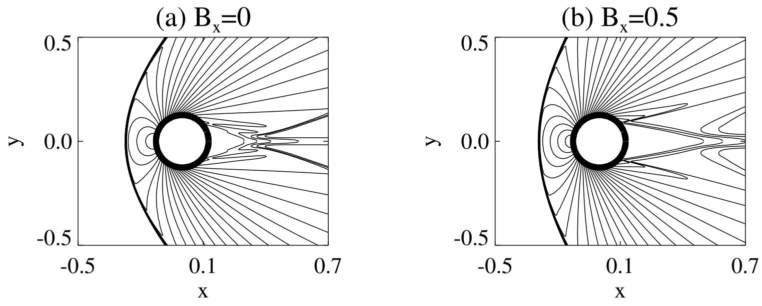

Figure 6.29: *Bow shock flows around a cylinder. (a) Hydrodynamic flow: $M_x = 2.6$ and $B_x = 0$. (b) Pressure-dominated MHD flow: $M_x = 2.6$, $M_{Ax} = 3$ and $B_x = 0.5$*

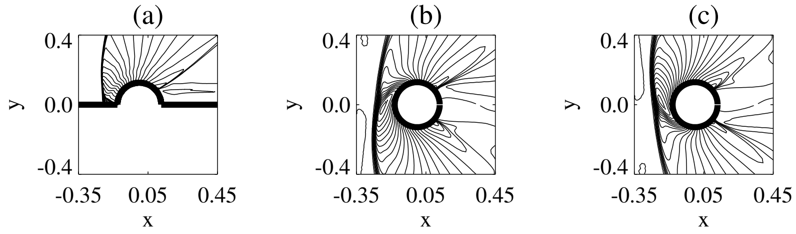

Figure 6.30: *Magnetically dominated MHD bow shock flow. (a) Symmetrical solution on a domain restricted to the upper half plane. (b) Non-symmetrical solution obtained when starting from an initial condition perturbed with a small downward velocity. (c) Non-symmetrical solution obtained when starting from an initial condition perturbed with a small upward velocity.*

$M_{Ax} = 1.5$. Fig. 6.30a shows the flow simulated in the upper half plane (400×400 grid), with the symmetry on the stagnation line explicitly imposed. In front of the cylinder we obtain the same stationary magnetically dominated flow topology that was described earlier. Simulation after perturbation of the initial condition or the stationary flow as described above, leads invariably back to the same stationary solution of Fig. 6.30a. Figs. 6.30b and c, however, show a completely different behavior for simulations on the full domain (100×200 grids). Perturbation of the initial condition with a small uniform upward (c) or downward (b) vertical velocity $v_y = \pm 0.01$, results in a flow topology which is *entirely* *different* from the symmetrical result. This is a strong indication that the symmetrical solution is unstable against non-symmetrical perturbations. The resulting non-symmetrical flow is intermittent. The leading shock front is again dimpled, and the leading shock front is followed by a secondary shock front. The V-shaped secondary feature of Fig. 6.2 is, however, completely absent in this non-symmetrical flow result.

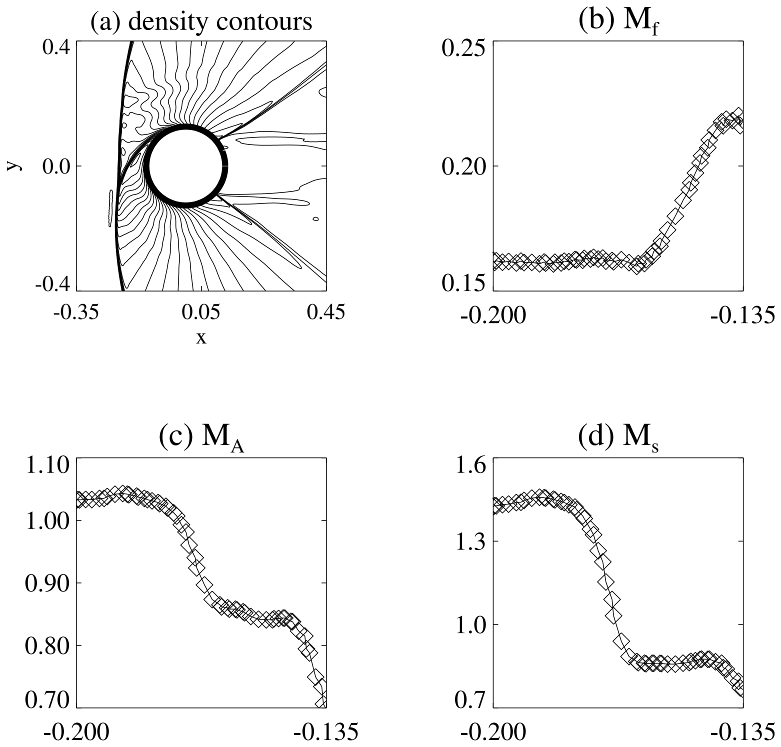

Figure 6.31: *(a) Non-symmetrical magnetically dominated bow shock flow. (c–d) Cuts along a line perpendicular to the secondary shock front.*

In Fig. 6.31 we determine the MHD shock type of the secondary shock front for a simulation on a 400×800 grid. Figs. 6.31c–d show cuts along a line perpendicular to this secondary shock. This shows that the shock is an intermediate shock of the 2–4 type, close to a 2=3–4 slow switch-off shock. This shock is thus of the same type as shock D–G–H–I in the topology of the symmetrical solution sketched in Fig. 6.7. In the next

Chapter we break the symmetry by introducing a small angle between the magnetic field and the velocity for the flow over a sphere. We obtain solutions which are topologically similar to the solutions of Figs. 6.28, 6.30 and 6.31.

We have to admit that in most cases we did not obtain the symmetrical solution when we performed our simulations of the non-perturbed problem on the full grid (the left half plane or the full plane) without the symmetry explicitly imposed at the stagnation line. This is because our code and the grid used are not perfectly symmetrical. It is extremely difficult to make a numerical code perfectly symmetrical, and the best way to make sure that simulation results are symmetrical, is to impose the symmetry explicitly, as we have done for our simulations on the restricted domain of the upper left quadrant.

What does this conclusion on instability imply for the symmetrical magnetically dominated bow shock topology presented and discussed in the previous Sections? The symmetrical solution is likely to be a *meta-stable* solution in the case of the full flow around a cylinder. Meta-stable solutions are not necessarily unphysical and can arise in physical systems under special conditions — the reader may recall the case of an undercooled fluid for instance —, but it is not likely to find the topology of Fig. 6.7 with a V-shaped secondary front in real stationary bow shock flows around obstacles, because small perturbations are probably sufficient to change this topology into the topology of Fig. 6.31a.

The symmetrical solution and the detailed discussion remain relevant for several reasons, however. First, we have shown that the symmetrical solution obtained by simulation in the upper left quadrant with the symmetry explicitly imposed is stable against perturbations as long as the symmetry remains strongly imposed. This flow thus constitutes an example of a stable 2D MHD flow in which various types of intermediate and compound shocks are present, and this rich structure and topology makes this flow certainly interesting in its own right. The physical interpretation as a flow over a perfectly conducting plate with a semi-circular bump or corner does not immediately seem to have realistic applications, but our solutions are excellent explicit examples to illustrate similar topologies and transitions between hyperbolic and elliptic regions involving shocks that may possibly be found in related configurations with astrophysical relevance. Second, the non-symmetrical topology of Figs. 6.30b and c still is typified by two conspicuous morphological properties, namely a concave-outward dimple in the leading shock front and a secondary shock front following the leading front. These important newly discovered properties remain intact from the symmetrical solution. Moreover, in the next Chapter we show that the V-shaped structure from the symmetrical topology can still arise in non-symmetrical configurations as a time-dependent *transient* structure (as in Fig. 6.28).

The detailed study performed in Secs. 6.2 and 6.4 of the shock types and waves present in the symmetrical solution turns out to be very helpful in the analysis of these time-dependent flows for the non-symmetrical case.

The reader may wonder why we do not study the stability of the symmetrical solution by perturbing the *boundary conditions* together with the initial condition. Indeed, it seems natural to introduce a-symmetry by introducing a small angle between the velocity and magnetic field in the boundary conditions of the stationary problem. In a 2D flow, however, we cannot do this because for a stationary solution in 2D the flow necessarily has to be field-aligned when ideal walls are present in the problem. Equivalently, and more physically, we can say that the magnetic flux would pile up in front of the cylinder in the case of non-field-aligned 2D flow, because field lines cannot break in ideal MHD. The non-field-aligned 2D ideal MHD problem would thus not lead to a steady state, since the field lines cannot be advected across the cylinder. In the case of field-aligned flow, the magnetic flux is split into two equal parts which can flow around the cylinder on the left and the right sides. In the case of 3D flow over a perfectly conducting sphere, however, we can introduce an angle between the velocity and magnetic fields. A non-symmetrical stationary flow then results, because the field lines can slip over the top and the bottom of the sphere in 3D space. This is studied in the next Chapter. There we also perform a simulation for the special case of field-aligned flow over a sphere, and we obtain a symmetrical flow configuration with a topology similar to the topology sketched in Fig. 6.7. We can study the stability of this symmetrical solution by introducing a small angle between the fields. In fact this way to study the stability of the symmetrical flow is more rigorous and well-defined than the approach to stability study of the 2D flow given in this Section.

6.6 Conclusion

Let us summarize the physical lessons we have learned in this Chapter. There are two basic topologies for symmetrical 2D MHD bow shock flows. For pressure-dominated upstream flows a single-front topology is obtained which is the same as the well-known topology of hydrodynamic bow shock flows. For magnetically dominated upstream flows, the intrinsically magnetic phenomena of switch-on shocks and intermediate shocks cause the bow shock flow to assume a complex topology which was previously unknown. This magnetically dominated flow topology involves not only shock fronts composed of segments of different MHD shock types, but also a multitude of interacting fronts. The manner in which these shock types arise on a front or the presence of multiple fronts all relate to the dynamics of information transfer by the MHD characteristic waves to guide the superfast flow around the obstacle. Put in these general terms, the numerical work presented in this Chapter has broadened our physical thinking on bow shock flows in MHD, in particular, and on hyperbolic systems with multiple characteristic waves, in general.

Chapter 7

Magnetically dominated MHD bow shock flows: three-dimensional flow over a sphere

In this Chapter we present numerical simulation results of 3D MHD bow shock flows around perfectly conducting rigid spheres.

Fig. 7.1 shows a 3D visualization of a bow shock flow around a sphere with magnetically dominated uniform upstream flow (switch-on shocks occur). In the 3D flow magnetic field lines can slip over the sphere, so we are not restricted to field-aligned flow like in the 2D case, but we can consider upstream flows with an angle θ_{vB} between the magnetic field and the velocity. In the flow of Fig. 7.1 the angle $\theta_{vB} = 5°$. The upstream magnetic field is aligned with the x-axis. The xy plane is the plane going through the center of the sphere to which the upstream magnetic field and velocity vectors are parallel. The xy plane is a plane of top-bottom symmetry. Shaded density contours and magnetic field lines are shown in the xy plane, and density contours are plotted in two additional grid planes. Fig. 7.1 shows that a complex topology involving two consecutive shock fronts is obtained for this magnetically dominated bow shock flow. This topology is very different from the traditional single-front topology known from hydrodynamic bow shock flows (Fig. 2.3). The magnetically dominated flow of Fig. 7.1 shows a slightly dimpled leading shock front and a secondary shock front which is attached to the leading front and which extends well out of the xy plane. The magnetic field lines are refracted strongly at the secondary shock, which indicates that this shock is of the slow or intermediate type.

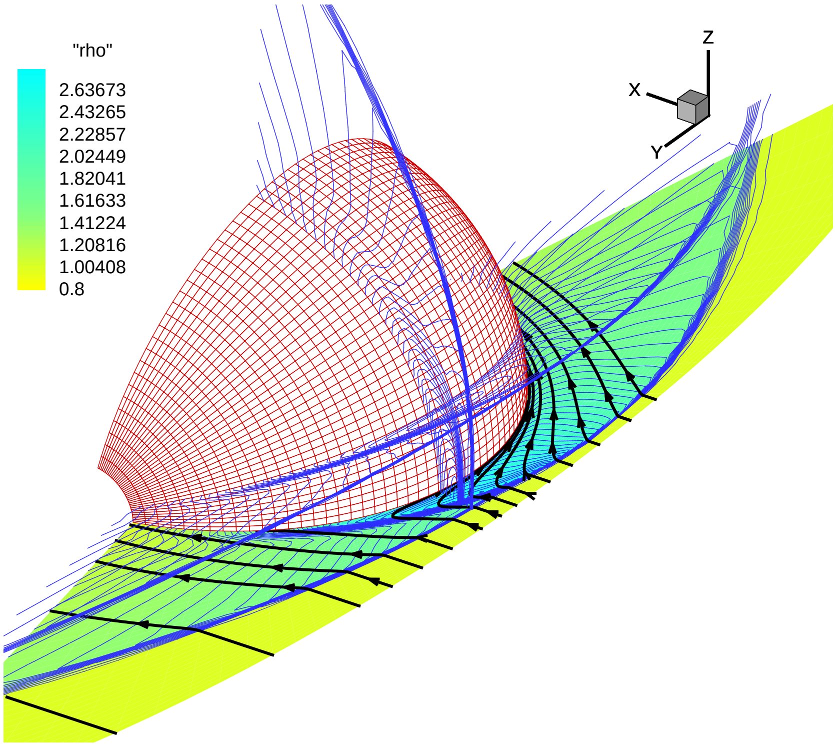

Figure 7.1: *Magnetically dominated 3D bow shock flow around a sphere with inflow* $\beta = 0.4$, $M_{Ax} = 1.49$, *and* $\theta_{vB} = 5°$. *Density contours and magnetic field lines are shown in the xy plane, which is a plane of symmetry parallel to the upstream magnetic field and velocity vectors and going through the center of the sphere. Density contours are also shown in two additional planes. In the upstream flow the magnetic field is aligned to the x-axis. The leading shock front is clearly followed by a secondary shock front, which is attached to the leading front, and which extends well out of the xy plane* ($40 \times 80 \times 40$ *grid).*

The numerical simulation results to be presented in this Chapter show that there exist two basic topologies for 3D MHD bow shock flows. For pressure-dominated upstream flows a single-front topology is obtained which is the same as the well-known topology of hydrodynamic bow shock flows. For magnetically dominated upstream flows, for which switch-on shocks occur, we find the complex bow shock topology of Fig. 7.1. This magnetically dominated bow shock topology was previously unknown.

3D MHD computations are numerically challenging and they push computer hardware performance to its limit. Therefore the 3D simulation results presented in this Chapter are less exhaustive than the 2D results presented in the previous Chapter. The 3D simulations have a rather low spatial resolution and only a limited set of parameter values has been investigated. Nevertheless, the simulation results reveal a new MHD bow shock topology which arises for all simulated bow shock flows for which the upstream flow is magnetically dominated (switch-on shocks occur), while for pressure-dominated flows the traditional single-front topology is obtained. It is confirmed by theoretical reasoning in terms of the geometrical properties of intermediate and switch-on shocks that two different 3D bow shock topologies have to exist for the magnetically dominated and the pressure-dominated regimes.

The present Chapter investigates the complex geometrical and topological phenomenology of 3D MHD bow shocks for magnetically dominated upstream parameters, in the abstract setting of stationary bow shock flows around perfectly conducting spheres. In the next Chapter we investigate observational evidence for the occurrence of such complex bow shock phenomena in space physics plasmas.

This Chapter is organized as follows. In Sec. 7.1 we present numerical simulation results which show that magnetically dominated 3D MHD bow shock flows exhibit a complex new topology. In Sec. 7.2 the special case of axi-symmetrical 3D bow shock flow over a sphere with the magnetic field aligned to the flow is considered. The stability of the symmetrical solution is discussed. In Sec. 7.3 the topology of the 3D magnetically dominated bow shock flows is explained in terms of the properties of MHD shocks. Sec. 7.4 treats transient wave phenomena which occur in the time-dependent evolution towards steady bow shock flows in 2D and 3D. We conclude briefly in Sec. 7.5.

7.1 3D bow shock flow over a sphere

7.1.1 Set-up of the simulations

In this Section we present numerical simulation results of 3D MHD bow shock flows over a sphere. We use the configuration of the simulation in Fig. 7.1. Fig. 7.2 shows the grid used for the 3D simulations. The 3D simulation code employs Cartesian xyz coordinates, but for convenience we also introduce a spherical $r\theta\phi$ coordinate system in Fig. 7.2. We place the origin O of the xyz coordinate system in the center of the sphere. The xy plane is a horizontal plane through the center of the sphere, and the xz plane is a vertical plane through the center of the sphere. In our simulations a uniform flow falls in from the left in Fig. 7.2. Generally we take the inflow magnetic field parallel to the x-axis. We align the

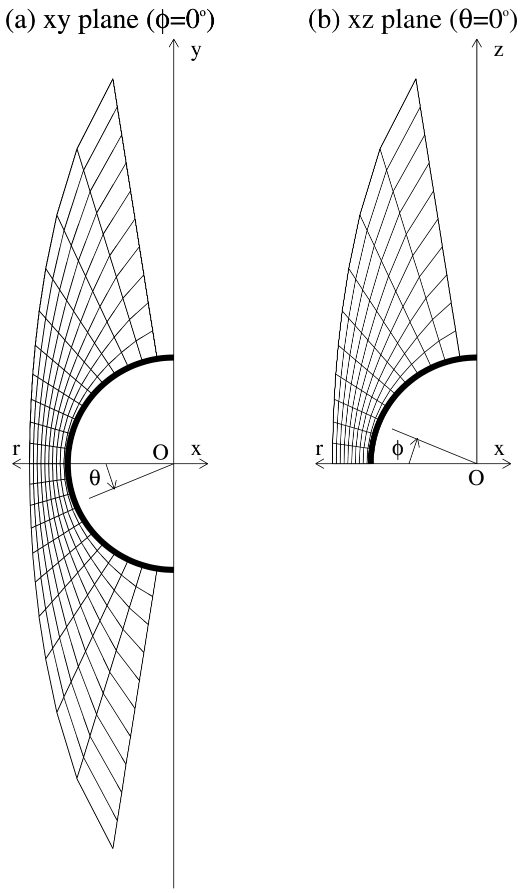

Figure 7.2: *Finite volume grid used for the 3D simulations. (a) Top view on the horizontal xy plane through the center of the sphere, which is aligned with the inflow velocity and magnetic field vectors. (b) Side view on the vertical xz plane through the center of the sphere.*

coordinate system such that $v_z = 0$ and $B_z = 0$ in the inflow. The xy plane through the sphere center is parallel to the incoming velocity and magnetic field vectors, and is thus a plane of symmetry. This symmetry allows us to restrict the simulation domain to the half-space above the xy plane. We are interested in the bow shock flow in front of the sphere, so we further restrict the simulation domain to the quadrant bordered by the xy and yz planes. For a given point P in the simulation domain, r is the distance from P to the origin O. The angle θ is the angle between the line PO and the xz plane. The angle ϕ is the angle between the plane defined by point P and the y-axis, and the xy plane. Surfaces of constant ϕ are planes which contain the y-axis.

Fig. 7.2 shows that the simulations are performed on a stretched polar-like elliptic grid. Fig. 7.2a shows the grid in the horizontal xy plane. The y-axis is a *singular* axis in the finite volume grid, because one side plane of the finite volume hexahedrals would degenerate into a line on the y-axis. The cell volumes would become very small, and the CFL time step condition would become too restrictive. Therefore we limit our simulations to a domain $\theta \in [-90° + \alpha, 90° - \alpha]$ and $\phi \in [0°, 90° - \alpha]$, with a typical value of $\alpha = 9°$ for the constant. The simulation of Fig. 7.1 was performed on a $40 \times 80 \times 40$ grid, with 40 computational cells in the radial direction r, 80 cells in the angular direction θ, and 40 cells in the angular direction ϕ. The grid resolution is increased near interesting features of the flow by accumulating or clustering grid points. This grid accumulation is done in a dimension by dimension way.

We impose ideal wall boundary conditions at the xy plane, which is a plane of symmetry. The $\phi = 90° - \alpha$ plane satisfies free outflow boundary conditions, and the $\theta = \pm(90° - \alpha)$ surfaces are free outflow boundaries as well. The outer boundary surface in the radial direction, of ellipsoid shape, is a free inflow boundary. The spherical inner radial boundary is the perfectly conducting sphere.

The problem of uniform MHD flow over a sphere has three free parameters. Two free parameters parametrize the scales (Sec. 3.1.3). We choose the inflow plasma β and Alfvénic Mach number M_{Ax} along the magnetic field. The third parameter is the upstream angle θ_{vB} between the magnetic field and the velocity. When this angle is non-vanishing, the problem is intrinsically 3D. The corresponding hydrodynamic problem of flow over a sphere has only *one* free parameter, for instance the Mach number M, and is essentially 2D because the solution is always axi-symmetric. The general problem of ideal MHD flow around a sphere has only very partially been explored in the literature. Only limited sets of parameter values have been considered, see e.g. [174, 144].

7.1.2 Pressure-dominated 3D bow shock flows

Fig. 7.3 shows the stationary simulation result for a bow shock flow with inflow parameters $\rho = 1$, $p = 0.2$, $B = 1$ and $v = 4$, obtained on a $30 \times 60 \times 30$ grid with the second order LF scheme (Sec. 4.2.5). We align the inflow fields with the xy plane, and the magnetic field with the x-axis. The angle between the velocity and magnetic field is $\theta_{vB} = 5°$, such that the velocity has a small positive y-component. The plasma

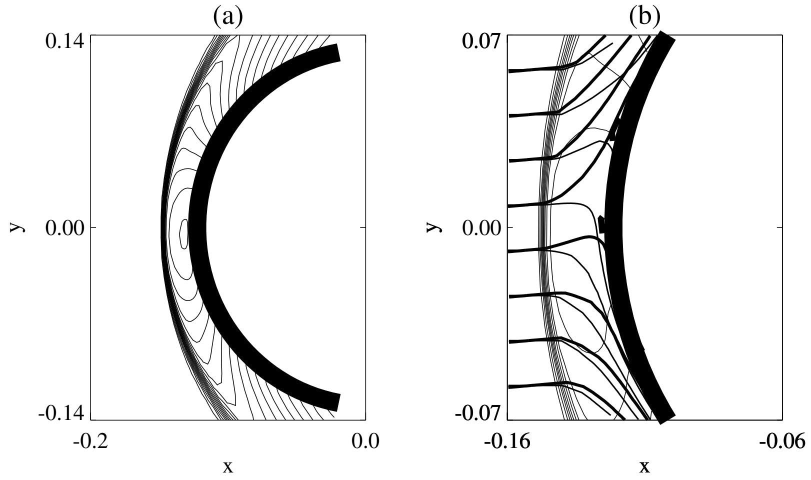

Figure 7.3: *Pressure-dominated 3D bow shock flow. (a) Density contours in the xy plane. (b) Density contours (thin solid) with streamlines (thick solid) and magnetic field lines (thin solid) in the xy plane. The two thick dots immediately in front of the sphere indicate the location of the velocity and magnetic field stagnation points* ($30 \times 60 \times 30$ *grid).*

$\beta = 0.4$, and the Alfvénic Mach number along the magnetic field lines M_{Ax}=3.98. Fig. 6.3a shows that switch-on shocks cannot arise for these parameters. The upstream flow is thus pressure-dominated.

Fig. 7.3a shows density contours in the xy plane. The bow shock solution has the traditional single-front concave-inward geometry. Fig. 7.3b shows a detailed representation of the solution near the sphere. Magnetic field lines (thin solid) come in horizontally from the left, and the incoming streamlines (thick solid) make a small angle with the magnetic field lines. Downstream of the bow shock, however, this angle is quite large at places.

It is interesting to study the location of the stagnation point in this flow. In a field-aligned flow, there is a single point where both the velocity and magnetic field strengths vanish. When the magnetic field is not aligned to the flow, points of vanishing magnetic field and velocity still exist, but those two points do generally not coincide anymore, such that there is a velocity stagnation point which is different from the magnetic stagnation point. Indeed, in the 3D bow shock flows under consideration, the streamlines and field lines which lie in the xy plane in the upstream part of the flow remain in this plane also in the downstream flow because of symmetry, such that the z components of the velocity and the magnetic field vanish everywhere in the xy plane. In the xy plane the fluid finds its way around the sphere using the two sides (top and bottom in Fig. 7.3b), such that there necessarily is a point on the sphere boundary in the xy plane where the velocity vanishes. This velocity stagnation point is indicated by the lower one of the two thick dots in Fig. 7.3b immediately in front of the sphere. A similar reasoning can be applied to the magnetic field, resulting in the existence of a magnetic stagnation point, which is indicated by the upper thick dot in Fig. 7.3b. The simulation results thus show that the two stagnation points do not coincide.

7.1.3 Magnetically dominated 3D bow shock flows

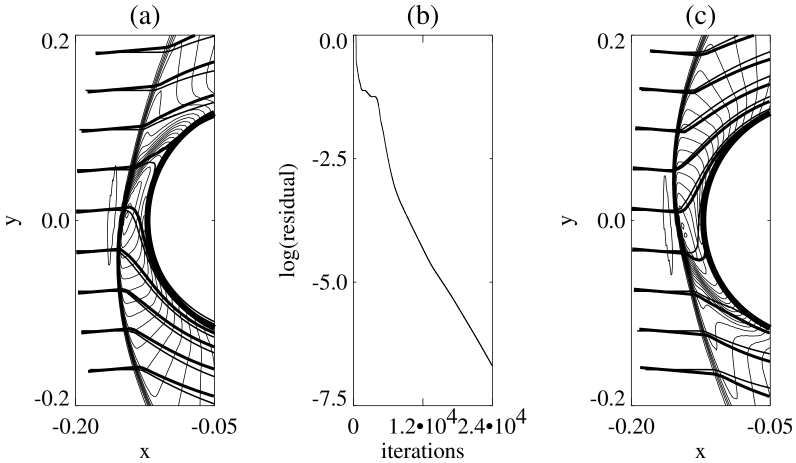

Figure 7.4: *Magnetically dominated 3D bow shock flows (switch-on shocks occur). (a) Density contours (thin solid) with streamlines (thick solid) and magnetic field lines (thin solid) in the xy plane for $\theta_{vB} = 5°$. This is the flow of Fig. 7.1. (b) Convergence of the density residual towards a steady state. (c) Bow shock flow for $\theta_{vB} = -5°$ ($60 \times 60 \times 40$ grid).*

We now consider bow shock flows with magnetically dominated upstream conditions, for which switch-on shocks occur. Fig. 7.4a shows the stationary simulation result for a bow shock flow with inflow parameters like for the flow of Fig. 7.3, except that we decrease the inflow velocity to $v = 1.5$. The simulations were performed on a $60 \times 60 \times 40$ grid with the second order LF scheme. With plasma $\beta = 0.4$ and Alfvénic

Mach number along the magnetic field lines M_{Ax}=1.49, Fig. 6.3a shows that switch-on shocks can exist, and the upstream flow is magnetically dominated. A 3D visualization of this flow was given in Fig. 7.1.

Fig. 7.4a shows that the geometry and topology of the magnetically dominated 3D bow shock flow is quite different from the topology of the pressure-dominated flow in Fig. 7.3. The shock front contains a slight dimple, and the leading front is followed by a secondary shock front. Fig. 7.4b shows that the simulation result converges to a perfect steady state. Fig. 7.4c shows that when the sign of the angle between the velocity and the magnetic field is changed ($\theta_{vB} = -5°$), the solution has the same topology but now with the secondary shock stretching out in the bottom part of the flow.

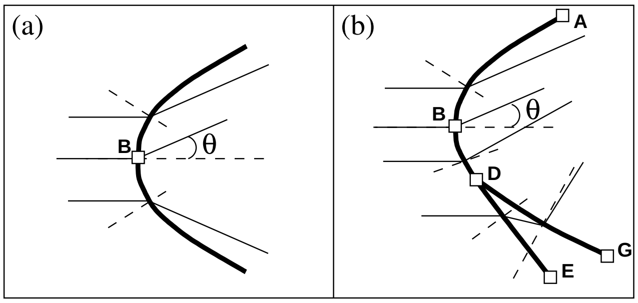

Figure 7.5: *(a) The shock front cannot entirely be of the 1–2 fast type in the neighborhood of a perpendicular point with a 1–2=3 switch-on shock. (b) A complex shock topology is necessary to channel the flow. Shock segment AB is of 1–2 fast type, BD is 1–3 intermediate, DE is 1–2 fast, and DG is 2–4 intermediate, evolving into 2=3–4 switch-off and 3–4 slow along the front. This shock topology is obtained in the numerical simulations of magnetically dominated 3D bow shock flows.*

We now investigate the topology of the magnetically dominated flow of Fig. 7.4c in the xy plane. Clearly only one perpendicular point is present in the xy plane, and the shock is a 1–2=3 switch-on shock at this point. The reasoning presented in Sec. 6.1 showed that for this case the topology represented in Fig. 6.4b (repeated in Fig. 7.5b) is needed to channel the flow. And indeed, inspection of the shock shapes in the flow of Fig. 7.4c indicates that we find exactly this topology! This is confirmed in the following paragraphs by identification of the types of all the shock segments in the simulation result. The shock segment above the 1–2=3 switch-on shock can be of 1–2 type, but the segment below the switch-on shock *cannot* be of 1–2 type (Fig. 7.5a). Instead, this shock segment has to be of 1–3 type. The curved 1–3 intermediate shock segment BD can only have a limited extent, however, because for increasing angle between the magnetic field and the shock normal, the 1–3 shock first becomes a 1–3=4 shock and then ceases to exist (Fig. 3.9). At this point the leading shock front splits up into two consecutive shock fronts. The leading shock segment DE is of the 1–2 fast type, and the secondary shock segment DG is 2–4 intermediate. The combination of the fast and the intermediate shock can deflect the magnetic field such that field lines merge continuously downstream of the so-called λ-point D where the three shock segments meet.

In the case of 2D field-aligned flow (Fig. 6.2), symmetry imposes extra constraints on the solution which makes that three perpendicular points arise in a complex flow topology, with the topology of Fig. 7.5b arising locally at several places along the leading shock front. In the 3D case, however, no extra symmetry constraints are imposed and the topology of Fig. 7.5b applies directly to the bow shock flow in the plane of symmetry (xy). The solutions of Fig. 7.4 are clearly far from being axi-symmetrical. The question thus arises what is the spatial form and extent of the secondary shock front away from the xy plane. Fig. 7.1 gives a good idea of this extent. We postpone further discussion of the 3D topology away from the xy plane to Sec. 7.3.

It is interesting to examine the shock types and the location of the stagnation points in bow shock flows with the topology of Fig. 7.4. Fig. 7.6 shows a detailed representation of a 3D bow shock flow with inflow parameters $\rho = 1$, $p = 0.2$, $B_x = 1$, $B_y = 0$, $v_x = 1.5$ and $v_y = 0.1$. The angle θ_{vB} thus equals $3.8°$. To obtain sufficient resolution we performed the simulation on a $60 \times 120 \times 60$ grid with Linde's second order HLLE scheme. The grid points are strongly clustered near the sphere. The velocity and magnetic stagnation points (the lower and the upper thick dots immediately in front of the sphere, respectively) are clearly separated and are located far above the horizontal line through the center of the sphere, even though the angle θ_{vB} is quite small in the upstream plasma.

It is conceivable that for larger angles θ_{vB} these stagnation points would shift away along the sphere even further. In that case, it would be difficult to simulate the flow on a domain restricted to one quadrant (the domain depicted in Fig. 7.2). For this reason we restrict ourselves to simulations of flows with small angles θ_{vB} in this Chapter. It seems that the structured grid approach adopted in our code is not ideally suited for the general problem of the flow around a sphere with arbitrary angle between the fields. Indeed, it is topologically difficult to fully cover a domain around a sphere by wrapping a logically rectangular box around it [155]. Adaptive or unstructured grid techniques would probably be more appropriate [56, 100, 167, 22]. On the other hand, it is not necessarily a good idea to consider the whole domain around

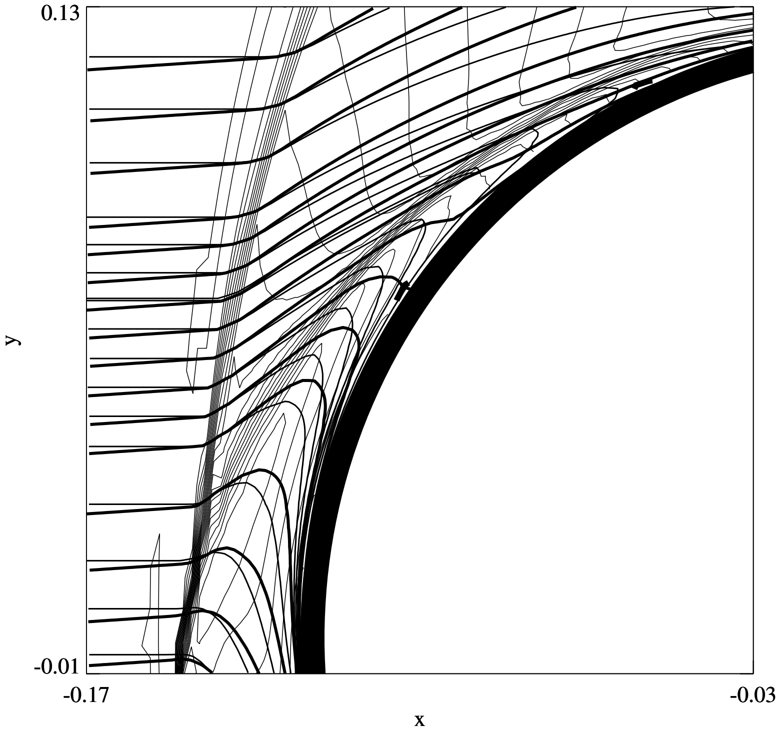

Figure 7.6: *Detailed representation of a magnetically dominated 3D bow shock flow. Density contours (thin solid) with streamlines (thick solid) and magnetic field lines (thin solid) are shown in the xy plane. The two thick dots immediately in front of the sphere indicate the location of the velocity and magnetic field stagnation points ($60 \times 120 \times 60$ grid).*

the sphere in simulations, because simulation of the wake region on the backside of an obstacle (e.g. Fig. 6.30) requires a high spatial resolution, which would necessitate excessive computing resources in the case of 3D problems. In the next Chapter we consider 3D MHD bow shock flows around a perfectly conducting paraboloid surface. Wake flows are largely avoided in this configuration, although boundary layer separation can occur. In the next Chapter we consider large angles θ_{vB} for this flow configuration with a paraboloid surface, and also for magnetically dominated bow shock flows with large angles θ_{vB} we consistently obtain the topology of Fig. 7.5b.

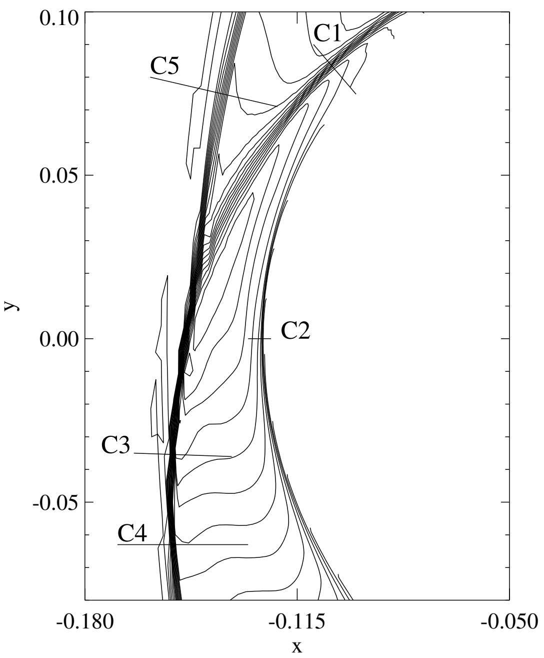

Figure 7.7: *Cuts perpendicular to various shock fronts.*

In Fig. 7.7 we indicate cuts perpendicular to various shock fronts which are now used to determine shock types for the flow of Fig. 7.6.

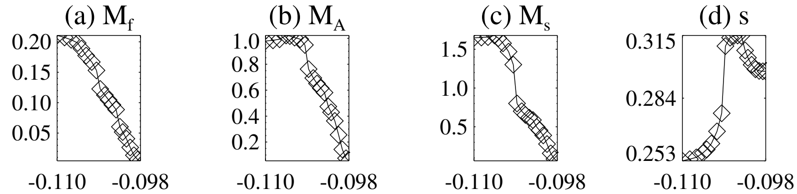

Figure 7.8: *Cut along C1 perpendicular to the secondary shock front in Fig. 7.7.*

Fig. 7.8 shows plots of Mach numbers and entropy along the cut C1 perpendicular to the secondary shock in Fig. 7.7. We see that the upstream Alfvénic Mach number is slightly larger than one, and the slow Mach number jumps from above one to below one. This shock is thus a 2–4 intermediate shock, which is very close to a 2=3–4 slow switch-off shock. This shock is of the same type as shock part D–G–H–I in the symmetrical 2D bow shock flow (Figs. 6.7 and 6.9), and as the secondary shock in the non-symmetrical 2D solution of Fig. 6.31.

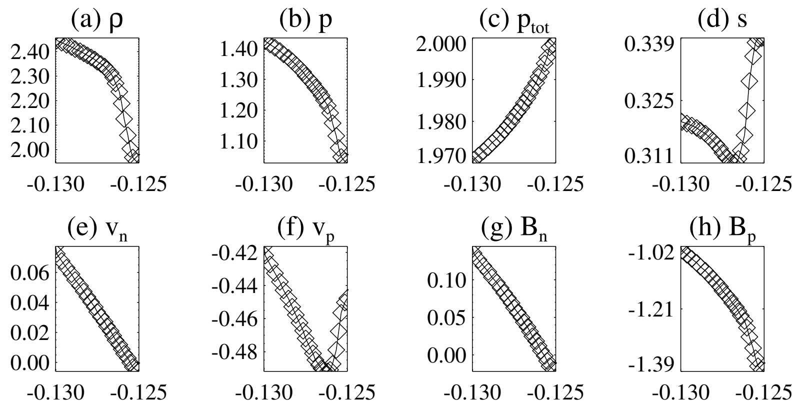

Figure 7.9: *Cut along C2 in Fig. 7.7.*

Fig. 7.9 shows plots of various quantities along the cut C2 in Fig. 7.7. Near the sphere some kind of *boundary layer* seems to be present. Such a boundary layer seems not to be present in the flow of Fig. 7.3 for pressure-dominated parameters. It is difficult to assert if this boundary layer is of physical nature or a numerical artefact. It may be a relevant part of the ideal MHD flow topology, or it may be a dissipative boundary layer, with the numerical dissipation playing the role of physical dissipation. The plots in Fig. 7.9 show some evidence that this boundary layer may be separated from the rest of the flow by a tangential discontinuity. Indeed, the normal velocity and magnetic field seem to vanish where the thermodynamic variables and the tangential fields make a jump. The total pressure does not make a noticeable jump. It seems that simulations with higher resolution are necessary to allow a more definite interpretation.

Figs. 7.10–7.12 show plots of Mach numbers and entropy along the cuts C3, C4 and C5 perpendicular to the leading shock front in Fig. 7.7. At cut C3 the shock is of the 1–3 intermediate type, but very close to 1–3=4. At cut C4, near the 'nose' of the bow shock, the shock is very close to a 1–2=3 fast switch-on shock. At cut C5, the shock is of the 1–2 fast type.

Fig. 7.13 shows that for the upstream parameter values of Fig. 7.6

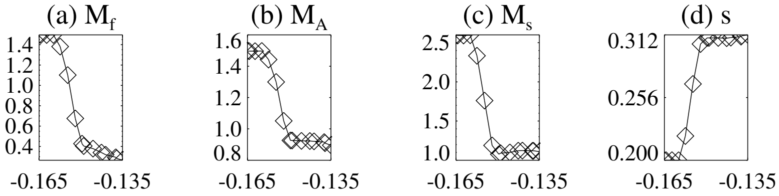

Figure 7.10: *Cut along C3 through the leading shock front in Fig. 7.7.*

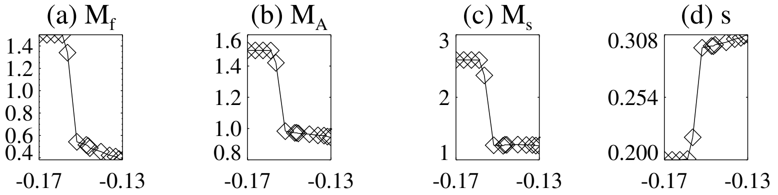

Figure 7.11: *Cut along C4 through the leading shock front in Fig. 7.7.*

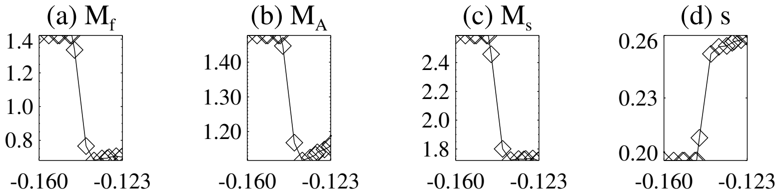

Figure 7.12: *Cut along C5 through the leading shock front in Fig. 7.7.*

the maximum angle between the magnetic field and the shock normal for which the 1–3 intermediate shock can occur is approximately 3°. This is consistent with the angle for which the leading shock front splits up into two consecutive shock fronts in Fig. 7.7.

Fig. 7.14 shows how magnetic field lines (black) and streamlines (blue) originating from points located slightly above the xy plane drape around the sphere for the bow shock flow solution of Fig. 7.1. The way in which field lines drape around obstacles is important in many space physics bow shock flows because field line orientation influences important physical processes like reconnection. This is discussed in the next Chapter. It is obvious that field line draping in the new magnetically dominated bow shock topology is quite different from field line draping

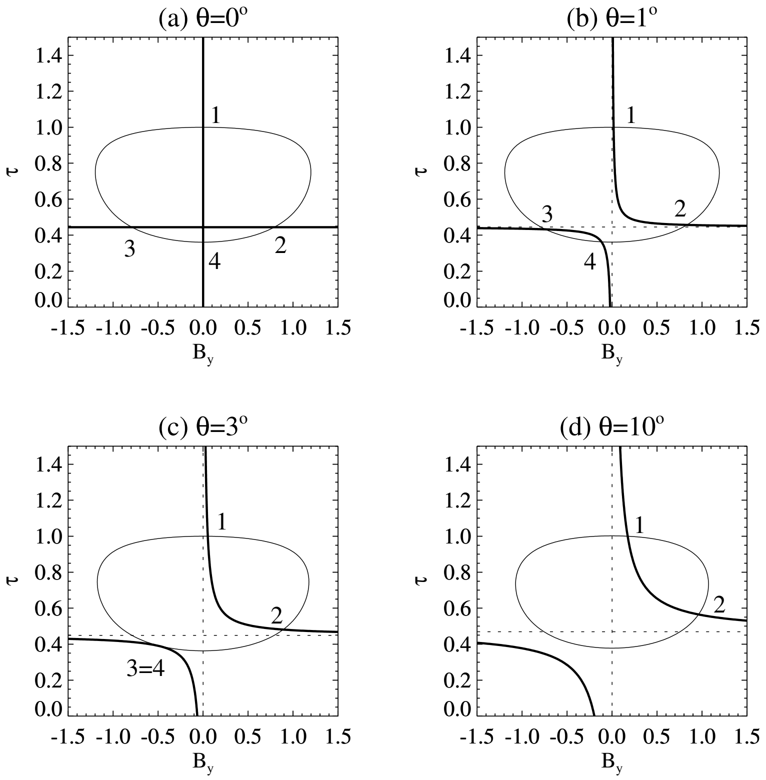

Figure 7.13: *Solutions of the RH relations for the upstream parameters of Fig. 7.6 with $\theta_{vB} = 3.8°$. These parameters are magnetically dominated. The maximum angle between the magnetic field and the shock normal for which intermediate shocks can occur is approximately* $3°$.

in the traditional pressure-dominated MHD bow shock flows, since magnetic field lines undergo a strong secondary refraction at the secondary shock, as can be seen in Figs. 7.14 and 7.1.

The results presented in this Section show that there are two basic topologies for 3D MHD bow shock flows. For pressure-dominated upstream flows a single-front topology is obtained which is the same as the well-known topology of hydrodynamic bow shock flows. For magnetically dominated upstream flows, we find the complex bow shock topology sketched in Fig. 7.5b.

The conclusion on 3D MHD bow shock topology formulated above is

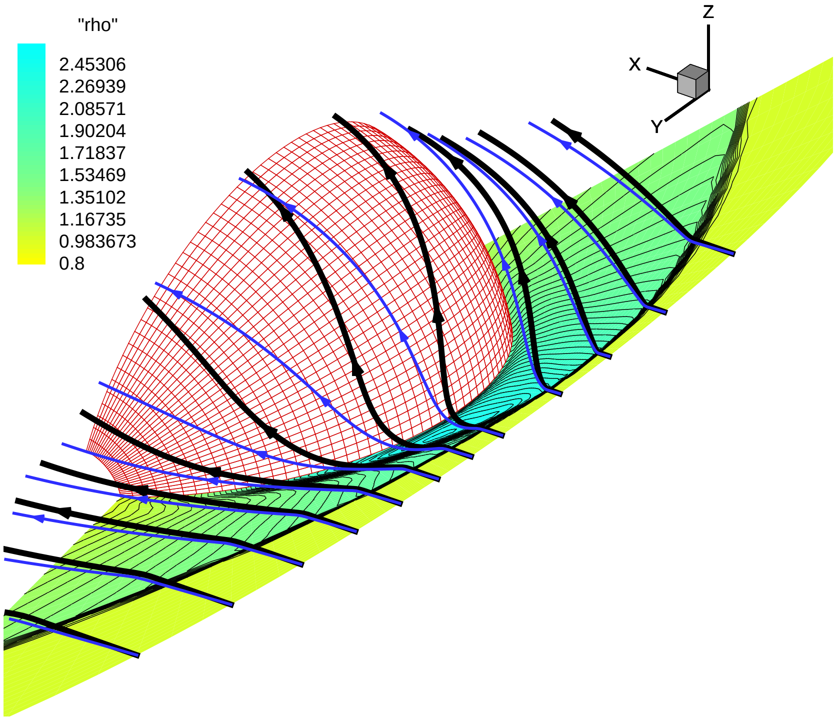

Figure 7.14: *Magnetic field lines (black) and streamlines (blue) for the bow shock flow solution of Fig. 7.1. The field lines and streamlines are drawn starting from points located slightly above the xy plane, and drape around the sphere.*

completely analogous to the conclusion reached for the case of symmetrical 2D flow (Sec. 6.3), and is a further justification for the terminology of magnetically dominated versus pressure-dominated upstream states, bow shock flows and bow shock flow topologies which we have been using since the Introductory Chapter.

We have to qualify the above formulated conclusion in the following way. Due to limited computer resources, we have not performed a complete parameter study for the 3D flows as we have done for the 2D flows (Sec. 6.3). Also, simulations were limited to small angles θ_{vB} because of limitations of the numerical technique. Nevertheless, we have simulated substantial numbers of flows around a sphere with both pressure-dominated and magnetically dominated upstream conditions. In all cases we have obtained the single-front topology for pressure-dominated upstream flows, and the multiple-front topology for magnetically dominated upstream flows. Combined with the theoretical reasoning leading to the topology of Fig. 7.5b for magnetically dominated upstream conditions, these results are a strong indication that the two different topologies indeed arise for the two different types of upstream conditions. In this context we have to remark that the topology of 3D MHD bow shock flows can be complicated further by the appearance of additional slow and intermediate shocks in the downstream flow. These additional features, however, are not related to the geometrical properties of switch-on shocks at perpendicular points on the leading shock front, but instead seem to depend more on the shape of the obstacle and the angle θ_{vB} and can be the result of other physical processes like boundary layer separation. Some examples of such additional features are given in the next Chapter (Sec. 8.2.2).

7.2 Field-aligned axially symmetrical flow over a sphere

In the present Section the special case of axi-symmetrical 3D bow shock flow over a sphere with the magnetic field aligned to the flow ($\theta_{vB} \equiv 0$) is considered. We present numerical simulation results for magnetically dominated inflow parameter values $\beta = 0.4$ and $M_{Ax} = 1.5$ for which switch-on shocks occur (Fig. 6.3a). These are the same parameters as for the bow shock flow around a cylinder which was studied in Sec. 6.2. First we discuss the simulation results obtained with our 2D axi-symmetrical scheme, which was described in Sec. 4.2.4.

In Fig. 7.15b we show a global view of the stationary axi-symmetrical bow shock solution, obtained with our second-order LF scheme on a stretched 100×100 grid restricted to one quadrant. The horizontal x-axis (coinciding with the stagnation streamline) is an axis of rotational symmetry. At the symmetry axis no boundary conditions need to be specified because the effective length of the cell interfaces on the axis vanishes, such that the flux through these interfaces does not contribute to the time evolution. At the three other boundaries we impose standard free in, free out and ideal wall conditions. The leading shock front shows a clear dimple. The shock front is much closer to the obstacle than in the case of the flow around a cylinder with the same inflow parameters, which is shown in Fig. 7.15a for comparison.

In Fig. 7.15c we show a detailed representation of the central part of the axi-symmetrical bow shock solution near the stagnation streamline. This plot is to be compared to its cylinder flow equivalent shown in Fig. 6.9 (where only the upper part of the symmetrical flow is plotted). The flow clearly exhibits a topology which is similar to the topology of

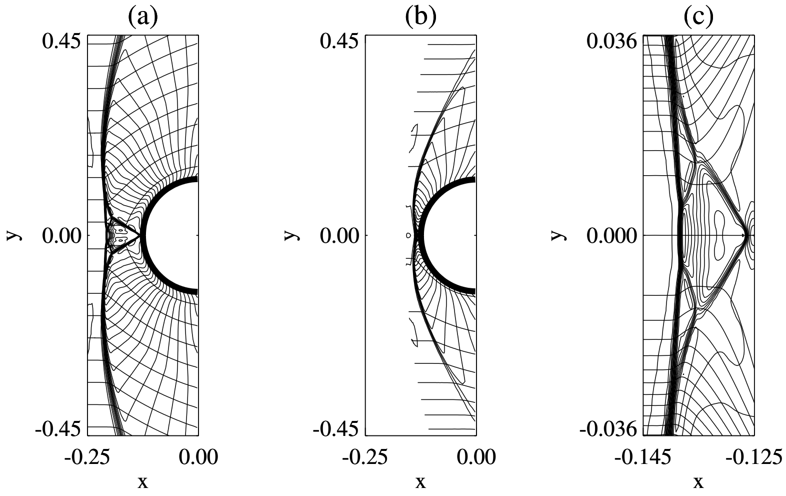

Figure 7.15: *Symmetrical field-aligned magnetically dominated bow shock flows with* $M_A = 1.5$ *and* $\beta = 0.4$. *Density contours and magnetic field lines are shown. (a) Flow around a cylinder. (b) Axi-symmetrical flow over a sphere. (c) Detail of the axi-symmetrical flow.*

the flow around a cylinder. Inspection of the way in which the field lines are refracted when the shocks are passed, reveals that the shocks in Fig. 7.15c are of the same type as the shocks in the cylinder flow of Fig. 6.9 which were discussed in Sec. 6.2, and detailed analysis of upstream and downstream Mach numbers, along the lines of the detailed analysis in the previous Chapter, confirms this conclusion.

We can thus conclude that magnetically dominated 3D axi-symmetrical flows over a sphere exhibit a complex bow shock topology very similar to the topology of a bow shock flow around a cylinder in that parameter regime.

The axi-symmetrical 3D flow over a sphere can of course also be simulated using our 3D simulation code, and the same result should be obtained as with the 2D axi-symmetrical code. In fact, comparison of the results constitutes a good test for the 3D code. Fig. 7.16 shows a comparison of simulation results for the axi-symmetrical bow shock flow obtained with the 3D code on a $50 \times 100 \times 50$ grid in the xy plane (solid) and in the xz plane (dashed), and the results obtained with the 2D axi-symmetrical code on a 80×80 grid (dotted). The results are in global agreement. The differences between the 2D and the 3D results are due

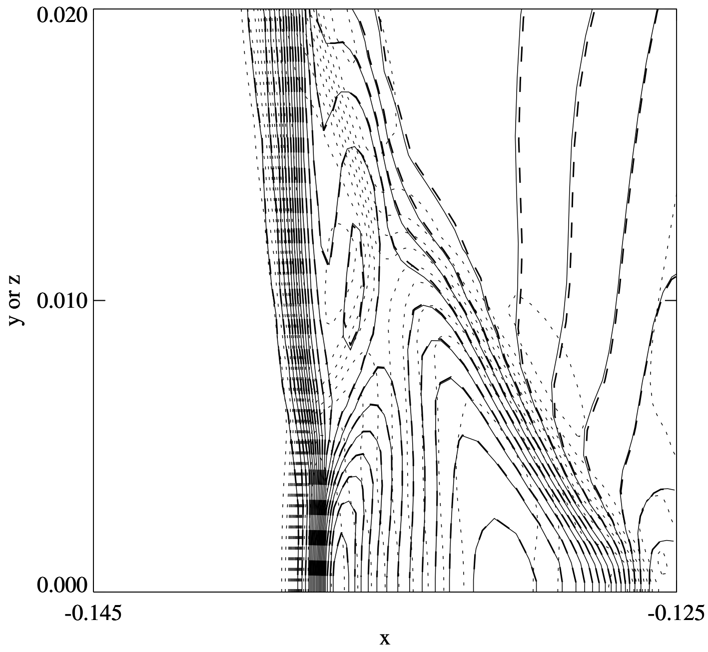

Figure 7.16: *Comparison of simulation results for the axi-symmetrical flow obtained with the 3D code in the xy plane (solid) and in the xz plane (dashed), and the results obtained with the 2D axi-symmetrical code (dotted).*

to the difference in grid resolution and structure.

The topology of the flow in Fig. 7.4a for $\theta_{vB} = 5°$ is very different from the solution for the axi-symmetrical field-aligned case which was shown in Figs. 7.15b and c, even though the angle $\theta_{vB} = 5°$ in Fig. 7.4a is quite small. We have performed simulations for even smaller but non-vanishing angles θ_{vB} between the inflow velocity and magnetic field. In all cases we find the topology of Fig. 7.4a for the stationary solution, and not the topology of the axi-symmetrical solution of Fig. 7.15c, which corresponds to the sketch in Fig. 6.7. This seems to be a clear example of symmetry breaking, because introduction of a small angle θ_{vB} between the magnetic field and the plasma flow, produces a steady state result which is topologically different from the symmetrical solution. The symmetrical flow is thus likely to be a meta-stable solution. This conclusion is consistent with the results of the discussion in Sec. 6.5 about the stability of the symmetrical 2D bow shock flow. In Sec. 7.4 it is discussed how transient waves form the link between the symmetrical and non-symmetrical flow solutions.

7.3 3D topology of magnetically dominated bow shock flows

As shown in Sec. 7.1.3, the reasoning leading to Fig. 7.5b explains the topology of 3D magnetically dominated bow shock flows in the plane of symmetry. However, the topology of the flow away from the xy plane remains to be investigated and explained. Fig. 7.1 shows that the secondary shock has a finite extent out of the plane of symmetry. We now investigate if this can be understood in terms of the properties of MHD shocks. First we study the local geometry of 3D MHD shock fronts near perpendicular points for magnetically dominated upstream parameters (switch-on shocks occur). For simplicity we consider again the case of a uniform upstream flow, but the upstream velocity and magnetic field need not be aligned.

Let us first consider the possible existence of an isolated perpendicular point at the nose of a fast MHD shock front with concave-inward orientation (Figs. 7.17a and b). The shock at the perpendicular point can either be a fast 1–2=3 switch-on shock or a 1–4 hydrodynamic shock. Suppose that the shock is a switch-on shock, as in Fig. 7.17a. Suppose that the magnetic field line is deflected leftward in the horizontal plane. The shock in the horizontal plane (thick solid) then necessarily has to be 1–2 on the left side, and a 1–3 shock segment can continuously be connected to the perpendicular point on the right, as in the 2D case of Fig. 6.5a. However, the shock segment in the vertical plane (thick dashed) cannot be connected continuously to the switch-on shock at the perpendicular point, because due to the co-planarity of MHD shocks the refracted magnetic field has to lie in the vertical plane containing the shock segment! This leads us to the conjecture that, for upstream parameters in the switch-on regime, isolated perpendicular points of switch-on type cannot exist on concave-inward shock fronts. The same conclusion seems to hold for concave-outward shock fronts (corresponding to the case of Fig. 6.5b).

If the shock at the perpendicular point is a hydrodynamic shock, as in Fig. 7.17b, then a concave-inward or concave-outward shock surface entirely of 1–4 type can exist with the isolated perpendicular point at

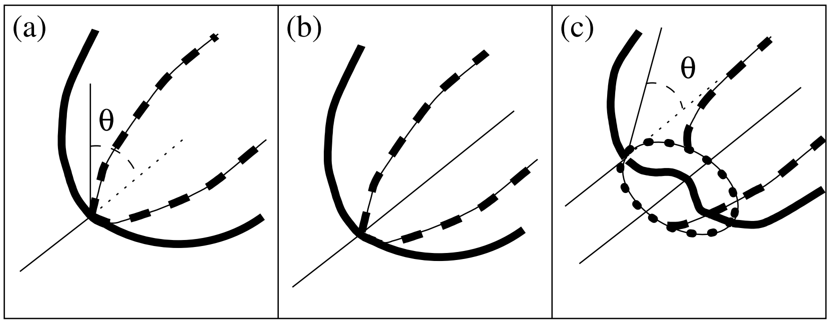

Figure 7.17: *3D bow shock geometries near perpendicular points for magnetically dominated upstream parameters. Thin lines are magnetic field lines. Shock fronts in the horizontal plane through the central perpendicular point are thick solid, and shock fronts are thick dashed in the vertical plane through the central perpendicular point which contains the incoming magnetic field line. (a) An isolated perpendicular point of 1–2=3 switch-on type cannot exist. (b) An isolated perpendicular point of 1–4 hydrodynamic type can exist. (c) A closed curve of perpendicular points of switch-on type (thick dotted) forms the transition between a 1–2 shock front on the outside and a central concave-outward dimple containing 1–3 and 1–4 shocks.*

the nose (corresponding to the cases of Figs. 6.5e and f).

However, 1–2 fast MHD shock fronts certainly exist in 3D MHD flows with magnetically dominated upstream parameters, so what happens if a 1–2 front assumes a shape such that the magnetic field becomes perpendicular to the 1–2 front at some point on the shock surface, where the fast shock then would turn into a switch-on shock? The reasoning described above shows that isolated perpendicular points are not possible in this case, but it seems that *continuous curves* of perpendicular points with switch-on shocks can exist on the shock front. Fig. 7.17c shows a possible symmetrical 3D shock geometry for the case of magnetically dominated upstream parameters. The shock front contains a concave-outward central part or 'dimple'. The central part of the dimple is of 1–4 type, and contains a perpendicular point of hydrodynamic type. A closed circular curve exists on the shock front at which the shock is of 1–2=3 switch-on type (thick dotted). Outside of this curve the shock front is of 1–2 type, and on the inside the shock is 1–3. This shock geometry is a direct 3D generalization of the geometry proposed by Steinolfson and Hundhausen for 2D flows (Fig. 6.6b). The simulation of a symmetrical field-aligned flow over a sphere represented in Fig. 7.15 shows that, like in the case of 2D flow around a cylinder, the single-front topology with a dimple which was proposed in Fig. 7.17c does not occur. Instead, the 1–3 and 1–4 shock segments split up into two consecutive shock fronts at the points where the shocks become 1–3=4.

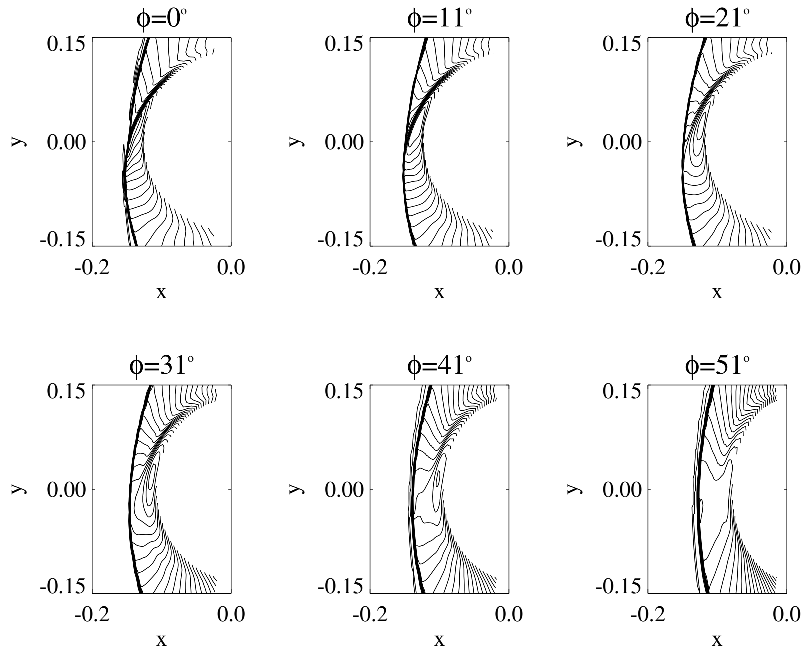

Figure 7.18: *The 3D bow shock flow of Fig. 7.1 in planes with various values of ϕ. Density contours in those planes are projected on the xy plane.*

For non-vanishing upstream angle θ_{vB}, the flow solution becomes highly non-symmetrical, and the flow topology changes accordingly. Fig. 7.4a shows that there is only one perpendicular point on the leading front in the xy plane. The question thus arises what is the spatial form and extent of the secondary shock front away from the xy plane, and how this is related to the flow topology. Fig. 7.1 gives some indication about the extent of the secondary shock.

Fig. 7.18 gives some more information about the precise flow topology. The secondary shock front remains attached to the leading front up to an angle of $\phi \approx 20°$. For higher values of ϕ the secondary shock is detached from the leading front. It is interesting to remark that the perpendicular point (at the nose) remains approximately at the same x

location for ϕ between 0° and approximately 20°. For ϕ increasing from 0° to approximately 20°, the perpendicular point seems to approach the point where the secondary shock is attached to the leading front. We propose the following possible interpretation for this behavior.

In Fig. 7.4a we see that a switch-on shock is present on the leading shock front at the perpendicular 'nose' point, where the shock front extends most into the undisturbed upstream plasma. The magnetic field is deflected downwards at this point. The above discussion indicates that this perpendicular point of switch-on type cannot be an isolated perpendicular point, which implies that a line of perpendicular points of switch-on type has to extend in two directions out of the xy plane and perpendicular to that plane. In the topology of Fig. 7.4a, this curve of perpendicular points on the leading shock front can clearly not be a closed curve. It is conceivable that this curve of perpendicular points would end when it connects to the secondary shock at some point on the leading front above the xy plane. Fig. 7.18 seems to suggest that this happens for an angle $\phi \approx 20°$. For higher values of ϕ both the secondary shock and the switch-on shock are not present anymore on the leading shock front. Perpendicular points of switch-on type thus exist on the leading front up to a value of $\phi \approx 20°$. Beyond this value, the leading front curves away and perpendicular points do not occur anymore. This would explain how the secondary shock has a limited extent out of the xy plane. This seems to be a reasonable interpretation for this aspect of the complex bow shock flow topology, but thorough study of high resolution simulation results is needed to confirm this interpretation.

7.4 Transient waves during the time evolution towards a steady state

The V-shaped secondary feature composed of intermediate and compound shocks which is present in the axi-symmetrical flow result of Fig. 7.15c is clearly not present in the stationary bow shock results of Fig. 7.4 for the case of a small angle θ_{vB} between the velocity and the magnetic field. The final stationary results thus differ substantially, and we have used the term symmetry breaking to refer to this phenomenon. The reader may wonder why the V-shaped feature is not present in the solution, even when the angle θ_{vB} is very small. It is interesting to look in detail at the dynamical time evolution of the flow towards a steady state solution. We show that transient waves provide a link between the symmetrical and non-symmetrical magnetically dominated bow shock topologies. Indeed, in our simulations the uniform initial conditions for field-aligned flow and for flow with a small angle θ_{vB} are very close to each other, so we can expect that the resulting flow patterns do not differ too much for small times. Let us examine the dynamical time evolution of symmetrical and non-symmetrical flows towards a steady state bow shock solution starting from a uniform initial condition.

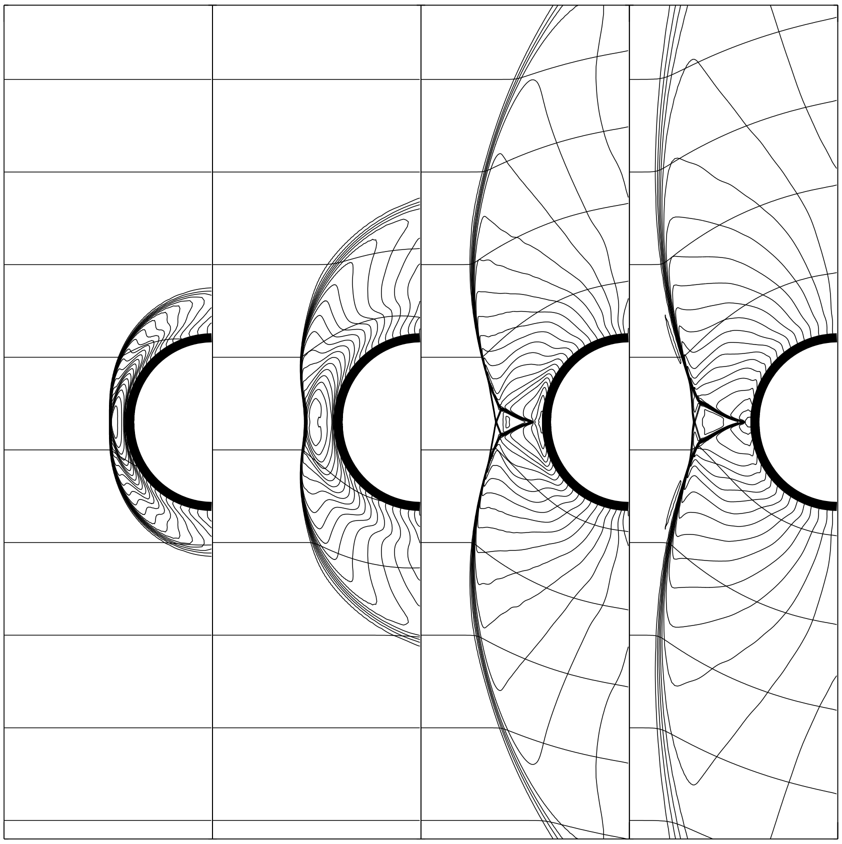

Figure 7.19: *Time evolution towards a steady state solution for the case of 2D magnetically dominated symmetrical flow around a cylinder. Density contours and magnetic field lines are shown* (200×400 *grid).*

Fig. 7.19 shows the time evolution towards a steady state solution for the case of 2D symmetrical flow around a cylinder, with $\beta = 0.4$ and $M_{Ax} = 1.2$ ($\rho = 1$, $p = 0.2$, $B_x = 1$, $v_x = 1.2$ and $r = 0.125$). The initially almost circular front ($t = 0.05$, first panel) deforms into a front composed of fast and intermediate shock parts, characterized by a concave-outward central part (the 'dimple') ($t = 0.15$, second panel). We also see traces of transient secondary shocks following the leading front. These transient features were also present in the time-dependent

CME simulations of Steinolfson and Hundhausen [147]. The shock on the stagnation line necessarily has to be a 1–4 intermediate shock. We propose as a possible explanation for these secondary shocks that at the point where the curving 1–4 shock becomes a 1–3=4 shock, the leading shock front splits up into two consecutive shock fronts.

At $t = 0.60$ (third panel), a V-shaped secondary shock front is seen to have separated from the leading shock front. It trails the leading front in a distinct V-shape, and the density is clearly depleted in the V-region ($\rho \approx 2$) as compared to the density in the two distinct lobes downstream of the slow shock front ($\rho \approx 3$). This V-shaped structure already has the topology of the steady symmetrical solution.

At $t = 1.00$ (fourth panel), the steady state is almost reached. Fig. 3.9 shows that for the parameter values of this flow the maximum angle between the magnetic field and the shock normal for which the 1–3 intermediate shock can occur is approximately $16°$. This is consistent with the angle for which the leading shock front splits up into two consecutive shock fronts in the fourth panel of Fig. 7.19.

It may be argued that this time evolution starting from a uniform initial condition is somewhat artificial. We could propose the instantaneous acceleration of an object in a static uniform plasma to a constant velocity as a physical interpretation for such time-dependent flows, and this scenario can be approached in physical systems. We solve the time-dependent ideal MHD equations in a time-accurate way, and all the transient wave phenomena observed in the simulations are thus valid dynamical MHD phenomena. These phenomena may be of real physical interest, maybe not directly in the abstract setting of the problem we simulate, but possibly in related real plasma flows.

Fig. 7.20 shows a detailed representation of a snapshot ($t = 0.3$) of the evolution towards a steady state 3D bow shock flow with inflow parameters $\rho = 1$, $p = 0.2$, $B_x = 1$, $B_y = 0.01$, $v_x = 1.5$, $v_y = 0$ and $r = 0.125$. The angle $\theta_{vB} = -0.57°$. The Alfvénic Mach number along the magnetic field line equals 1.4999, and $\beta = 0.4$. To obtain sufficient resolution we performed the simulation on a $60 \times 120 \times 60$ grid with Linde's second order HLLE scheme.

The final stationary solution of this flow problem has the topology of Fig. 7.4c, with the secondary shock front stretching out along the sphere in the bottom part of the flow. We see that in the initial stage of the evolution shown in Fig. 7.20 a clear V-shaped secondary shock feature is present in the flow. Detailed analysis shows that this V-shaped feature has the same topology as the V-shaped feature of the stationary axi-symmetrical flow in Fig. 7.15c, although its proportions are different and its shape is non-symmetrical. The upper triangle D–G–E of Fig. 6.7 is much larger in this non-symmetrical flow, and the corresponding lower triangle is so small that it hardly can be identified. At this stage of

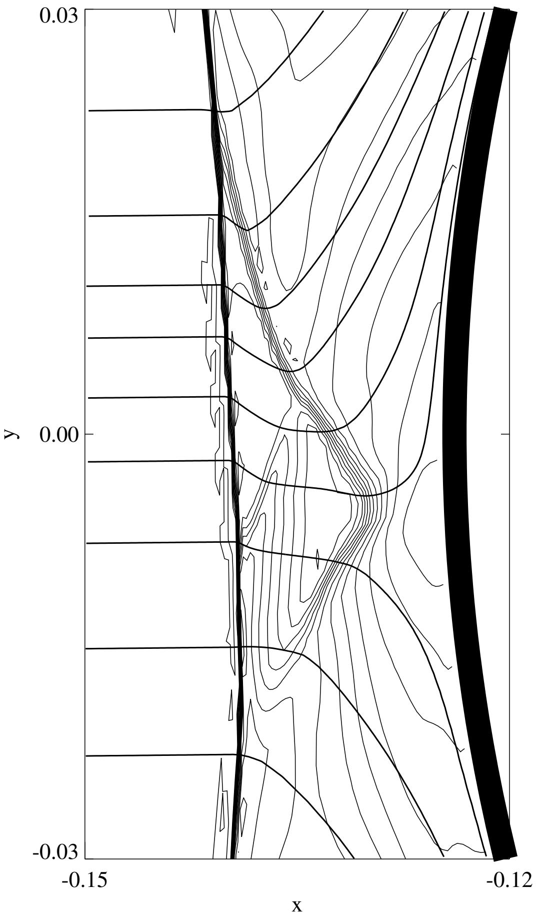

Figure 7.20: *Detailed representation of a snapshot ($t = 0.3$) of the evolution towards a steady state 3D magnetically dominated bow shock flow with non-field-aligned inflow. Density contours and magnetic field lines in the xy plane are shown ($60 \times 120 \times 60$ grid).*

the flow there are *three* perpendicular points on the leading shock front — the 1–4 point can be identified in the region plotted; the two 1–2=3 points lie above and below the plotted region. It is especially noteworthy that the 1=2–3=4 compound shock (E–G in Fig. 6.7, clearly visible in the upper triangle), is present in these 3D simulation results.

Later in the time evolution the V-shaped feature slips away along the sphere on the bottom side, and disappears completely. The remaining secondary shock (like in Fig. 7.4c) can be identified with the shock D–G–H–I in the V-shaped feature (they are both of 2–4 type), and is the sole remainder of the V-shaped feature in the stationary bow shock solution. In the final solution there is only one perpendicular point.

When the incoming magnetic field is aligned to the flow, the V-shaped feature is not biased to slip away on the top or the bottom side, and consequently it reaches a stationary position in front of the sphere. For small angles θ_{vB}, however, the V-shaped feature finds a way to slip around the sphere. This explains why the symmetrical solution with a stationary V-shaped feature is likely to be a meta-stable solution. The important conclusion from the analysis in this Section is that the V-shaped feature with all its constituting intermediate and compound shocks can be present in non-field-aligned 3D bow shock flows as a transient feature.

7.5 Conclusion

The main lesson to be learned from the results described in this Chapter is that there are two basic topologies for 3D MHD bow shock flows. For pressure-dominated upstream flows a single-front topology is obtained which is the same as the well-known topology of hydrodynamic bow shock flows. For magnetically dominated upstream flows we find the complex bow shock topology sketched in Fig. 7.5b. The complexity of the magnetically dominated MHD bow shock topology is due to intrinsically magnetic effects. It was previously thought that all MHD bow shock flows exhibit the traditional pressure-dominated topology, and the magnetically dominated MHD bow shock topology was unknown. The new magnetically dominated MHD bow shock topology has important applications in space physics plasma flows, which are discussed in the next Chapter.

Chapter 8

Applications in space physics

Space physics is the scientific discipline which studies the physical processes that are at work in our solar system and in the coupled solar-terrestrial system. Processes in the earth's magnetosphere and phenomena in the solar corona are important topics of research, and the knowledge gained from studying these topics may help us to understand the connection between solar activity and perturbations of the earth's magnetic system or 'space weather'.

Newly discovered physics regarding complex MHD shock phenomena in a magnetically dominated medium has been described in the previous Chapters. The discussion in these previous Chapters was set in an abstract context, which enabled us to concentrate on the basic physical effects and to state the results in all their generality. In the present Chapter we leave this abstract setting and we apply what we learned about MHD shocks to plasma flows with shocks in the solar system. The new results on MHD shocks may also have applications in astrophysical plasma flows beyond our solar system. This is not addressed in this dissertation, but certainly remains an interesting and unexplored research topic.

Shocks are ubiquitous in space physics plasma flows and shock phenomena play an important role in space weather. The supersonic and super-Alfvénic solar wind generates a bow shock in front of the earth [114], which forms the transition between the solar wind flow and the earth's magnetosphere. Strong shocks are generated in front of solar coronal mass ejections (CMEs) when CMEs leave the corona at super-Alfvénic speeds [68]. These CMEs propagate in the solar wind through the interplanetary medium, and their leading shocks are observed by space probes as interplanetary shock waves. Some of the CMEs that reach the earth have been observed *in situ* as magnetic clouds with a preceding shock [15, 58]. The interaction of such a shock–cloud structure with the earth's bow shock and magnetosphere can generate violent perturbations of the earth's magnetic system called magnetic storms. Magnetic storms can adversely affect satellites, communication systems and power grids on the earth, and resulting failures are referred to as the effect of 'space weather'.

In this Chapter we present two examples of space physics plasma flows with shocks for which the newly discovered intrinsically magnetic effects on bow shock topology are important. In Sec. 8.1 we discuss complex shock phenomena induced by fast solar CMEs. In Sec. 8.2 we apply the new results on MHD shock topology to the bow shock generated by the interaction of the solar wind with the earth and its magnetic system. Remark that the secondary shock in the magnetically dominated bow shock topology (Fig. 7.1) is of intermediate, slow switch-off or slow type depending on the exact location along the shock front. For definiteness we refer to the secondary shock front as a secondary *slow* shock front in this Chapter.

8.1 Shocks induced by fast CMEs

We begin this Section with a brief overview of some properties and observations of the solar corona and CMEs. Then we discuss if the magnetically dominated shock topology described in Chap. 7 may arise when fast CMEs generate preceding shock fronts, and we ask ourselves whether those multiple interacting shocks could be observed with present-day observational means.

8.1.1 Coronal mass ejections

Up to several times per day, large-scale structures in the solar corona disrupt and are ejected out of the corona at speeds ranging from 10 to 2×10^3 km/s, carrying a mass of 10^{12-13} kg and liberating an energy of 10^{24-25} J [66, 104, 68]. The propagation of CMEs in the highly ideal solar coronal plasma may be described by the equations of ideal MHD. CMEs are ejected into interplanetary space from low in the solar corona where magnetic forces dominate over thermal pressure forces, such that the plasma β is substantially smaller than $2/\gamma = 1.2$. Switch-on shock phenomena can arise when $\beta < 2/\gamma$. Further away from the sun the solar wind becomes pressure-dominated and the plasma β rises above 1.2. This transition can be estimated to be located at around 3 solar radii (R_s) measured from the center of the sun. The solar wind is subsonic and sub-Alfvénic in the lower corona, but becomes supersonic and super-Alfvénic at larger distances. The Alfvén speed is estimated to be 600 km/s at 3 R_s, and decreases outward as the magnetic field becomes weaker [68].

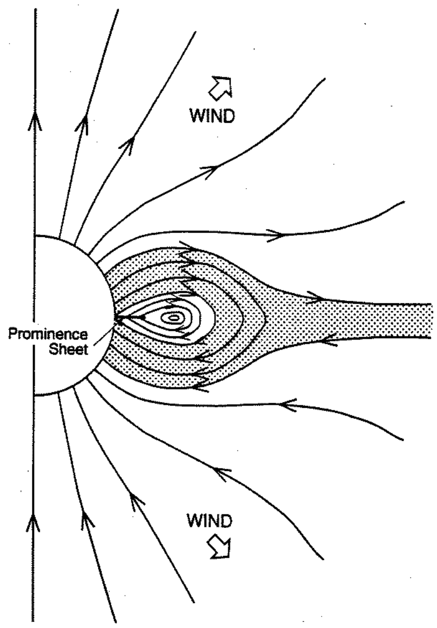

Figure 8.1: *Sketch of a hypothetical pre-CME configuration in the lower solar corona idealized to be axi-symmetric. CMEs generally occur when helmet streamers erupt. A helmet streamer is shown, which has a three-part structure: a high-density shell consisting of closed magnetic field lines rooted in the solar photosphere (shaded), a low-density cavity at the base, and a high-density prominence in the cavity (from Low (1996) [104]).*

Observations show that CMEs generally occur when arcade-like structures in the lower corona — which are called helmet streamers — erupt. We now briefly describe a theoretical model of the configuration which is believed to exist in the corona prior to CME eruption. This model is due to B. C. Low [104]. The model may not be applicable to all CMEs, but there is substantial observational evidence that a large class of CME events originate from the hypothetical pre-CME configuration sketched in Fig. 8.1. The pre-CME helmet streamer has a three-part structure: a high-density shell (seen as a bright dome-like structure in coronagraph observations) consisting of closed magnetic field lines rooted in the solar photosphere (shaded), a low-density cavity at the base, and a high-density prominence in the cavity. Energy estimates indicate that the eruption of a helmet streamer and the ejection of the CME material must mainly be driven by magnetic energy, and this energy is presumably stored in the form of a detached flux rope of helically twisted magnetic field which forms the cavity. In realistic geometry, as opposed to the axi-symmetric idealization in Fig. 8.1, the cavity flux rope may be anchored to the coronal base at the two ends of the rope. When a CME takes off, the initially closed magnetic field lines which form the bright dome overlying the cavity open up and a current sheet is formed as a layer separating the open magnetic field lines of opposite polarities. In a later stage those magnetic fields of opposite polarities reconnect resistively low in the corona where the magnetic field dominates over the pressure, which presumably results in a solar flare and finally reformation of the helmet structure as a region of closed magnetic field.

8.1.2 Coronagraph observations

Coronagraph observations are the most important source of information on CMEs. Fig. 8.2 shows images of a CME taken by the space-borne Solar Maximum Mission (SMM) coronagraph [14], which was operational from 1980 to 1989. A coronagraph determines the electron density in the corona by measuring intensities of white light Thomson scattered by coronal free electrons. Direct light from the solar surface is blocked out by a disc covering the sun. Intensities on a coronagraph image are a direct measure of the coronal density integrated along the line of sight through the optically thin corona. This line of sight projection effect makes coronagraph images generally hard to interpret.

The SMM images of Fig. 8.2 show an erupting CME. The outer loop is seen to expand, with the bright structure closer to the sun being the prominence in the low-density cavity. In the right hand panel both the outer loop and the prominence have expanded substantially. The prominence material reveals a helical magnetic field structure. For the purpose of studying MHD shock effects induced by fast CMEs, we are now mainly interested in what happens near the leading feature of the outward moving CME. In the left panel a small 'dimple' can be seen in the leading front. In the subsequent image, taken about 16 minutes later, the dimple has become much more pronounced, and secondary bright features (indicated by arrows) following the leading front can be observed. The CME accelerates to an estimated speed of 1055 km/s [14], which is higher than the expected coronal Alfvén speed.

Fig. 8.3 shows difference images of a fast CME taken by the LASCO C3 coronagraph aboard the SOHO spacecraft [31]. SOHO became operational in 1996, and the C3 coronagraph has a much larger field of view (up to $30R_s$) than previous coronagraphs. A dimpling of the leading

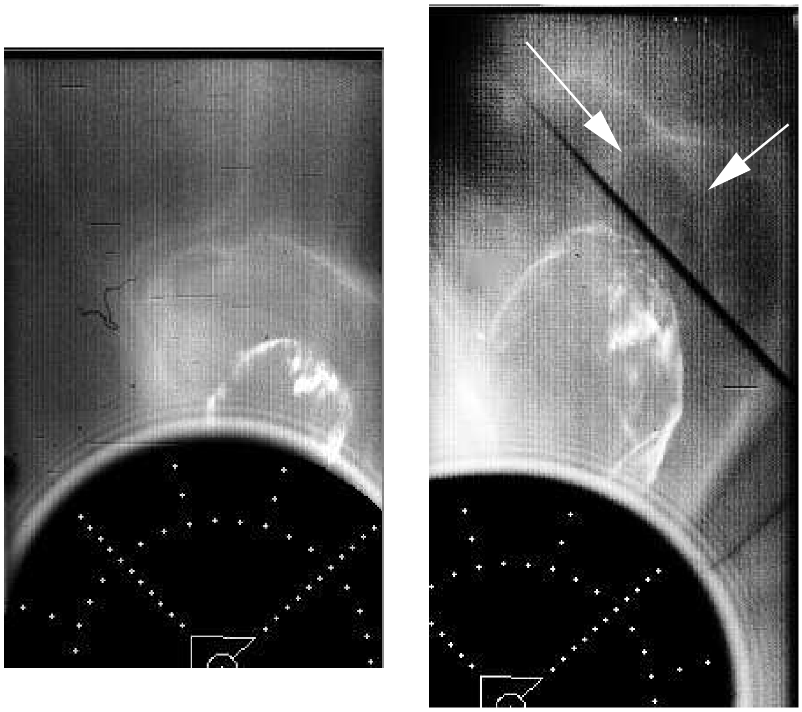

Figure 8.2: *Observation of a solar CME with the SMM coronagraph. The black disc covers the sun and has a radius of 1.6 × R_{sun}. The field of view of the SMM coronagraph stretches out to approximately 6 × R_{sun}. The images, taken on January 30, 1990, at 2:11, and 2:27 UT (from left to right), show the initial dimpling of a fast CME front and a more clearly dimpled leading front with several trailing structures (indicated by arrows) in a later stage. (Coronagraph data courtesy HAO/NCAR.)*

front can clearly be observed, and secondary features are clearly visible behind the leading front. We want to draw the attention on the conspicuous straight-line feature (indicated by the yellow arrow) which follows the leading front in the lower part of the CME, and which is consistently present in all the images.

8.1.3 CMEs and shocks

Do fast CMEs induce shocks?

There is a wide variation in the speeds with which CMEs propagate out of the solar corona. Statistical analysis of six years of SMM data [69, 68] shows that up to 20% of mass ejections move with a projected speed

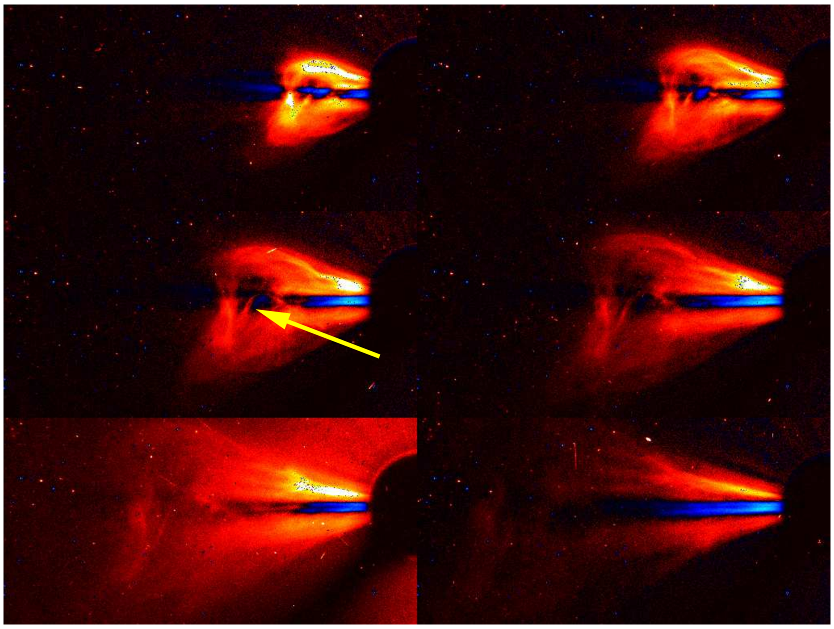

Figure 8.3: *Observation of a solar CME with the LASCO C3 coronagraph. The field of view stretches out from approximately 6 × R_{sun} to approximately 30 × R_{sun}. The images are taken on December 14, 1997, from 2:11 to 12:28 UT, and a pre-event image has been subtracted. A dimpling of the leading front can clearly be observed, and a straight-line secondary feature (indicated by the yellow arrow) is clearly visible behind the leading front. (Coronagraph data courtesy LASCO consortium.)*

which is higher than the estimated Alfvén speed. CMEs generally move outward almost radially, and the magnetic field in the solar corona is mostly radial too, so these fast CMEs move presumably faster than the fast MHD wave speed — which coincides with the Alfvén speed along the radial field lines. The solar wind speed is small in the lower corona, so many of those fast CMEs also move with superfast speeds relative to the solar wind. This means that fast CMEs (up to 20% of the total number of CMEs) move faster than the fastest wave speed in the coronal plasma. Then it follows from first-principle physical arguments (see also Chap. 2) that a shock wave must be generated in front of the moving CME. The shock forms the transition between the undisturbed superfast (in the shockframe!) upstream region and the subfast region downstream from the shock. This situation is similar to the case of an object flying through a stationary plasma with superfast speed, in which case the object is preceded by a shock. In this sense the simulation results presented in Chap. 7 for uniform stationary MHD bow shock flows around a sphere apply also to the case of CMEs moving through the solar corona. The CME, however, is a highly time-dependent process, because the CME material can deform and expand during its outward motion, and because the upstream solar wind is not uniform. The simulation of a stationary flow around a rigid obstacle can thus only be an approximation of CME flow, and in such simulations only the aspects of MHD shock formation which are independent from the details of the downstream flow may be potentially relevant for CME propagation.

It is believed that CMEs moving outwards with a speed slower than the fast speed, but faster than the slow MHD speed, may induce preceding *slow* mode MHD shock fronts [145, 68]. This is an interesting separate topic, and the simulation results for the transition from superfast to subfast flow presented in this dissertation do no apply to this class of events.

The shocks induced by fast CMEs have been observed in space, and many observed interplanetary shock waves are believed to be associated with CMEs. The physical link between interplanetary shock waves and CMEs is, however, not always very clear. It is believed that the impulsive post-CME reconnection flare may drive blast waves to propagate into interplanetary space as shocks quite distinct from those induced by outward moving CME material. There is thus still a lot of discussion about where and how interplanetary shock waves are generated. We now briefly review some of the observations regarding shocks induced by CMEs and regarding interplanetary shock waves.

Observations of shocks induced by CMEs

There are several different sources of observational information about CME-induced shock waves.

First, in the late 70s the HELIOS satellites performed in-situ measurements as close to the sun as $10R_s$. Fast MHD shocks were observed, and there was a good correlation with fast CMEs observed by the Solwind coronagraph [136]. This was the first clear observational confirmation that fast CMEs do indeed generate fast MHD shocks.

Second, Ulysses and other heliospheric spacecraft have observed many fast MHD shocks which are believed to be associated with CMEs, at distances up to several Astronomical Units (AU) from the sun [57]. One AU is the average distance between the sun and the earth.

Third, upstream from the earth's bow shock, observations by the ACE and WIND satellites routinely show the arrival of interplanetary shocks. A magnetic cloud is a transient ejection in the solar wind defined by relatively strong magnetic fields, a smooth rotation of the magnetic field direction and a low plasma β [15]. Magnetic clouds are believed to originate from CMEs, and they often are preceded by a shock front. The interaction of magnetic clouds with the earth's magnetic system is discussed in Sec. 8.2.3.

Radio observations are a fourth way to observe interplanetary shocks. MHD shocks produce so-called type II radio bursts [125]. The frequency of the radio signal depends on the ambient density at the emission site. Using a model for the variation of the density in the radial direction, the propagation of shock fronts can be followed all the way from the sun to the earth. Unfortunately there is a large uncertainty in the density profiles which results from the available density models so that interpretations based on these models are not unique. Radio observations seem to indicate that when fast CMEs erupt, shocks are formed well inside the field of view of coronagraphs [75].

Fifth, the most direct observations of CMEs are provided by white-light coronagraph images. From first-principle reasoning it follows that CMEs which propagate with a superfast speed relative to the ambient solar wind induce a preceding shock front, and that no perturbations can precede this shock wave. The leading feature of a fast CME in a coronagraph image can thus naturally be identified with the induced shock. However, line of sight integration effects complicate the interpretation of coronagraph images considerably. Our simulation results in Chap. 7 show that at a leading shock the post-shock density should be about a factor 2 to 3 higher than the pre-shock density. In the real corona this factor is likely to be larger due to the large heat conduction. Such a density contrast should show up in coronagraph images, but the line of sight effect would smear the discontinuous jump out into a jump not of the intensity but of the gradient of the intensity. In the strict sense, shocks — defined as discontinuous variations in intensity — can thus not readily be seen on coronagraph images. Instead, a relatively sharp transition in intensity gradient at the leading edge of a fast CME could well be a signature of a fast shock. The change in intensity gradient at the leading edge of a CME in a coronagraph image should then correspond to the expected density jump at a leading shock. Hundhausen (private communication) has analyzed the coronagraph intensity variation at leading edges of fast CMEs, and has found good agreement with the intensity variation derived from the expected density jump at preceding shocks. Leading bright edges of fast CMEs in coronagraph images can thus be interpreted as signatures of fast MHD shocks, or, more precisely, at least a portion of the bright signature may have been produced by shock compression of the ambient corona [146]. It has to be noted that there is no general agreement on this interpretation.

CMEs and multiple interacting shock fronts

In Chap. 7 it was argued that the magnetically dominated bow shock topology of Fig. 7.1 with a secondary slow shock following the leading fast shock, is independent from the details of the downstream flow, because this topology is imposed by the geometrical properties of switch-on shocks at perpendicular points on the leading shock front. In this sense we can expect that the magnetically dominated topology described in Chap. 7 may also occur in the case of shocks induced by fast CMEs, when upstream flows are magnetically dominated and switch-on shocks occur on the leading shock front. In the lower corona the plasma β is indeed likely to be lower than 1.2, the upstream magnetic field is presumably close to radial in many cases, and there must certainly be fast CMEs which move with speeds between the Alfvén speed and about two times this speed relative to the solar wind. The switch-on condition Eq. 3.77 must thus be satisfied for the shocks induced in front of these fast CMEs, and we can expect that secondary slow shocks form as in Fig. 7.1. This reasoning seems to indicate that in the lower corona secondary slow shocks should be present between the leading fast shock and the CME material in the case of fast CMEs. If those shocks are indeed formed, could we be able to detect them with present-day observational capabilities?

Let us first consider coronagraph observations. In Figs. 8.2 and 8.3 we clearly see dimpled leading fronts and secondary features following the leading fronts (indicated by arrows). The dimpling of the leading front is reminiscent of the dimpled leading shock fronts arising in our simulations of MHD bow shock flows with magnetically dominated upstream parameter values (e. g. Figs. 6.2 and 7.4). Steinolfson and Hundhausen [147] found dimpled leading shock fronts in their 2D simulation results of fast moving CMEs, and the apparent dimpling of leading features of fast CMEs in coronagraph observations has indeed been interpreted as indirect observational evidence for the occurrence of MHD switch-on shock phenomena ahead of fast CMEs [68, 147]. In our simulation results for magnetically dominated parameter values, secondary slow shocks follow the leading shock front, and the coronagraph observations do indeed suggest secondary features which have developed behind the leading bright fronts.

The secondary features indicated by arrows in Fig. 8.2 are vaguely reminiscent of the slow shocks following the leading front in the simulation result of Fig. 7.19 (first and second panel). The secondary feature indicated by the arrow in Fig. 8.3 is not unlike the secondary feature in the simulation result of Fig. 7.4a. Some coronagraph images may show evidence of the V-shaped features present in our simulation results for the transient phase of the flows (Figs. 7.19 and 7.20). Indeed, if we estimate the effective 'radius' of the ejected CME material to be typically 7×10^6 km (or approximately 1 R_s) and the Alfvén speed to be 600 km/s, then the simulation of Fig. 7.20 shows that the V-shaped feature is formed and convected away in the simulation on time scales of about one hour. LASCO coronagraph images are taken several times per hour, so the V-shaped feature could be observable. In fact, some observations of secondary features in CMEs [32] could be related to the simulated structure of Fig. 7.20.

Like for the dimple, we can argue that the secondary features visible in Figs. 8.2 and 8.3 may be signatures of the secondary slow shocks present in our simulation results. Of course this observational evidence is indirect and inconclusive. It is indeed not difficult to think of alternative interpretations for the secondary features in the coronagraph images, and the coronagraph observations do not seem to provide enough information to enable conclusive interpretation of features like this.

Our simulation results lead us to predict the possible observation of secondary shock-like features lagging the leading front of fast CMEs, but unfortunately present-day observational capabilities seem not to be able to identify such features conclusively. Future time-dependent 3D MHD simulations with a realistic CME structure may strengthen this prediction if they were to confirm the formation of secondary slow shocks. Line of sight integration could be performed on such simulation results to mimic coronagraph images, which could be compared with real coronagraph images. This may help in the identification of secondary slow shocks, but it is our expectation that interpretation would remain difficult and that the results might still be inconclusive. The STEREO satellites which may be launched a few years from now, will look at CMEs from two different angles. Tomographic techniques may help to reconstruct the 3D structure of CME features. This may allow for the observation of secondary slow shocks.

In situ satellite observations may also be able to provide more conclusive evidence for secondary slow shocks than coronagraph observations. It would certainly be interesting to reinvestigate the old HELIOS data in this respect. The satellite, however, would have to be located in the low-β region close to the sun in order to be able to observe the slow shocks, because presumably the secondary slow shock would disappear as the CME moves out into upstream plasma with a high plasma β. Signatures of the secondary slow shock may remain present for later times in the possibly nearly self-similar further expansion of the CME [50]. Unfortunately no missions have been planned for the near future which would provide in situ measurements close enough to the sun. At present the coronal magnetic field cannot directly be measured. When such measurements would become available, this would certainly be a big help for the interpretation of structures in coronagraph images.

It seems that our simulation results on magnetically dominated shock topology stand a better chance of getting observational confirmation in the context of the earth's bow shock flow than in the context of solar CMEs, at least for the near future. This is discussed in the next Section.

8.2 Slow shocks in the earth's magnetosheath

We begin this Section with a brief discussion of the properties of the solar wind, the earth's magnetosphere and magnetic clouds, followed by a presentation of simulation results which show that slow shocks can be present in the earth's magnetosheath following the bow shock under magnetically dominated solar wind conditions for which switch-on shocks occur. Then we discuss observational evidence for the presence of slow shocks in the earth's magnetosheath. A preliminary discussion of some of the simulation results described in this Chapter has been presented as a brief report [153]. A more complete account will appear in [154].

8.2.1 The solar wind, the earth's magnetosphere and magnetic clouds

Fig. 8.4 shows solar wind parameters measured by the ACE satellite [156] in front of the earth's bow shock during the full month of February 1999. The solar wind plasma β is most often larger than one but has a large variation (the axis is logarithmic). The (total) sonic and Alfvénic Mach numbers are high (often higher than ten), so the (total) dynamic pressure is generally large compared to the magnetic and thermal pressures. The ecliptic plane is the plane in which the earth orbits around the sun. On average the solar wind magnetic field — or Interplanetary Magnetic Field (IMF) — is expected to lie in the ecliptic plane and to make an angle θ_B of approximately 45° with the sun-earth line [67]. This angle is due to the spiraling of the magnetic field lines rooted in the rotating sun, an effect that can be seen for instance in the model flow of Fig. 5.12. It can be seen in Fig. 8.4 that the angle θ_B often deviates substantially from the value of 45°. The angle θ_v between the solar wind velocity and the sun-earth line is generally quite small, less than 5° or so (see Fig. 8.6).

Fig. 8.5 shows a sketch of the earth's magnetic environment. The earth has an intrinsic magnetic field which is roughly a dipole with axis perpendicular to the ecliptic plane, and which is confined to a region called the *magnetosphere*. The supersonic and super-Alfvénic (and thus superfast) solar wind forms a bow shock in front of the earth. The region just downstream from the bow shock is called the magnetosheath, which

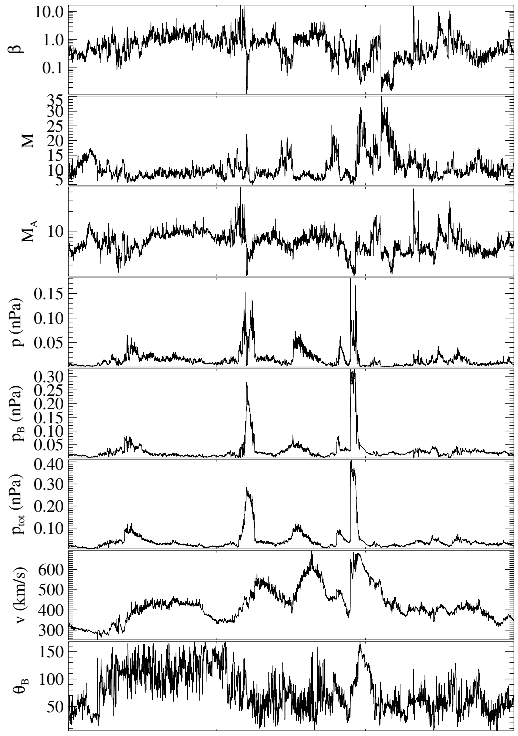

Figure 8.4: *ACE solar wind data for the full month of February 1999. p_{tot} and p_B are the total and the magnetic pressure respectively, and θ_B is the angle between the magnetic field and the sun-earth line.*

is separated from the magnetosphere by a contact surface called the *magnetopause*. In coordinate systems generally used in magnetospheric physics, the sun-earth line is the x-axis, the ecliptic plane is the xy plane and the z-axis is perpendicular to the ecliptic plane. The orientation of the z-axis is chosen such that the earth's magnetic field has a positive B_z component.

When the magnetosheath magnetic field in front of the magnetopause lies in the ecliptic plane, — in the direction perpendicular to the paper in Fig. 8.5 —, then it is oriented perpendicular to the earth's dipole field, such that at the dayside magnetopause the two fields do not reconnect. Positive B_z magnetosheath field has the same orientation as the earth's field, such that again reconnection is not enhanced. For negative B_z magnetosheath field, however, the two fields are anti-parallel such that magnetopause reconnection is strongly enhanced. This increased reconnection enhances the energetic coupling between the solar wind and the

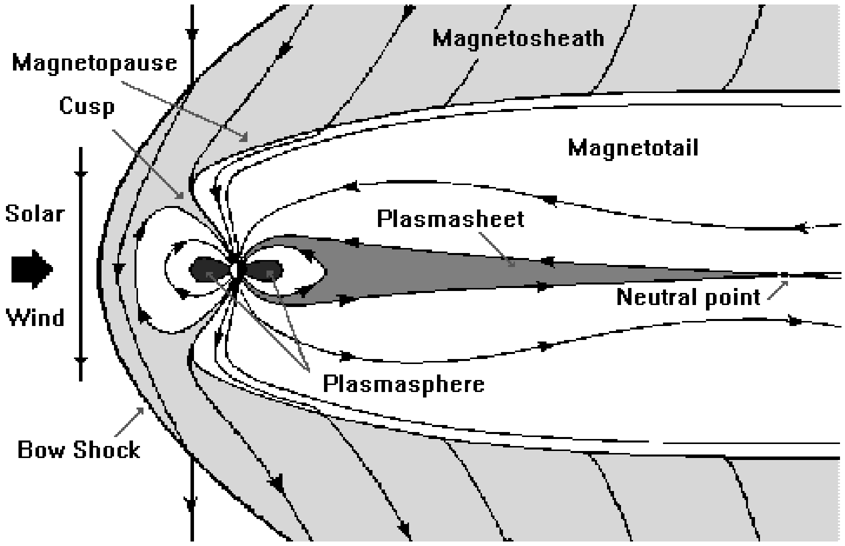

Figure 8.5: *The earth's magnetic environment (xz plane). (courtesy ISPEC)*

magnetosphere, which leads to magnetic storms. It is believed that there is a direct relation between the IMF orientation, as measured upstream from the bow shock, and the orientation of the magnetosheath magnetic field in front of the magnetopause at later times. It is thus said that magnetic storms occur when the IMF has a large negative B_z component for an extended period of time.

A magnetic cloud is a transient ejection in the solar wind defined by relatively strong magnetic fields, a smooth rotation of the magnetic field direction and a low plasma β [15]. Fig. 8.6 shows WIND satellite data describing a magnetic cloud arriving at the earth in January 1997 [15]. The dotted line indicates the arrival of the magnetic cloud, which is preceded by a fast shock. B_z turns gradually from strongly negative to strongly positive during the 22 hours that the cloud event lasts. The cloud is interpreted to be the magnetic flux rope which forms the cavity in the pre-CME structure of Fig. 8.1, while the high-pressure material at the trailing edge of the cloud is believed to be prominence material [15]. The persistent strong negative B_z magnetic field introduced by the magnetic cloud of Fig. 8.6 caused a magnetic storm of moderate strength through enhanced magnetic reconnection at the magnetopause. These conceptual scenarios are generally accepted often mainly based on correlation analysis arguments, but the physical mechanisms of how a magnetic cloud precisely leads to a magnetic storm remain largely un-

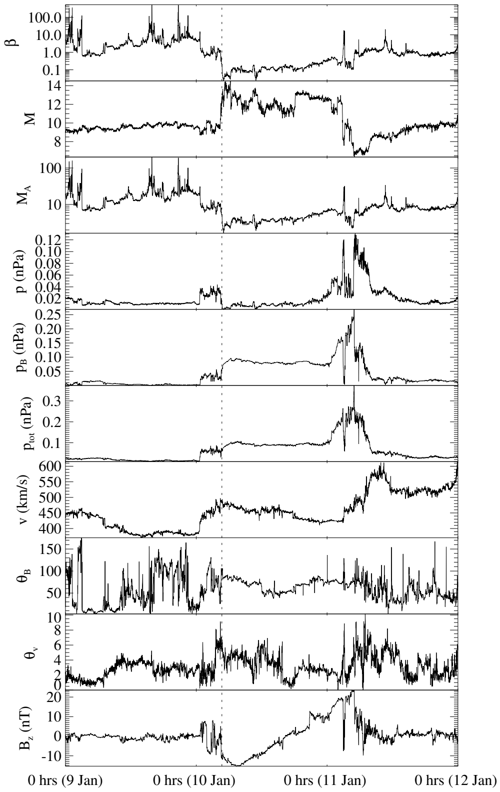

Figure 8.6: *WIND data describing a magnetic cloud arriving at the earth in January 1997. θ_v is the angle between the velocity and the sun-earth line. The dotted line indicates the arrival of the magnetic cloud, which is thought to be a flux rope. In the magnetic cloud the magnetic field dominates, such that the plasma β is low. The cloud is preceded by a fast shock, and is followed by high-pressure material, which is thought to originate from a solar prominence.*

known. For instance, it is not well known how and how fast the negative B_z field of the magnetic cloud propagates through the magnetosheath and reaches the magnetopause.

8.2.2 3D bow shock flows around a paraboloid surface

This Section describes 3D MHD simulations which model the interaction of the solar wind with the earth. The flow of the solar wind around the

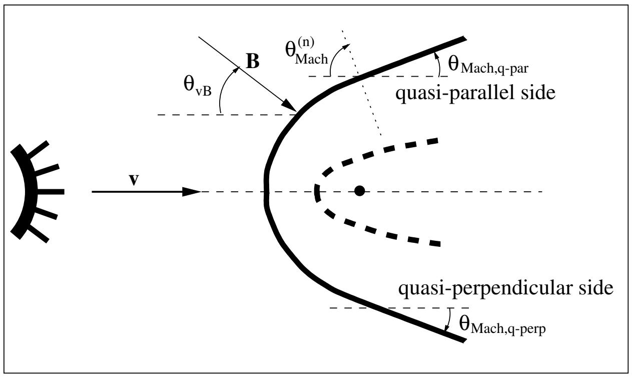

Figure 8.7: *Sketch of the simulation set-up for the problem of solar wind flow around the earth. We model the magnetopause (thick dashed) as a conducting paraboloid. The bow shock is thick solid. $\theta_{Mach,q-par}$ is the Mach angle on the quasi-parallel side of the bow shock, where the magnetic field is close to parallel to the shock normal. $\theta_{Mach,q-perp}$ is the Mach angle on the quasi-perpendicular side. $\theta^{(n)}_{Mach}$ is the normal Mach angle on the quasi-parallel side.*

earth can best be modeled taking into account the inner magnetosphere and the ionosphere — see e. g. [122] and references therein —, but we are primarily interested in investigating the bow shock and the flow in the magnetosheath behind the bow shock, so we can as a first approximation study the flow around a perfectly conducting paraboloid surface which models the magnetopause [174, 16] (Fig. 8.7). This approximation implies that the process of magnetic reconnection at the magnetopause is not considered in our simulations. The solar wind flow is most of the time almost radial along the sun-earth line, so for simplicity we align the velocity of the incoming plasma with the sun-earth line and with the symmetry axis of the paraboloid. In our simulations we consider a uniform upstream flow in which the magnetic field $\vec{B}$ makes an angle θ_{vB} with the velocity $\vec{v}$. For definiteness we think of the magnetic field as lying in the ecliptic plane, but a field rotated out of that plane would simply make the solutions presented below rotate around the sun-earth line. This flow problem has three independent free upstream parameters, for which we choose the Mach number in the direction of the incoming flow $M = v/c$, the plasma $\beta = 2p/B^2$, and the angle θ_{vB}. As before we simulate the 3D bow shock flows starting from a uniform initial condition and by advancing the time-dependent MHD equations until a steady state solution is reached. The simulations are performed on stretched polar-like structured grids with $30 \times 60 \times 30$ or $60 \times 120 \times 60$ cells.

We are interested in the influence of intrinsically magnetic effects on the bow shock and magnetosheath flow, so we start out with a discussion of bow shock flows with magnetically dominated solar wind parameters for which switch-on shocks occur, followed by a discussion of bow shock flow simulations for pressure-dominated parameter values.

The reader will notice many similarities between the simulation results to be presented in this Section for 3D bow shock flows around a paraboloid surface, and the results for flow around a sphere which were presented in Chap. 7. This is not surprising, because it confirms the argumentation in Chap. 7 that the results on magnetically dominated bow shock topology are generic and do not depend on the shape of the obstructing obstacle.

Magnetically dominated bow shock flows

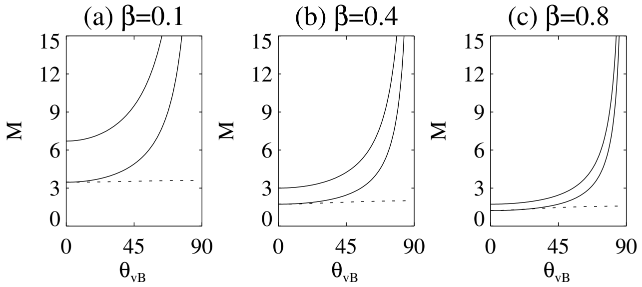

Figure 8.8: *Magnetically dominated parameter regime (switch-on shocks occur) for various values of β. For given plasma β and angle θ_{vB}, switch-on shocks can arise for (total) Mach numbers between the two solid lines.*

As was described in Chap. 3, the occurrence of switch-on shocks is an intrinsically magnetic effect which can only arise in a certain regime for the upstream parameters. At a point on a shock front where the magnetic field is perpendicular to the shock front — we call such a point a perpendicular point —, the shock is switch-on when the upstream Alfvénic Mach number M_{An} in the direction n normal to the shock surface — and thus along the incoming magnetic field — satisfies [80, 150]

$$1 < M_{An} < \sqrt{\frac{\gamma(1-\beta)+1}{\gamma-1}}. \tag{8.1}$$

Switch-on shocks cannot arise for $\beta > 2/\gamma = 1.2$.

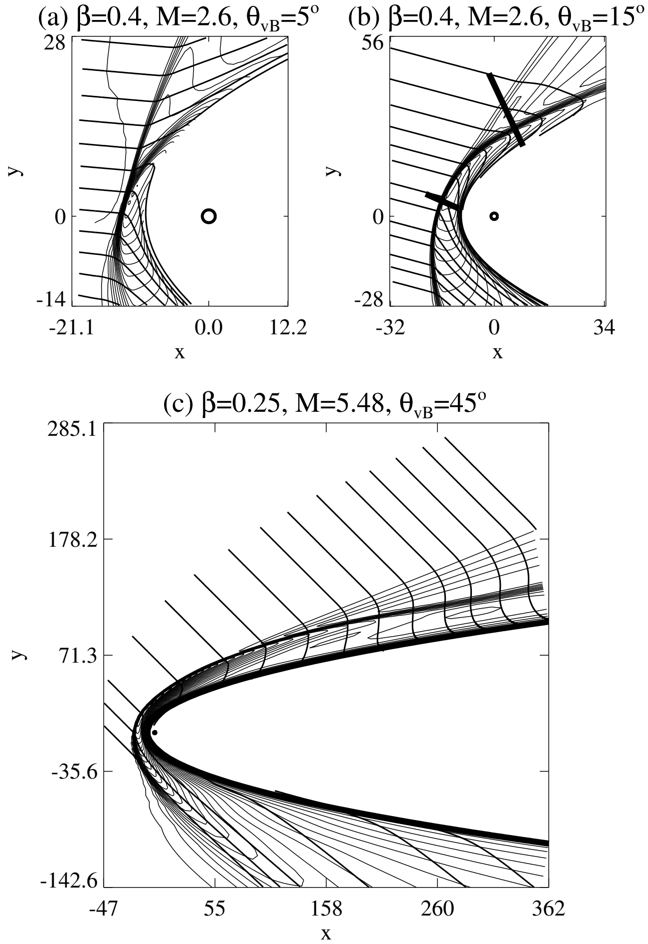

Figure 8.9: *3D bow shock flows around a paraboloid surface for magnetically dominated upstream parameter values. Density contours and magnetic field lines in the ecliptic plane are shown. In all flows a slow shock is following the leading shock.*

It follows from Eq. 8.1 that the condition for the occurrence of switch-on shocks in the configuration of Fig. 8.7 can be written as

$$M_- = \frac{1}{\cos\theta_{vB}}\sqrt{\frac{2}{\gamma\beta}} < M < M_+ = \frac{1}{\cos\theta_{vB}}\sqrt{\frac{2}{\gamma\beta}}\sqrt{\frac{\gamma(1-\beta)+1}{\gamma-1}}, \quad (8.2)$$

with the total Mach number $M = v/c$ and v the magnitude of the velocity. In Fig. 8.8 the switch-on parameter regime in the θ_{vB}–M plane is plotted for various values of β. For a given value of θ_{vB}, switch-on shocks can arise for values of M between M_- and M_+ (corresponding to the two solid lines). The Mach number has to be higher than $M_0 = c_f/c$ (dotted line), with c_f the fast MHD speed along the sun-earth line, because the inflow along the sun-earth line has to be superfast in order to have a fast leading shock. The limit $M = M_-$ corresponds to $\theta_{vB} = \theta^{(n)}_{Mach}$ (Fig. 8.7). For $M < M_-$, the normal Mach angle $\theta^{(n)}_{Mach}$ is smaller than the angle θ_{vB}, such that there is no perpendicular point on the shock front.

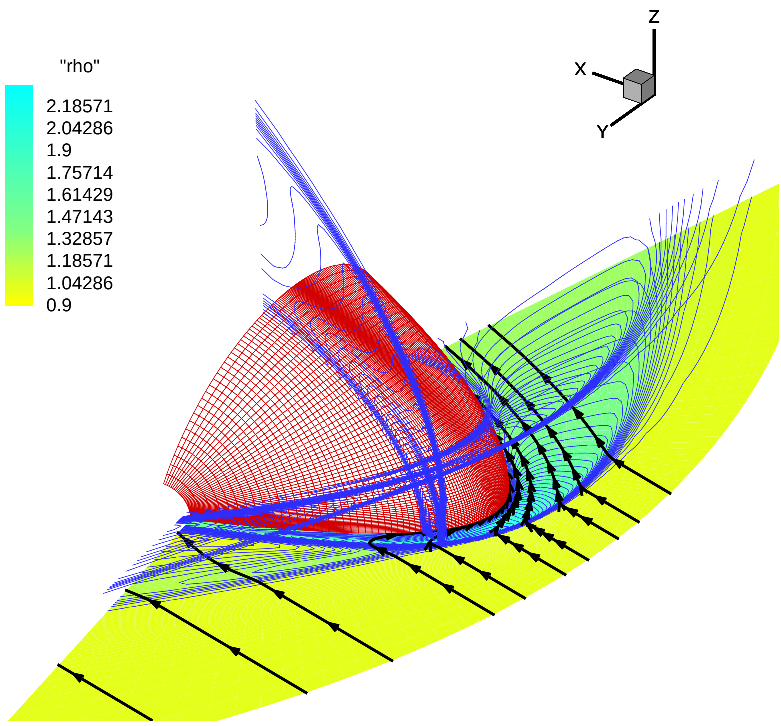

Figure 8.10: *3D bow shock flow around a paraboloid surface with inflow $\beta = 0.4$, $M = 2.6$, and $\theta_{vB} = 15°$. This is the simulation of Fig. 8.9b. Density contours and field lines are shown in the ecliptic plane — the xy plane — , and density contours in two additional planes. The leading shock front is clearly followed by a secondary shock front, which is attached to the leading front, and which extends well out of the ecliptic plane. The secondary shock front is of the slow type.*

Fig. 8.9 shows the results of three 3D bow shock simulations with magnetically dominated upstream parameter values (switch-on shocks arise, Eq. 8.2). Density contours and magnetic field lines are shown in the ecliptic plane. Units are expressed in earth radii R_E, and the approximate size and location of the earth is indicated by a circle in the origin of the coordinate system. The distance between the earth and the magnetopause is taken as $10\,R_E$ along the sun-earth line, and $17\,R_E$ in the direction perpendicular to this line. In all three flows a slow shock is following the leading shock and is attached to it. Intrinsically magnetic effects thus substantially modify the flow topology compared to the single-front bow shock solution which arises for a pressure-dominated upstream flow. We have performed many more simulations with parameter values in the switch-on regime (Eq. 8.2), and in the resulting flows we have always obtained the same basic flow topology, with a secondary slow shock front following the leading front and attached to it. This is the topology of Fig. 7.5b, which has been explained in terms of the properties of MHD shocks in Sec. 7.1.3.

A 3D visualization of the flow of Fig. 8.9b is shown in Fig. 8.10. Fig. 8.11 shows how streamlines and magnetic field lines originating from points slightly above the ecliptic plane drape around the paraboloid obstacle. It is clear that the presence of the secondary slow shock greatly influences the field line draping, as the magnetic field is refracted strongly at the slow shock front. This change in field line topology may influence the reconnection process at the earth's magnetopause. Fig. 8.12 shows how the secondary shock front is curved. The surface drawn is an isosurface of $||\nabla\rho||$, which wraps around the shock surfaces where $||\nabla\rho||$ peaks. A cut-off value $c_{cut-off}$ is chosen which defines the isosurface $||\nabla\rho|| = c_{cut-off}$ drawn. A smaller cut-off value would lead to an iso-surface with larger spatial extent. The shock surfaces thus actually extend further than one would infer from Fig. 8.12.

In Fig. 8.9, the way in which the magnetic field is refracted at the secondary shocks shows that those shocks are of the slow type. The slow shocks are almost switch-off shocks, such that the magnetic field is almost parallel to the shock normal downstream from the shock. In Figs. 8.9a and b the slow shock is followed by a strong rarefaction region, in which the magnetic field rotates further. We can determine the types of the shocks more accurately by considering the variation of flow parameters along cuts perpendicular to the shock fronts.

Fig. 8.13 shows such cuts along the thick solid lines perpendicular to slow and intermediate shock segments in Fig. 8.9b. Let us first look at the cut perpendicular to the secondary slow shock, presented in Fig. 8.13a–f. Going from left to right, the density, pressure and magnetic field strength first increase when the leading fast shock is passed. At the second discontinuity, the density and the pressure rise whereas the

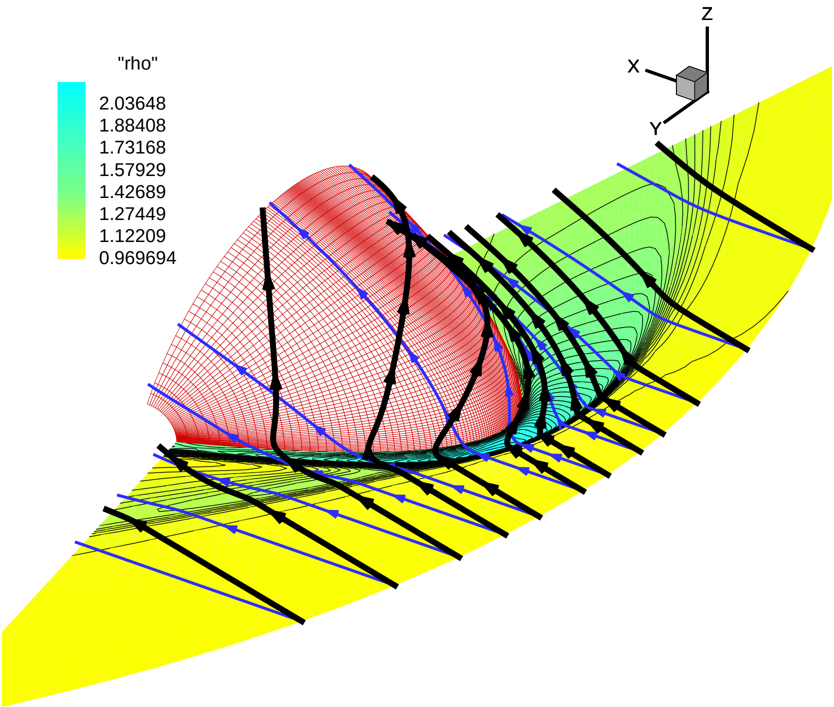

Figure 8.11: *Magnetic field lines (black) and streamlines (blue) for the bow shock flow solution of Fig. 8.9b. The field lines and streamlines are drawn starting from points located slightly above the ecliptic plane, and drape around the paraboloid obstacle in the magnetosheath region.*

magnetic field strength decreases sharply. This is a clear signature of a slow shock. This diagnosis is confirmed by the normal Mach number plots of Fig. 8.13d-f. The flow is superslow but sub-Alfvénic upstream, and subslow downstream. The shock is thus a 3–4 slow shock. The upstream Alfvénic Mach number is very close to one, however, so the shock is very close to a 2=3–4 slow switch-off shock.

In Fig. 8.13g–l we consider the cut perpendicular to the leading shock front in Fig. 8.9b. We cut the leading shock front between the point where the magnetic field is perpendicular to the shock front, and the point where the secondary slow shock is attached to the leading front. The density and pressure increase at the discontinuity, and the component $B^{(t)}$ of the magnetic field tangential to the shock front changes sign. This is a clear signature of an intermediate shock. We can again confirm

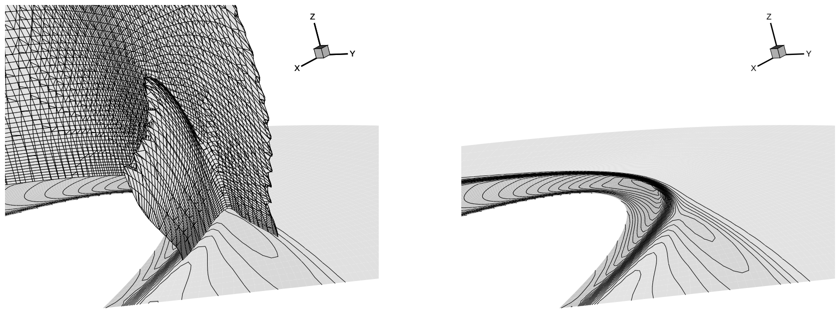

Figure 8.12: *Visualization of the shock fronts for the bow shock flow solution of Figs. 8.9b, 8.10 and 8.11. The secondary slow shock clearly extends out of the ecliptic plane.*

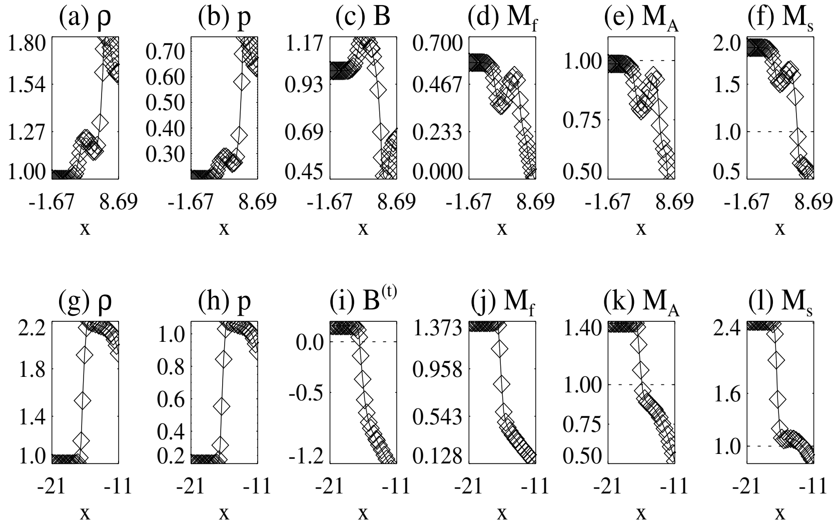

Figure 8.13: *(a–f) Cut along the upper thick solid line in Fig. 8.9b. Going form left to right, we first pas the leading fast shock. The second discontinuity is a 3–4 slow shock, which is very close to a 2=3–4 slow switch-off shock. (g–l) Cut along the lower thick solid line in Fig. 8.9b. The shock is a 1–3 intermediate shock, which is very close to a 1–3=4 intermediate shock.*

this diagnosis by looking at normal Mach numbers (Fig. 8.13j–l). The flow is superfast (and thus super-Alfvénic) upstream, and sub-Alfvénic but superslow downstream. The shock is thus a 1–3 intermediate shock, but very close to 1–3=4.

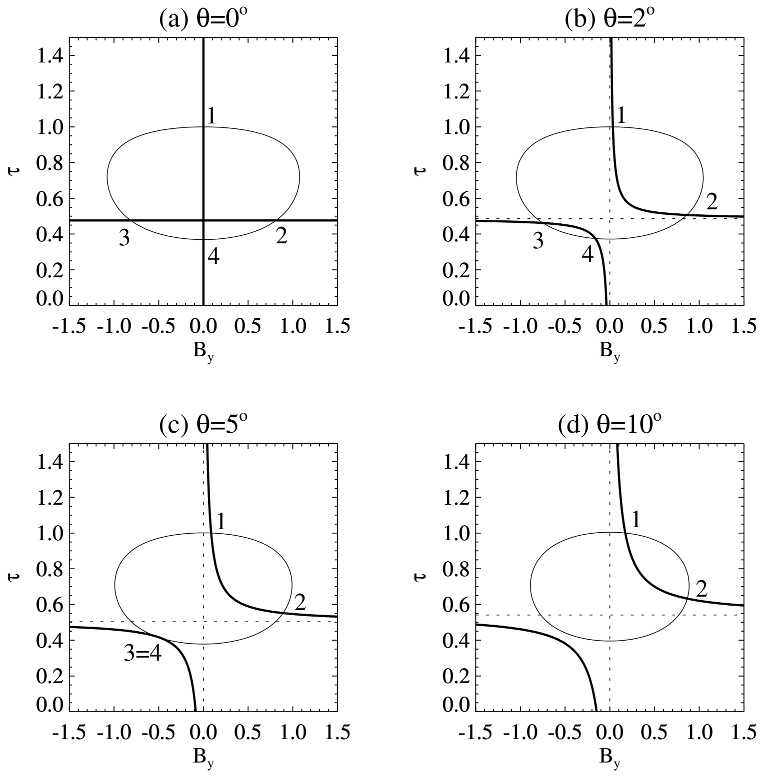

Figure 8.14: *Solutions of the RH relations for the upstream parameters of Fig. 8.9b with* $\theta_{vB} = 15°$. *These parameters are magnetically dominated. The maximum angle between the magnetic field and the shock normal for which intermediate shocks can occur is approximately* $5°$.

Fig. 8.14 shows that for the upstream parameter values of Fig. 8.9b the maximum angle between the magnetic field and the shock normal for which the 1–3 intermediate shock can occur is approximately $5°$. This is consistent with the angle for which the leading shock front splits up into two consecutive shock fronts in Fig. 8.9b.

The results shown here for 3D flows around a paraboloid surface have the same basic topology as the magnetically dominated flow around a conducting sphere which was described in Chap. 7. All this indicates that this topology is generic for 3D bow shock flows with magnetically dominated parameter values. The secondary slow shock is required because of the geometrical properties of switch-on shocks, as was argued in Chap. 7. These findings are an important addition to the general theory of MHD bow shocks [114].

Pressure-dominated bow shock flows

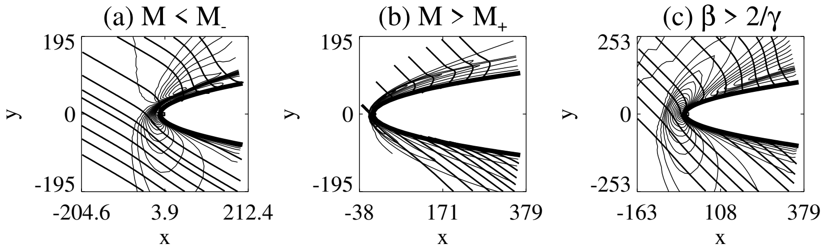

Figure 8.15: *3D bow shock flows around a paraboloid surface for pressure-dominated upstream parameter values (switch-on shocks do not occur). Density contours and magnetic field lines in the ecliptic plane are shown.*

It is interesting to consider bow shock flows in the configuration of Fig. 8.7 for pressure-dominated upstream parameter values for which switch-on shocks do not occur. Indeed, in Fig. 8.15 we present preliminary results of such simulations for which we *do* find secondary shocks behind the leading shock. Based on our discussion of the switch-on parameter regime above (Eq. 8.2), we can distinguish between three different parameter regimes outside the switch-on regime. First there is the case that $\beta > 2/\gamma$. For $\beta < 2/\gamma$, we have the two cases $M < M_-$ and $M > M_+$. As shown in Fig. 8.15, in all of those three regimes we have found secondary shocks for some choices of parameter values, while for most choices of parameter values in these three regimes we did not find secondary shocks. Fig. 8.15a considers a bow shock flow with $M < M_-$ ($\beta = 0.4$, M=1.91, $\theta_{vB} = 30°$). In Fig. 8.15b a bow shock flow with $M > M_+$ is considered ($\beta = 0.25$, M=8.76, $\theta_{vB} = 45°$). Fig. 8.15c shows a bow shock flow with $\beta > 2/\gamma$ ($\beta = 1.5$, M=1.34, $\theta_{vB} = 45°$). The secondary shock is not always attached to the leading shock front. The reader may notice that these preliminary simulations were carried out at low resolution and contain some unexplained features. The need for an extensive parameter study with high resolution simulations is apparent.

On one hand it is surprising to find slow secondary shocks for flows with pressure-dominated upstream parameter values, because in the 2D case slow shocks arise if and only if the upstream flow is magnetically dominated and switch-on shocks occur (Sec. 6.3). On the other hand, it is not so surprising, because in principle every fast shock could be followed by slow or intermediate shocks. For pressure-dominated parameter values, the formation of the secondary slow shock is not related to the geometrical properties of switch-on shocks at perpendicular points on the leading shock front, but instead seems to depend more on the shape of the obstacle and the angle θ_{vB}. The secondary shocks in Fig. 8.15a and c may be due to boundary layer separation. For the case of solar wind flow around the earth, the precise shape of the magnetopause and the reconnection process at the magnetopause may become important in determining if slow shocks in this parameter regime exist or not.

8.2.3 Observations of slow shocks in the magnetosheath

Observations by Song et al. (1992) [141]

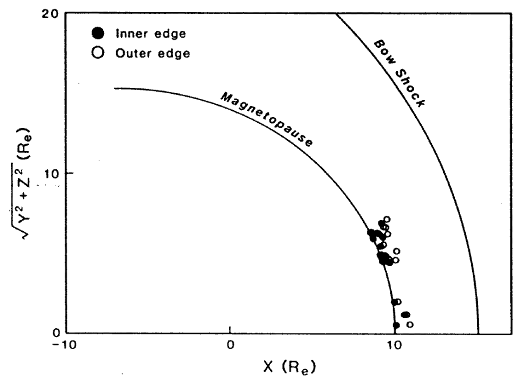

Figure 8.16: *Locations of observed density enhancements in the magnetosheath near the magnetopause. (From Song et al. (1992) [141])*

The results described in the above Section on slow shocks following fast shocks may have direct implications for the structure of the flow in the earth's magnetosheath under some solar wind conditions. Indeed, slow shocks have been observed in the dayside magnetosheath and in the distant magnetotail region.

Song et al. [140, 141, 138] claim the existence of density enhancements

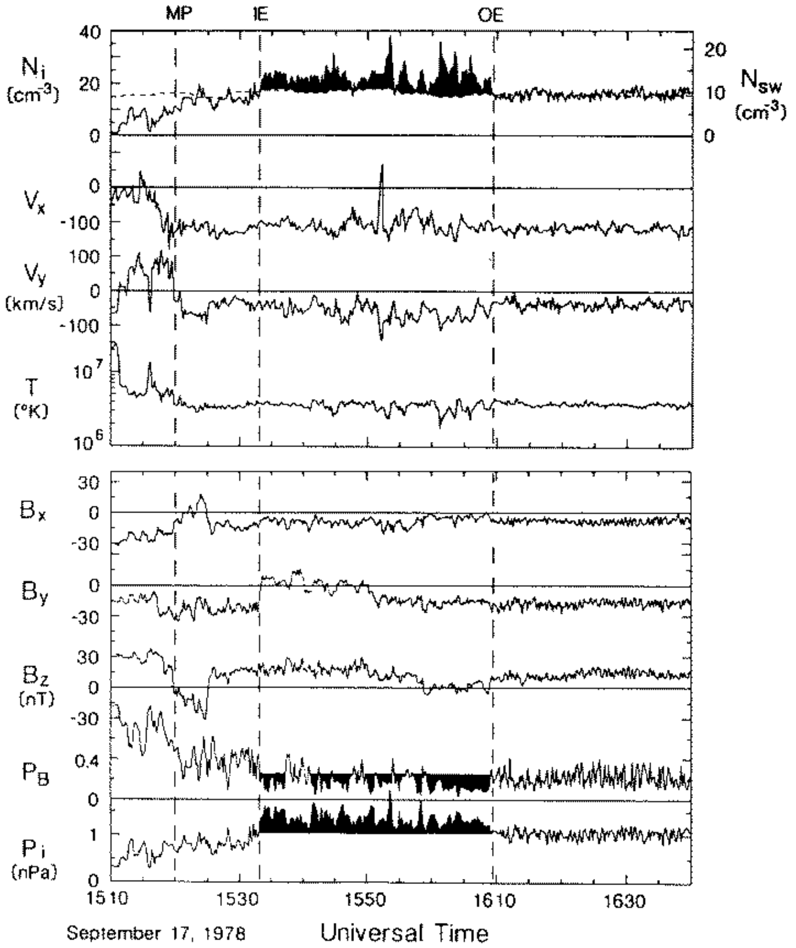

Figure 8.17: *An outbound magnetosheath pass on September 17, 1978, by ISEE2. MP stands for magnetopause, IE for inner edge, and OE for outer edge. The region with enhanced ion density N_i, ion pressure P_i and magnetic pressure P_B is shaded. The magnetosheath flow is disturbed by kinetic waves of various kinds which complicate a clear interpretation. The jump at OE is interpreted as a slow shock, and results of a Rankine-Hugoniot analysis of the shock are presented in Table 8.1. (From Song et al. (1992) [141])*

of slow mode type in front of the dayside magnetopause in more than

50% of ISEE-1 and ISEE-2 satellite passes. The slow mode structures were interpreted as slow shock fronts. Fig. 8.16 shows where the inner and outer edges of the density enhancements were observed between the earth's bow shock and magnetopause close to the sun-earth line. Fig. 8.17 gives an example of an observation of such a density enhancement. The density drop at the inner edge (IE) may be due to the boundary layer effect shown in Fig. 7.9.

As can be seen in Fig. 8.17, the magnetopause flow tends to be disturbed by kinetic waves of various kinds which often complicate a clear interpretation of macroscopic flow structures. For this and other reasons some skepticism has arisen about the interpretation of the observations in [140, 141] as stationary slow shocks.

Indeed, the observed slow mode waves may not be stationary, but may be transient structures. It has been shown in 2D MHD simulations [180] that transient slow mode waves and shocks can be generated by the interaction of various types of solar wind waves with the earth's bow shock and magnetosphere. This has been confirmed in 2D hybrid simulations [97] and in 3D MHD simulations [16]. The relevance of these alternative explanations was questioned in recent work by Song et al. [139, 142]. We have to proceed cautiously and have to keep in mind alternative interpretations, but it seems justified to investigate if at least some of the structures observed by Song et al. may be related to the stationary slow shocks found in our 3D MHD simulations of magnetically dominated bow shock flows.

Table 8.1: *Comparison of upstream and downstream Mach numbers for a slow switch-off shock, a slow shock observed in the earth's magnetosheath (Song et al. (1992) [141]), and the secondary slow shock in the simulation of Fig. 8.9b.*

slow switch-off shock Fig. 3.8e	**Song et al. (1992)** Fig. 8.17	**slow shock** Fig. 8.9b
upstream		
$M_A = 1$	$M_A = 1.17$	$M_A = 0.99$
$M_s > 1$	$M_s = 1.38$	$M_s = 1.6$
downstream		
$M_A = M_s < 1$	$M_A = 0.93$	$M_A = 0.65$
	$M_s = 1.00$	$M_s = 0.65$

First we investigate if the observed and simulated shocks are similar regarding jumps in normal Mach number. Rankine-Hugoniot analysis of the observed slow shock of Fig. 8.17 leads to upstream Mach numbers $M_A^{(u)} = 1.17$ and $M_s^{(u)} = 1.38$, and to downstream Mach numbers $M_A^{(d)} = 0.93$ and $M_s^{(d)} = 1.00$ [141]. Note that these Mach numbers are taken in the direction normal to the slow shock front, but that we have dropped the subscript n here. In Table 8.1 these values are compared with the Mach numbers of a slow switch-on shock, for which $M_A^{(u)} = 1$ and $M_s^{(u)} > 1$, and $M_A^{(d)} = M_s^{(d)} < 1$. It turns out that the secondary slow shock in Fig. 8.9b has Mach numbers in a similar range: $M_A^{(u)} = 0.99$ and $M_s^{(u)} = 1.6$, and $M_A^{(d)} = 0.65$ and $M_s^{(d)} = 0.65$. This suggests that at least some of the slow shocks observed by Song et al. may be of the same type and origin as the slow shocks in Fig. 8.9.

Second we investigate if the solar wind has parameter values in the switch-on regime often enough to explain secondary slow shocks in the dayside magnetosheath in 50% of ISEE-1 and ISEE-2 passes. It turns out that this cannot be the case, because the solar wind often has a high plasma β and/or high Mach numbers (Fig. 8.4). We have made an analysis of three arbitraryly chosen months of ACE [156] solar wind satellite data (July 1998, and January and February 1999) and have found that for each of these months the solar wind averaged over five-minute time-intervals was magnetically dominated (switch-on shocks occur, Eq. 8.2) for about 8% of the time (7.0% for June 1998, 7.8% for January 1999, and 7.7% for February 1999). This is clearly not enough to explain stationary slow shocks in the dayside magnetosheath in more than 50% of the cases, as reported in [141], especially if one realizes that the solar wind is often quite oscillatory and that it may not often reside in the switch-on regime long enough for the slow shock to form as a stationary feature. However, we have found that several times per month the solar wind seems to reside in the switch-on regime for half an hour or more. This can be seen from the solar wind histogram plots of Fig. 8.18. Estimates of the dynamical response time of the magnetosheath flow indicate that the slow shock could be formed in a time span of half an hour. This has to be confirmed in future time-dependent MHD simulations which take into account the rather erratic behavior of the solar wind.

Based on our investigation of the solar wind parameters, we can thus expect that several times per month well-formed stationary slow shocks exist in the earth's magnetosheath. During short intervals amounting to 8% of the total time the solar wind is temporarily in the switch-on regime and the magnetosheath flow is probably disturbed such that slow shocks start to form, but stationarity of the slow shocks is presumably not attained.

Slow shocks of the type present in our simulation results for magnetically dominated parameter values may thus explain part of the observations done by Song et al. [141]. We can speculate that the existence

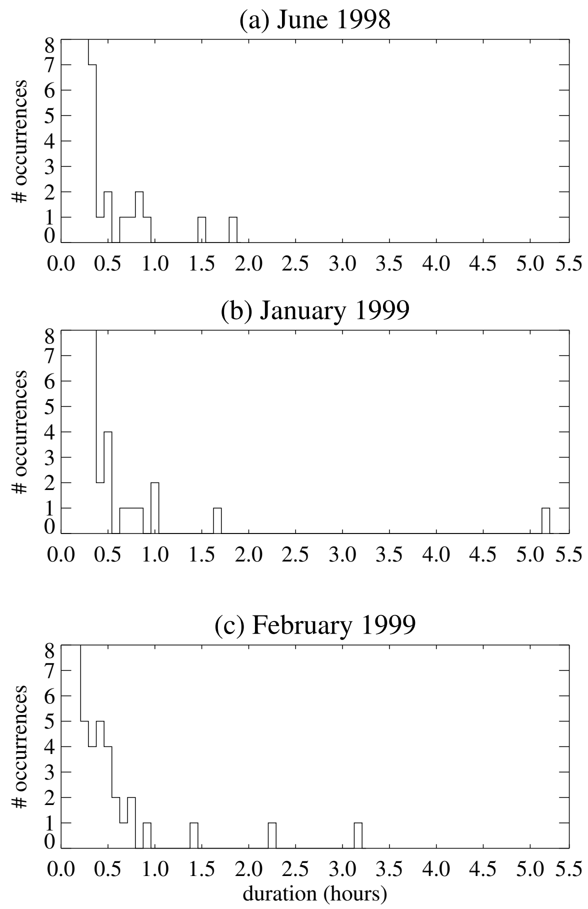

Figure 8.18: *Histograms for three months of ACE solar wind data. Several times per month the solar wind is in the switch-on regime for a period longer than 0.5 hours.*

of secondary shocks for certain parameter values not in the switch-on regime may partially explain why Song et al. observed secondary slow shocks in more than 8% of ISEE-1 and ISEE-2 magnetosheath passes. It is hard to quantify this effect, however, because our discussion in Sec. 8.2.2 indicated that the occurrence of secondary shocks outside the switch-on regime seems not to be systematic.

Third we look at the location in the magnetosheath where the slow shocks are present in our simulation results. Given the observational fact that the solar wind is most often a high Mach number flow (Fig. 8.4), we can see from Fig. 8.8 that secondary slow shocks are more likely to occur for relatively large angles θ_{vB}. Fig. 8.9 shows clearly that the point where the secondary slow shock is attached to the leading fast shock, shifts tailwards when θ_{vB} increases. The secondary shock is then not present in the dayside magnetosheath close to the sun-earth line, where the shocks studied in [141] were encountered. However, in [141] it is mentioned that slow shocks were also found in the flanks of the magnetosheath. Slow shocks have also been reported in the distant magnetotail region [38, 37], and the secondary shocks present in our simulation results may be related to these observed slow shocks. These slow shocks may alternatively be due to magnetic reconnection in the magnetotail (Fig. 2.15).

We may thus conclude that our simulation results for bow shock flows with magnetically dominated upstream parameters offer a physically attractive explanation for the possible observation of stationary slow shocks in the magnetosheath. Some of the slow shock observations by Song et al. [141] may be explained by our simulation results, but certainly not all. Our simulation results make some clear predictions about when and where slow shocks could be observed, and it would be interesting to re-investigate the observational data in this respect. Slow shocks should be observed preferably when $\beta < 2/\gamma$ and θ_{vB} is large in the solar wind, and only on the quasi-parallel side of the magnetosheath and not too far from the symmetry plane containing the inflow magnetic field.

Global reconfiguration of the magnetosheath flow during magnetic cloud events and the mechanism and timing of magnetic storms

The solar wind is often low-β for a substantial time when a magnetic cloud hits the earth's magnetic environment. Indeed, for instance in the magnetic cloud event of January 1997 (Fig. 8.6) [15] the plasma β was approximately equal to 0.1 for about 22 hours, with a Mach number $M \sim 12$ and $\theta_{vB} \sim 70°$. This flow is magnetically dominated (switch-on shocks occur, Eq. 8.2). We have performed a simulation with these parameter values (Fig. 8.19a), and have found a secondary slow shock and the topology of Fig. 7.5b. This indicates that during this event a slow shock may have been formed in the magnetosheath in the direction of the magnetotail on the quasi-parallel side of the magnetosheath. It seems thus that secondary slow shocks in the magnetosheath are likely to be formed during magnetic cloud events because of the low-β nature of magnetic clouds and because of large angles θ_{vB}. Fig. 8.19b–d shows what a satellite which crosses the magnetotail would observe when such a secondary slow shock were to be present. It would be interesting to

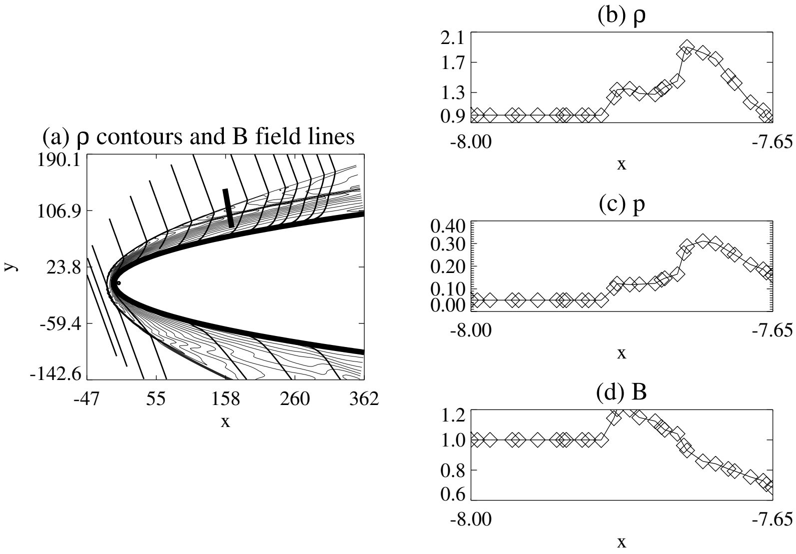

Figure 8.19: *3D bow shock flow around a paraboloid surface with inflow $\beta = 0.1$, $M = 12$, and $\theta_{vB} = 70°$. These are the parameter values in the magnetic cloud of Fig. 8.6, and they lie in the switch-on regime. (a) The leading shock front is clearly followed by a secondary shock front, which is attached to the leading front. (b–d) A satellite passing through the magnetosheath in the tail region on the quasi-parallel side — along the thick line in (a) — would observe a slow shock following a fast shock.*

investigate the observational data and to look for signatures of slow shocks during magnetic cloud events.

In the solar wind thermal and dynamic pressure effects normally dominate over magnetic effects, and the magnetosphere is generally in dynamic equilibrium with this pressure-dominated solar wind. During the magnetic cloud event of Fig. 8.6, however, the solar wind abruptly becomes low-β and the angle θ_{vB} becomes large, such that intrinsically magnetic effects become dominant. When a magnetic cloud arrives, the magnetosphere has to adjust to the now magnetically dominated solar wind on short time scales.

This adjustment involves a temporary global reconfiguration of the magnetosheath flow from a pressure-dominated single-front bow shock flow topology to a magnetically dominated topology with a secondary slow shock. We can speculate that this temporary global reconfiguration may have a profound influence on the mechanism of magnetic storms and on the timing of magnetic storm onset in the following ways.

Fig. 8.9b shows that in the magnetically dominated bow shock topology the field lines at the magnetopause are highly elongated and stretch out around a large part of the dayside magnetopause. In the case of negative B_z magnetosheath field, this may change the location where reconnection occurs, and increased field strength at the magnetopause may increase the rate of reconnection. In Fig. 8.12 one can see that the slow shock front has a limited spatial extent which is centered around the plane of the incoming magnetic field. The magnetic field rotates slowly during a magnetic cloud event, and if a slow shock would be formed, then this slow shock front would presumably rotate in the magnetosheath along with the rotating cloud field, thus influencing the reconnection location.

These effects may influence the storm mechanism and intensity. Solar wind perturbations which introduce a certain amount of negative B_z and which reconfigure the magnetosheath because they are magnetically dominated, may cause more severe storms — it is said that they are more *geo-effective* — than perturbations which introduce the same amount of negative B_z but do not reconfigure the magnetosheath flow because they remain pressure-dominated. If this is true, then the plasma β and the angle θ_{vB} may be important indicators for geo-effectiveness, next to B_z.

It is generally believed that geo-effective magnetic clouds introduce magnetic field with a negative-B_z component into the magnetosheath which, upon arrival at the magnetopause, leads to enhanced reconnection with the earth's positive-B_z magnetic field and thus causes a magnetic storm. It is not well understood how and how fast this negative-B_z field reaches the magnetopause. Our simulation results suggest that magnetic clouds would not simply *propagate through* the magnetosheath, as is often believed [130], but could rather cause a *global reconfiguration* of the magnetosheath flow involving a slow shock. When a magnetic cloud arrives at the bow shock and a slow shock forms, the characteristic time of this global reconfiguration of the magnetosheath may determine when negative B_z reaches the magnetopause, and may thus influence the timing of magnetic storm onset. This may explain the time delay which is observed between the measurement of negative B_z IMF in front of the bow shock and the arrival of negative B_z field at the magnetopause. This time delay cannot be explained as a simple propagation effect.

These scenarios remain speculative for now, but it would certainly be interesting to investigate them more closely in time-dependent numerical simulations, and to look for observational signatures which would confirm them. The important role of reconnection has to be considered explicitly as well. In the near future the CLUSTER mission will provide us with detailed observations of the dayside magnetosheath region, which may confirm the existence of slow shocks in the magnetosheath for magnetically dominated solar wind conditions.

Chapter 9

On the admissibility of intermediate shocks

9.1 Introduction

In this Chapter we discuss the admissibility of intermediate shocks in MHD. In Sec. 3.3 we have reviewed the various types of MHD discontinuities which are allowed by the MHD Rankine-Hugoniot (RH) relations. Not all types of MHD discontinuities allowed by the RH relations can arise in MHD flows, however. A clear example are the so-called *expansion shocks*, which take fluid elements from a high-entropy state to a low-entropy state. Expansion shocks are perfectly allowed by the RH relations and are weak solutions of the ideal MHD equations, but they cannot exist in ideal MHD flows because they cannot be formed through wave steepening and because they would disintegrate immediately upon even the smallest perturbation. Another way to see that expansion shocks cannot exist is that they violate the second law of thermodynamics. Such improper shock solutions of the equations are called *inadmissible* shocks, as opposed to *admissible* shocks which can arise in flow solutions.

The hydrodynamic (HD) equations are strictly hyperbolic — wave speeds do not coincide — and convex (see Sec. 3.3.5). Expansion shocks are the only type of inadmissible discontinuities in HD. Ideal HD and dissipative HD behave completely similarly regarding admissibility of shocks.

In contrast, the MHD equations are non-strictly hyperbolic and non-convex, and have a peculiar type of rotational invariance. Because of these properties, next to expansion shocks also other types of discontinuities can be inadmissible in MHD. The matter is complicated by the fact that for MHD admissibility of shocks is *different* for the ideal system and the dissipative system. It is said that dissipative MHD does not uniformly approach ideal MHD in the limit of vanishing dissipation.

In ideal MHD several types of intermediate shocks are inadmissible. For this reason intermediate shocks have been considered *extraneous* or *unphysical* since the early sixties [2, 71, 87]. However, recently it has been shown that intermediate shocks are admissible in dissipative MHD [170, 43, 110], and can thus not be termed 'unphysical'.

The MHD system is extremely complex and allows for many types of degeneracies and singularities which can coincide and interact. For these reasons the problem of the admissibility of MHD shocks has probably not been solved yet in full. Much can be learned about the possible pathologies by considering *model problems* of reduced complexity which each retain certain aspects of the singular behavior of the MHD system. In Sec. 9.2 we describe the admissibility of discontinuities in such model systems. Due to space constraints we limit ourselves to sketching the general ideas while omitting technical details which can be found in the literature.

The admissibility of shocks is very different in the planar and the full MHD systems. Planar MHD ($v_z \equiv B_z \equiv 0$) does not allow for Alfvén waves, whereas full MHD does. In Sec. 9.3 we discuss the admissibility of shocks in the planar MHD system. We show how the planar 2D magnetically dominated bow shock flows around cylinders that were discussed in Chap. 6 form excellent illustrations in 2D of the theory on the admissibility of shocks in planar MHD. We compare the performance of various numerical schemes for the calculation of these flows and relate the results to the occurrence of physical and numerical instabilities. In Sec. 9.4 the admissibility of shocks in the full MHD system is discussed. The 3D magnetically dominated bow shock flows around spheres that were discussed in Chap. 7 are shown to be excellent illustrations in 3D of the theory on the admissibility of shocks in full MHD. Intermediate shocks have been found previously in 1D and in some 2D simulation results [12, 147], but the bow shock flows described in Chaps. 6 and 7 are the first clear illustrations in 2D and 3D of the whole variety of intermediate shock phenomena that can arise in MHD flows.

We limit our exposition of the theory of MHD shock admissibility in Secs. 9.3 and 9.4 to sketching general results which are illustrated by analogies with the model systems discussed in Sec. 9.2. A complete and rigorous derivation of the theoretical results is far beyond the scope of this dissertation, not only due to space constraints but also because many aspects of the problem have not been solved yet in full. For instance, theoretical results have only been derived for systems which are limited to variation in one spatial dimension. Some of the reasonings presented in this Chapter have obvious loose ends, and many open problems remain for which we can only provide speculative answers. We have found the recent literature on this subject very confusing and contradictory [173, 46, 110, 35]. As is often true in such cases, the confusion and contradiction mainly seem to stem from vagueness in concepts, terminology and problem definition. We think that a reasonably consistent picture of the admissibility of shocks in MHD can be distilled from the recent literature. We have found references [103, 102, 48, 46] the most useful. References [170, 173, 110, 35] are also of interest. In this Chapter it is our aim to sketch a consistent theory of the admissibility of MHD shocks, and to verify whether the simulation results with shock fronts of various types that were described in Chaps. 6 and 7 confirm this theory.

9.2 Admissibility of shocks in model systems

9.2.1 Scalar model

Consider the Burgers equation (see also Secs. 3.2.1 and 3.3.5) which describes the evolution of scalar $u(x,t)$ as

$$\frac{\partial u}{\partial t} + \frac{\partial u^2/2}{\partial x} = \eta \frac{\partial^2 u}{\partial x^2}, \tag{9.1}$$

with flux $f(u) = u^2/2$ and the dissipative coefficient η a positive constant. We choose $s = 0$ and $f_{const} = 1/2$ in the Rankine-Hugoniot relation (see Sec. 3.3.1)

$$-su + f(u) = f_{const}. \tag{9.2}$$

Eq. 9.2 then allows for two solutions, $u_1 = 1$ and $u_2 = -1$. Let us consider the case that $\eta \equiv 0$ in Eq. 9.1. In this case Eq. 9.1 allows for discontinuous weak solutions with vanishing shock thickness. The two states satisfying the RH relations can be connected with a shock in two ways, with u_1 either on the left or on the right side of the shock, and with u_2 on the other side.

Fig. 9.1 sketches the behavior of the characteristic curves (see Sec. 3.2.1) with slope $f'(u) = u$ in the xt plane for the two possible configurations. These configurations both are solutions of the integral form of Eq. 9.1 with $\eta \equiv 0$. In Sec. 3.3 we have postulated that only shocks in which the characteristics converge are admissible. Following this criterion, the configuration of Fig. 9.1a is inadmissible, while the configuration of Fig. 9.1b is admissible. We now review several possible shock admissibility criteria and the reasoning which leads to them. We start out with admissibility criteria for discontinuous solutions of the ideal dissipation-free equation ($\eta \equiv 0$ in Eq. 9.1), followed by admissibility criteria for shocks described by the dissipative equation.

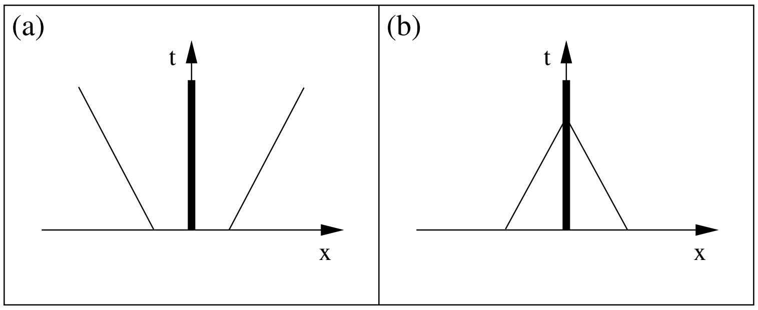

Figure 9.1: *Two possible ways in which a pair of states satisfying the RH relations for the ideal Burgers equation can be connected by a shock (thick). (a) (u_l,u_r)=(-1,1). The characteristics (thin) diverge from the shock on the two sides. This configuration is inadmissible. (b) (u_l,u_r)=(1,-1). The characteristics converge into the shock on the two sides. This configuration is admissible.*

Admissibility of shocks described by the ideal equation

The following are four important criteria used in the literature (e.g. [109]).

- **I1: Steepening criterion**
  The shock of Fig. 9.1b is admissible because it can be formed through wave steepening due to the nonlinearity of the equation (Fig. 3.2), whereas the shock of Fig. 9.1a is inadmissible because it cannot be formed through wave steepening. Indeed, if we replace the discontinuities in Fig. 9.1 by steep linear profiles connecting the left and the right states, then the profile of Fig. 9.1b steepens into a shock because the characteristics are bound to intersect. In contrast, the profile of Fig. 9.1a decays into a rarefaction wave which broadens in time because characteristics diverge.

- **I2: Perturbation criterion**
  Let us perturb the configuration $u(x,t)$ of Fig. 9.1b with a profile $m(x,0)$ which has limited spatial extent such that the weight of the perturbation
  $$M = \int m(x,0)\,dx, \tag{9.3}$$
  is bounded (Fig. 9.2a). The time evolution of the solution of the perturbed problem $u'(x,t) = u(x,t) + m(x,t)$ is governed by the constraint that $\int m(x,t)\,dx$ remains constant in time, as follows from the conservation law Eq. 9.1. Due to the convergence of the

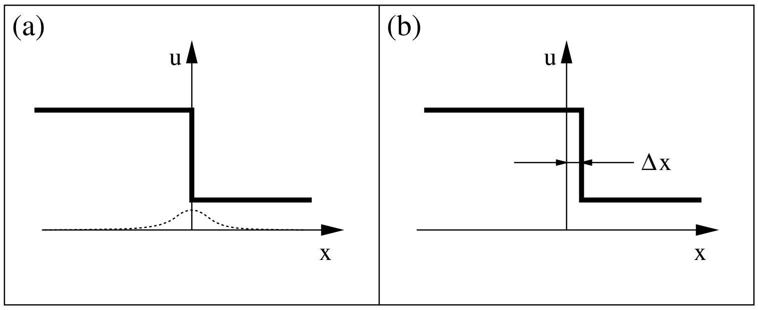

Figure 9.2: *Perturbation of the configuration of Fig. 9.1b with a profile $m(x, 0)$ which has limited spatial extent. The solution of the perturbed problem (a) evolves in finite time to the solution represented in (b) with a shock connecting the original left and right state and with the same shock speed (stationary in this case) as the original shock. The shock is translated over a distance Δx.*

characteristics the perturbed system evolves in finite time to the solution of Fig. 9.2b with a shock connecting the original left and right state and with the same shock speed (stationary in this case) as the original shock. The only difference between the unperturbed configuration and the final state of the perturbed problem is that the shock is translated over a distance Δx, with $\Delta x = M/\Delta u$, and $\Delta u = u_l - u_r$. The distance of translation Δx decreases with decreasing perturbation weight M. The evolution of the perturbed system is subject to one constraint, and by adjusting the free parameter of the shock location a solution can be found for which this constraint is satisfied. The shock in the configuration of Fig. 9.1b is stable against perturbations, and is thus admissible. The shock in the configuration of Fig. 9.1a, however, breaks up into a rarefaction wave upon even the smallest perturbation, since characteristics diverge. We say that it is unstable against *generic* perturbations, and thus inadmissible.

- **I3: Lax criterion**
  Motivated by the theory of free boundary value problems [88], the following admissibility criterion has been proposed. The scalar version of the RH relation reads $(f(u_r) - f(u_l))/(u_r - u_l) = s$. This constitutes one equation in three variables. If the values of u_r and u_l are specified externally, then this relation can be satisfied at a discontinuity and determines the shock speed s. Two incoming characteristics specify the values of u_r and u_l, and it is concluded that in this case the shock is admissible. When the characteris-

tics leave the shock, the RH relation is underdetermined and it is concluded that the shock is inadmissible. This criterion is due to Lax [88]. It constitutes a condition on the geometry of shocks and characteristic curves in the xt plane, and is therefore also called the *geometrical* admissibility criterion. Shocks admissible under the Lax criterion are called *Lax shocks*.

- **I4: Linearized stability or evolutionarity criterion**
  The linearized stability or evolutionarity criterion is closely related to the Lax criterion. It is argued that the perturbation problem of the linearized RH relation should have a unique solution for shocks to be admissible [2, 71, 87, 44]. In this case it is said that shocks are *evolutionary* or *linearized stable*. For the scalar case it is found that shocks with impinging characteristics are evolutionary, while shocks with diverging characteristics are non-evolutionary.

In this case of a scalar equation the criteria I1–I4 all give the same result for the admissibility of shocks. These criteria are extended to systems of conservation laws in Sec. 9.2.2. As is shown below, these admissibility criteria for ideal shocks can be related to criteria for dissipative shocks. In the case of physical systems like the HD equations, this allows for instance to relate the ideal criteria I1–I4 to the concept of increasing entropy.

It is interesting to discuss the implications of the obtained results on shock admissibility for the solution of Riemann problems. For the case of the Burgers equation, shocks admissible under criteria I1–I4 allow for a unique solution of all Riemann problems. Riemann problems are well-posed in the usual sense, namely that a unique solution exists and that small changes in the initial conditions (left and right states) only imply small changes in the solution. If this is true, it is said that a continuous solution operator exists for the Riemann problem [46]. For the Burgers equation a continuous solution operator exists which contains the admissible shocks and rarefaction waves [88].

Admissibility of shocks described by the dissipative equation

A co-stationary traveling wave solution of Eq. 9.1 with non-vanishing dissipation satisfies

$$-su + f(u) - f_{const} = \eta \frac{\partial u}{\partial x}. \tag{9.4}$$

We now investigate under which conditions traveling wave solutions with uniform left and right states u_l and u_r connected by a narrow smooth profile are possible. These solutions can be formed through nonlinear steepening and are the analogs of the shocks described by the ideal equation. The width of the dissipative shock layer is determined by the balance between nonlinear steepening and dissipation. In the uniform regions where $u = u_l$ or $u = u_r$ the dissipative term vanishes, such that the left and the right state still have to satisfy the RH relation Eq. 9.2.

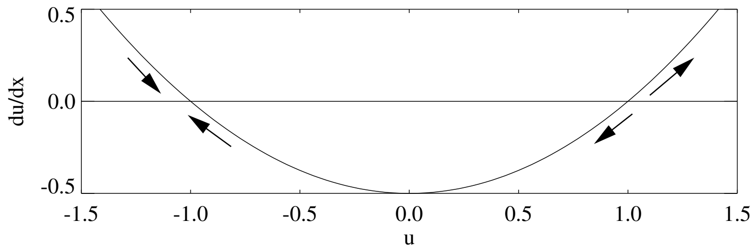

Figure 9.3: *Autonomous system describing viscous profiles of the Burgers equation. The system has fixed points where $\partial u/\partial x = 0$. $u = 1$ is an unstable fixed point, but $u = -1$ is stable. A viscous profile exists from $u_l = 1$ to $u_r = -1$.*

We choose shock speed $s = 0$, flux constant $f_{const} = 1/2$ and dissipation coefficient $\eta = 1$ in Eq. 9.4. The shock structure equation 9.4 now mathematically describes an *autonomous system* of first order, which relates variable u and its derivative $\partial u/\partial x$. This autonomous system can be analyzed using the theory of dynamical systems [113]. This autonomous system has *fixed points* when $\partial u/\partial x = 0$. For the flux function and parameters s and f_{const} under consideration, these fixed points — which satisfy the RH relations — are $u = 1$ and $u = -1$. Fig. 9.3 plots the relation between u and $\partial u/\partial x$. The fixed points are located where this curve crosses the $\partial u/\partial x = 0$ axis, and we want to determine now if a trajectory or a *viscous profile* exists on the plotted curve which can connect the two fixed points. Strictly speaking we should rather call the profile a *dissipative profile*, but the terminology of the Navier-Stokes case for which viscosity acts as dissipation is often used in a generalized manner.

Suppose $u_l = 1$ and $u_r = -1$. Can these two states in this ordering be connected by a viscous profile? If we start from $u_l = 1$ and want to decrease u_l towards $u_r = -1$ in moving to the right (increasing x), we see from the curve in Fig. 9.3 that $\partial u/\partial x$ becomes negative, such that u can indeed decrease further while moving further to the right (increasing x). When we approach $u_r = -1$, $\partial u/\partial x$ increases towards zero. We can reach $u_r = -1$, but once we reach this right state, $\partial u/\partial x = 0$, and

u does not change anymore. This is exactly what we want: $u_l = 1$ can be connected to $u_r = -1$ by a viscous profile. For given left and right states this viscous profile is unique, and an explicit solution can be found [90]. If we would take $u_l = -1$ and $u_r = 1$, then we see that no viscous profile exists, because state $u = -1$ cannot be increased in going to the right. Fixed point $u = 1$ is an *unstable node*, because the slope of the curve is positive, and fixed point $u = -1$ is a *stable node*, with negative slope. In going from left to right (increasing x), we can connect an unstable node with a stable node via a viscous profile. For the dissipative equation, admissible shocks are shocks which have a viscous profile. The configuration of Fig. 9.1a, with diverging characteristics, is not admissible, while the configuration of Fig. 9.1b, with converging characteristics, is admissible.

As in Fig. 9.2 localized perturbation of the viscous shock by a perturbation $m(x,t)$ with finite weight M results in a translation of the shock over a distance Δx which is determined by the constraint that $\int m(x,t)\,dx$ remains constant in time. The translated shock has the same left and right states, shock speed and shock profile as the original shock. The existence of the viscous profile and the behavior under perturbations does not depend on the magnitude of the dissipation η, so we say that the shock profile is *uniformly stable* in the dissipative parameter.

An additional requirement for the admissibility of the shock is that the autonomous system has to be *structurally stable*, which means that small variations in shock speed s, flux constant f_{const} and dissipative coefficient η (which imply small variations in the fixed points) may not change the existence and stability properties of viscous profiles. It is intuitively clear that in the above described case the autonomous system is structurally stable, and this can be proven rigorously as well [48].

Ideal solutions as uniform vanishing viscosity limits of dissipative solutions

An important observation is that precisely the shocks which are admissible in the ideal analysis (Lax shocks) turn out to have viscous profiles! The (ideal) Lax criterion and the (dissipative) viscosity admissibility criterion give the same result for the admissibility of shocks in the respective ideal and dissipative context. This suggests that solutions of the ideal equation 9.1 with $\eta \equiv 0$ may be the *vanishing viscosity limits* of solutions of the dissipative equation 9.1. The admissibility properties of dissipative shocks are indeed uniform in the dissipative parameter, which is required if one wants to take the limit of *vanishing viscosity* in a meaningful way. It can be proven rigorously [48, 90] that in the limit of vanishing viscosity the solutions of the dissipative equation 9.1

uniformly approach the solutions of the ideal equation ($\eta \equiv 0$). It would seem that this behavior should always arise, but in the following Sections we show that this is not the case.

The fact that the ideal and dissipative physical systems uniformly approach each other warrants the use of the *dissipative* viscosity admissibility criterion to determine or motivate the admissibility of shocks in the *ideal* system, and vice versa. This means that the ideal criteria I1–I4 can be justified *a posteriori* by the results of the viscosity admissibility study.

9.2.2 Convex strictly hyperbolic system

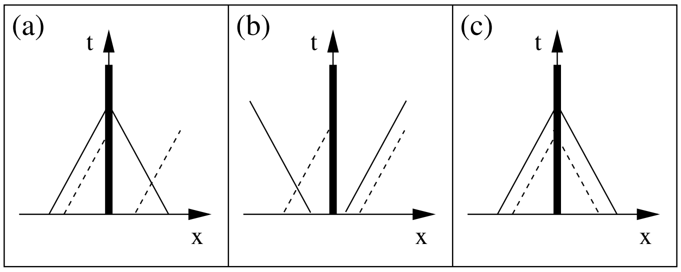

Figure 9.4: *Shock configurations for a* 2×2 *system. (a) Lax shock with* $n+1$ *converging characteristics. (b) Undercompressive shock with less than* $n+1$ *converging characteristics. (c) Overcompressive shock with more than* $n+1$ *converging characteristics.*

Most of the results on shock admissibility described above for the Burgers equation carry over to the case of a convex strictly hyperbolic system of conservation laws. In this Section we do therefore not repeat all considerations, but we limit the discussion to some aspects which are slightly different from the scalar case.

Consider the 2×2 *system* of strictly hyperbolic conservation laws

$$\frac{\partial}{\partial t}\begin{bmatrix} u \\ v \end{bmatrix} + \frac{\partial}{\partial x}\begin{bmatrix} f(u,v) \\ g(u,v) \end{bmatrix} = 0, \tag{9.5}$$

with the flux functions f and g chosen such that wave speeds cannot coincide. In the xt plane 2 families of characteristic curves exist. Fig. 9.4 shows some possible shock configurations that can arise for a 2×2 system. For the configuration in Fig. 9.4a exactly one family of characteristics converges into the shock, while the other family has one diverging and one converging characteristic. This type of shock is called a Lax shock. For a general strictly hyperbolic $n \times n$ system a Lax shock has $n +$

1 converging characteristics. It is explained below that for a strictly hyperbolic system all admissible shocks have to be of this type. The shock in Fig. 9.4b has less than $n+1$ converging characteristics, and is called *undercompressive*. The shock in Fig. 9.4c is called *overcompressive* since it has more than $n+1$ converging characteristics.

Admissibility of shocks described by the ideal system

Some of the ideal admissibility criteria I1–I4 that were described above have to be altered slightly to make them applicable to systems of conservation laws.

- **I2: Perturbation criterion**

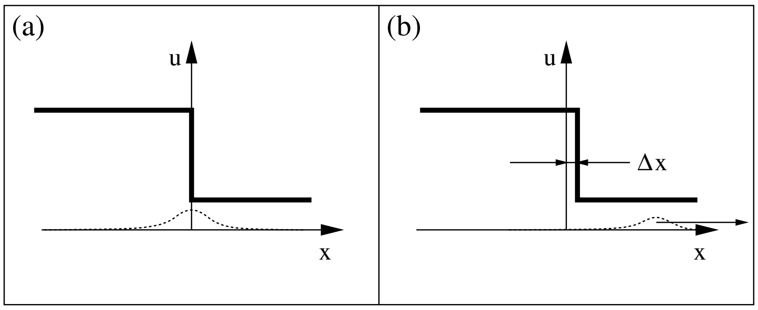

Figure 9.5: *Perturbation of the configuration of Fig. 9.4a with a profile which has limited spatial extent (only the u component is sketched). The solution of the perturbed problem (a) evolves in finite time to the solution represented in (b) with a shock which connects the original left and right state and which has the same shock speed (stationary in this case) as the original shock, and with a wave perturbation which travels away from the shock. The shock is translated over a distance Δx.*

Let us perturb the u and v components of the configuration of Fig. 9.4a with perturbation profiles $m_u(x,0)$ and $m_v(x,0)$ which have bounded weight (Fig. 9.5a). The time evolution of the solution of the perturbed problem is now governed by the two constraints that $\int m_u(x,t)\,dx$ and $\int m_v(x,t)\,dx$ remain constant in time, as follows from the conservation laws. The perturbed system evolves in finite time to the solution of Fig. 9.5b with a shock which connects the original left and right state and which has the same shock speed (stationary in this case) as the original shock, and with a wave perturbation traveling away from the shock. The wave can travel outwards because one of the characteristics diverges away from the shock (Fig. 9.4a). The shock is translated over a distance Δx which is determined by the weights of the perturbation. The distance of translation Δx decreases with decreasing perturbation weight. The evolution of the perturbed system is subject to two constraints, which can be satisfied by adjusting the shock location (one free parameter) and by sending out a wave. The shock in the configuration of Fig. 9.4a is stable against perturbations, and is thus admissible. The shock in the configuration of Fig. 9.4b, however, breaks up into a rarefaction wave upon even the smallest perturbation. It is unstable against *generic* perturbations, and thus inadmissible.

- **I3: Lax criterion**
  For a general $n \times n$ system, the RH relations constitute n relations between $2n+1$ variables. $n+1$ variables have thus to be specified externally, which means that $n+1$ characteristics have to impinge on a shock in order to make the shock admissible. Shocks with $n+1$ impinging characteristics are called Lax shocks. Lax shocks are admissible, and overcompressive and undercompressive shocks are inadmissible.

- **I4: Linearized stability or evolutionarity criterion**
  For a general $n \times n$ system, the perturbation problem of the linearized RH relations has a unique solution when $n+1$ characteristics impinge on the shock. It is concluded that only shocks with $n+1$ impinging characteristics are admissible. Those shocks are called evolutionary.

Admissibility of shocks described by the dissipative system

For given left and right states, dissipative shocks are admissible when traveling wave solutions exist which connect the two states. The shock structure equations — the systems version of Eq. 9.4 — now mathematically describe a higher order autonomous system, which relates state variables and their spatial derivatives. This autonomous system can be analyzed using the theory of dynamical systems [113]. The fixed points of the autonomous system satisfy the RH relations. For a convex strictly hyperbolic system, two fixed points generally exist for given shock speed and flux constants in Eq. 3.73. One fixed point is an unstable node, and the other one is of saddle type. There thus exists a unique viscous profile connecting the two fixed points. This profile is structurally stable. Configurations like in Fig. 9.4b do not have a viscous profile and are not admissible, while configurations like in Fig. 9.4a do have a viscous profile and are admissible.

As in Fig. 9.5 localized perturbation of the viscous shock results in a translation of the shock over a distance Δx and in the emission of a wave. The translated shock has the same left and right states, shock speed and shock profile as the original shock. The existence of the viscous profile and the behavior under perturbations does not depend on the magnitude of the dissipative coefficients, so we say that the shock profile is *uniformly stable* in the dissipative parameters.

9.2.3 Non-strictly hyperbolic system

Consider the non-strictly hyperbolic system

$$\frac{\partial}{\partial t}\begin{bmatrix} u \\ v \end{bmatrix} + \frac{\partial}{\partial x}\begin{bmatrix} a\,u^2/2 + b\,v \\ v^2/2 \end{bmatrix} = 0, \tag{9.6}$$

with a and b positive constants. We follow the analysis of this model problem which was presented in [103]. The characteristic speeds are $\lambda_1 = a\,u$ and $\lambda_2 = v$. They coincide when $au = v$. The system is thus non-strictly hyperbolic.

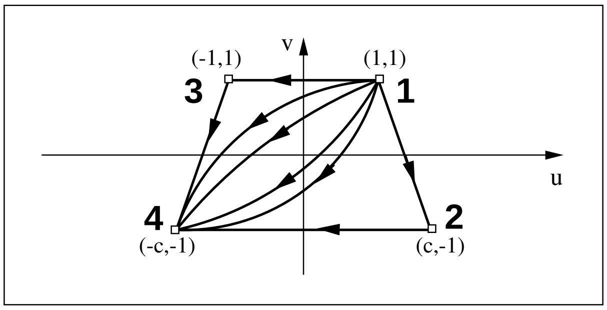

Figure 9.6: *Points in phase space uv that can be connected to the state $(1,1)$ by a discontinuity with speed zero. The constant $c = \sqrt{1 + 4b/a}$. The thick curves with arrows represent viscous profiles.*

In Fig. 9.6 we show which points in phase space uv can be connected to the state $(1,1)$ by a discontinuity with speed zero. The state $(1,1)$ and the shock speed determine the flux constants in Eq. 3.73, and this equation then has the four solutions indicated in Fig. 9.6. We now investigate the admissibility of ideal and dissipative shocks.

Admissibility of shocks described by the ideal system

A simple calculation of the characteristic speeds in states 1, 2, 3 and 4 of Fig. 9.6 shows that according to the Lax and evolutionarity criteria

(I3 and I4), shocks 1–2, 1–3, 2–4 and 3–4 are admissible because they have $n + 1 = 3$ converging characteristics. Shock 1–4, however, has 4 incoming characteristics, and is thus overcompressive and inadmissible! Shocks 2–3 and 3–2 are undercompressive.

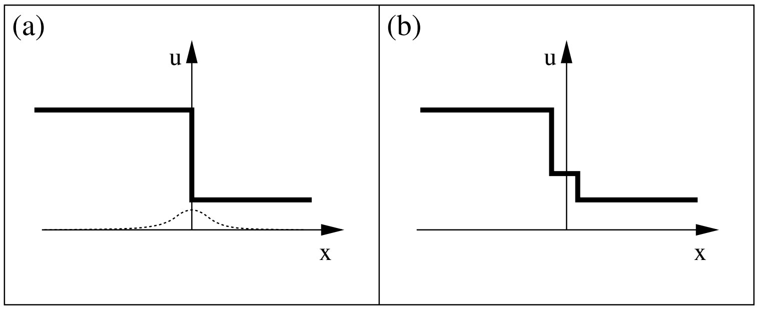

Figure 9.7: *A localized perturbation of an ideal 1–4 overcompressive shock makes the shock split into two shocks of 1–3 and 3–4 (or 1–2 and 2–4) types with the same speed.*

1–4 shocks are indeed unstable against generic perturbations (criterion I2). Fig. 9.7 sketches how a localized perturbation of a 1–4 overcompressive shock makes the shock split into two shocks of 1–3 and 3–4 (or 1–2 and 2–4) types. The time evolution of the solution of the perturbed problem is again governed by the two conservation constraints that $\int m_u(x,t)\,dx$ and $\int m_v(x,t)\,dx$ remain constant in time. In the case of an overcompressive shock, a wave cannot be sent out from the shock because all the characteristics converge into the shock! The two constraints can also not be satisfied by adjusting the free parameter which describes the shock location, because this is only one free parameter. It follows from detailed analysis of the time evolution [103] or from numerical simulation that the shock necessarily has to break up. The two shocks still connect the original left state with the original right state, and have the same speed as the original overcompressive 1–4 shock. The distance of separation between the two shocks decreases with decreasing perturbation weight.

Like the non-evolutionary undercompressive shock of Fig. 9.1a, 1–4 shocks are inadmissible according to the evolutionarity criterion, but the behavior of these two types of shocks upon perturbation is quite different. The shock of Fig. 9.1a degenerates completely upon the smallest perturbation and the resulting flow is not in any way close to the unperturbed flow for large times. The 1–4 shock also ceases to exist upon a generic perturbation, but the flow after perturbation remains close to the unperturbed flow for all times. In some flow problems 1–2 and 2–4 (and also 1–3 and 3–4) shocks coincide and may then be considered as a single 1–4 shock. In this sense 1–4 shocks are admissible in ideal flows described by system 9.6.

Admissibility of shocks described by the dissipative system

State 1 in Fig. 9.6 is an unstable node, 4 is a stable node, and 2 and 3 are saddles. Shocks 1–2, 1–3, 2–4 and 3–4 have unique viscous profiles and are thus admissible. Shock 1–4 has a one-parameter family of viscous profiles, and is thus admissible too.

Localized perturbation of a viscous 1–4 shock does *not* result in break-up of the shock in two separate shocks! Again, translation of the shock can only account for one constraint, and the other constraint cannot be satisfied by sending out a wave because the shock is overcompressive. However, the one-parameter family of viscous profiles provides another free parameter. Upon perturbation, the shock is translated and the viscous profile jumps to a different member of the one-parameter family, such that the two constraints are met. 1–4 shocks are thus admissible solutions of the dissipative system. The existence of the viscous profile and the behavior under perturbations do not depend on the magnitude of the dissipative coefficients, so we say that the shock profile is *uniformly stable* in the dissipative parameters. There seems to be a contradiction between the fact that 1–4 shocks are non-evolutionary in the ideal system, but have viscous profiles in the dissipative system. This contradiction is partially resolved by noting that 1–4 shocks can arise in ideal flows as the limit of coinciding 1–2 and 2–4 (or 1–3 and 3–4) shocks.

9.2.4 Rotationally invariant non-strictly hyperbolic system

Consider the non-strictly hyperbolic system

$$\frac{\partial}{\partial t}\begin{bmatrix} u \\ v \end{bmatrix} + \frac{\partial}{\partial x}\begin{bmatrix} u\,(u^2+v^2) \\ v\,(u^2+v^2) \end{bmatrix} = 0. \tag{9.7}$$

We follow the analysis of this model problem which was presented in [102] and [48]. The characteristic speeds are $\lambda_1 = u^2+v^2$ and $\lambda_2 = 3\,(u^2+v^2)$, which describe waves in the angular and radial directions in phase space respectively (see Fig. 9.10). The characteristic speeds coincide when $u = v = 0$. The system is thus non-strictly hyperbolic. We can consider the restricted system obtained by setting $v \equiv 0$. This restricted system has the non-convex flux function $f(u) = u^3$ which is of the type discussed in Sec. 3.3.5. The flux function $\mathbf{F}$ of system 9.7 satisfies a peculiar kind of *rotational invariance* [48], namely that

$$\mathbf{F}(\mathbf{U}) = \phi(||\mathbf{U}||^2)\,\mathbf{U}, \tag{9.8}$$

with ϕ the identity function in this case.

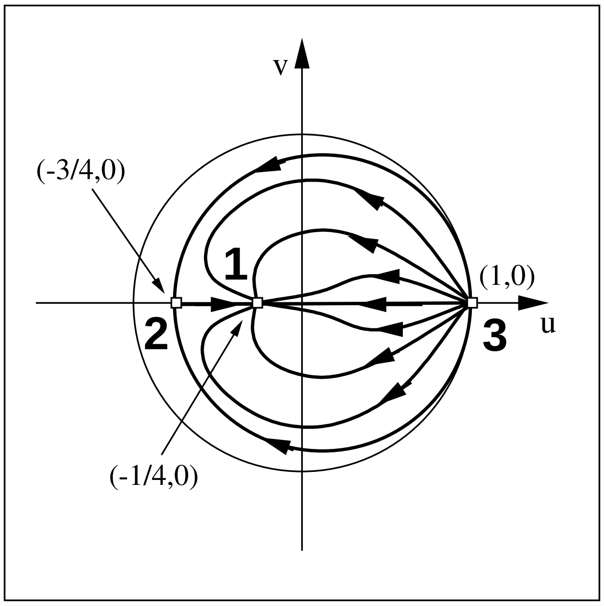

Figure 9.8: *Points in phase space uv that can be connected to the state* $(1,0)$ *by a discontinuity with speed 13/16. The thick curves with arrows represent viscous profiles.*

In Fig. 9.8 we show which points in phase space uv can be connected to the state $(1,0)$ by a discontinuity with speed $13/16$. The state $(1,0)$ and the shock speed determine the flux constants in Eq. 3.73, and this equation then has the three solutions indicated in Fig. 9.8. We now investigate the admissibility of ideal and dissipative shocks.

Admissibility of shocks described by the ideal system

A simple calculation of the characteristic speeds in states 1, 2 and 3 of Fig. 9.8 shows that shock 3–1 is overcompressive (and 1–3 thus undercompressive), 3–2 is a Lax shock and 2–1 is Lax too. According to the Lax and evolutionarity criteria (I3 and I4), shocks 3–2 and 2–1 are admissible because they have $n+1=3$ converging characteristics. Shock 3–1 has 4 incoming characteristics and is thus inadmissible!

3–1 shocks are indeed unstable against generic perturbations (criterion I2). Fig. 9.9 sketches how a localized perturbation of a 3–1 overcompressive shock makes the shock split into two shocks. This can be understood by a reasoning on conservative constraints and converging

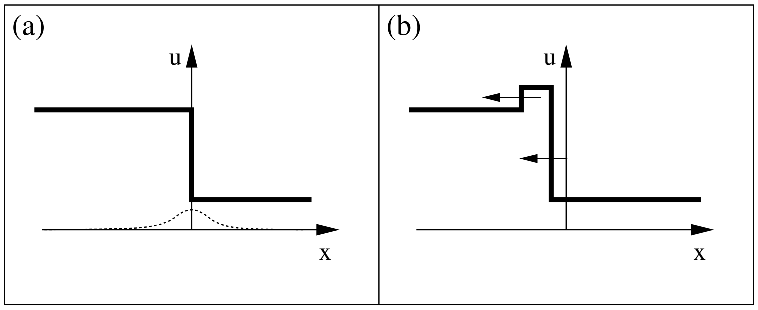

Figure 9.9: *A localized perturbation of an ideal 3–1 overcompressive shock makes the shock split into two shocks which propagate away from the location of the original shock.*

characteristics similar to the reasoning presented in Sec. 9.2.3. A crucial difference with the case of Sec. 9.2.3, however, is that the two shocks do *not* propagate with the same speed as the original unperturbed shock. This behavior, like most other peculiar properties of system 9.7 described in this Section, is generic for non-strictly hyperbolic systems with a rotationally invariant flux function [48]. The distance of separation between the two shocks thus increases in time without bounds for even the smallest perturbation.

The 3–1 shock described by system 9.7 thus behaves similarly to the non-evolutionary undercompressive shock of Fig. 9.1a, in the sense that the resulting flow is not in any way close to the unperturbed flow for large times. 3–1 shocks are thus inadmissible in ideal flows, not only according to the evolutionarity criterion, but also according to the perturbation criterion. 3–1 shocks cannot exist in ideal flows. This behavior is very different from the behavior of the 1–4 shocks in the system of Sec. 9.2.3.

Remark that in the restricted system 9.7 with $v \equiv 0$ ideal shock admissibility is entirely different. The rotational mode λ_1 disappears. 3–1 shocks become admissible Lax shocks. 2–1 shocks remain Lax shocks, but 3–2 and 2–3 shocks are both undercompressive (Fig. 3.17). The presence of the rotational wave mode in the full system thus completely destabilizes ideal 3–1 shocks, and stabilizes 3–2 shocks.

Admissibility of shocks described by the dissipative system

In Fig. 9.8 state 1 is a stable node, 3 is an unstable node, and 2 is a saddle. Shocks 3–2 and 2–1 have unique viscous profiles and are thus admissible. Shock 3–1 has a one-parameter family of viscous profiles, and is thus admissible too.

Localized perturbation of a viscous 3–1 shock does *not* result in break-up of the shock in two separate shocks when the perturbation weight is small. Upon perturbation, the shock is translated and the viscous profile jumps to a different member of the one-parameter family, such that the two conservation constraints are met. 3–1 shocks are thus admissible solutions of the system 9.7 with dissipation. This conclusion seems to be analogous to the conclusion for the 1–4 shocks described by system 9.6 as discussed in Sec. 9.2.3.

However, there are two crucial differences.

First, when the weight M_v of the perturbation of v increases, the viscous profile of the 3–1 shock approaches the 3–2–1 orbit (Fig. 9.8). When M_v is further increased, the 3–1 shock splits up into a 3–2 and a 2–1 shock. Those shocks propagate away with speeds which are different from the speed of the original unperturbed shock (Because of the larger M_v state 2 shifts to the left in Fig. 9.8!). The resulting flow is not in any way close to the unperturbed flow for large times, similar to the ideal case discussed above.

Second, the critical perturbation mass M_v required for break-up of the shock decreases with decreasing dissipation, and vanishes for vanishing dissipation. This means that 3–1 shocks become less stable when the dissipation is decreased. For the 3–1 shock the behavior under perturbations does thus depend on the magnitude of the dissipative coefficients, so we conclude that the shock profile is *not* uniformly stable in the dissipative parameters!

3–1 shocks are admissible in the dissipative system, and inadmissible in the ideal system. This contradiction is resolved by the fact that the dissipative 3–1 shocks become generically unstable for vanishing dissipation. The dissipative system thus approaches the ideal system for vanishing dissipation, but not in a uniform way, since 3–1 shocks are admissible in the dissipative system and not in the ideal system.

Solution of Riemann problems

It is interesting to investigate the implications of the above described results on shock admissibility for the solution of Riemann problems. In Fig. 9.10 a Riemann problem with $\mathbf{U}_l = (1,0)$ and $\mathbf{U}_r = (-1,0)$ is sketched in phase space. Two different solutions are proposed.

The restriction of the system to the u-axis suggests the solution which contains a sonic shock connecting $\mathbf{U}_l$ with $\mathbf{U}^* = (-1/2,0)$, followed by a rarefaction wave which connects $\mathbf{U}^*$ with $\mathbf{U}_r$. This is the compound shock type solution which has been discussed in Sec. 3.3.5 for a non-convex scalar system. Another solution is a single rotational wave (associated with the angular mode λ_1) which brings $\mathbf{U}_l$ directly to $\mathbf{U}_r$.

Which solution is valid? The reader may anticipate from the above

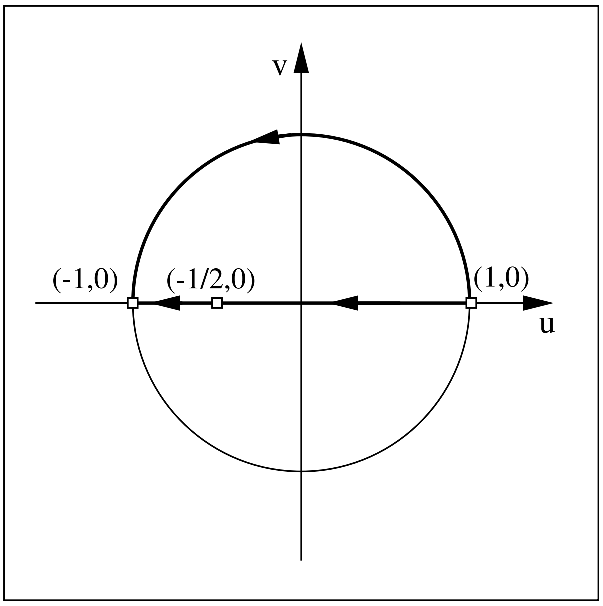

Figure 9.10: *Riemann problem with* $\mathbf{U}_l = (1,0)$ *and* $\mathbf{U}_r = (-1,0)$*. Two different solutions are proposed (thick lines with arrows).*

discussion that the answer depends on whether one considers the ideal or the dissipative system.

In the ideal system, the compound shock solution cannot arise because the sonic shock is a 3–1 shock which is inadmissible in the ideal system. The 3–2 rotational shock is admissible, so the solution to the Riemann problem is the rotational shock. The Riemann problem is thus well-posed, because the solution is unique and depends continuously on the initial data. Indeed, consider a Riemann problem with left state $\mathbf{U}_l = (1,0)$ and right state $\mathbf{U}_r = (-\cos\delta, \sin\delta)$. The solution with a rotational wave over angle $\pi - \delta$ for non-vanishing δ goes over smoothly in the solution with angle π for vanishing δ.

It is remarkable that the solution of the Riemann problem for the ideal system restricted to the u-axis — with the compound shock — is very different from the Riemann problem solution for the full system. How can a Riemann problem which is in a way 'the same' in the two cases have so different solutions? The answer lies in the influence of the rotational mode, which is present in the full system but not in the restricted system. On one hand the rotational mode destabilizes ideal 3–1 shocks such that compound shocks cannot arise in Riemann problem solutions of the full system. On the other hand the rotational mode introduces a new wave mode which can play the role of the 3–1 shock — which consists in changing the sign of u — in solutions of Riemann problems for the full system.

In the dissipative system, the compound shock solution can arise because the 3–1 shock is admissible. The 3–2 rotational shock is admissible too, but due to the symmetry of the initial condition — $v \equiv 0$ in the initial condition of the Riemann problem, and thus has to remain zero in the Riemann problem solution, also in the profile of the viscous shock —, the compound shock solution is obtained. This symmetry constraint did not play in the ideal problem because the 3–2 rotational shock has no profile in the ideal case!

The fact that Riemann problems can have a completely different solution in the ideal and dissipative system has been illustrated beautifully by Freistuehler and Pitman [48]. They perform numerical simulations of the ideal problem using a dissipation-free numerical technique based on the *Glimm scheme*, and do indeed find the solution with the rotational wave for the Riemann problem of Fig. 9.10. Use of numerical techniques with intrinsic numerical dissipation results in the solution with the compound shock, because the numerical dissipation plays a role analogous to a physical dissipation.

Freistuehler and Pitman [48] also analyze numerically the *vanishing viscosity limit* solution of the Riemann problem of Fig. 9.10. It turns out that in the limit of vanishing viscosity the solution of the Riemann problem of Fig. 9.10 is the compound shock solution! How can the vanishing viscosity limit solution be different from the solution of the ideal problem? The reason for this is that the dissipative system does not uniformly approach the ideal system for vanishing dissipation. We propose the following analogy to illustrate this.

Let us first recall the concept of a uniformly convergent row of functions. The row of functions $\{y_n(x) = exp(-n\,x) | x \in (0, +\infty), n = 0, 1, 2, ...\}$ clearly converges to the function $y(x) = 0$ in $(0, +\infty)$, but it is said that the convergence is not uniform because if one wants to approach the limit $y(x) = 0$ within a certain distance ϵ, then arbitrary large values of n are required if one moves closer to $x = 0$ (Fig. 9.11, left panel). The limit function $y(x) = 0$ can be extended continuously to the domain $x \in [0, +\infty)$ which includes the point $x = 0$ by defining $y(0) = 0$.

In [48] the Riemann problem with left state $\mathbf{U}_l = (1, 0)$ and right state $\mathbf{U}_r = (-\cos\delta, \sin\delta)$ is investigated numerically for the two limits of vanishing dissipation and vanishing δ. For a finite value of the dissipation and δ, it is found that the solution to the Riemann problem consists of some kind of 'mixed solution' with elements from both the rotational wave and the compound shock. For a constant δ and decreasing dissipa-

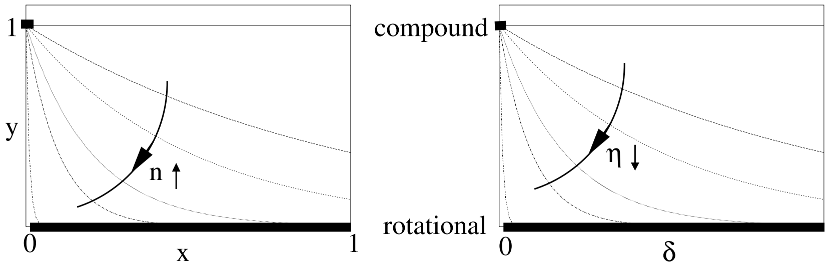

Figure 9.11: *Left panel: The row of functions* $\{y_n(x) = exp(-n\,x) | x \in (0, +\infty), n = 0, 1, 2, ...\}$ *clearly converges to the function* $y(x) = 0$ *in* $(0, +\infty)$ *(thick), but the convergence is not uniform. Right panel: The vanishing viscosity approach for Riemann problems does not converge uniformly.*

tion, the solution becomes more like a rotational wave, and the rotational solution is perfectly obtained in the limit of vanishing dissipation. For constant dissipation but decreasing δ, the solution becomes more like the compound shock solution, and the compound shock solution is perfectly obtained in the limit of $\delta = 0$. The vanishing viscosity limits of the Riemann problem solutions — $\eta \downarrow 0$ with δ constant — do thus not contain compound shocks, except for the case $\delta = 0$, for which a compound shock solution is obtained. Remark that for vanishing dissipation the compound shock solution becomes generically unstable because the perturbation weight required for destruction of the 3–1 shock vanishes [46]. The vanishing viscosity limit of the Riemann problem is not uniform, or the vanishing viscosity approach — consisting in determining the vanishing viscosity limit of flow solutions — does not converge uniformly for the system 9.7. The vanishing viscosity Riemann solution operator is not continuous. The right panel of Fig. 9.11 draws an analogy between this behavior and the non-uniformly converging row of functions described above.

The non-uniform convergence of the vanishing viscosity approach for the Riemann problems described above is related to the fact that 3–1 shocks are stable non-uniformly in the dissipation strength. Indeed, 3–1 shocks are less stable for smaller dissipation, and become less dominant in Riemann problem solutions for a given δ when the dissipation is decreased. Both these phenomena are manifestations of the fact that the dissipative system does not uniformly approach the ideal system for vanishing dissipation [46].

For the ideal system the Riemann problem solution for $\delta = 0$ contains the rotational wave — like for non-vanishing δ. The ideal Riemann solution operator is thus continuous, and can be interpreted as the continuous extension of the vanishing viscosity Riemann solution operator.

9.2.5 Discussion

The most important lessons to be learned from the discussion in this Section are that for non-strictly hyperbolic systems shock admissibility can be very different in the ideal and the dissipative case, and that a dissipative system may not uniformly approach its associated ideal system for vanishing dissipation.

The criterion of evolutionarity is not a good criterion for shock admissibility in dissipative systems because non-evolutionary shocks can be admissible in dissipative systems. Even in the ideal context the evolutionarity criterion is not very appropriate to determine shock admissibility, because it does not differentiate enough. For instance, the overcompressive shock of Fig. 9.4c is considered inadmissible according to the evolutionary criterion, but the behavior of this type of shock under perturbations is very different for different non-strictly hyperbolic systems. The overcompressive 3–1 shock discussed in Sec. 9.2.4 is inadmissible under the perturbation criterion, but the 1–4 shock discussed in Sec. 9.2.3, although non-evolutionary, can arise in ideal flows as the limit of two coinciding admissible shocks. Evolutionarity is thus not a good criterion to determine shock admissibility. Most authors agree with this conclusion [173, 109], but other authors do not agree [107, 35].

Freistuehler and Pitman [48] discuss how for some non-strictly hyperbolic systems the non-uniform nature of the vanishing dissipation limit has profound implications for the numerical calculation of solutions. A clear distinction has to be made between solving the ideal system and its associated dissipative system. For some problems the ideal and the dissipative solutions are entirely different. Numerical solutions of the ideal system are to be calculated by numerical methods which do not introduce any numerical dissipation. Solutions of the dissipative system are obtained when numerical methods are used which introduce numerical dissipation. Stability of shocks may depend on the precise mechanism and magnitude of the dissipation, such that the dissipative terms should preferably be discretized explicitly. When the dissipation is decreased there is no guarantee that the ideal solution is approached, as the vanishing viscosity limit may differ from the ideal solution.

The HD system is strictly hyperbolic. The associated dissipative system — the Navier-Stokes equations — approaches the ideal system — the Euler equations — uniformly for vanishing dissipation. Ideal HD is thus a good approximation of dissipative HD with small dissipation. We have to remark that this holds at least as far as shock admissibility and Riemann problem solutions are concerned, while it may not hold in the context of turbulence. Dissipative shock admissibility criteria can be applied directly to select admissible shock solutions of the ideal system. This is called the entropy or vanishing viscosity approach to determine the admissibility of ideal shocks. Numerical simulations with codes which introduce numerical dissipation produce solutions which approach solutions of the ideal system when the (numerical) dissipation is decreased.

In contrast, the MHD system is non-strictly hyperbolic and many of the desirable properties that were sketched above for the HD system do not hold. This is discussed in more detail in the following sections.

9.3 Planar MHD

9.3.1 Admissibility of shocks in planar MHD

The 6×6 system of planar MHD (Eq. 3.12 with $v_z \equiv B_z \equiv 0$) in one dimension has six characteristic waves: two fast waves which propagate with speeds $v_x \pm c_{fx}$, two slow waves with propagation speeds $v_x \pm c_{sx}$, and entropy and divergence waves which propagate with speed v_x (Eq. 3.35). The planar MHD system is non-strictly hyperbolic, because in the direction perpendicular to the magnetic field the slow wave speed c_{sx} vanishes, such that the slow characteristic speeds $v_x \pm c_{sx}$ coincide with the speed v_x of the entropy and divergence waves. The Alfvén waves, which are rotational waves of the type discussed in Sec. 9.2.4, are not present in planar MHD. The planar MHD system is not rotationally invariant.

Shock admissibility in the planar MHD system is analogous to the case of the non-rotationally invariant and non-strictly hyperbolic system discussed in Sec. 9.2.3. In addition the fast and slow characteristic fields are non-convex, such that compound shocks can occur (see Sec. 3.3.5). The discussion in Sec. 3.3 showed that for given shock speed s and flux constant vector $\mathbf{F}_{const}$ the RH relation 3.73 has up to four solutions which can be connected by shocks. Fig. 3.9b shows an example. The four states are labeled 1, 2, 3 and 4 in order of increasing entropy (Fig. 3.7).

Let us first consider the ideal system. Shocks which do not increase the entropy are undercompressive and thus non-evolutionary. Shocks 1–2, 1–3, 2–4 and 3–4 are evolutionary and are thus admissible. This means that 1–3 and 2–4 intermediate shocks are admissible in planar ideal MHD. The 1–4 shock is overcompressive, and the 2–3 shock is undercompressive. According to the evolutionarity criterion they thus both are inadmissible. However, analogous to the case of the 1–4 shock in Sec. 9.2.3, the 1–4 shock can arise in ideal MHD flows when 1–2 and 2–4 (or 1–3 and 3–4) shocks coincide.

For the dissipative system, the 1–2, 1–3, 2–4 and 3–4 shocks have a unique viscous profile. The 1–4 shock has a 1-parameter family of viscous profiles. Because of the non-convexity of the flux function, compound shocks arise. The 2–3 shock does not have a viscous profile. When the flow is such that a 2–3 shock would be required, a compound shock with a 1=2–3 or 2–3=4 sonic shock preceded or followed by a rarefaction wave is obtained instead [109].

Myong and Roe [109, 110] show that with these admissible waves all planar MHD Riemann problems have a unique solution. The planar Riemann problem is thus well-posed.

The admissibility of shocks is thus similar in the ideal and the dissipative cases. The only problem seems to be the 1–4 shock which has a viscous profile which is stable uniformly in the dissipation, but which is not evolutionary. However, this contradiction can partially be resolved by realizing that the 1–4 shock can be found in ideal flows when 1–2 and 2–4 (or 1–3 and 3–4) shocks coincide, and that small perturbations split up the 1–4 shock over a distance which vanishes for vanishing perturbation weight. This indicates that the dissipative system uniformly approaches the ideal system for vanishing dissipation. It can thus be speculated that the vanishing viscosity limit of dissipative flow problems converges to the ideal solution. This would mean that in numerical simulations the ideal solution can be approached by refining the grid and thus reducing the numerical dissipation. Myong (private communication) indeed argues that the solution of the planar MHD Riemann problem which was proposed in [109, 110] is valid for the ideal system as well as for the dissipative system.

9.3.2 Shock types in 2D magnetically dominated bow shock flows

All shocks of type 1–2, 1–3, 2–4, 3–4 and 1–4 are admissible in planar MHD. Compound shocks with 1=2–3 and 2–3=4 intermediate shocks can arise in flow problems. Fast 1–2 and slow 3–4 shocks have of course been known for a long time. All the other types of shocks have been found recently in 1D numerical simulation results [12, 172], and the presence of 1–3 and 1–4 shocks has been claimed in simulated time-dependent 2D flows [146]. The planar magnetically dominated bow shock flows around cylinders that were discussed in Chap. 6 are the first clear example of 2D flows containing intermediate shocks. Moreover, these flows contain *all* the shock types allowed in planar MHD flows, and form thus excellent new illustrations in 2D of the theory on the admissibility of shocks in planar MHD.

We recall from Figs. 6.7, 6.9 and 6.10 that shock segments A–B and D–E are of 1–2 type, B–D is 1–3, E–F is 1–4, D–G–H–I is 2–4, 2=3–4 or 3–4 depending on the exact location along the shock front, and E–H is a tangential discontinuity. Shock segment E–G is a 1=2–3=4 double compound shock. This type of shock is required for the solution of some planar MHD Riemann problems [110], and it is remarkable that the shock E–G forms a double steady xy compound shock which is mathematically completely equivalent to the double time-dependent xt compound shock that was described in [110]. This has been discussed in detail in Sec. 6.4.3.

Falle and Komissarov [35] argue that the 1–4 shock front in the magnetically dominated bow shock flows breaks up at points D and E (Fig. 6.9) because the 1–4 shock is non-evolutionary. We argue that the 1–4 front does not break up because of evolutionarity reasons, but because the intermediate 1–4 shock cannot exist for angles between the upstream magnetic field and the shock normal which are larger than a critical angle. This critical angle is 3° (Fig. 3.9c) for the flow of Fig. 6.9. The break-up of the 1–4 shock front has thus nothing to do with non-evolutionarity or instability against generic perturbations, but is due to the properties of the RH relations.

The planar magnetically dominated bow shock flows described in Chap. 6 were obtained by simulation with a numerical scheme which introduces numerical dissipation. Based on the discussion on vanishing viscosity limits given above, we argue that the solution we obtain approaches the solution to the ideal problem and that the ideal solution thus most probably has the topology of Fig. 6.7.

9.3.3 Numerical and physical instabilities

The numerical simulation results of the 2D magnetically dominated bow shock flows presented in Chap. 6 were obtained with the Lax-Friedrichs flux function (see Sec. 4.2.5) on moderately fine grids. The resulting flow solutions are in a perfect steady state, and the physically consistent interpretation given validates the numerical results. However, we have found that various instabilities occur when we decrease the numerical dissipation further, by considering very fine grids or by employing less dissipative numerical flux functions, while keeping the simulation domain limited to the upper left quadrant. These instabilities may be of a numerical nature, or they may be caused by physical mechanisms, some of which may be related to the stability of shocks as discussed above. We have found that instabilities can change the flow locally while the global topology is conserved, and the flow can become intermittent or quasi-periodic, instead of stationary. It is often difficult to reach definite conclusions about the nature of instabilities in numerical results. In this Section we leave the discussion on MHD shock stability for a while and report on our experiences regarding these local instabilities. We attempt to find explanations for the observed behavior of numerical methods and physical flows.

Failure of numerical schemes for bow shock flows

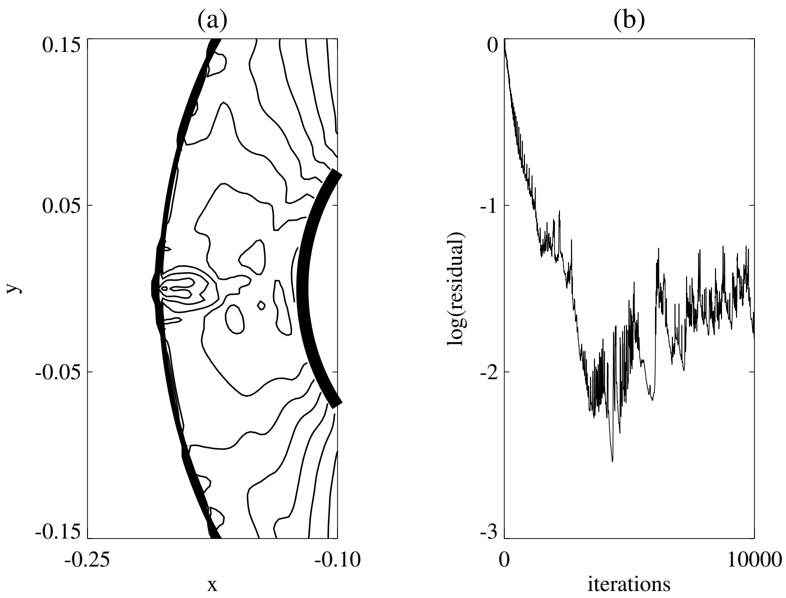

Figure 9.12: *Mach 10 hydrodynamic bow shock flow simulated using Roe's flux function. (a) The density contours show a deformation of the bow shock at the nose. (b) The solution is intermittent.*

It is well-known that numerical flux functions may suffer from various types of numerical instability problems [121, 108, 91]. In this Section we give some examples of the so-called carbuncle phenomenon, which is a well-known failure of many flux functions. For steady state, blunt body calculations the bow shock close to the stagnation line can be deformed, as can be seen in Fig. 9.12a for a Mach 10 hydrodynamic bow shock flow on a 100×201 grid simulated with our code using the second order scheme and Roe's flux function (see Sec. 4.2.5). The inflow quantities are $\rho = 1$, $p = 1$ and $v_x = 11.8$. Fig. 9.12b shows that the solution is intermittent and does not reach a steady state. The carbuncle effect appears to be more pronounced the more closely the grid is aligned to the bow shock, and for high Mach number flows. It is sometimes argued that this problem can be cured by applying the so-called *entropy fix* to all the characteristic waves [121], but we have found that this does not help for high resolution simulations. The result in Fig. 9.12a is not perfectly symmetrical, although the initial and boundary conditions are symmetrical and this symmetry is conserved by the HD equations. This means that our code and the grid we use is not perfectly symmetrical (as in [121]). It is very hard to make a numerical code perfectly symmetrical, for instance because numerical operations are not fully associative up to the last digit on a computer. The order of computation is thus important, and compilers may change this order and may thus introduce a-symmetry in the process of optimizing the code.

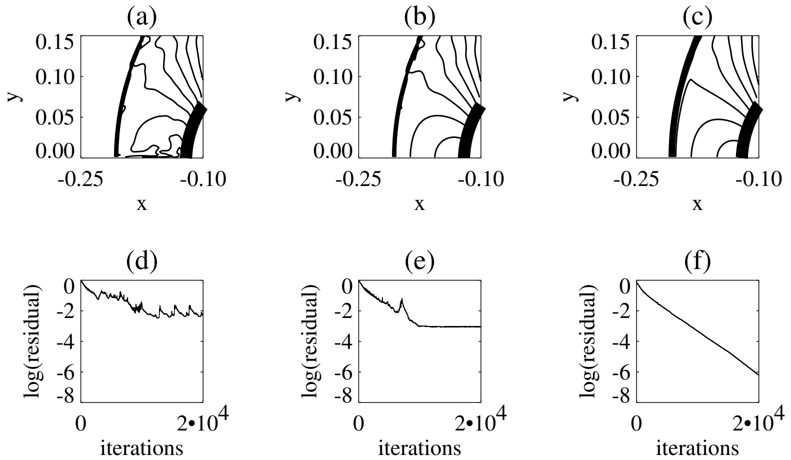

Figure 9.13: *Mach 10 hydrodynamic bow shock flows simulated in the upper left quadrant. Density contours and time convergence plots. (a,d) Roe. (b,e) HLLE. (c,f) LF.*

The bow shock flow simulations presented in Chap. 6 have been performed on a grid restricted to the upper left quadrant and with the symmetry explicitly imposed. The carbuncle phenomenon appears at the stagnation line in this configuration, as can be seen in Fig. 9.13a for simulation with the Roe flux on a 120×160 grid. The HLLE flux is known to be more robust [121, 99], and does not show the carbuncle in Fig. 9.13b, but the solution does not reach a steady state (Fig. 9.13e). The Lax-Friedrichs scheme (Fig. 9.13c and f) performs well due to its high and well-behaved numerical dissipation, but we are not aware of a proof that for very high grid resolution the carbuncle phenomenon does not appear.

Numerical dissipation

In general numerical instabilities are more likely to occur when the numerical diffusion is low or ill-behaved. Numerical diffusion is low on fine grids or for numerical flux functions which introduce a very small amount of diffusion for some characteristic waves. Some numerical flux functions introduce an ill-behaved numerical dissipation in the sense that the effective dissipation coefficient can become *negative*. This means that those numerical flux functions can *decrease* the entropy of fluid elements in numerically calculated flows. It is said that those numerical flux functions are not entropy consistent or not entropy stable [7]. The Roe scheme, for instance, is not entropy stable [7]. It follows clearly from the discussion on shock admissibility given above that an ill-behaved numerical dissipation may produce inadmissible shocks in numerical simulation results. For instance, for a negative value of the dissipative coefficient state -1 in Fig. 9.3 becomes unstable, and state 1 becomes stable, such that only shocks with diverging characteristics (Fig. 9.1a) would have viscous profiles! Expansion shocks can be produced by the Roe scheme [121]. An entropy fix is proposed to cure these problems with the Roe scheme [121, 90], but this fix does not cure all problems, like for instance the carbuncle phenomenon. The LF flux function has a well-behaved numerical dissipation, so we expect less influence from numerical instabilities. This was a motivation for the use of the LF flux function in the simulations presented in Chap. 6.

Decreasing the numerical dissipation in the 2D bow shock flow simulations

We now describe what happens when we substantially decrease the numerical dissipation for the bow shock flow simulation described in Sec. 6.2.

Let us first discuss simulations in which we used the Lax-Friedrichs flux function. The stationary simulation result discussed in Sec. 6.2 was faithfully reproduced on grids of size 60×60 to about 160×160. The solution has been reproduced with a different numerical code by Keppens *et al.* [83]. For finer resolutions, however, we have noticed some instabilities. In Fig. 9.14 we show the result of a simulation on a 320×320 grid. We have failed to obtain convergence to a perfect steady state, as can be seen in the convergence plot Fig. 9.14c. The solution is still close to a steady state though, and the fluctuations visible on time-animations of the solution are very small. Comparison of Fig. 9.14a with Fig. 6.9 shows some differences which can be interpreted as local instabilities, notably along the stagnation line, along the tangential discontinuity E–H, and near the intersection of the tangential discontinuity E–H with the intermediate shock D–G–H–I at point H. It is well-known that shear layers

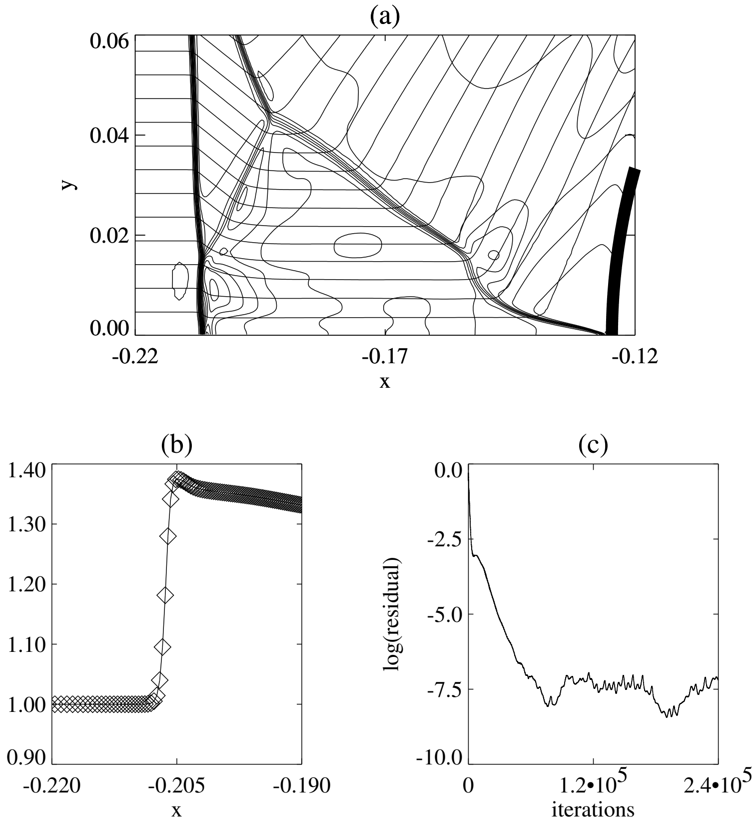

Figure 9.14: *LF simulation on a* 320×320 *grid. (a) Density contours and magnetic field lines. (b) Magnetic field profile along the stagnation line. (c) Convergence of the density residual.*

are physically unstable and show roll-up behavior, so this may explain the instability at the tangential discontinuity E–H. The instability on the stagnation line may be related to the numerical instability of carbuncle type discussed in the previous Section. The fact that the magnetic field is discontinuous in point F, as shown in Fig. 9.14b, seems to support this interpretation, because due to symmetry a continuous variation is required, as in the solution shown in Fig. 6.11d.

Regardless of these local instabilities and their nature, and regardless of the fact that the solution has become intermittent, we see that the flow retains the same general topology as the solution of Fig. 6.9. All the different segments of various MHD shock types are still present, including the intermediate and compound shocks, so the analysis and interpretation given in Chap. 6 remains valid for flows with lower (numerical) dissipation.

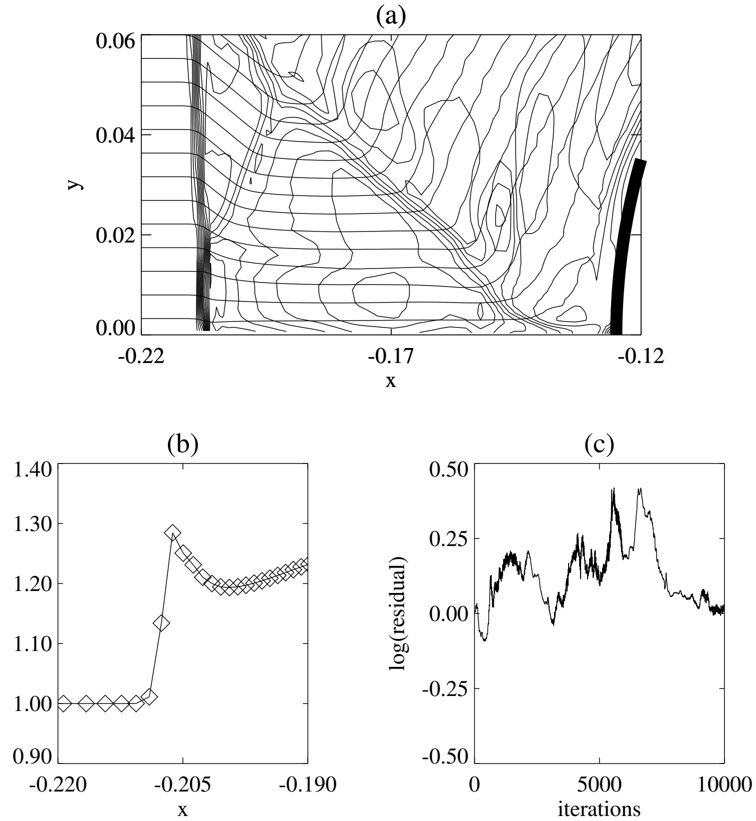

Figure 9.15: *Roe simulation on a* 80×80 *grid. (a) Density contours and magnetic field lines. (b) Magnetic field profile along the stagnation line. (c) Convergence of the density residual.*

Now we discuss the simulation results obtained with the Roe scheme and Linde's HLLE scheme. In Fig. 9.15 we show the result of a simulation on a 80×80 grid using Roe's scheme. This scheme has a lower and less well-behaved numerical dissipation than the LF scheme, and local instabilities already show up for coarse grids. This time the instabilities have a stronger influence on the temporal behavior of the solution. The residual fluctuates strongly and at high levels (Fig. 9.15c shows a part of the residual profile for a time interval well after the start of the simulation, and re-normalized to start with a value of zero), and animation of the simulation results shows strong fluctuations. Instabilities seem to be present at similar locations as in the case of LF simulations on fine grids. The instability at the stagnation line is probably a manifestation of the numerical carbuncle instability. We see an additional density layer at the ideal cylinder, which is probably related to the numerical effect of wall heating [90], a well-known defect of the Roe solver.

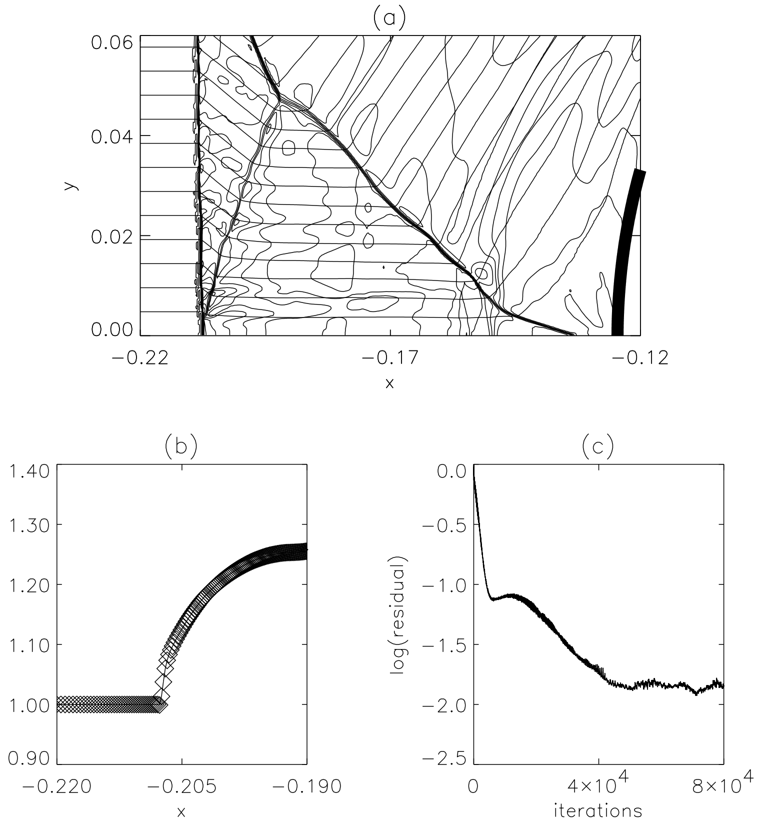

Figure 9.16: *HLLE simulation on a* 480×480 *grid. (a) Density contours and magnetic field lines. (b) Magnetic field profile along the stagnation line. (c) Convergence of the density residual.*

In Fig. 9.16 we show the result of a simulation on a 480×480 grid using Linde's HLLE scheme. This scheme is also much less dissipative than the LF scheme, so local instabilities show up quite strongly on fine grids. The instabilities again have a strong influence on the temporal behavior of the solution. The residual fluctuates at high levels, and animation of the simulation results shows strong fluctuations. Instabilities seem to be present at similar locations as in the case of LF simulations on fine grids. The density is very oscillatory also away from the shocks, and this is due to the effect of entropy oscillations generated at the shocks — which are in a way too sharp — , which are transported along streamlines, as in Fig. 5.10a. This effect is much stronger on fine grids and for flux functions with low dissipation, like the HLLE flux function. The HLLE scheme seems to be remarkably robust against the carbuncle instability at point F, as the continuity of the magnetic field profile on the stagnation line proves. At point I, however, the solution is markedly different from the LF solution in Fig. 6.9. Also, the 1–4 shock segment E–F seems to become much smaller as point E migrates towards the stagnation streamline. This effect is investigated in more detail below. Wall heating effects seem not to be present in these HLLE simulations.

For both the Roe and the HLLE solver, the effects of the instabilities seem to be more severe than for the LF solver. However, the flow retains the same general topology as the LF solution of Fig. 6.9.

Stability of the 1–4 shock segment

We now look in some more detail at the behavior of the 1–4 shock segment for increasing grid resolution.

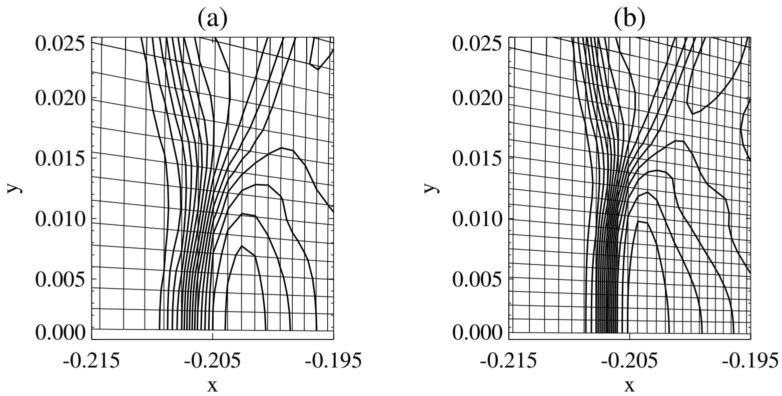

Figure 9.17: *Detailed representation of the 1–4 shock segment (density contours) near the perpendicular point F on the stagnation line, for LF simulations with different grid resolutions. (a)* 80×80 *grid. (b)* 120×120 *grid.*

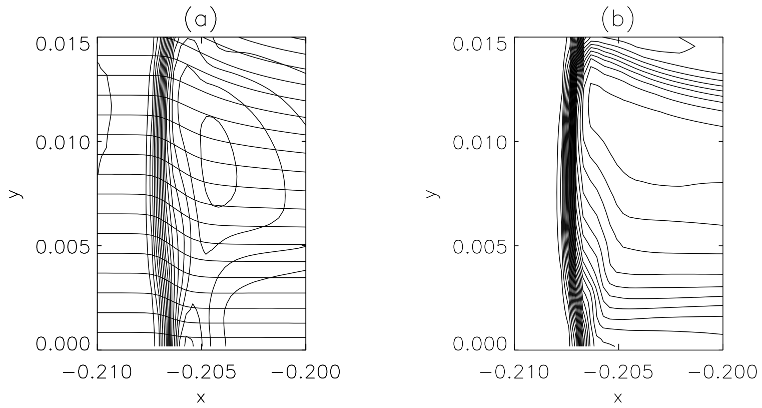

Figure 9.18: *Detailed representation of the 1–4 shock segment for LF simulation on a* 320×320 *grid. (a) Density contours and field lines. (b) Entropy contours.*

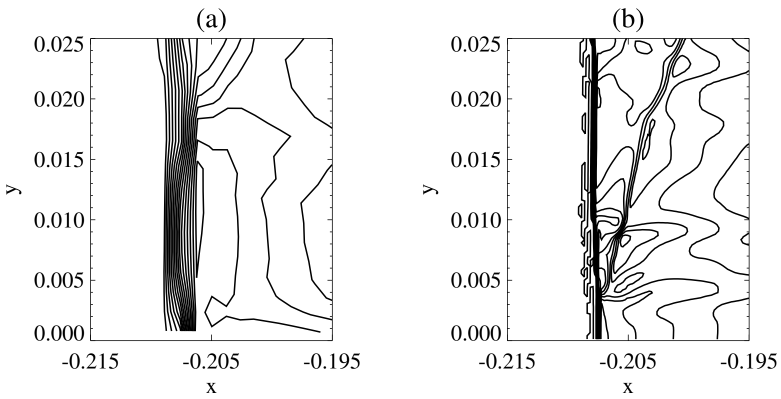

Figure 9.19: *Detailed representation of the 1–4 shock segment (density contours). (a) Roe on* 80×80 *grid. (b) HLLE on* 480×480 *grid.*

Fig. 9.17 shows detailed representations of this 1–4 shock segment for LF simulations with intermediate grid resolutions. The Figure shows that the 1–4 shock segment seems to be well-defined in the sense that it does not change its shape or extent when the grid is refined. However, in the LF simulation result with fine grid of Fig. 9.18, the 1–4 shock seems to split up into two shocks.

Fig. 9.19 shows detailed representations of this 1–4 shock segment for the Roe and HLLE simulations presented above. The 1–4 shock remains intact for the Roe simulation on a 80×80 grid, but breaks down in the fine grid HLLE simulation such that point E moves much closer to the stagnation line. Close to the stagnation line, however, the 1–4 shock seems to remain intact. We have to admit that these results do not show much consistency. We can propose several possible explanations for the behavior of the 1–4 segment for increasing grid resolution. In Figs. 9.18 and 9.19b the 1–4 segment seems to split up into two shocks. This may be interpreted as supporting Falle and Komissarov's claim [35] that the 1–4 shock is non-evolutionary and should split up into two evolutionary shocks as the ideal MHD solution is approached by decreasing the dissipation. However, we have argued that a 1–4 shock can exist in ideal MHD flows. In simulations with numerical dissipation the 1–4 shock is stable against perturbations. Therefore we favor the following alternative interpretation for the breakup of the 1–4 shock. Physical or numerical instabilities, e. g. roll-up of the tangential discontinuity E-H or occurrence of the carbuncle instability at point F, may perturb the orientation of the 1–4 shock front EF. When in this process somewhere along the shock front EF the angle between the upstream magnetic field and the shock normal exceeds $3°$, the shock front splits up (Fig. 3.10). Another possible explanation for the break-up in Fig. 9.19b is that the numerical dissipation of the HLLE scheme may not be well-behaved. It seems that high-resolution simulations of the MHD equations with a well-controlled small dissipation or with a code which does not introduce any numerical dissipation [35, 48] are needed to clarify the issue of the stability of the 1–4 front.

Comparison of the Powell technique and the projection approach

It is interesting to compare the Powell technique and the projection approach for the 2D bow shock flows and to verify if the approach used to control the $\nabla \cdot \vec{B}$ constraint (see Sec. 4.4) influences the stability of the solution.

Fig. 9.20 shows the comparison of LF flow simulation results on a 120×120 grid for simulation with the Powell source term (thin) and simulation with the projection scheme (thick), for various quantities along the stagnation streamline. First we can remark that the solutions are almost everywhere very close, so the two approaches both seem to produce valid results. Only near the stagnation point the results differ appreciably — see for instance the density in Fig. 9.20a. Then the question is which of the two results is more accurate. Fig. 9.20c shows that the

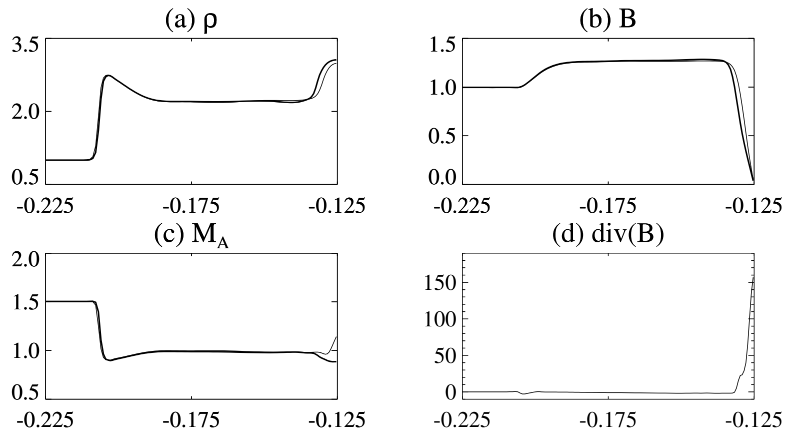

Figure 9.20: *Comparison of LF flow simulation results for simulation with the Powell source term (thin) and the projection scheme (thick), for various quantities along the stagnation streamline.*

Powell technique produces a solution for which the Alfvénic Mach number rises above one close to the cylinder. This is of course not physical, so the projection technique is more accurate. It is not unexpected that the Powell technique performs not so well at stagnation points, because the Powell technique can be interpreted as to advect $\nabla \cdot \vec{B}$ away with the flow. At a stagnation point the flow velocity vanishes, so $\nabla \cdot \vec{B}$ can accumulate. Fig. 9.20d shows that this is indeed the case ($\nabla \cdot \vec{B} = 0$ up to machine accuracy in our projection scheme approach). This accumulation of $\nabla \cdot \vec{B}$ leads to inaccuracies near the stagnation point, as the Powell technique is based on the cancellation of terms proportional to $\nabla \cdot \vec{B}$ on both sides of Eq. 3.12. Subtraction of two big numbers that are almost equal then leads to a high absolute error.

The projection scheme may thus lead to more accurate results in some cases, but still we have chosen to perform most simulations using Powell's technique, for several reasons. First, the Powell technique is much faster. Second, it can easily be parallelized, whereas the projection scheme necessitates the solution of a linear system in every time step, which is a non-local operation and thus hard to parallelize. Third, the solution of the elliptic projection equation introduces a coupling between all the points in the domain, and this may lead to contamination of upstream superfast regions which in theory should not be affected. Fourth, the projection scheme we use, like the schemes proposed in [129, 162, 161], leads to spurious modes due to odd-even decoupling. These oscillations are effectively damped out by the LF dissipation for the results shown in Fig. 9.20, but on finer grids or for less dissipative flux functions the oscillations are much more pronounced.

9.4 Full MHD

9.4.1 Admissibility of shocks in full MHD

Shock admissibility

The 8×8 system of full MHD (Eq. 3.12) in one dimension has eight characteristic waves: two fast waves which propagate with speeds $v_x \pm c_{fx}$, two Alfvén waves with propagation speeds $v_x \pm c_{Ax}$, two slow waves with propagation speeds $v_x \pm c_{sx}$, and entropy and divergence waves which propagate with speed v_x (Eq. 3.35).

The full MHD system is non-strictly hyperbolic. In the direction parallel to the magnetic field the Alfvén speed c_{Ax} coincides with c_{fx} when $c_{Ax} > c$, or with c_{sx} when $c_{Ax} < c$. In each of these cases there are two degeneracies in which two characteristic speeds coincide. When additionally $c_{Ax} = c$, there are two degeneracies in which three characteristic speeds coincide, since $c_{fx} = c_{Ax} = c_{sx}$. In the direction perpendicular to the magnetic field c_{Ax} and c_{sx} vanish, such that the Alfvén and slow characteristic speeds coincide with the speed v_x of the entropy and divergence waves, implying a six-fold degeneracy.

The Alfvén waves are rotational waves of the type discussed in Sec. 9.2.4, and the full MHD system is rotationally invariant in the sense discussed in Sec. 9.2.4 [42, 46]. The fast and slow characteristic fields are non-convex, such that compound shocks can occur (see Sec. 3.3.5).

Some aspects of shock admissibility in the full MHD system are analogous to the case of the rotationally invariant and non-strictly hyperbolic system discussed in Sec. 9.2.4, but due to the many possibilities of multiple-fold degeneracies, the overall behavior is quite more complex.

Like in the planar case, for given shock speed s and flux constant vector $\mathbf{F}_{const}$ the RH relation 3.73 has up to four solutions which can be connected by shocks, labeled 1, 2, 3 and 4 in order of increasing entropy (Fig. 3.7). The shock admissibility in the full MHD system is, however, entirely different from the admissibility in the planar system, because rotational Alfvén waves exist which destabilize intermediate shocks.

Let us first consider the ideal system. Shocks which do not increase the entropy are undercompressive and thus non-evolutionary. Fast 1–2 shocks and slow 3–4 shocks are evolutionary and are thus admissible. All intermediate shocks (1–3, 1–4, 2–3 and 2–4) are overcompressive [87, 35]. According to the evolutionarity criterion they are inadmissible.

For the dissipative system, the dissipative parameters are the electric resistivity η, the thermal conduction κ, and two coefficients of viscosity

μ and ν [46]. Fast 1–2 shocks and slow 3–4 shocks have unique viscous profiles for all values of the dissipative parameter vector $\delta =(\eta, \kappa, \mu, \nu)$. All intermediate shocks do not have viscous profiles for some range of δ, with this range depending on the shock type and the left and right states. All intermediate shocks do have viscous profiles for some range of δ. This has been proven in [49], where it is shown that the profiles are generated in a global heteroclinic bifurcation controlled by ratios of the dissipative coefficients. Good numerical illustrations of the effect of this bifurcation for MHD flows can be found in [173].

When profiles exist for intermediate shocks, they generally are not unique but are members of families of profiles. As shown in Sec. 9.2.4, this allows the overcompressive intermediate shocks to be conditionally stable against Alfvénic perturbations which introduce magnetic field out of the plane of coplanarity of the shock. The quantity $I_z = \int B_z \, dx$, with z the direction out of the plane of coplanarity, x the direction perpendicular to the shock front and integration over the length of the shock profile, plays an important role in the stability of intermediate shocks [173, 109]. For a given intermediate shock — left and right states satisfying the RH relations — and for a given value of δ for which the shock can have viscous profiles, a shock profile can exist only if the weight I_z of B_z in the profile is smaller than a certain I_z^{crit}. When the shock is perturbed — for instance by sending in an Alfvén wave packet — I_z builds up in the shock profile, until it exceeds the critical value and the shock splits up in other waves. The stability is non-uniform in the magnitude of the dissipation, in the sense that the critical value I_z^{crit} vanishes for vanishing δ with constant $\delta/||\delta||$ [46, 47]. This resolves the contradiction between the fact that intermediate shocks are inadmissible in the ideal system, but have viscous profiles in the dissipative system. Dissipative MHD thus approaches ideal MHD for vanishing dissipation. Vanishing viscosity limits are not uniform and are not unique because the existence of intermediate shocks in solutions depends on ratios of dissipative coefficients.

The dissipative system does thus not *uniformly* approach the ideal system for vanishing dissipation. One manifestation of this is that shock admissibility is different for the ideal and the dissipative systems. This implies that shock admissibility criteria from the ideal system cannot simply be used to determine admissibility of dissipative shocks — what Falle and Komissarov [35] apparently try to do —, and vice versa, that dissipative criteria cannot simply be used to determine admissibility of ideal shocks — what Myong and Roe [109, 110] apparently try to do. For strictly hyperbolic systems like the HD equations, ideal admissibility criteria can be applied to the dissipative system and vice versa. For MHD this is not true, and it seems that much of the confusion in the literature on the admissibility of MHD shocks stems from attempts to apply dissipative criteria to the ideal system [109, 110] or the other way around [35]. It has been argued that dissipative criteria can be used to determine admissibility of ideal shocks if one considers waves that are non-uniformly stable in the dissipation inadmissible in the ideal system, while considering uniformly stable waves admissible [102]. Indeed, dissipative and ideal MHD do approach each other, but the non-uniformity has to be taken into account.

Riemann problems

The non-uniformity of vanishing viscosity limits can be illustrated by considering Riemann problems, analogous to the Riemann problem for the rotationally invariant model problem which was discussed in Sec. 9.2.4. Fig. 9.21 shows a solution of the Riemann problem introduced by Brio and Wu [12] obtained by our numerical code. A slow compound shock arises in the solution. The 2–3=4 sonic intermediate shock is admissible in the dissipative system, so our numerical code with numerical dissipation produces a solution with the compound shock. We have performed the simulation in full MHD, so Alfvénic perturbations due to non-perfect symmetry of the code would destroy the shock if it were generically unstable. Such small perturbations of B_z do indeed arise, but the shock clearly persists. In the ideal system, intermediate shocks are not admissible. Rotational Alfvén waves destabilize intermediate shocks, and at the same time provide a different way of changing the sign of the tangential magnetic field component. A rotational discontinuity thus takes over the role of the compound shock in the ideal solution of the Riemann problem. Falle and Komissarov indeed produce this ideal solution with their dissipation-free numerical code based on the Glimm scheme [35].

It seems that the fact that numerical codes with or without numerical dissipation produce different solutions to this Riemann problem is thus satisfactorily explained by the above observations. Some authors still seem to think that the existence of two solutions is a problem, and claim that one of the two is the only valid solution. Falle and Komissarov [35] argue that the solution with the rotational discontinuity is 'the only physically admissible solution to the Riemann problem'. This is of course not true. Their claim is probably true if they were to restrict it to the ideal MHD system (which they do not!), but in the dissipative MHD system the solution with the compound shock is certainly admissible! Even in the limit of vanishing dissipation — equivalent to refining the grid in a code which employs numerical dissipation — the solution of this problem is the compound shock solution [48]. Myong and Roe [109] claim that intermediate shocks are 'physical'. They argue that intermediate shocks are admissible in full MHD, and can thus arise in Riemann

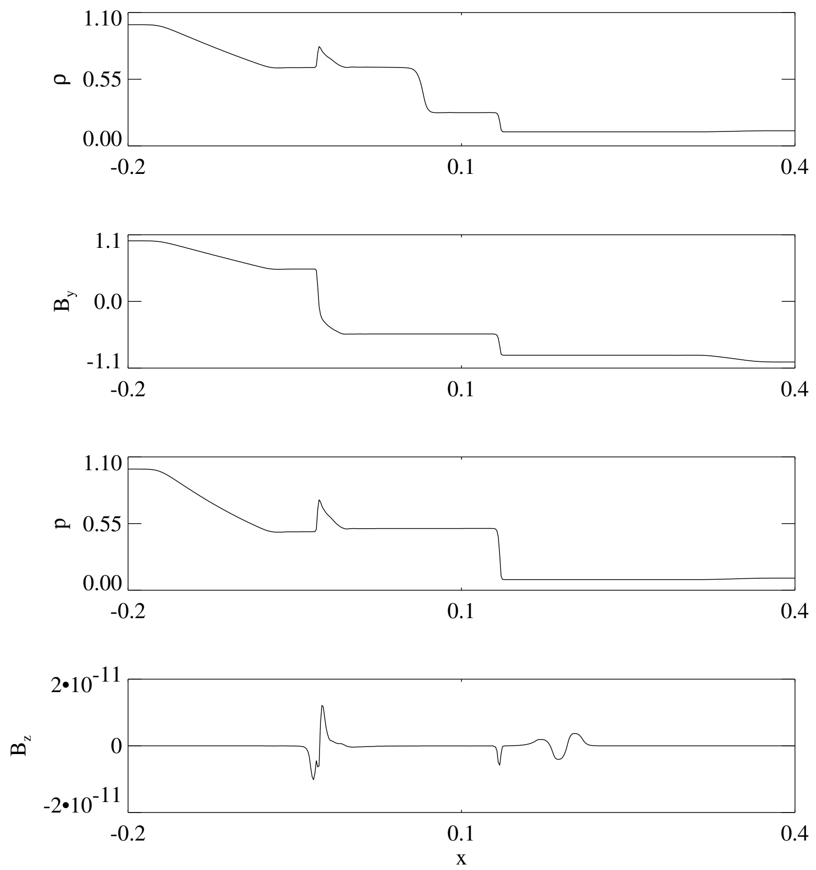

Figure 9.21: *Riemann problem solution. The density, the pressure, the tangential component B_y of the magnetic field in the plane of coplanarity and the component B_z out of this plane are shown. The following waves can be identified (from left to right): a fast rarefaction, a slow compound shock (a sonic slow shock with an attached rarefaction), a contact discontinuity, a slow shock and a fast rarefaction.*

problem solutions. This claim would be true if they were to specify that they talk about the dissipative system only (which they do not specify!). In solutions of the ideal system intermediate shocks can probably not arise. We can thus conclude that if controversy remains, this is mainly due to the fact that some authors do not precisely formulate the range of validity for their claims or, equivalently, do not specify precisely what they mean by 'physically admissible'. We come back to the question of 'physical admissibility' in Sec. 9.4.3.

Time-dependent intermediate shocks

Due to the non-strictly hyperbolic nature of MHD, the dissipative MHD system allows for the peculiar phenomenon of *time-dependent intermediate shocks* [173, 178, 177]. This phenomenon has no analogy in HD flow.

In the strictly hyperbolic HD system, an initial discontinuity which does not satisfy the RH relations — this is the initial condition of a Riemann problem — splits up in waves which each satisfy the RH conditions and move with the shock speeds dictated by the RH relations. This is true for both ideal and dissipative HD. In dissipative HD the shocks have unique viscous profiles.

In the dissipative MHD system, however, an initial discontinuity which does not satisfy the RH relations splits up in waves of which some may be compressive waves which do not satisfy the RH conditions. In these compressive waves dissipation balances compressional steepening — characteristics converge into the wave — and they thus have a profile of limited spatial extent. The flow is sub-Alfvénic upstream and sub-Alfvénic downstream. These waves are called time-dependent intermediate shocks. The profile of waves that do not satisfy the RH relations necessarily undergoes a change in time. This can be seen by integrating the conservation law over the length of the profile in the frame moving with the wave. For a wave satisfying the RH relations we find that $\partial(\int u\,dx)/\partial t = f(u_r) - f(u_l) = 0$, while for a wave not satisfying the RH relations the weight $\int u\,dx$ of the profile has to change in time according to $\partial(\int u\,dx)/\partial t = f(u_r) - f(u_l) \neq 0$. We propose the conjecture that this continuous change in profile is possible in MHD because intermediate shocks have *families* of viscous profiles, whereas in the HD system shocks have *unique* profiles and time-dependent shocks do not occur in 1D Riemann problems. In dissipative MHD, time-dependent intermediate shocks arise in the solution of non-coplanar Riemann problems. They do not move with constant speed. For large times they evolve to non-intermediate discontinuities which satisfy the RH relations.

In ideal MHD time-dependent intermediate shocks cannot occur because ideal discontinuities do not have a profile and thus necessarily have to satisfy the RH relations! Solutions of non-coplanar Riemann problems do not contain any intermediate shocks, but instead they contain from the start the shocks which appear in the dissipative solution for large times.

9.4.2 Shock types in 3D magnetically dominated bow shock flows

Intermediate shocks have to our best knowledge previously not been observed in 3D MHD simulations.

The magnetically dominated bow shock flows around spheres that were presented in Chap. 7 (e.g. Fig. 7.1) clearly show the presence of stationary intermediate shocks of 1–3 and 2–4 types. The necessary presence of intermediate shocks in the bow shock topology for the magnetically dominated parameter regime is confirmed by reasoning based on the geometric properties of MHD shocks (Fig. 7.5b). A 1–3 shock segment arises in the leading shock front of the flow of Fig. 7.1, and the secondary front is of 2–4 type (Figs. 7.10 and 7.8).

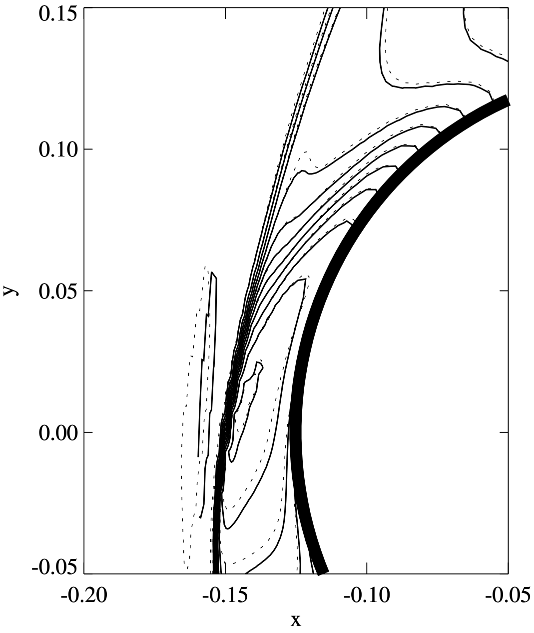

Figure 9.22: *Bow shock simulation results in the xy plane for the parameters of Fig. 7.1, on a randomly perturbed* $60 \times 80 \times 80$ *grid covering the half space on the upstream side of the sphere (solid), and on a symmetrical* $60 \times 60 \times 40$ *grid covering the upper upstream quadrant (dotted). The two solutions agree, thus the solution containing 3D intermediate shocks is stable against non-symmetrical grid perturbations.*

Falle and Komissarov [35] argue that intermediate shocks can sometimes 'pollute' full MHD flows due to artificial symmetry. One could argue that the simulation result of Fig. 7.1 contains artificial symmetry because we have performed the simulation only in the top left quadrant and we explicitly impose the symmetry at the xy plane. Uniform MHD flow around a sphere always has such a plane of symmetry, however. This symmetry is intrinsic to the physical problem, and is thus not artificial. We have verified if the intermediate shocks remain present in the bow shock flow solution when the symmetry at the xy plane is not perfectly imposed. To this end we have simulated the bow shock flow of Fig. 7.1 on a randomly perturbed grid covering the half space on the upstream side of the sphere, and not just the upper upstream quadrant. Fig. 9.22 shows that the solution with intermediate shocks survives when we perturb the symmetry of the xy plane slightly by perturbing the grid. The two solutions in Fig. 9.22 agree, thus the solution containing 3D intermediate shocks is stable against non-symmetrical grid perturbations.

Fig. 7.20 shows that compound shocks can arise in 3D simulations of the full MHD system. Falle and Komissarov [35] claim that full MHD is effectively convex and that compound shocks cannot arise in full MHD flows. Again, there claim may be justified for the ideal MHD system, but is clearly false in the general way they put it, because compound shocks can arise in full MHD flows with small dissipation.

In brief, our simulation results of 3D bow shock flows show that in physically realistic flows described by full MHD with small dissipation intermediate shocks can exist and persist.

9.4.3 Physical admissibility of intermediate shocks

Are intermediate shocks physical?

Intermediate shocks are physical if they can be observed in plasmas in nature. It seems justified to suppose that dissipative processes are active in some way in all plasmas in nature. These dissipative processes do not necessarily have to be of a collisional nature, but may be due to microscopic particle-wave interactions and instabilities. Let us thus assume that all physical plasmas undergo some kind of dissipation. Let us further assume that MHD is a good description of shock phenomena in plasmas. This is not entirely obvious, and we refer the reader back to Sec. 2.3.1 for some thoughts on this issue. Under these assumptions we can say that intermediate shocks are physical if they can arise in solutions of the full MHD equations with small dissipation.

The discussion in Sec. 9.4.1 has shown that intermediate shocks are admissible in full MHD for large ranges of the dissipative parameters. Our 3D simulation results of bow shock flows have shown that intermediate shocks can be formed and can persist in realistic MHD flows with small dissipation. We thus conclude that intermediate shocks are physical.

It is probably true that intermediate shocks cannot arise in *ideal* MHD flows. But this does not mean that intermediate shocks are unphysical, because all plasma flows are presumably subject to dissipation and ideal MHD is in some sense not a good description of small dissipation MHD.

Falle and Komissarov [35] indeed agree that intermediate shocks 'may, perhaps, appear under some exceptional circumstances as transient phenomena' (at which point we have to assume that they speak in the context of dissipative MHD, although again this is not clearly specified). It then seems unjustified that they keep on calling intermediate shocks 'unphysical'. The reason why they still do so, is their claim that in any physical system intermediate shocks can never exist long enough to be observed, because existing intermediate shocks would supposedly be destroyed by small Alfvénic perturbations. They argue that the amplitude of Alfvénic perturbations necessary for destroying intermediate shocks is very small in space plasmas because the dissipation is very low. They give the example of interplanetary intermediate shocks traveling in the solar wind. Chao [18] claims the observation of an interplanetary intermediate shock by the Voyager 1 spacecraft. Falle and Komissarov [35] argue that when an intermediate shock would travel from the sun in the direction of a satellite, Alfvénic perturbations in the solar wind would destroy the intermediate shock before it can reach the satellite. This may be true, but does in our opinion not mean that intermediate shocks cannot be observed in other physical contexts.

Indeed, Falle and Komissarov [35] never consider how intermediate shocks can be *formed* in space plasmas. Their reasoning is based on physical intuition which stems from considering 1D Riemann problems. Riemann problems are artificial in a sense, because the initial state is given as such and has not been formed by physical processes. Once shocks are destroyed by perturbations, there is no driving mechanism to reform them. When a certain symmetry or coplanarity is present in a given Riemann problem, it can always be argued that the symmetry is arbitrarily imposed and that Riemann problems with symmetry do not constitute generic cases [35]. The shocks arising in these symmetrical or coplanar cases are then considered artificial too, and it is easily concluded that these 'exceptional' shocks do not arise in 'generic' physical flows. These interpretations are based on physical intuition stemming from Riemann problems. In the literature shock admissibility is almost always discussed in the context of 1D Riemann problems. This context is not necessarily the most physically relevant. For instance, perturbation of the left or right states of a Riemann problem implies a perturbation with an unbounded weight I_z, which certainly is not the only physically relevant way of perturbing a shock. We think that a different and more pertinent physical intuition is provided by considering *driven* problems in multiple dimensions.

The bow shock flows we have discussed in Chaps. 6 and 7 are *driven* problems in which shocks are formed by physical processes. When shocks are destroyed by perturbations, they can possibly be reformed. The bow shock flows possess an intrinsic symmetry due to the physical nature of the problem. In the case of 3D flow over a sphere the uniform inflow can be changed — for instance by rotating the magnetic field vector around the velocity vector — such that the plane of symmetry of the solution ceases to be a plane of symmetry, but by the physical nature of the problem the new inflow defines a new plane of symmetry! The bow shock flows are 2D and 3D. In 2D and 3D geometrical constraints can arise which necessitate the occurrence of certain shocks like switch-on shocks and intermediate shocks. For instance, the reasoning leading to the topology of Fig. 7.5b was clearly based on such constraints. These constraints do not arise in 1D Riemann problems.

The physical nature of driven problems in multiple dimensions is thus entirely different from the nature of 1D Riemann problems. In contrast to the conclusions often derived from considerations in the context of Riemann problems, we conclude from our simulation results of driven bow shock problems that intermediate shocks can be formed and can persist in physically relevant flows. If they are destroyed by perturbations, they can be reformed by the same process by which they were formed initially. The symmetry or coplanarity required for this reformation is intrinsic to the physical nature of realistic driven problems in multiple dimensions. This indicates that intermediate shocks are physical and can be observed. They may even be observable as close to the earth as in the bow shock formed in front of the earth by the solar wind when the solar wind is magnetically dominated! The 4 CLUSTER satellites, planned to be launched by mid-2000, may be able to detect a 1–3 intermediate shock segment in the earth's bow shock under magnetically dominated solar wind conditions.

On the relevance of ideal MHD

The discussion above raises questions about the relevance of ideal MHD for the description of real plasmas.

In their writing Falle and Komissarov [35] seem to claim implicitly that ideal MHD can be used to describe real plasmas because the differences between ideal and dissipative MHD are considered small and not observable because of omni-present small perturbations.

In contrast, Wu [173] argues strongly against the use of ideal MHD to describe real plasmas. He claims that 'whenever a rotation of the magnetic field occurs, (ideal MHD) is not a good approximation to dissipative MHD'. He argues that small dissipation MHD is the physically relevant case, and that ideal MHD is not a good description of small dissipation MHD. He shows that solutions to Riemann problems critically depend on shock profiles, on the nature of the dissipation mechanism, and on the magnitude of the dissipative parameters. Ideal MHD can clearly not describe these aspects of small dissipation MHD flows. Wu even seems to imply that ideal MHD is not a valid or consistent theory. He argues that the ideal Riemann problem is not well-posed, because a given Riemann problem can have many different solutions.

Freistuehler [45] states that the fact that intermediate shocks are not admissible in ideal MHD while they can be admissible in dissipative MHD, 'shows severe limitations of ideal MHD in its role as a model of small dissipation MHD. On the other hand, these limitations are non-uniform themselves and they will not make ideal MHD completely useless for *physical* interpretation whenever discontinuities are present. Certainly, they do not preclude *mathematical* self-consistency of ideal MHD.' Freistuehler argues that 'ideal MHD has a self-consistent theory in which intermediate shocks do not occur' [46], although he does not prove this. The objection of Wu against ideal MHD, namely that ideal MHD is ill-posed because Riemann problems can have multiple solutions, is neutralized by arguing that of these many solutions only the one without intermediate shocks is admissible in ideal MHD.

The picture sketched by Freistuehler seems the most attractive. Ideal MHD is well-posed and has a self-consistent solution theory. Ideal and dissipative MHD do approach each other for small dissipation, so ideal MHD can describe flows with small dissipation up to a certain extent. However, they do not *uniformly* approach each other. For instance, intermediate shocks can exist in dissipative MHD, but not in ideal MHD. Therefore detailed description of some phenomena in real (dissipative) plasmas requires dissipative MHD with precise control of the mechanism and magnitude of the dissipation.

On the relevance of shock-capturing numerical techniques for non-strictly hyperbolic systems

Freistuehler's [48] and Wu's [173] work implies that in numerical simulations dissipation mechanisms and magnitudes have to be specified precisely and that shock profiles have to be resolved in order to be able to properly describe some shock phenomena in real MHD plasmas with dissipation.

Such a numerical approach is entirely opposite to the approach generally followed for the simulation of flows with shocks described by strictly hyperbolic systems like the HD equations. Indeed, in modern *high-*

resolution shock capturing codes [90] one discretizes the ideal equations, and one aims at minimizing the numerical dissipation in order to approach as closely as possible the dissipation in the physical system, which is often much lower than the attainable minimum numerical dissipation. Shock profiles are typically not resolved, but one aims at reducing the shock width to a minimal number of computational cells. Can these shock-capturing numerical techniques be used for the simulation of flows with shocks described by non-strictly hyperbolic systems?

It would obviously be better to discretize the dissipative terms and to resolve shock profiles. However, this approach requires much larger computer resources. For some problems, like the study of the detailed interaction of an Alfvén wave with an intermediate shock, this may be required, but for other problems less computationally intensive methods may suffice. When intermediate shocks do not arise — in pressure-dominated flows with high upstream plasma β for instance —, shock-capturing methods can safely be used. When intermediate shocks arise shock-capturing methods may still produce relevant results in the following sense. First of all it seems essential that the numerical dissipation is well-behaved. This is generally required for any numerical method and any flow problem, but seems extremely important for the stability of intermediate shocks. The topology of flow solutions depends on the existence of intermediate shocks, which in turn depends on the values of the dissipative parameters. The existence of intermediate shocks is controlled by bifurcation. For large ranges of the dissipative parameters the existence properties of intermediate shocks do not change. This means that flow solutions of a given problem come in classes with the same topology for large ranges of the dissipative parameters. A flow solution obtained by a shock-capturing code with well-behaved numerical dissipation can thus be expected to be generic for large ranges of the dissipative parameters. Such a solution is presumably physically relevant, especially in the case of steady problems without dynamical perturbations. When perturbations and small-time behavior are important in the problem, however, the dissipation mechanism should be specified and shock profiles should be resolved. It has to be admitted that dissipation mechanisms and magnitudes are often not well known for space plasmas or cannot be simulated because the numerical dissipation necessary for stability is much larger. In such cases the use of shock-capturing codes with a well-behaved numerical dissipation may be justified.

Vanishing viscosity limit and ideal solution for the 3D magnetically dominated bow shock flows

The 3D simulations of magnetically dominated bow shock flows that were described in Chaps. 7 and 8 were performed with a shock-capturing numerical code. They are solutions of the MHD equations with a certain unspecified (numerical) dissipation. We did not observe a change in flow solution when we varied grid sizes. We expect that the topology obtained has some general validity for a large range of the dissipative parameters. This should be verified by repeating the calculations for various sets of dissipative parameters with a code which discretizes the dissipative terms and resolves shock profiles.

It is an interesting question what the vanishing viscosity limit solution of these magnetically dominated bow shock flows (e.g. Fig. 7.1) would be. This could be investigated by refining the grid in simulations with a shock-capturing code. We anticipate that in the symmetry plane (xy) the topology would not change, because the reasoning which lead to the topology of Fig. 7.5b and to the break-up of the 1–3 shock at a certain critical angle is independent from the dissipation. The extent of the secondary shock out of the xy plane could possibly depend on the magnitude of the dissipation, but most probably it is also determined by geometrical constraints which do not depend on dissipation. The topology of Fig. 7.1 may thus be the topology of the vanishing viscosity solution.

Another interesting question is what the ideal solution to this flow problem would be. The ideal solution would presumably not contain intermediate shocks [46]. The 1–3 shock segment in the topology of Fig. 7.5b would presumably break up in a fast 1–2 shock followed by other waves. A 3D code without numerical dissipation would be required to investigate this. Numerical investigation of this problem seems to be a daunting task.

We may not exclude the following possibility, however. The conclusion that intermediate shocks are inadmissible in ideal MHD was reached based on stability study in one spatial dimension. The ideal MHD system is strongly degenerate as is for instance clear from the fact that wave speeds can coincide in multiple ways. It is possible that some of the degeneracies are lifted in 2D or 3D and that intermediate shocks would turn out to be admissible in ideal MHD in 2D and 3D. If so, then the topology of Fig. 7.1 may be the topology of the ideal flow solution. The reasoning leading to the topology of Fig. 7.5b is indeed convincing, and it seems not immediately clear why it should not be valid for ideal MHD. The geometrical properties of MHD shocks seem to require the presence of 1–3 intermediate shocks on the leading shock front of a 3D bow shock flow for magnetically dominated upstream parameters, and this could be so also in the ideal MHD case. Study of shock stability beyond the 1D approach has only briefly been touched upon in the literature [105]. The theoretical study of shock stability in multiple dimensions has recently been begun [184].

9.5 Conclusion

We have shown how the planar 2D magnetically dominated bow shock flows around cylinders that were discussed in Chap. 6 form excellent illustrations in 2D of the theory on the admissibility of shocks in planar MHD. The 3D magnetically dominated bow shock flows around spheres that were discussed in Chap. 7 were shown to be excellent illustrations in 3D of the theory on the admissibility of shocks in full MHD. Intermediate shocks had been found previously in 1D and in some 2D simulation results, but the bow shock flows described in Chaps. 6 and 7 are the first clear illustrations in 2D and 3D of the whole variety of intermediate shock phenomena that can arise in MHD flows.

Some authors argue that intermediate shocks cannot be observed in physical systems [107, 35]. Our simulation results of driven bow shock flow problems indicate that intermediate shocks can be formed and can persist in physically relevant flows with small dissipation. Intermediate shocks should thus be observable in physical plasmas.

Chapter 10

Conclusions and outlook

10.1 Conclusions

In this dissertation new results have been presented on the topology of stationary magnetohydrodynamic (MHD) bow shock flows. These findings result from interdisciplinary scientific research in several domains. Using techniques from Computational Fluid Dynamics (CFD), we have developed the PAR-MA (PARallel MAgnetohydrodynamics) code which solves the nonlinear time-dependent MHD equations numerically. Simulation results were validated and interpreted using theoretical concepts which derive from the field of applied mathematics. The simulation results were applied to space physics flows in the solar corona and in the earth's magnetic environment.

In this Section we briefly summarize the main findings described in this dissertation.

10.1.1 Contributions to the physics of MHD plasma flows with shocks

General theory of MHD bow shock flows

It is well-known that supersonic hydrodynamic flow of a neutral gas around a blunt obstacle generates a bow shock in front of the obstacle. For geometrically simple obstacles this bow shock has a single shock front and has a smooth paraboloid-like shape (Fig. 2.4). In an ionized gas or plasma magnetic forces influence the dynamics of the flow. Analogous to the case of a neutral gas, a bow shock is formed for superfast flow of an MHD plasma around an obstacle. When the upstream magnetic field strength is small and thermal or dynamic pressure effects dominate, a single-front bow shock flow is obtained which is morphologically similar to the bow shock in a neutral gas flow (Fig. 7.3).

The new result presented in this dissertation is that when the upstream magnetic field strength is large, intrinsically magnetic effects can alter the bow shock flow topology significantly. For upstream parameter values for which the intrinsically magnetic effect of MHD switch-on shocks occurs — we say that the upstream flow is magnetically dominated —, the leading bow shock front is followed by a secondary shock front of slow and intermediate MHD type which is attached to the leading front. This was shown in numerical simulation results of symmetrical 2D flows around cylinders (Fig. 6.2) and of 3D flows around spheres and paraboloids (Fig. 8.10). In this magnetically dominated parameter regime the bow shock flow thus assumes a complex topology (Fig. 7.5b) involving multiple shock fronts with segments of various MHD shock types.

We have concluded that there are two basic topologies for MHD bow shock flows. For pressure-dominated upstream flows the well-known single-front topology is obtained. For magnetically dominated upstream flows the bow shock flow assumes a complex multiple-front topology which was previously unknown. This result is an important addition to the general theory of MHD bow shock flows [114].

Existence of intermediate and compound shocks

We have clearly identified stationary MHD shock fronts of intermediate type in our 3D MHD simulation results (Fig. 8.13). This finding is relevant for the ongoing debate on the physical existence of intermediate shocks. For a long time it has been commonly believed that intermediate shocks cannot arise in MHD flows and are unphysical [87]. Recently, however, it has been shown theoretically that intermediate shocks can be stable in the dissipative MHD system for wide ranges of the dissipation coefficients [173, 43, 46, 110]. Our simulation results seem to be the first confirmation in 3D that intermediate shocks can indeed exist and persist for small dissipation MHD in a realistic flow configuration.

We have identified compound shocks, which are a manifestation of the non-convex nature of the MHD flux function, in our 2D and 3D simulation results (Figs. 6.25 and 7.20).

Characteristic analysis of 2D MHD flows

We have provided a new systematic derivation of the characteristic properties of stationary 2D MHD flows. We have shown how characteristic analysis can be a useful tool for the physical interpretation of 2D MHD flows and for grid convergence studies. We have applied this analysis to numerical simulation results which illustrate the most basic MHD wave phenomena, and to magnetically dominated bow shock flows with interacting shocks of different types and alternating elliptic and hyperbolic regions (Fig. 6.22).

Applications in space physics

Intrinsically magnetic effects are expected to play a role in many plasma flows with shocks in space physics and astrophysics. We have discussed two examples of bow shock flows in the solar system for which intrinsically magnetic effects can be important.

We predict that the new magnetically dominated complex bow shock flow topology which involves secondary slow shocks arises in shocks induced by fast solar coronal mass ejections (CMEs) propagating out of the solar corona (Fig. 8.3). It seems hard, however, to obtain conclusive observational evidence for this phenomenon given the limitations of present-day observational techniques.

A slow shock is also expected to form in the earth's magnetosheath following the bow shock (Fig. 2.9) when the solar wind is in the magnetically dominated regime for which switch-on shocks can exist. Slow shocks have indeed been observed in the magnetosheath [141]. Our simulation results offer a physically attractive explanation for at least some of these observed slow shocks. Slow shocks are especially likely to form in the magnetosheath during magnetic cloud events. Magnetic clouds are believed to cause magnetic storms of concern to space weather. The characteristic time of the formation of the slow shock and the influence of the complex topology on reconnection processes at the magnetopause are potentially important for the mechanism and timing of magnetic storms. The temporary global reconfiguration of the magnetosheath flow during magnetic cloud events may thus be an important new element in scenarios for magnetic storms.

10.1.2 Numerical simulation of MHD flows with shocks

The use of advanced numerical techniques and fast parallel computers was essential for obtaining the new results on intrinsically magnetic effects in 3D MHD bow shock flows. We have shown that well-developed techniques from Computational Fluid Dynamics which are directly based on the wave properties of the hyperbolic system of equations, can be extended to MHD for the successful simulation of complex flows with multiple shocks of different types. This is not a trivial result, because the MHD system allows for three strongly anisotropic wave modes, whereas only one isotropic wave mode arises in hydrodynamic flows.

Numerical techniques similar to the one implemented in PAR-MA are currently being used in several application codes [118, 162, 124, 117]. When we started our thesis work, however, these techniques were not available, and we have been actively involved in the research on extending CFD techniques to MHD. We have invested a lot of effort in validating the simulation code through grid convergence studies (Fig. 5.8). We believe that such validation should be standard practice, but unfortunately this step is all too often omitted in the field of space physics simulations. These grid convergence studies also show that the efficient technique to treat the $\nabla \cdot \vec{B}$ constraint by adding a source term [118] produces valid solutions. Efficient implementation of the numerical algorithm on massively parallel computers made the simulation of large 3D MHD flow problems possible.

10.2 Outlook

10.2.1 Physics of MHD plasma flows with shocks

The results described in this dissertation regarding MHD bow shock flows can be extended in many ways. We now give a brief indication of some directions for future research.

General theory of MHD bow shock flows

Our study of 3D MHD bow shock topology for pressure-dominated and magnetically dominated upstream flows is not complete because only a limited region of the parameter space has been explored. This study of the general problem of 3D MHD flow around an obstacle deserves further investigation.

More detailed investigation of the turbulent wake behind the cylinder and sphere flows is another interesting topic. MHD turbulence is not a completely unexplored domain of research, but it seems that much remains to be discovered. Models which parametrize MHD turbulence could be developed and could be used in simulations similar to the way they are used in simulations of hydrodynamic flows [167, 101]. It would be interesting to study the stabilizing or destabilizing effect of magnetic fields on turbulent wakes [63].

Existence of intermediate shocks

We have argued that the 3D bow shock topology obtained for magnetically dominated upstream parameters is valid for small dissipation MHD. In our simulations the numerical dissipation plays a role analogous to a physical dissipation. The simulations should be repeated with a well-controlled modeled physical dissipation if we are to interpret the dissipation in a more meaningful way. It would then be interesting to see if it is indeed true that the solution we obtained is reproduced for large ranges of the dissipative parameters, and that the same solution is found in the limit of vanishing dissipation [48]. If a 3D MHD code can be developed which does not introduce any dissipation [48, 35], then it could be investigated what the ideal MHD solution to the 3D bow shock problem could be, which may not contain intermediate shocks as some recent work seems to imply [48, 46, 35]. The small dissipation case would seem the most appropriate to describe physical systems, so the discussion on vanishing dissipation limits and ideal MHD solutions is probably not so relevant for space physics applications [173], but these topics certainly remain interesting mathematical problems.

Applications in space physics

Time-dependent CME flows should be considered in a realistic solar wind background. Short of better observations than currently available, it is not trivial to find a realistic way to initiate a CME in a numerical simulation. Theoretical constraints and considerations are an important guideline in studying the CME initiation problem. Simulations of fast CMEs, preferentially based on theoretically and observationally credible initiation scenarios, could reproduce the formation of the complex bow shock topology with a slow shock following a fast shock. Line of sight integration could be performed on simulation results to mimic coronagraph images, which could be compared to real coronagraph images. Such scientific visualization techniques may contribute to the identification of secondary slow shocks on coronagraph images. It is interesting to know where exactly in the solar corona shocks would be induced by CMEs, and if reconnection flares can also generate shocks. Possible changes in shock types and topology at transitions in the solar wind from low-β to high-β and from subfast to superfast flow are other points of interest.

Time-dependent simulations of the earth's bow shock and magnetosheath flow under varying solar wind conditions should shed some light on how solar wind perturbations propagate through the magnetosheath. The characteristic time of the global reconfiguration of the magnetosheath flow through the formation of slow secondary shocks during magnetic cloud events may be important for magnetic storm scenarios. The influence of the resulting complex magnetic field topology on reconnection at the magnetopause should be investigated in simulations which include the inner magnetosphere and the ionosphere.

Ultimately CME flows in the solar wind and the influence of the CME perturbations on the magnetosphere could be simulated on one large simulation domain stretching from the sun to the earth. This could improve our understanding of CME propagation and of the processes affecting the whole solar-terrestrial environment. It may ultimately lead to simulation codes which can be useful for space weather nowcasting and possibly prediction.

CME-induced shocks and the earth's bow shock are just two examples of MHD shocks in space physics plasmas. The flow topology of cometary, lunar and planetary bow shock flows under magnetically dominated solar wind conditions should be investigated by simulations and observationally. Recent observations reveal that galactic and extragalactic jets may exhibit multiple bow shock fronts. It thus seems that our results on MHD bow shock flow topology may have many unexplored applications in space physics and astrophysics plasma flows.

10.2.2 New numerical simulation techniques

The numerical tools of solution-adaptive grid refinement and implicit time integration seem to be required to be able to tackle flow problems with varying spatial and temporal scales — like the space weather problem described above — efficiently. These tools have not been implemented in the PAR-MA code which was used for the simulations described in this dissertation. Rather than implementing these techniques in the finite volume PAR-MA code in a way which has become quite standard by now, it seems more promising to use new techniques. New generation shock-capturing numerical techniques using multi-dimensional approaches on unstructured grids have recently been developed for the hydrodynamic equations [167]. The unstructured grid approach naturally allows for adaptive refinement of grids. The multi-dimensional approach leads to good shock-capturing using compact numerical stencils. This compactness allows for efficient implicit time integration. A promising beginning has been made to apply this new approach to the MHD system [22]. Additional development is necessary during the coming years, and will probably lead to a numerical code well-suited to tackle space physics simulation problems.

10.2.3 Other directions

Many of the topics described in the two previous Sections are direct extensions of the thesis work and seem worthwhile of further investigation. However, it is sometimes interesting to look a little further and discover some less obvious related subjects which may deserve attention.

The MHD equations form a hyperbolic system. Our work involved numerical techniques and analytical concepts which are especially tailored to hyperbolic systems, and the simulation results give some insight into the physical properties of a hyperbolic system with multiple anisotropic wave modes. It may be interesting to apply this knowledge to other physical systems which are described by hyperbolic equations.

The equations of special relativistic MHD are an obvious candidate. It would be interesting to see if in relativistic MHD intrinsically magnetic effects influence bow shock flows in a way similar to the non-relativistic case. Applications would include the formation of shocks induced by relativistic jets in astrophysical plasmas. The hyperbolic nature of special relativistic MHD is well understood, and it seems that numerical schemes and analytical concepts would carry over smoothly from non-relativistic MHD.

On a next level, the equations of general relativity are also considered to form a hyperbolic system. However, a consistent hyperbolic formulation has not been found yet. The application of symmetrization theory, much like it has been used in the MHD case [7], may help to obtain such a formulation. It has been suggested by T. Barth that the general relativity constraints may be imposed weakly in a numerical scheme much in the same way as the $\nabla \cdot \vec{B}$ constraint is weakly imposed in our MHD scheme. Characteristic theory may help in clarifying the hyperbolic nature of the general relativistic equations, and in interpreting general relativistic flow solutions — also numerically obtained solutions. Recently analytical shock wave solutions of the general relativity equations have been found by matching regions with different metrics [137]. The possible existence of general relativistic shock waves suggests new scenarios for the cosmology of our universe. We have the impression that fascinating discoveries remain to be done in these fields.

The relevance of the results presented in this dissertation for the general class of hyperbolic systems with multiple characteristic waves becomes apparent when we summarize the physical lesson we have learned in this dissertation. We have discovered a new topology for magnetically dominated MHD bow shock flows involving multiple shock fronts with segments of various MHD shock types. The manner in which these various shock types arise on a front or the presence of multiple fronts all relate to the dynamics of information transfer by the MHD characteristic waves to guide the superfast flow around the obstacle. Put in these general terms, the numerical work presented in this dissertation has broadened our physical thinking on bow shock flows in MHD, in particular, and on hyperbolic systems with multiple characteristic waves, in general.

Samenvatting

Het onderwerp van deze thesis situeert zich in de numerische studie van schokfenomenen in magnetohydrodynamische (MHD) plasma's.

Schokken komen veelvuldig voor in gassen en kunnen ervaren worden in alledaagse verschijnselen — een bekend voorbeeld is de schok die veroorzaakt wordt door een vliegtuig dat voortbeweegt met supersonische snelheid. Schokken zijn discontinue sprongen in macroscopische grootheden als snelheid, druk en dichtheid.

Een plasma is een *geïoniseerd* gas, en vertoont een complexer gedrag dan een neutraal gas wegens electromagnetische effecten. Electrische en magnetische velden oefenen anisotropische krachten uit op de *geladen* deeltjes die het plasma vormen, en de lading en de stroom gedragen door de deeltjes beïnvloedt het electrische en magnetische veld. Zoals in neutrale gassen kunnen schokken ook gevormd worden in plasma's, maar schokfenomenen in plasma's vertonen een rijkere complexiteit en veelzijdigheid dan schokken in neutrale gassen. Schokfenomenen in plasma's zijn een actief onderzoeksdomein omdat de fundamentele fysische processen nog niet volledig gekend zijn.

Het grootste deel van de materie in ons zonnestelsel bevindt zich in de plasmatoestand, en plasmaschokken komen veelvuldig voor in ons zonnestelsel. Stroomopwaarts van planeten en kometen worden boogschokken gevormd door de supersonische zonnewind (Fig. 2.9). Snelle massa-ejecties vanuit de corona van de zon veroorzaken schokfronten die de massa-ejecties voorafgaan (Fig. 2.12). Deze ejecta met geassocieerde schokken kunnen zich voortbewegen in de richting van de aarde als magnetische wolken (Fig. 8.6). Magnetische wolken kunnen ernstige verstoringen veroorzaken van het magneetveld van de aarde. Schokfenomenen spelen ook een belangrijke rol in andere astrofysische plasma's (Fig. 2.14) en in laboratorium plasma's.

In de laatste tientallen jaren werden er vele wetenschappelijke ruimtetuigen gelanceerd met als doel het observeren van plasma's in ons zonnestelsel. Drie belangrijke voorbeelden zijn de Ulysses missie die planeten en het interplanetaire medium bestudeert, het Solar and Heliospheric Observatory (SOHO) dat gewijd is aan de studie van de zon, en de

CLUSTER missie die midden-2000 zal galanceerd worden met als doel het observeren van de boogschok en de magnetosfeer van de aarde. Deze ruimtetuigen verschaffen een weelde aan observationele gegevens over schokfenomenen in de plasma's van ons zonnestelsel. Deze observaties tonen vele verschijnselen waarvoor nog geen verklaring voorhanden is. Een beter theoretisch begrip van schokfenomenen in plasma's is nodig voor de interpretatie van deze observationele gegevens.

Er bestaat een hiërarchie van theoretische modellen voor de beschrijving van plasmastromingen met verschillende niveaus van complexiteit. De MHD benadering beschrijft een plasma als een continu electrisch geleidend fluïdum. Deze aanpak houdt geen rekening met microscopische plasmaprocessen die belangrijk kunnen zijn voor de verklaring van sommige fysische fenomenen, maar MHD verschaft een consistente beschrijving met een beheersbare complexiteit van plasmastromingen met schokken. Het MHD model wordt aangenomen in deze thesis.

De resultaten voorgesteld in deze thesis hebben als doel bij te dragen to de algemene theorie van schokfenomenen in MHD plasma's. In het bijzonder wordt de invloed van intrinsiek magnetische effecten op the topologie van boogschokstromingen bestudeerd via numerische simulaties van MHD boogschokstromingen in twee en drie ruimtelijke dimensies. Het probleem wordt bestudeerd in de klassieke configuratie van stationaire boogschokstromingen rond perfect geleidende vaste obstakels — cylinders, bollen en paraboloïde objecten (Fig. 7.1). Deze abstracte context laat toe van de fundamentele fysische effecten te isoleren en illustreert de algemeenheid van de resultaten. Tegelijkertijd zijn echte toepassingen uit de ruimtefysica — bijvoorbeeld de stroming van de supersonische zonnewind rond een niet-gemagnetiseerde planeet — conceptueel nauw verwant aan deze abstracte configuraties. Het is dus niet moeilijk om de practische toepassingen van deze fundamentele abstracte stromingsproblemen voor ogen te houden.

De volgende specifieke onderwerpen worden behandeld in deze thesis.

In de eerste plaats wordt aangetoond dat wanneer het plasma stroomopwaarts van het obstakel magnetisch gedomineerd is, stationaire MHD boogschokstromingen een verrassend complexe topologie vertonen met verschillende interagerende schokken en schoksegmenten van verschillend MHD schok type (Fig. 7.1). We noemen het stroomopwaartse plasma magnetisch gedomineerd — in tegenstelling tot een druk-gedomineerd stroomopwaarts plasma — wanneer magnetische krachten domineren over effecten van thermische en dynamische druk zodanig dat het intrinsiek magnetische fenomeen van de *schakel-aan schok* voorkomt op het boogschokfront. De resulterende boogschock stroming en boogschoktopologie worden ook magnetisch gedomineerd genoemd. De complexe magnetisch gedomineerde boogschoktopologie was tot nog toe ongekend, maar kan verklaard worden met behulp van de geometrische eigenschappen van MHD golven en schokken (Fig. 7.5). Dit resultaat draagt bij tot onze algemene kennis van de fenomenologie van MHD boogschokstromingen. Het toont aan dat er twee fundamentele topologieën bestaan voor MHD boogschok stromingen. Voor druk-gedomineerde stroomopwaartse plasma's de traditionele topologie met één schokfront treedt op die welgekend is van hydrodynamische boogschokstromingen (Fig. 7.3). Magnetisch gedomineerde MHD boogschokstromingen vertonen de nieuwe complexe topologie met verschillende interagerende schokfronten (Fig. 7.1).

Ten tweede wordt er een gedetailleerde analyse gegeven van de simulatieresultaten gebruikmakend van de analytische eigenschappen van de MHD vergelijkingen. Deze analyse bevestigt de aanwezigheid van specifieke niet-lineaire MHD golfverschijnselen — in het bijzonder *intermediaire schokken* (Fig. 7.8 en 7.10) en *samengestelde schokken* (Fig. 6.25 en 7.20) — in de twee-dimensionele (2D) en drie-dimensionele (3D) simulatieresultaten. Er is veel discussie in de literatuur over het bestaan van deze types van schokken. Tot nog toe werden deze types van schokken enkel bestudeerd in één-dimensionele systemen. Onze simulatieresultaten lijken de eerste duidelijke bevestiging te zijn van hun bestaan in 2D en in 3D.

Ten derde wordt er beschreven hoe een robuust en accuraat numeriek programma werd ontwikkeld voor de simulatie van MHD stromingen met schokken. Het PAR-MA (PARallelle MAgnetohydrodynamica) programma simuleert de mathematisch consistente MHD vergelijkingen op massief parallelle computers gebruikmakend van geavanceerde numerieke technieken. Het numerieke schema is afgeleid van beproefde methodes uit de computationele vloeistofmechanica. Via zorgvuldige valideringsstudies wordt aangetoond dat het uitgebreide numerieke schema betrouwbare resultaten berekent. Het gebruik van geavanceerde numerieke methodes en snelle parallelle computers was essentieel voor het verkrijgen van de nieuwe resultaten over magnetische effecten in 2D en 3D MHD boogschokstromingen.

In de vierde plaats wordt er aangetoond hoe de simulatieresultaten belangrijk zijn voor boogschokstromingen met magnetisch gedomineerd stroomopwaarts plasma in ons zonnestelsel. Twee voorbeelden worden besproken, namelijk schokken geïnduceerd door snelle coronale massaejecties die wegpropageren vanuit de corona van de zon (Fig. 8.3), en de boogschok gevormd door de interactie van de soms magnetisch gedomineerde zonnewind met de magnetosfeer van de aarde (Fig. 8.5).

Deze onderwerpen worden als volgt beschreven in de thesis.

Hoofdstuk 1 introduceert kort het algemene onderwerp en de resultaten van de thesis.

Hoofdstuk 2 geeft een breed maar intuïtief overzicht van de fysica van schokverschijnselen in neutrale en geïoniseerde gassen, en van het wetenschappelijke domein van de ruimtefysica dat plasma's bestudeert in ons zonnestelsel. De nieuwe resultaten over MHD boogschokstromingen die besproken worden verderop in de thesis worden kort voorgesteld en er wordt aangegeven waar deze resultaten belangrijk kunnen zijn voor schokverschijnselen in ruimteplasma's.

In hoofdstuk 3 beschrijven we analytische eigenschappen van de ideale MHD vergelijkingen. We presenteren een nieuwe compacte afleiding van de karakteristieke eigenschappen van continue ideale MHD stromingen in twee onafhankelijke variabelen, zowel voor tijdsafhankelijke MHD in één ruimtelijke dimensie, als voor stationaire MHD in twee ruimtelijke dimensies. Deze eigenschappen worden gebruikt voor de analyse van roosterconvergentie van numerieke oplossingen in hoofdstuk 5, en voor de analyse van MHD golfverschijnselen in 2D boogschok stromingen in hoofdstuk 6. We bespreken de eigenschappen van MHD discontinuïteiten. MHD beschrijft drie soorten golven, de snelle golven, de Alfvén golven en de trage golven. Er zijn ook drie verschillende soorten schokken, de snelle, intermediaire en trage schokken. De MHD flux functie heeft de eigenschap van *niet-convexiteit*, waardoor *samengestelde schokken*, die bestaan uit een sonische intermediaire schok voorafgegaan of gevolgd door een rarefactie golf (Fig. 3.14), kunnen voorkomen in MHD stromingen.

In hoofdstuk 4 beschrijven we het PAR-MA programma dat ontwikkeld werd als onderdeel van het thesiswerk. De ruimtelijke discretisatie van de MHD vergelijkingen is gebaseerd op de eindige volume methode op gestructureerde roosters. De tijdsintegratie gebeurt met een expliciet Runge-Kutta algorithme. De $\nabla \cdot \vec{B} = 0$ conditie wordt opgelegd via een bronterm in de MHD vergelijkingen. De implementatie op parallelle computers gebeurt door middel van de MPI bibliotheek. Het PAR-MA programma werd gebruikt voor al de simulaties van 2D en 3D MHD stromingen die voorgesteld worden in deze thesis.

Hoofdstuk 5 bevat een zorgvuldige valideringsstudie van de gebruikte numerieke technieken. Verscheidene 2D modelstromingen die fundamentele golfverschijnselen beschrijven worden gesimuleerd op roosters met verschillende resolutie (Fig. 5.7), en gebruik makend van de karakteristieke eigenschappen van 2D MHD stromingen wordt de convergentie van het numerieke schema in functie van de roosterresolutie aangetoond (Fig. 5.8).

In hoofdstuk 6 worden 2D boogschokstromingen rond perfect geleidende cylinders besproken. In deze 2D stromingen wordt het magneetveld overal parallel aan de plasmasnelheid genomen. Een parameterstudie toont aan dat intrinsiek magnetische effecten de topologie van de boogschokstromingen substantieel wijzigen wanneer het stroomopwaartse plasma magnetisch gedomineerd is (Fig. 6.16). In de nieuwe magnetisch gedomineerde topologie wordt het leidende schokfront met segmenten van snel en intermediair type gevolgd door secundaire schokfronten van intermediair en traag type (Fig. 6.9). De aanwezigheid van stationaire samengestelde schokken in deze stromingen wordt aangetoond met behulp van de karakteristieke eigenschappen van de MHD vergelijkingen (Fig. 6.25).

In hoofdstuk 7 worden 3D MHD boogschokstromingen rond een sfeer besproken. Wanneer het stroomopwaartse plasma magnetisch gedomineerd is vertoont de boogschokstroming een nieuwe topologie met het leidende schokfront van snel en intermediair type gevolgd door een secundair schokfront van intermediair en traag type (Fig. 7.1).

In hoofdstuk 8 bespreken we hoe de nieuwe resultaten over boogschok stromingen met magnetisch gedomineerde stroomopwaartse plasma's belangrijk zijn voor twee voorbeelden van boogschokstromingen in ons zonnestelsel. Redenering volgens fundamentele fysische principes toont aan dat snelle coronale massa-ejecties voorafgegaan moeten worden door boogschokken die de nieuwe magnetisch gedomineerde boogschoktopologie kunnen aannemen. Coronagraaf observaties geven indirecte aanwijzingen dat dit inderdaad het geval is (Fig. 8.2), maar voor meer overtuigende observationele bewijzen moet gewacht worden op toekomstige stereoscopische waarnemingen uitgevoerd door twee satellieten. Zulke waarnemingen laten toe van 3D stromingen te reconstrueren via tomografische technieken. De zonnewind in de buurt van de aarde is meestal druk-gedomineerd, zodat een enkelvoudige boogschok wordt geobserveerd stroomopwaarts van de aarde (Fig. 8.5). De zonnewind kan echter ook magnetisch gedomineerd zijn, en de simulatieresultaten voor 3D magnetisch gedomineerde boogschokstromingen suggereren dat onder die omstandigheden de boogschok van de aarde kan gevolgd worden door een trage schok (Fig. 8.10). Trage schokken werden inderdaad geobserveerd na de leidende boogschok van de aarde, maar ook hier moeten toekomstige meer gedetailleerde observaties bevestigen of de nieuwe boogschoktopologie van de simulaties inderdaad optreedt.

Het onderwerp van het bestaan van intermediaire schokken wordt besproken in hoofdstuk 9. Er werd lang aangenomen dat intermediaire schokken niet kunnen voorkomen in MHD stromingen omdat ze voor ideale MHD onstabiel zijn tegen generische perturbaties. Recent werd echter ontdekt dat intermediaire schokken stabiel kunnen zijn tegen kleine perturbaties in dissipatieve MHD. Intermediaire schokken werden tevoren gevonden in 1D numerieke simulatieresultaten, maar de boogschokstromingen besproken in deze thesis zijn de eerste duidelijke bevestiging van het bestaan van intermediaire schokken in 2D (Fig. 6.13) en 3D (Fig. 7.8 en 7.10) MHD stromingen. We voorspellen dat een intermediair schoksegment kan geobserveerd worden in de boogschok van de aarde wanneer de zonnewind magnetisch gedomineerd is.

In hoofdstuk 10 formuleren we onze conclusies en beschrijven we mogelijk toekomstig werk. Het belangrijkste resultaat voorgesteld in deze thesis is dat voor magnetisch gedomineerde MHD boogschokstromingen een nieuwe topologie optreedt met verschillende opeenvolgende schokken en segmenten van verschillenden MHD schoktypes (Fig. 7.1). De manier waarop deze verschillende schoktypes verschijnen op een schokfront en de aanwezigheid van verschillende opeenvolgende schokfronten zijn bepaald door de dynamica van de informatietransfer door de karakteristieke MHD golven om de supersone stroming rond het obstakel te leiden. Vanuit dit algemene gezichtspunt bekeken heeft het numerieke werk gepresenteerd in deze thesis ons fysisch denken verrijkt over boogschokstromingen in MHD in het bijzonder, en over hyperbolische systemen met meerdere karakteristieke golven in het algemeen.

Bibliography

[1] D. Vanden Abeele and H. Deconinck. Development of a Godunov-type solver for 2D ideal MHD problems. Technical Report 13, von Karman Institute, 1995.

[2] A. Akhiezer, G. Liubarskii, and R. Polovin. The stability of shock waves in magnetohydrodynamics. *Sov. Phys. JETP*, 35:507–511, 1959.

[3] A. I. Akhiezer, I. A. Akhiezer, R. V. Polovin, A. G. Sitenko, and K. N. Stepanov. *Plasma electrodynamics*, volume 1. Pergamon Press, Oxford, 1975.

[4] J. Edward Anderson. *Magnetohydrodynamic shock waves.* PhD thesis, M. I. T., 1963.

[5] D. S. Balsara and D. S. Spicer. A staggered mesh algorithm using high order Godunov fluxes to ensure solenoidal magnetic fields in magnetohydrodynamic simulations. *J. Comput. Phys.*, 149:270–292, 1999.

[6] A. A. Barmin, A. G. Kulikovskiy, and N. V. Pogorelov. Shock-capturing approach and nonevolutionary solutions in magnetohydrodynamics. *J. Comput. Phys.*, 126:77–90, 1996.

[7] Timothy J. Barth. Numerical methods for gasdynamic systems on unstructured meshes. In D. Kröner, M. Ohlberger, and C. Rohde, editors, *An introduction to recent developments in theory and numerics for conservation laws*, Lecture notes in Computational Science and Engineering, pages 195–284. Springer-Verlag, Berlin, 1998.

[8] D. Biskamp. *Nonlinear Magnetohydrodynamics.* Cambridge University Press, Cambridge, 1993.

[9] B. Bottin, M. Carbonaro, S. Zemsch, and G. Degrez. Aerothermodynamic design of an inductively-coupled plasma wind tunnel. *AIAA Paper*, 97-2498, 1997.

[10] J. U. Brackbill and D. C. Barnes. The effect of nonzero $\nabla \cdot \vec{B}$ on the numerical solution of the magnetohydrodynamic equations. *J. Comput. Phys.*, 35:426–430, 1980.

[11] M. Brio and C. C. Wu. Characteristic fields for the equations of magnetohydrodynamics. *Contemporary mathematics*, 60:19–23, 1987.

[12] M. Brio and C. C. Wu. An upwind differencing scheme for the equations of ideal magnetohydrodynamics. *J. Comput. Phys.*, 75:400–422, 1988.

[13] R. Broglia, M. Manna, H. Deconinck, and G. Degrez. Development and validation of an axi-symmetric Navier-Stokes solver for hypersonic flows. Technical Report 188, von Karman Institute, 1995.

[14] J. T. Burkepile and O. C. St. Cyr. A revised and expanded catalogue of mass ejections observed by the Solar Maximum Mission coronagraph. Technical Report NCAR/TN-369+STR, National Center for Atmospheric Research, Boulder, Colorado, USA, 1993.

[15] L. Burlaga, R. Fitzenreiter, R. Lepping, K. Ogilvie, A. Szabo, A. Lazarus, J. Steinberg, G. Gloeckler, R. Howard, D. Michels, C. Farrugia, R. P. Lin, and D. E. Larson. A magnetic cloud containing prominence material: January 1997. *J. Geophys. Res.*, 103(A1):277–285, 1998.

[16] S. Cable and Y. Lin. Three-dimensional MHD simulations of interplanetary rotational discontinuities impacting the Earth's bow shock and magnetosheath. *J. Geophys. Res.*, 103(A12):29,551–29,567, 1998.

[17] S. Cable and R. S. Steinolfson. Three-dimensional MHD simulations of the interaction between Venus and the solar wind. *J. Geophys. Res.*, 100(A11):21,645–21,658, 1995.

[18] J. K. Chao. Intermediate shocks: observations. *Adv. Space Res.*, 15(8/9):521–530, 1995.

[19] J. Contopoulos. General axisymmetric magnetohydrodynamic flows: theory and solutions. *ApJ*, 460:185–198, 1996.

[20] R. Courant and K. O. Friedrichs. *Supersonic flow and shock waves.* Interscience publishers, New York, 1948.

[21] R. Courant and D. Hilbert. *Methods of mathematical physics*, volume 2. Interscience publishers, New York, 1962.

[22] A. Csik, H. Deconinck, and S. Poedts. Monotone residual distribution schemes for the ideal 2D magnetohydrodynamic equations on unstructured grids. *AIAA*, paper:99–3325, 1999.

[23] W. Dai and P. R. Woodward. An approximate Riemann solver for ideal magnetohydrodynamics. *J. Comput. Phys.*, 111:354–372, 1994.

[24] W. Dai and P. R. Woodward. Extension of the piecewise parabolic method (PPM) to multidimensional ideal magnetohydrodynamics. *J. Comput. Phys.*, 115:485, 1994.

[25] W. Dai and P. R. Woodward. Interactions between magnetohydrodynamical shocks and denser clouds. *Astrophys. J.*, 436:776–783, 1994.

[26] W. Dai and P. R. Woodward. On the divergence-free condition and conservation laws in numerical simulations for supersonic magnetohydrodynamic flows. *Astrophys. J.*, 494:317–335, 1998.

[27] D.Burgess. Collisionless shocks. In M. G. Kivelson and C. T. Russell, editors, *Introduction to space physics*, pages 129–163. Cambridge University Press, Cambridge, 1995.

[28] C. R. DeVore. Flux-corrected transport techniques for multidimensional compressible magnetohydrodynamics. *J. Comput. Phys.*, 92:142, 1991.

[29] M. A. Dopita, I. Evans, and R. D. Schwartz. Herbig-haro objects 46 and 47 - evidence for bipolar ejection from a young star. *Astrophys. J. Lett.*, 263:L73–L77, 1982.

[30] M. Van Dyke. *An Album of Fluid Motion.* Parabolic Press, Stanford, 1982.

[31] G. E. Brueckner et al. The large angle spectroscopic coronagraph (LASCO). *Solar Phys.*, 162:357–402, 1995.

[32] G. M. Simnett et al. LASCO observations of disconnected magnetic structures out to beyond 28 solar radii during coronal mass ejections. *Solar Phys.*, 175(2), 1997.

[33] C. R. Evans and J. F. Hawley. Simulation of magnetohydrodynamic flows: a constrained transport method. *Astrophys. J.*, 332:659–677, 1988.

[34] S. A. E. G. Falle. Some notes on magnetohydrodynamics. 1994.

[35] S. A. E. G. Falle and S. S. Komissarov. On the inadmissibility of non-evolutionary shocks. *Submitted to J. Plasma Phys.*, 1999.

[36] S. A. E. G. Falle, S. S. Komissarov, and P. Joarder. A multidimensional upwind scheme for magnetohydrodynamics. *Mon. Not. R. Astron. Soc.*, 297:265–277, 1998.

[37] W. C. Feldman, D. N. Baker, S. J. Bame, J. Birn, J. T. Gosling, , Jr. E. W. Hones, and S. J. Schwartz. Slow-mode shocks: a semipermanent feature of the distant geomagnetic tail. *J. Geophys. Res.*, 90(A1):233–240, 1985.

[38] W. C. Feldman, S. J. Schwartz, S. J. Bame, D. N. Baker, J. Birn, J. T. Gosling, Jr. E. W. Hones, J. A. Slavin, E. J. Smith, and R. D. Zwickl. Evidence for slow-mode shocks in the deep geomagnetic tail. *Geophys. Res. Lett.*, 11(6):599–602, 1984.

[39] T. G. Forbes and E. R. Priest. A comparison of analytical and numerical models for steadily driven magnetic reconnection. *Rev. Geophysics*, 25(8):1583–1607, 1987.

[40] H. Freistuehler. Instability of vanishing viscosity approximation to hyperbolic systems of conservation laws with rotational invariance. *J. Differential Equations*, 87(2):205–226, 1990.

[41] H. Freistuehler. Linear degeneracy and shock waves. *Math. Z.*, 207:583–596, 1991.

[42] H. Freistuehler. Rotational degeneracy of hyperbolic systems of conservation laws. *Arch. Rational Mech. Anal.*, 113:39–64, 1991.

[43] H. Freistuehler. Some remarks on the structure of intermediate magnetohydrodynamic shocks. *J. Geophys. Res.*, 96(A3):3825–3827, 1991.

[44] H. Freistuehler. Dynamical stability and vanishing viscosity: a case-study of a non-strictly hyperbolic system. *Comm. Pure. Appl. Math.*, 45:561–582, 1992.

[45] H. Freistuehler. Hyperbolic systems of conservation laws with rotationally equivariant flux function. *Mat. Aplic. Comp.*, 11(2):167–188, 1992.

[46] H. Freistuehler. Contributions to the mathematical theory of magnetohydrodynamic shock waves. In X.-X. Ding and T.-P. Liu, editors, *Nonlinear evolutionary partial differential equations*, volume 3 of *AMS/IP Studies in Advanced Mathematics*, pages 175–187. AMS/IP, 1997.

[47] H. Freistuehler. Small amplitude intermediate magnetohydrodynamic shock waves. *Phys. Scripta*, T74:26–29, 1998.

[48] H. Freistuehler and E. B. Pitman. A numerical study of a rotationally degenerate hyperbolic system. Part 1. The Riemann problem. *J. Comput. Phys.*, 100:306–321, 1992.

[49] H. Freistuehler and P. Szmolyan. Existence and bifurcation of viscous profiles for all intermediate magnetohydrodynamic shock waves. *SIAM J. Math. Anal.*, 26(1):112–128, 1995.

[50] S. E. Gibson and B. C. Low. A time-dependent three-dimensional hydromagnetic model of the coronal mass ejection. *ApJ*, 1998.

[51] S. K. Godunov. Symmetrical form of the magnetohydrodynamic equations. *report of the Computer center of the Siberian branch of the USSR Academy of Sciences*, pages 26–34, 1972.

[52] S. K. Godunov. In C. Carasso, P.-A. Raviart, and D. Serre, editors, *Nonlinear hyperbolic problems: Proceedings of an advanced research workshop*, volume 1270 of *Lecture Notes in Mathematics*, Springer-Verlag, Berlin, 1987.

[53] J. P. Goedbloed and A. Lifshitz. Stationary symmetric magnetohydrodynamic flows. *Phys. Plasmas*, 4(10):3544–3564, 1997.

[54] T. I. Gombosi. *Physics of the space environment.* Atmospheric and space science series. Cambridge University Press, Cambridge, 1998.

[55] T. I. Gombosi, K. G. Powell, and D. L. De Zeeuw. Axisymmetric modeling of cometary mass loading on an adaptively refined grid: MHD results. *J. Geophys. Res.*, 99(A11):21,525–21,539, 1994.

[56] T. I. Gombosi, D. L. De Zeeuw, R. L. Haberli, and K. G. Powell. Three-dimensional multiscale MHD model of cometary plasma environments. *J. Geophys. Res.*, 101:15233–15253, 1996.

[57] J. A. Gonzalez-Esparza, M. Neugebauer, E. J. Smith, and J. L. Phillips. Radial evolution of ejecta characteristics and transient shocks - ulysses in-ecliptic observations. *J. Geophys. Res.*, 103:4767, 1998.

[58] N. Gopalswamy, Y. Hanaoka, T. Kosugi, R. P. Lepping, J. T. Steinberg, S. Plunkett, R. A. Howard, B. J. Thompson, J. Gurman, G. Ho, N. Nitta, and H. S. Hudson. On the relationship between coronal mass ejections and magnetic clouds. *Geophys. Res. Lett.*, 25:2485–2488, 1998.

[59] H. Grad. Reducible problems in magneto-fluid dynamic steady flows. *Revs. Modern Phys.*, 32(4):830–847, 1960.

[60] W. Gropp, E. Lusk, and A. Skjellum. *Using MPI.* Scientific and Engineering Computation. MIT Press, Cambridge, Massachusetts, 1994.

[61] E. Hameiri. The equilibrium and stability of rotating plasmas. *Phys. Fluids*, 26(1):230–237, 1983.

[62] M. Heinemann and S. Olbert. Axisymmetric ideal MHD stellar wind flow. *J. Geophys. Res.*, 83:2457–2460, 1978.

[63] R. D. Henderson. Adaptive spectral element methods for turbulence and transition. In H. Deconinck and T. J. Barth, editors, *High order discretization methods in computational fluid dynamics*, von Karman Institute Lecture Series. 1998.

[64] T. E. Holzer. Interaction between the solar wind and the interstellar medium. *Annu. Rev. Astron. Astrophys.*, 27:199–234, 1989.

[65] G. Hornig. *Zur kovarianten Formulierung der magnetischen Rekonnexion.* PhD thesis, Ruhr-Universität Bochum, 1997.

[66] R. A. Howard, Jr. N. R. Sheely, M. J. Koomen, and D. J. Michels. Coronal mass ejections: 1979-1981. *J. Geophys. Res.*, 90:8173–8191, 1985.

[67] A. J. Hundhausen. The solar wind. In M. G. Kivelson and C. T. Russell, editors, *Introduction to space physics*, pages 91–128. Cambridge University Press, Cambridge, 1995.

[68] A. J. Hundhausen. Coronal mass ejections. In Keith T. Strong, Julia L. R. Saba, Bernhard M. Haisch, and Joan T. Schmelz, editors, *The many faces of the sun*, pages 143–200. Springer-Verlag, New York, 1998.

[69] A. J. Hundhausen, J. T. Burkepile, and O. C. St. Cyr. Speeds of coronal mass ejections: SMM observations from 1980 and 1984-1989. *J. Geophys. Res.*, 99(A4):6543–6552, 1994.

[70] A. Jeffrey. *Magnetohydrodynamics.* Oliver & Boyd, Edinburgh, 1966.

[71] A. Jeffrey and T. Taniuti. *Non-linear wave propagation.* Academic Press, New York, 1964.

[72] H. Ji, M. Yamada, and S. Hsu R. Kulsrud. Experimental test of the Sweet-Parker model of magnetic reconnection. *Phys. Rev. Lett.*, 80(15):3256–3259, 1998.

[73] D. E. Jones, E. J. Smith, J. A. Slavin, B. T. Tsurutani, G. L. Siscoe, and D. A. Mendis. The bow wave of comet Giacobini-Zinner: ICE magnetic field observations. *Geophys. Res. Lett.*, 13(3):243–246, 1986.

[74] K. Kabin, T. I. Gombosi, D. L. De Zeeuw, K. G. Powell, and P. L. Israelevich. Interaction of the Saturnian magnetosphere with Titan: results of a three-dimensional MHD simulation. *To appear in J. Geophys. Res.*, 1999.

[75] M. L. Kaiser, M. J. Reiner, N. Gopalswamy, R. A. Howard, O. C. St. Cyr, B. J. Thompson, and J.-L. Bougeret. Type II radio emissions in the frequency range from 1–14 Mhz associated with the April 7, 1997 solar event. *Geophys. Res. Lett.*, 25(14):2501–2504, 1998.

[76] H. Karimabadi. Physics of intermediate shocks: a review. *Adv. Space Res.*, 15(8/9):507–520, 1995.

[77] H. Karimabadi, D. Krauss-Varban, and N. Omidi. Kinetic structure of intermediate shocks: implications for the magnetopause. *J. Geophys. Res.*, 100(A7):11,957–11,979, 1995.

[78] H. Karimabadi and N. Omidi. Hybrid simulations of intermediate shocks: coplanar and noncoplanar solutions. *Geophys. Res. Lett.*, 19(17):1723–1726, 1992.

[79] Y. Kato and T. Taniuti. Hydromagnetic plane steady flow in compressible ionized gases. *Prog. Theor. Phys.*, 21(4):606–612, 1959.

[80] C. F. Kennel, R. D. Blandford, and P. Coppi. MHD intermediate shock discontinuities. Part 1. Rankine-Hugoniot conditions. *J. Plasma Physics*, 42:299–319, 1989.

[81] C. F. Kennel, R. D. Blandford, and C. C. Wu. Structure and evolution of small-amplitude intermediate shock waves. *Phys. Fluids B*, 2(2):253–269, 1990.

[82] R. Keppens and J. P. Goedbloed. Numerical simulations of stellar winds: polytropic models. *Astron. Astrophys.*, 343:251–260, 1998.

[83] R. Keppens, G. Toth, M. A. Botchev, and A. Van Der Ploeg. Implicit and semi-implicit schemes: algorithms. *Int. J. Numer. Meth. Fluids*, 30:335–352, 1999.

[84] M. G. Kivelson and C. T. Russell. *Introduction to space physics.* Cambridge University Press, Cambridge, 1995.

[85] A. G. Kulikovskiy and G. A. Lyubimov. *Magnetohydrodynamics.* Addison-Wesley, Reading, MA, 1965.

[86] R. M. Kulsrud. Magnetic reconnection in a magnetohydrodynamic plasma. *Phys. Plasmas*, 5(5):1599–1606, 1998.

[87] L. D. Landau and E. M. Lifshitz. *Electrodynamics of continuous media.* Pergamon Press, Oxford, 1984.

[88] P. D. Lax. Hyperbolic systems of conservation laws II. *Comm. Pure Appl. Math.*, 10:537–566, 1957.

[89] L. C. Lee, L. Huang, and J. K. Chao. On the stability of rotational discontinuities and intermediate shocks. *J. Geophys. Res.*, 94(A7):8813–8825, 1989.

[90] R. J. Leveque. *Numerical methods for conservation laws.* Lectures in Mathematics ETH Zurich. Birkhauser-Verlag, Basel, 1992.

[91] R. J. Leveque. Nonlinear conservation laws and finite volume methods for astrophysical fluid flow. In O. Steiner and A. Gautschy, editors, *Computational methods for astrophysical fluid flow.* Springer-Verlag, Berlin, 1998.

[92] M. A. Liberman and A. L. Velikovich. *Physics of shock waves in gases and plasmas*, volume 19 of *Springer Series in Electrophysics.* Springer-Verlag, Berlin, 1985.

[93] A. Lifshitz and J. P. Goedbloed. Transonic magnetohydrodynamic flows. *J. Plasma Physics*, 58(1):61–99, 1997.

[94] Y. Lin and L. C. Lee. Study of the dayside reconnection layer in resistive MHD and hybrid models. *J. Geophys. Res.*, 98(A3):3919–3934, 1993.

[95] Y. Lin and L. C. Lee. Reconnection layer at the flank magnetopause in the presence of shear flow. *Geophys. Res. Lett.*, 21(10):855–858, 1994.

[96] Y. Lin, L. C. Lee, and C. F. Kennel. The role of intermediate shocks in magnetic reconnection. *Geophys. Res. Lett.*, 19(3):229–232, 1992.

[97] Y. Lin, D. W. Swift, and L. C. Lee. Simulation of pressure pulses in the bow shock and magnetosheath driven by variations in interplanetary magnetic field direction. *J. Geophys. Res.*, 101(A12):27,251–27,269, 1996.

[98] Y. Lin and H. Xie. Formation of reconnection layer at the dayside magnetopause. *Geophys. Res. Lett.*, 24(24):3145–3148, 1997.

[99] T. J. Linde. *A three-dimensional adaptive multifluid MHD model of the heliosphere.* PhD thesis, University of Michigan, 1998.

[100] Timur J. Linde, Tamas I. Gombosi, Philip L. Roe, Kenneth G. Powell, and Darren L. De Zeeuw. Heliosphere in the magnetized local interstellar medium: Results of a three-dimensional MHD simulation. *J. Geophys. Res.*, 103(A2):1889–1904, 1998.

[101] H.-L. Liu and M. E. Hagan. Local heating/cooling of the mesosphere due to gravity wave and tidal coupling. *Geophys. Res. Lett.*, 25:2941, 1998.

[102] T.-P. Liu. On the viscosity criterion for hyperbolic conservation laws. In M. Shearer, editor, *Viscous profiles and numerical methods for shock waves*, Siam Proceedings Series, pages 105–114. SIAM, Philadelphia, 1991.

[103] T.-P. Liu and Z. Xin. Overcompressive shock waves. In B. L. Keyfitz and M. Shearer, editors, *Nonlinear evolution equations that change type*, The IMA volumes in mathematics and its applications, pages 139–145. Springer-Verlag, Berlin, 1990.

[104] B. C. Low. Solar activity and the corona. *Solar Phys.*, 167:217–265, 1996.

[105] G. S. S. Ludford. The structure of a hydromagnetic shock in steady plasma motion. *J. Fluid Mech.*, 5:67–80, 1959.

[106] M. Manna. *A three dimensional high resolution compressible flow solver.* PhD thesis, Universite Catholique de Louvain, 1992.

[107] S. A. Markovskii. Nonevolutionary discontinuous magnetohydrodynamic flows in a dissipative medium. *Phys. Plasmas*, 5(7):2596–2604, 1998.

[108] E. Morano, R. Sanders, and M.-C. Druguet. Multidimensional dissipation for upwind schemes: stability and applications to gas dynamics. *Preprint*, 1997.

[109] R. S. Myong and P. L. Roe. Shock waves and rarefaction waves in magnetohydrodynamics. Part 1. A model system. *J. Plasma Physics*, 58:485–519, 1997.

[110] R. S. Myong and P. L. Roe. Shock waves and rarefaction waves in magnetohydrodynamics. Part 2. The MHD system. *J. Plasma Physics*, 58:521–552, 1997.

[111] R. S. Myong and P. L. Roe. On Godunov-type schemes for magnetohydrodynamics. 1. A model system. *J. Comput. Phys.*, 147:545–567, 1998.

[112] N. Omidi, H. Karimabadi, and D. Krauss-Varban. Hybrid simulation of the curved dayside magnetopause during southward IMF. *Geophys. Res. Lett.*, 25(17):3273–3276, 1998.

[113] I. Percival and D. Richards. *Introduction to dynamics.* Cambridge University Press, Cambridge, 1982.

[114] S. M. Petrinec and C. T. Russell. Hydrodynamic and MHD equations across the bow shock and along the surfaces of planetary obstacles. *Space Sci. Rev.*, 79:757–791, 1997.

[115] J. L. Phillips, S. J. Bame, M. F. Thomsen, B. E. Goldstein, and E. J. Smith. Ulysses plasma observations in the Jovian magnetosheath. *J. Geophys. Res.*, 98(A12):21,189–21,202, 1993.

[116] S. Poedts and E. Schwartz. Computation of the ideal-MHD continuous spectrum in axisymmetric plasmas. *Journal of Computational Physics*, 105:165–168, 1993.

[117] N. V. Pogorelov and T. Matsuda. Influence of the interstellar magnetic field direction on the shape of the global heliopause. *J. Geophys. Res.*, 103(A1):237–245, 1998.

[118] K. G. Powell, P. L. Roe, R. S. Myong, T. I. Gombosi, and D. L. De Zeeuw. An upwind scheme for magnetohydrodynamics. *AIAA Paper*, 95-1704-CP, 1995.

[119] E.R. Priest. *Solar Magnetohydrodynamics.* Geophysics and Astrophysics Monographs. D. Reidel Publishing Company, Dordrecht, 1982.

[120] K. B. Quest. Theory and simulation of collisionless parallel shocks. *J. Geophys. Res.*, 93(A9):9649–9680, 1988.

[121] James J. Quirk. A contribution to the great Riemann solver debate. *Int. J. Numer. Methods Fluids*, 18:555–574, 1994.

[122] J. Raeder, J. Berchem, and M. Ashour-Abdalla. The Geospace Environment Modeling grand challenge: results from a Global Geospace Circulation Model. *J. Geophys. Res.*, 103:14,787, 1998.

[123] H. U. Rahman, G. Yur, G. Wong, and R. S. White. Laboratory simulation of the large-scale Birkeland current system in the polar region with northward interplanetary magnetic field. *J. Geophys. Res.*, 94(A6):6873–6878, 1989.

[124] R. Ratkiewicz, A. Barnes, G. A. Molvik, J. R. Spreiter, S. S. Stahara, M. Vinokur, and S. Venkateswaran. Effect of varying strength and orientation of local interstellar magnetic field on configuration of exterior heliosphere: 3D MHD simulations. *Astron. Astrophys.*, 335:363–369, 1998.

[125] M. J. Reiner, M. L. Kaiser, J. Fainberg, and R. G. Stone. A new method for studying remote type ii radio emissions from coronal mass ejection-driven shocks. *J. Geophys. Res.*, 103:29651, 1998.

[126] B. Reipurth and S. Heathcote. The jet and energy source of HH 46/47. *Astron. Astrophys.*, 246:511–534, 1991.

[127] P. L. Roe and D. S. Balsara. Notes on the eigensystem of magnetohydrodynamics. *SIAM J. Appl. Math.*, 56:57–67, 1996.

[128] D. Ryu and T. W. Jones. Numerical magnetohydrodynamics in astrophysics: algorithm and tests for one-dimensional flow. *Astrophys. J.*, 442:228–258, 1995.

[129] D. Ryu, T. W. Jones, and A. Frank. Numerical magnetohydrodynamics in astrophysics: algorithm and tests for multidimensional flow. *Astrophys. J.*, 452:785–796, 1995.

[130] J. Safrankova, Z. Nemecek, L. Prech, G. Zastenker, K. I. Paularena, N. Nikolaeva, M. Nozdrachev, A. Skalsky, and T. Mukai. The January 10–11, 1997 magnetic cloud: multipoint measurements. *Geophys. Res. Lett.*, 25(14):2549–2552, 1998.

[131] T. Sakurai. Magnetohydrodynamic solar/stellar wind models. *Comput. Phys. Rep.*, 12:247, 1990.

[132] T. Sato, T. Hayashi, K. Watanabe, R. Horiuchi, M. Tanaka, N. Sawairi, and K. Kusano. Role of compressibility on driven magnetic reconnection. *Phys. Fluids B*, 4(2):450–457, 1992.

[133] M. Scholer. Asymmetric time-dependent and stationary magnetic reconnection at the dayside magnetopause. *J. Geophys. Res.*, 94(A11):15,099–15,111, 1989.

[134] M. Scholer and R.-F. Lottermoser. On the kinetic structure of the magnetotail reconnection layer. *Geophys. Res. Lett.*, 25(17):3281–3284, 1998.

[135] C. Schwab. hp-fem for fluid flow simulation. In H. Deconinck and T. J. Barth, editors, *High order discretization methods in computational fluid dynamics*, von Karman Institute Lecture Series. 1998.

[136] Jr. Sheeley, N. R., R. A. Howard, D. J. Michels, M. J. Koomen, R. Schwenn, K. H. Muehlhaeuser, and H. Rosenbauer. Coronal mass ejections and interplanetary shocks. *J. Geophys. Res.*, 90:163–175, 1985.

[137] J. Smoller and B. Temple. Shock-wave solutions in closed form and the Oppenheimer–Snyder limit in general relativity. *SIAM Journal on Applied Mathematics*, 58(1):15–33, 1998.

[138] P. Song and C. T. Russell. What do we really know about the magnetosheath. *Adv. Space Res.*, 20(4/5):747–765, 1997.

[139] P. Song, C. T. Russell, T. I. Gombosi, J. R. Spreiter, S. S. Stahara, and X. X. Zhang. On the processes in the terrestrial magnetosheath, 1: scheme development. *To appear in J. Geophys. Res.*, 1999.

[140] P. Song, C. T. Russell, J. T. Gosling, M. F. Thomsen, and R. C. Elphic. Observations of the density profile in the magnetosheath near the stagnation streamline. *Geophys. Res. Lett.*, 17(11):2035–2038, 1990.

[141] P. Song, C. T. Russell, and M. F. Thomsen. Slow mode transition in the frontside magnetosheath. *J. Geophys. Res.*, 97(A6):8295–8305, 1992.

[142] P. Song, C. T. Russell, X. X. Zhang, S. S. Stahara, J. R. Spreiter, and T. I. Gombosi. On the processes in the terrestrial magnetosheath, 2: case study. *To appear in J. Geophys. Res.*, 1999.

[143] J. R. Spreiter and S. S. Stahara. The location of planetary bow shocks: a critical overview of theory and observations. *Adv. Space Res.*, 15(8/9):433–449, 1995.

[144] R. S. Steinolfson and S. Cable. Venus bow shocks at unusually large distances from the planet. *Geophys. Res. Lett.*, 20(8):755–758, 1993.

[145] R. S. Steinolfson and A. J. Hundhausen. Concave-outward slow shocks in coronal mass ejections. *J. Geophys. Res.*, 95:15,251, 1990.

[146] R. S. Steinolfson and A. J. Hundhausen. Coronal mass ejection shock fronts containing the two types of intermediate shocks. *J. Geophys. Res.*, 95(A12):20,693–20,699, 1990.

[147] R. S. Steinolfson and A. J. Hundhausen. MHD intermediate shocks in coronal mass ejections. *J. Geophys. Res.*, 95(A5):6389–6401, 1990.

[148] H. De Sterck, A. Csik, D. Vanden Abeele, S. Poedts, and H. Deconinck. Stationary two-dimensional magnetohydrodynamic flows with shocks: characteristic analysis and grid convergence study. *J. Comput. Phys.*, 2000. in press.

[149] H. De Sterck, H. Deconinck, S. Poedts, and D. Roose. A bow shock flow containing (almost) all types of ('exotic') MHD discontinuities. In *Proceedings of the Seventh International Conference on Hyperbolic Problems*, pages 195–204, Birkhauser-Verlag, Basel, 1998.

[150] H. De Sterck, B. C. Low, and S. Poedts. Complex magnetohydrodynamic bow shock topology in field-aligned low-β flow around a perfectly conducting cylinder. *Phys. Plasmas*, 5(11):4015–4027, 1998.

[151] H. De Sterck, B. C. Low, and S. Poedts. Characteristic analysis of a complex two-dimensional magnetohydrodynamic bow shock flow with steady compound shocks. *Phys. Plasmas*, 6(3):954–969, 1999.

[152] H. De Sterck and S. Poedts. Field-aligned magnetohydrodynamic bow shock flows in the switch-on regime. Parameter study of the flow around a cylinder and results for the axi-symmetrical flow over a sphere. *Astron. Astrophys.*, 343:641–649, 1999.

[153] H. De Sterck and S. Poedts. Stationary slow shocks in the magnetosheath for solar wind conditions with $\beta < 2/\gamma$: Three-dimensional MHD simulations. *J. Geophys. Res.*, 104(A10):22,401, 1999.

[154] H. De Sterck and S. Poedts. Slow shocks and space weather: 3d MHD simulations of the earth's bow shock and magnetosheath. *Submitted to J. Atmos. Solar-Terr. Phys.*, July 1999.

[155] H. De Sterck, S. Poedts, and J. P. Goedbloed. Dynamics of hot filaments in a tokamak plasma. *J. Plasma Physics*, 59/2:277–302, 1998.

[156] E.C. Stone, A.M. Frandsen, R.A. Mewaldt, E.R. Christian, D. Margolies, J.F. Ormes, and F. Snow. The advanced composition explorer. *Space Science Reviews*, 86:1, 1998.

[157] J. M. Stone, J. F. Hawley, C. R. Evans, and M. L. Norman. A test suite for magnetohydrodynamical simulations. *Astrophys. J.*, 388:415–437, 1992.

[158] J. M. Stone and M. L. Norman. ZEUS-2D: A radiation magnetohydrodynamics code for astrophysical flows in two space dimensions.

ii. the magnetohydrodynamic algorithms and tests. *Astrophys. J. Suppl.*, 80:791–818, 1992.

[159] T. Tanaka. Configurations of the solar wind flow and magnetic field around the planets with no magnetic field: calculation by a new MHD simulation scheme. *J. Geophys. Res.*, 98(A10):17,251–17,262, 1993.

[160] P. A. Thompson. *Compressible-fluid dynamics.* McGraw-Hill, New York, 1972.

[161] G. Toth, R. Keppens, and M. A. Botchev. Implicit and semi-implicit schemes in the Versatile Advection Code: numerical tests. *Astron. Astrophys.*, 332:1159–1170, 1998.

[162] G. Toth and D. Odstrcil. Comparison of some Flux Corrected Transport and Total Variation Diminishing numerical schemes for hydrodynamic and magnetohydrodynamic problems. *J. Comput. Phys.*, 128:82, 1996.

[163] K. Tsinganos, C. Sauty, G. Surlantzis, E. Trussoni, and J. Contopoulos. On the relation of limiting characteristics to critical surfaces in magnetohydrodynamic flows. *Mon. Not. R. Astron. Soc.*, 283:811–820, 1996.

[164] E. Turkel. Accuracy of schemes with non-uniform meshes for compressible fluid flows. Technical Report 85-43, ICASE Langley, VA, 1985.

[165] Y. Uchida, Y. Todo, R. Rosner, and K. Shibata. A magnetohydrodynamic model for Herwig-Haro objects: magnetically guided shocked flows associated with optical jets from young stellar objects. *Publ. Astron. Soc. Japan*, 44:227–243, 1992.

[166] S. Umemura, K. Iki, K. Shibata, and Y. Sofue. MHD shock waves through a galactic nuclear disk with a vertical magnetic field. *Publ. Astron. Soc. Japan*, 40:25–46, 1988.

[167] E. van der Weide. *Compressible flow simulation on unstructured grids using multi-dimensional upwind schemes.* PhD thesis, Technische Universiteit Delft, 1998.

[168] R. J. Walker and C. T. Russell. Solar-wind interactions with magnetized planets. In M. G. Kivelson and C. T. Russell, editors, *Introduction to space physics*, pages 164–182. Cambridge University Press, Cambridge, 1995.

[169] G. B. Whitham. *Linear and nonlinear waves.* Wiley-Interscience. John Wiley, New York, 1974.

[170] C. C. Wu. On MHD intermediate shocks. *Geophys. Res. Lett.*, 14(6):668–671, 1987.

[171] C. C. Wu. The MHD intermediate shock interaction with an intermediate wave: are intermediate shocks physical? *J. Geophys. Res.*, 93(A2):987–990, 1988.

[172] C. C. Wu. Formation, structure and stability of MHD intermediate shocks. *J. Geophys. Res.*, 95:8149, 1990.

[173] C. C. Wu. New theory of MHD shock waves. In M. Shearer, editor, *Viscous profiles and numerical methods for shock waves*, Siam Proceedings Series, pages 209–236. SIAM, Philadelphia, 1991.

[174] C. C. Wu. MHD flow past an obstacle: large-scale flow in the magnetosheath. *Geophys. Res. Lett.*, 19(2):87–90, 1992.

[175] C. C. Wu. Magnetohydrodynamic Riemann problem and the structure of the magnetic reconnection layer. *J. Geophys. Res.*, 100(A04):5579–5598, 1995.

[176] C. C. Wu and T. Hada. Formation of intermediate shocks in both two-fluid and hybrid models. *J. Geophys. Res.*, 96(A3):3769–3778, 1991.

[177] C. C. Wu and C. F. Kennel. Structural relations for time-dependent intermediate shocks. *Geophys. Res. Lett.*, 19(20):2087–2090, 1992.

[178] C. C. Wu and C. F. Kennel. Structure and evolution of time-dependent intermediate shocks. *Phys. Rev. Lett.*, 68(1):56–59, 1992.

[179] M. Yamada, H. Ji, S. Hsu, T. Carter, R. Kulsrud, N. Bretz, F. Jobes, Y. Ono, and F. Perkins. Study of driven magnetic reconnection in a laboratory plasma. *Phys. Plasmas*, 4(5):1936–1944, 1997.

[180] M. Yan and L. C. Lee. Generation of slow-mode waves in front of the dayside magnetopause. *Geophys. Res. Lett.*, 21(7):629–632, 1994.

[181] M. Yokosawa. Formation of shock wave in magnetohydrodynamical accretion onto a black hole. *Publ. Astron. Soc. Japan*, 46:73–86, 1994.

[182] T. Yokoyama and K. Shibata. Numerical simulation of solar coronal X-ray jets based on the magnetic reconnection model. *Publ. Astron. Soc. Japan*, 48:353–376, 1996.

[183] A. L. Zachary, A. Malagoli, and P. Colella. A higher-order method for multidimensional ideal magnetohydrodynamics. *SIAM J. Sci. Comput.*, 15(2):263–284, 1994.

[184] K Zumbrun and D. Serre. Viscous and inviscid stability of multidimensional planar shock fronts. *Preprint*, 1999.